Clarkson University

GAS-LIQUID-SOLID THREE-PHASE FLOWS AND PARTICLE DETACHMENT IN TURBULENT FLOWS AND PARTICLE RESUSPENSION DUE TO HUMAN WALKING

A DISSERTATION

by

Xinyu Zhang

Department of Mechanical and Aeronautical Engineering

Submitted in Partial Fulfillment of the Requirements

For the Degree of

Doctor of Philosophy

(Mechanical Engineering)

September 2009

Accept by the Graduate School

DATE DEAN

The undersigned have examined the dissertation entitled

GAS-LIQUID-SOLID THREE-PHASE FLOWS AND PARTICLE DETACHMENT IN TURBULENT FLOWS AND PARTICLE RESUSPENSION DUE TO HUMAN WALKING

presented by Xinyu Zhang, a candidate for the degree of Doctor of Philosophy, and hereby certify that it is worthy of acceptance.

_____

Date ADVISOR Prof. Goodarz Ahmadi

EXAMINING COMMITTEE

Prof. John B. McLaughlin

_____

Prof. Andrea Ferro

_____

Prof. Pier Marzocca

_____

Prof. Weiqiang Ding

_____

Abstract

This thesis contains three parts covering gas-liquid-solid flows in three–phase slurry reactors, particle removal in turbulent flows and particle resuspension and transport due to indoor human walking.

In Chapter 1, a general introduction to different sections of this thesis is presented and the objectives of the study are discussed.

In Chapter 2, An Eulerian-Lagrangian computational model for simulations of gas-liquid-solid flows in three–phase slurry reactors is developed. In this approach, the liquid flow is modeled using a volume-averaged system of governing equations, whereas motions of bubbles and particles are evaluated by Lagrangian trajectory analysis procedure. It is assumed that the bubbles remain spherical and their shape variations are neglected. The two-way interactions between bubble-liquid and particle-liquid are included in the analysis. The discrete phase equations include drag, lift, buoyancy, and virtual mass forces. Particle-particle interactions and bubble-bubble interactions are accounted for by the hard particle model approach. The bubble coalescence is also included in the model. The predicted results are compared with the experimental data, and good agreement is obtained. The transient flow characteristics of the three-phase flow are studied and the effects of bubble size on variation of flow characteristics are discussed. The simulations show that the transient characteristics of the three-phase flow in a column are dominated by time-dependent staggered vortices. The bubble plumes move along the S-shape path and exhibit an oscillatory behavior. While particles are mainly located outside the vortices, some bubbles and particles are retained in the vortices. Bubble upward velocities are much larger than both liquid and particle velocities. In the lower part of the column, particle upward velocities are slightly smaller than the liquid velocities, while in the upper part of the column, particle upward velocities are slightly larger. The bubble size significantly affects the characteristics of the three-phase flows and flows with larger bubbles appear to evolve faster.

In Chapter 3, Three phase liquid-gas-solid flows under microgravity condition is studied. The transient flow characteristics of the three-phase flow were studied and the effects of gravity, inlet bubble size and G-jitter acceleration on variation of flow characteristics were discussed. The low gravity simulations showed that most bubbles are aggregated in the inlet region. Also under microgravity condition, bubbles transient time is much longer than that in normal gravity. As a result, the Sauter mean bubble diameter, which is proportional to the transient time of the bubbles, become rather large reaches to more than 9 mm. The bubble plume in microgravity exhibits a plug type flow behavior. After bubble plume reaches the free surface, particle volume fraction increases along the height of the column. The particles are mainly located outside the bubble plume, with very few particles being retained in the plume. In contrast to the normal gravity condition, the three phases in the column are poorly mixed under microgravity conditions. The velocities of three phases were also found to be of the same order. Bubble size significantly affects the characteristics of the three-phase flows under microgravity conditions. For the same inlet bubble number density, the flow with larger bubbles evolves faster. The effect of G-jitter acceleration on the gas-liquid-particle three flows is small.

In Chapter 4, Numerical simulations of gas-liquid-solid flows in different gravity were performed. The transient flow characteristics of the three-phase flow under different gravity were studied and the effects of gravity variation were discussed. The results show that gravity variation has magnificent influence on the transient characteristics of the flow in the bubble column; The location of the maximum upward velocities of bubbles, particles and liquid can be different, because of the relaxation effects; The bubble volume fraction increases with the evolution of the flow; The Sauter mean diameter of the bubbles not only increases along the column height, but also increases with development of the flow; The phase velocities under high gravity are larger than that of the flow under low gravity; While the bubble volume fraction and the bubble diameter under high gravity are smaller than that of the flow under low gravity. For the condition of same inlet bubble number density, the flow with larger gravity evolves faster

In Chapter 5, a new rolling detachment model for particle removal in the presence of capillary forces based on the maximum adhesion resistance is developed. The new model uses an effective thermodynamic work of adhesion model that includes the effects of capillary forces generated by the formation of liquid meniscus at the interface. The JKR and DMT models for elastic particle and surface deformations and the Maugis and Pollock model for the plastic deformation are extended to include the effect of capillary forces. Under turbulent flow conditions, the criteria for incipient rolling detachments are evaluated. The turbulence burst model is used to evaluate the air velocity near the substrate. The critical shear velocities for resuspension of particles of different sizes are evaluated and the results are compared with those without capillary force. The model predictions are compared with the available experimental data and good agreement is found.

In Chapter 6**,** rolling detachment of particles from surfaces in the presence of electrostatic and capillary forces based on the maximum adhesion resistance was studied. The effective thermodynamic work of adhesion including the effects of electrostatic and capillary forces was used in the analysis. The JKR, DMT and the Maugis-Pollock models were extended to include the effect of electrostatic and capillary forces. Under turbulent flow conditions, the criteria for incipient rolling detachments were evaluated. The critical shear velocities for removal of particles of different sizes were evaluated and the results were compared with those without electrostatic and capillary forces. The results were compared with the available experimental data and good agreement was obtained.

In Chapter 7**,** particle resuspension and transport due to indoor human walking are studied numerically and experimentally. The stepping motions of the foot, down and up, are modeled using a combination of two effective circular disks. The flow generated by the squeezing film at the shoe-floor interface is assumed laminar and the corresponding velocity field is evaluated. The flow outside of the foot is modeled based on a wall jet theory. The effect of adhesion force and surface roughness is included in the analysis. The roughness parameter is assumed to have a dual-Gaussian distribution. Models for

particle detachment and resuspension are developed including the recapture effect of the falling disk. The effects of particle-wall adhesion force and the hydrodynamic drag and lift forces are included in the particle detachment model. Spreading and dispersion of resuspended particle clouds is also evaluated. Particle deposition, turbulent diffusion and Brownian diffusion are also included in the particle transport model. Comparisons of the model predictions for particle concentration in the room and for particle resuspension rate with the performed experimental data show good agreements. The simulation results show that shoe bottom roughness, foot size, walking velocity, background velocity as well as the foot stepping velocities, down and up, affect particle resuspension rate from the floor and the corresponding particle concentrations in the indoor environment.

Keywords

Numerical simulation, three phase flows, particle adhesion , particle detachment, particle resuspension, human walking

Acknowledgement

I would like to thank my advisor Professor Goodarz Ahmadi for invaluable guidance, remarkable encouragement and great patience over the years to complete this work.

I would also like to thank my examining committee: Dr. John B. McLaughlin, Dr. Andrea Ferro, Dr. Pier Marzocca and Dr. Weiqing Ding for their interest, time and advice.

Special thanks to my friends in Dr. Ahmadi's group and in Clarkson University for their helps and for the friendly environment they created.

My appreciation also goes to all my friends in U.S. and China

My heartful thanks goes to my family for their support and selflessly help.

Financial supports for this work were provided in parts by grants from the Department of Energy, NYSTAR and EPA and are greatly appreciated.

Table of Contents

List of Tables

List of Figures

CHAPTER 1. INTRODUCTION

This thesis is concerned with fundamentals of gas-liquid-solid flows in bubble columns, particle removal in turbulent flows and particle resuspension and transport due to indoor human walking. Here a brief overview is presented and thesis objectives are described.

In Chapter 2, to better understand gas-liquid-solid slurry reactors in coal conversion processes, particularly in synthetic liquid fuel production, a detailed Eulerian-Lagrangian model for liquid-gas-solid flows in three-phase slurry reactors is developed. In this model, the liquid is the continuous phase, and the bubbles and particles are treated as the dispersed discrete phases. The small bubbles are assumed to remain spherical and their shape variations are neglected. The volume averaged, incompressible, transient Navier-Stokes equation is solved for the liquid phase. The bubble and particle motions are simulated by the Lagrangian trajectory analysis procedure. Two-way coupling momentum exchange between the liquid phase and the bubbles and particles are accounted for in the continuous phase momentum equation. Forces acting on the dispersed phases include drag, lift, buoyancy, and virtual mass. A finite difference method is used to discretize the liquid phase equations on a structured equidistant grid. The discrete phase equations are solved with the Runge-Kutta and the Euler methods, for particles and bubbles, respectively. In addition to considering the interactions between particle-particle, bubble-bubble, and particle-bubble, bubble coalescence is also included. The simulation results are compared with the experimental data of Delnoij et al. (1997a) and good agreement was observed.

In Chapter 3, based on the models developed in Chapter 2, three phase liquid-gas-solid flows under microgravity condition is studied. The transient flow characteristics of the three-phase flow under zero g gravity and G-jitter acceleration were studied and the effects of gravity, inlet bubble size and G-jitter acceleration on variation of flow characteristics were discussed.

In Chapter 4, based on the models developed in Chapter 2, numerical simulations of gas-liquid-solid flows in different gravity were performed. The transient flow characteristics of the three-phase flow under 2g and 0.5g gravity were studied and the effects of gravity variation on flow characteristics were discussed.

Chapter 5 presents a study of particle removal in turbulent flows. A new model for rolling detachment of spherical particles in the presence of capillary forces for both elastic and plastic surface deformations is developed. An effective thermodynamic work of adhesion model is used to account for the effects of capillary force for hydrophilic materials. The maximum adhesion resistance moments are evaluated using the JKR and the DMT models for elastic surface deformation and the Maugis-Pollock model is used for the plastic surface deformation. The turbulence burst/inrush model is used for evaluating the near-wall velocity field. The potential for rolling detachment of spherical particles is studied and the critical shear velocities for detaching particles of various sizes are evaluated, and the results are compared with those obtained in the absence of the capillary force. It is shown that the capillary force significantly increases the particle adhesion and decreases the opportunity for resuspension. The model predictions for glass particles on glass and steel substrates are compared with the available experimental data for dry and humid air conditions.

In Chapter 6**,** Rolling detachment of particles from surfaces in the presence of electrostatic and capillary forces based on the maximum adhesion resistance was studied. The effective thermodynamic work of adhesion including the effects of electrostatic and capillary forces was used in the analysis. The JKR, DMT and the Maugis-Pollock models were extended to include the effect of electrostatic and capillary forces. In most cases of this study, the particles and substrates are made of the same material, so the electrical double layer force is neglected. Two electric fields are presented in the study, 5000 kV/m and 10000kV/m. A charge analysis for the average Boltzmann, the saturation and fixed 20 μC/g charge distributions is given. A force analysis for the electrostatic, capillary and pull-off forces is also presented and discussed. Under turbulent flow conditions, the criteria for incipient rolling detachments were evaluated. The critical

shear velocities for removal of particles of different sizes were evaluated and the results were compared with those without electrostatic and capillary forces. It was shown that the capillary and electrostatic forces significantly affected the particle adhesion and the opportunity for resuspension. The model predictions for resuspension of glass particles from a glass substrate with an average Boltzmann charge distribution were compared with the available experimental data.

In Chapter 7, resuspension, deposition and the spreading of particles from floors due to human walking are studied. A model for particle resuspension, deposition and transport is developed. The foot stepping process, down and up, is treated as the motions of two equivalent circular disks moving toward or away from the floor. The airflow generated from this squeezing film is assumed to be laminar, and the corresponding gas velocity is evaluated. The effects of grooves on the shoe bottom are accounted for in the analysis. The effect of surface roughness is included in the analysis and the roughness parameter is assumed to have a dual-Gaussian distribution. The recapture effect of the falling disk to the resuspended or detached particles is also included. The JKR adhesion theory and the hydrodynamic drag and lift forces are included in the rolling detachment model that is used in the analysis. The areas under the shoe for which the particles of different sizes are detached in one gait cycle are evaluated. Particle re-deposition, turbulent dispersion and Brownian diffusion effects are included in the model. PM concentrations in a room due to resuspension of particles of different sizes from the floor for a number of gait cycles are evaluated. Particle resuspension is also investigated experimentally while people walk in a full size chamber in a controlled lab. The particle concentrations for certain size range are measured. The model predictions for the concentration in the room and resuspension rate are compared with the experimental data and good agreement is found.

1.1 OBJECTIVES

The general objective is to develop computational tools for analyzing the details of gas-liquid-solid flows in three–phase slurry reactors, particle removal in turbulent flows

and particle resuspension and transport due to indoor human walking. The specific objects are:

Gas-liquid-solid flows in three–phase slurry reactors

The general goal is to provide a better understanding of gas-liquid-solid slurry reactors in coal conversion processes, particularly in synthetic liquid fuel production. The specific objectives are:

- To develop a computational model for analyzing gas-liquid-solid flows in the bubble column.
- To provide an understanding of the effects of superficial velocities on three phase flows in a column.
- To analyze the spatial distributions of bubble, liquid and particle velocities.
- To provide an understanding of flow patterns in the column under various conditions.

Particle removal in turbulent flows

The general goal is to provide a detailed understanding of particle detachment in turbulent flows. The specific objectives are:

- To develop a new rolling detachment model for particle removal in the presence of capillary forces including the effects of surface deformation.
- To evaluate the effect of electrostatic and capillary forces on particle detachment in turbulent flows.
- To evaluate the critical shear velocities for particles with various materials.

Particle resuspension and transport due to indoor human walking

The general goal is to provide a detailed understanding of particle resuspension and transport due to indoor human walking. The specific objectives are:

- To evaluate the flow velocity generated by the stepping motions of the foot.
- To evaluate the spreading and dispersion of resuspended particle clouds.
- To evaluate the particle resuspension rate from the floor.
- To find the parameters that affect the particle resuspension rate from the floor and the corresponding particle concentrations in the indoor environment.

CHAPTER 2. EULERIAN-LAGRANGIAN SIMULATIONS OF LIQUID-GAS-SOLID FLOWS IN THREE-PHASE SLURRY

2.1 INTRODUCTION

Three-phase flows with liquids, bubbles, and solid particles occur in a wide range of industrial processes (Fan, 1989). Important applications include three-phase slurry reactors in coal conversion processes, and in particular, in synthetic liquid fuel production. Optimization of three-phase slurry reactors requires a fundamental understanding of multiphase hydrodynamics coupled with heat and mass transfer processes. Despite a number of investigations on multiphase flows, the three-phase slurry reactor technology is far from being matured with many critical unresolved issues.

There are two main approaches to modeling multiphase flows that account for the interactions between the phases. These are the Eulerian-Eulerian and the Eulerian-Lagrangian approaches. The former is based on the concept of interpenetrating continua, for which all the phases are treated as continuous media with properties analogous to those of a fluid. The Eulerian-Lagrangian approach adopts a continuum description for the liquid phase and tracks the discrete phases using Lagrangian particle trajectory analysis.

In recent years a number of simulation results using Eulerian-Eulerian model were reported in the literature. For gas-particle flows, Sinclair and Jackson (1989) studied gas-particle flows in a vertical pipe including particle-particle interactions. Ahmadi and Ma (1990) developed a thermodynamical formulation for dispersed multiphase fluid-solid turbulent flows, which was used to study dense simple shear flows (Ma and Ahmadi, 1990). Ding and Gidaspow (1990) developed a bubbling fluidization model using kinetic theory of granular flows. Pita and Sundaresan (1993) performed numerical study on developing flow of a gas-particle mixture in a vertical riser. Abu-Zaid and Ahmadi (1992) proposed a stress transport model for rapid granular flows in a rotating frame of

reference. Abu-Zaid and Ahmadi (1996) also developed a rate-dependent model for turbulent flows of dilute and dense two-phase mixtures. Cao and Ahmadi (1995, 2000) reported their numerical simulation results for gas-particle two-phase turbulent flows in vertical, horizontal and inclined ducts. They accounted for the phasic fluctuation energy transport and interactions.

For gas-liquid flows, Gasche et al. (1990) developed a two-fluid model for bubble column reactors. Torvik and Svendsen (1990), Svendsen et al. (1992), and Hillmer et al. (1994) included the effects of turbulence kinetic energy and the dissipation rate caused by the interaction between the two phases in their models. Hjertager and Morud (1993, 1995) treated the liquid and gas phases as space-sharing interdispersed continua and described the interactions through interfacial friction terms. Sokolichin et al. (1993, 1994) reported their simulations using Eulerian-Eulerian method. Krishna et al. (1999) studied the influence of scale on the hydrodynamics of bubble columns using Eulerian-Eulerian model approach and a k-ε turbulence model. Sanyal et al. (1999) studied gas-liquid flows in a cylindrical bubble column using Eulerian-Eulerian approach and compared their result with algebraic slip mixture model. Borchers et al. (1999) discussed the applicability of the standard k-ε turbulence model in an Eulerian-Eulerian approach for simulation of bubble columns. Mudde and Simonin (1999) reported their two- and three-dimensional simulation of a meandering bubble plume using Eulerian-Eulerian method that included the k-ε turbulence model. Additional progress in simulating bubble columns were reported by Rande (1992), Grienberger and Hofman (1992), Boisson and Malin (1996), and Pfleger et al. (1999).

The accuracy of Eulerian-Eulerian approach heavily relies on the empirical constitutive equations used. Furthermore, the approach has limitations in predicting certain discrete flow characteristics. For example, particle size effect, particle agglomeration or bubble coalescence and breakage cannot be fully accounted for. The Eulerian-Lagrangian model, however, involves smaller number of empirical equations and is more suitable for providing detailed information of discrete phases. The disadvantage of this approach is its requirement for more extensive computing time.

The Eulerian-Lagrangian model has been widely used in two-phase flows. Li and Ahmadi (1992), and Kvasnak and Ahmadi (1996) simulated the instantaneous turbulent velocity field across channels and ducts using an anisotropic Gaussian random field model. Sommerfeld and Zivkovic (1992) reported a simulation of pneumatic conveying through pipe systems, in which they incorporated their particle-wall and particle-particle collision models. Using a model described by Crowe (1977), Fan et al. (1997) performed numerical simulations of gas-particle two-phase turbulent flows in a vertical pipe. Tsuji et al. (1993) provided a discrete particle simulation of two-dimensional fluidized bed using a soft particle model. Their model was further modified by Hoomans et al. (1996) and Xu and Yu (1997) who developed hard sphere collision models. Andrews and O'Rourke (1996), Snider et al. (1998) reported a multiphase particle-in-cell method for dense particulate flows. Zhang (1998) conducted a simulation of gas-particle flows in curved ducts using particle-wall and particle-particle random impact models. Patankar and Joseph (2001a,b) performed simulations of particulate flows using a Chorin-type fractional-step method for gas phase equations. Fan et al. (2001) reported simulations of particle dispersion in a three-dimensional temporal mixing layer. They found that the particle dispersion patterns were governed by the large-scale vortex structures.

Early works based on Eulerian-Lagrangian simulation models for bubbly flows include those of Webb et al. (1992), Trapp and Mortensen (1993), Lapin and Lubbert (1994), and Devanathan et al. (1995). Sokolichin et al. (1996) compared the simulation results of Eulerian-Eulerian model and Eulerian-Lagrangian model with the experimental data, but neglected bubble-bubble interactions. Delnoij et al. (1997a,b) developed an Eulerian-Lagrangian model for a bubble column operating in the homogeneous flow regime. Their simulations incorporated bubble-bubble interactions using a collision model, but ignored bubble coalescence. Lain et al. (1999) developed an Eulerian-Lagrangian approach including turbulence using the $k-\varepsilon$ turbulence model. Their model, however, neglected the effect of phase volume fractions. More recently, igonoring bubble-bubble interactions, Lapin et al. (2002) reported their Eulerian-Lagrangian simulations of slender bubble columns. Their prediction suggests that the

flow moves downwards near the axis and rises close to the wall in the lower part of the column, but in the upper part the opposite trend is observed.

While there is an extensive literature of two-phase flow model, studies of three phase flow hydrodynamics are rather limited. Gidaspow et al. (1994) described a model for three-phase-slurry hydrodynamics. Grevskott et al. (1996) developed a two-fluid model for three-phase bubble columns in cylindrical coordinates. They used a k-ε turbulence model and included bubble-generated turbulence. Mitra-Majumdar et al. (1997) proposed a computational fluid dynamic (CFD) model for examining the structure of three-phase flows through a vertical column. They suggested new correlations for the drag between the liquid and the bubbles and accounted for the particle effects on bubble motions. Recently Wu and Gidaspow (2000) reported their simulation results for gas-liquid-slurry bubble column using the kinetic theory of granular flows for particle collisions. Padial et al. (2000) performed simulations of three-phase flows in a three-dimensional draft-tube bubble column using a finite-volume technique. Gamwo et al. (2003) reported a CFD model for chemically active three-phase slurry reactor for methanol synthesis. Zhou et al. (2005) reported a second-order moment three-phase turbulence model for simulating gas–liquid–solid flows. However, all these models were based on Eulerian-Eulerian approach. Computer simulations of gas-liquid-solid flows using an Eulerian-Lagrangian model are rather limited. Only recently Zhang (1999) performed a series of simulations of three-phase flow using volume-of-fluid (VOF) method for the liquid and the gas phases and a Lagrangian method for particles. Their study, however, were limited to consideration of only a small number of bubbles.

Duineveld (1994) reported that bubble shape is related to the bubble rising velocity. The rising velocities of flat bubble are larger than those of spherical bubbles.

In this study a detailed Eulerian-Lagrangian model for liquid-gas-solid flows in three-phase slurry reactors is developed. In this model, the liquid is the continuous phase, and the bubbles and particles are treated as the dispersed discrete phases. The bubbles are assumed to remain spherical and their shape variations are neglected. The volume averaged, incompressible, transient Navier-Stokes equation is solved for the

liquid phase. The bubble and particle motions are simulated by the Lagrangian trajectory analysis procedure. Two-way coupling momentum exchange between the liquid phase and the bubbles and particles are accounted for in the continuous phase momentum equation. Forces acting on the dispersed phases include drag, lift, buoyancy, and virtual mass. A finite difference method is used to discretize the liquid phase equations on a structured equidistant grid. The discrete phase equations are solved with the Runge-Kutta and the Euler methods, for particles and bubbles, respectively. In addition to considering the interactions between particle-particle, bubble-bubble, and particle-bubble, bubble coalescence is also included. The simulation results are compared with the experimental data of Delnoij et al. (1997a) and good agreement was observed.

Because all particles and bubbles are tracked in the present model, detailed information can be predicted in this study. But on the other side, it is numerically expensive to simulate a three-phase flow with large amounts of particles and bubbles.

2.2 GOVERNING EQUATIONS AND MODELS

2.2.1 Fluid Phase Hydrodynamics

The liquid phase is described by volume averaged, incompressible, transient Navier-Stokes equations. The volume-averaged continuity equation and momentum equation are given by

$$\frac{\partial(\varepsilon_f \rho_f)}{\partial t} + \nabla \cdot (\varepsilon_f \rho_f \mathbf{u_f}) = 0 \tag{2-1}$$

and:

$$\rho_f \varepsilon_f \frac{d(\mathbf{u_f})}{dt} = -\varepsilon_f \nabla p + \nabla \cdot (\varepsilon_f \boldsymbol{\tau_f}) + \rho_f \mathbf{g} \varepsilon_f + \mathbf{P} \tag{2-2}$$

where ε_f is the liquid phase volume fraction, ρ_f is the liquid phase density, $\mathbf{u_f}$ is the fluid phase average velocity, p is pressure, **g** is the acceleration of gravity, **P** is interaction momentum per unit mass transferred from the discrete phases, and $\boldsymbol{\tau_f}$ is the liquid phase viscous stress tensor, which is assumed to obey the general Newtonian fluid form given as

$$\boldsymbol{\tau}_{\mathbf{f}} = -\frac{2}{3}\mu_f(\nabla \cdot \mathbf{u_f})\mathrm{I} + \mu_f\left((\nabla \mathbf{u_f}) + (\nabla \mathbf{u_f})^{\mathrm{T}}\right) \tag{2-3}$$

where μ_f is the liquid viscosity.

The volume fraction, ε_f, is defined as:

$$\varepsilon_f = (V_{cell} - V_d)/V_{cell} \tag{2-4}$$

where V_d is the volume occupied by the discrete phases and V_{cell} is the volume of the grid cell given as

$$V_{cell} = dxdydz \tag{2-5}$$

where dx, dy, and dz are grid size in x, y, and z direction, respectively.

2.2.2 Dispersed Phase Dynamics

The bubbles and particles are treated as discrete phases and their motions are governed by Newton's second law. i.e.,

$$m_d \frac{d\mathbf{u_d}}{dt} = \mathbf{F_d} + \mathbf{F_b} + \mathbf{F_{vm}} + \mathbf{F_l} + \mathbf{F}_{\mathrm{Int}} \tag{2-6}$$

where $\mathbf{u_d}$ and m_d are, respectively, the discrete phase velocity and mass. The terms on the right hand side of Equation (2-6) are, respectively, drag, buoyancy, virtual mass, lift and interaction forces. Here the interaction force F_{Int} includes particle-particle, bubble-bubble and particle-bubble collisions.

The drag force, $\mathbf{F_d}$, is given by

$$\mathbf{F_d} = \begin{cases} 0.125\rho_f C_D \pi d_d^2 |\mathbf{u_f} - \mathbf{u_d}|(\mathbf{u_f} - \mathbf{u_d}), & \mathrm{Re}_d \geq 1 \\ \alpha_d \pi \mu_f d_d (\mathbf{u_f} - \mathbf{u_d}), & \mathrm{Re}_d < 1 \end{cases}. \tag{2-7}$$

Here d_d is the discrete phase diameter, α_d is a phase coefficient whose value is 3 to account for the variation of the Stokes drag force for bubbles and particles in low Reynolds number flows. (α_d is used only when Re_d is smaller than 1.) In Equation (2-7), Re_d is the discrete phase Reynolds number defined as

$$\mathrm{Re}_d = \rho_f d_d \frac{|\mathbf{u_f} - \mathbf{u_d}|}{\mu_f}, \tag{2-8}$$

and C_D is the drag coefficient given as

$$C_D = f_d \frac{24}{Re_d}, \tag{2-9}$$

where f_d is given by

$$f_d = \begin{cases} 1 + 0.15\,Re_d^{0.687}, Re_d \le 1000 \\ 0.0183\,Re_d, Re_d > 1000 \end{cases}. \tag{2-10}$$

In Equation (2-6), $\mathbf{F_l}$ is the Saffman lift force given as

$$\mathbf{F_l} = 1.61 d_d^2 (\mu_f \rho_f)^{0.5} |\boldsymbol{\omega_f}|^{-0.5} [(\mathbf{u_f} - \mathbf{u_d}) \times \boldsymbol{\omega_f}], \tag{2-11}$$

where flow vorticity $\boldsymbol{\omega_f}$ is defined as

$$\boldsymbol{\omega_f} = \nabla \times \mathbf{u_f}. \tag{2-12}$$

In Equation (2-6), $\mathbf{F_b}$ is the buoyancy force given by:

$$\mathbf{F_b} = \frac{\pi d_d^{\ 3}}{6} (\rho_f - \rho_d)\mathbf{g}, \tag{2-13}$$

where ρ_d is the discrete phase density.

In Equation (2-6), $\mathbf{F_{vm}}$ is the virtual mass force given by

$$\mathbf{F_{vm}} = -\frac{1}{12} \pi d_d^3 \rho_f \frac{d}{dt} (\mathbf{u_d} - \mathbf{u_f}). \tag{2-14}$$

2.2.3 Bubble-Bubble and Particle-Particle Collisions

Bubble-bubble and particle-particle collisions are included in this study using a hard sphere collision model along the line of the model developed by Hoomans et al. (1996). The effects of the rotation of bubbles and particles, however, were neglected. Assume all the bubble-bubble and particle-particle collisions are binary collisions, and a and b are discrete phase collision pairs where both can be bubbles or solid particles, the velocities of a and b after a collision are given as

$$u_{a2} = \frac{p_x}{m_a} + u_{a1}, \quad v_{a2} = \frac{p_y}{m_a} + v_{a1}, \tag{2-15}$$

$$u_{b2} = \frac{p_x}{m_b} + u_{b1}, \quad v_{b2} = \frac{p_y}{m_b} + v_{b1}. \tag{2-16}$$

where u and v are components of velocity and subscript 1 and 2 refers, respectively, to before and after collision. In Equations (2-15) and (2-16), p_x and p_y are the tangential and normal components of the impulse and, respectively, are given by

$$p_x = \begin{cases} -\mu p_y \, \mathrm{sgn}(u_{a1} - u_{b1}) & \text{(For sliding case)} \\ -(u_{a1} - u_{b1})/B & \text{(For stick case)} \end{cases}, \tag{2-17}$$

$$p_y = -\frac{(1.+e)(v_{a1} - v_{b1})}{C}. \tag{2-18}$$

Here e is the restitution coefficient, μ is the friction coefficient, B and C are collision constants given as

$$B = \frac{1}{m_a} + \frac{1}{m_b} + \frac{R_a^2}{I_a} + \frac{R_b^2}{I_b}, \quad C = \frac{1}{m_a} + \frac{1}{m_b}, \tag{2-19}$$

where R_a and R_b are, respectively, the radii of particles a and b, and I_a and I_b are the corresponding moments of inertia given by

$$I_a = \frac{2}{5} m_a R_a^2, \qquad I_b = \frac{2}{5} m_b R_b^2. \tag{2-20}$$

The slip and stick conditions during the collision is determined according to

$$\begin{cases} |u_{a1} - u_{b1}| \geq \mu B p_y & (\textit{sliding}) \\ |u_{a1} - u_{b1}| < \mu B p_y & (\textit{sticking}) \end{cases} \tag{2-21}$$

In the analysis, restitution coefficients of 0.2 and 0.5 are, respectively, used for bubble-bubble and particle-particle collision. Friction coefficients of 0.02 and 0.1 are assumed for bubbles and particles.

Tsao and Koch (1994) pointed out that in salt water, when two bubbles collide, it is more likely that they bounce back than coalesce. Tsao and Koch (1997) reported that the critical Weber number of coalescence for a rising bubble and a stationary bubble is 1.6, and the two bubbles coalesce upon impact at Weber numbers below this value and bounce at higher Weber numbers. Duineveld (1994), however, reported a critical Weber number of 0.18 for the coalescence of two adjacent bubbles based on the relative velocities. Tsao and Koch (1997) suggested that this difference is the result of the major differences in the flow fields. For Duineveld's case, the two bubbles rise side by side, the

bubble deformation and fluid flow in the film between the two bubbles may have significant effects on the criterion for coalescence or bouncing. In the present analysis, there are thousands of bubbles in the column that are generally moving side by side. The flow in the bubble column is much more complicated and is expected to have larger effects on bubble-bubble collision process. In the present simulation, bubble coalescence is accounted by assuming that two bubbles coalesce upon impact when the Weber number less than 0.14, while they bounce for larger Weber numbers. Here the Weber number We is defined as

$$We = \frac{d_b U_b^2 \rho_f}{\gamma}, \tag{2-22}$$

where d_b is bubble diameter, U_b is bubble relative velocity, ρ_f is liquid density, γ is the surface tension.

2.2.4 Bubble-Particle Interactions

Bubble-particle interactions are included in the analysis by assuming the particles always go through the bubbles when bubble–particle collision occurs. The particle environment fluid property parameters are then changed from liquid to gas parameters until the particles leave the bubbles. Unlike bubble-bubble and particle-particle encounters, which are assumed to be binary collisions, multi-interactions between bubble and particle are accounted for in this model, which means at the same time, many particles can enter the same bubble or different bubbles. The effect of bubble-particle interface is not included in this study.

2.2.5 Coupling between Phases

Two-way coupling is included in the model. The coupling between bubbles and particles is implemented through bubble-particle interactions. When a particle enters a bubble, all the forces acting on the particles by the new gaseous environment are calculated using the bubble hydrodynamic properties. The exact force with opposite direction is then added to the bubble equation of motion.

The coupling between fluid and dispersed phases is implemented through momentum interaction term, **P**, from the discrete phase to fluid phase. **P** is the negative of the sum of all forces acting on the particles and bubbles exerted by the fluid in a certain Eulerian cell.

2.2.6 Eulerian to Lagrangian and Lagrangian to Eularian Gridmaping

Liquid phase velocities and pressure from Eulerian approach are evaluated at the face and center of the staggered grids, respectively. However, for calculating the forces acting on the bubbles and particles, the liquid velocities at the locations of bubbles and particles must be evaluated by certain interpolation technique. On the other hand, the forces acting from the bubbles and particles on the liquid phase are exerted at the bubble and particle position. To account for two-way interactions in the computation of the liquid phase motion, an interpolation technique is needed to transfer these forces onto the staggered computational grids. Here an area averaged interpolation scheme for Eulerian to Lagrangian Gridmaping is used. i.e.,

$$\phi_L = \frac{1}{dxdy}[\phi_{E1}A_3 + \phi_{E2}A_4 + \phi_{E3}A_1 + \phi_{E4}A_2], \qquad (2\text{-}23)$$

where, ϕ_L is the estimated local liquid velocity for the Lagrangian approach, $\phi_{E1} \sim \phi_{E4}$ are liquid velocities at the grid nodes of the Eulerian frame, and $A_1 \sim A_4$ are areas of cell fractions shown in Figure 2-1.

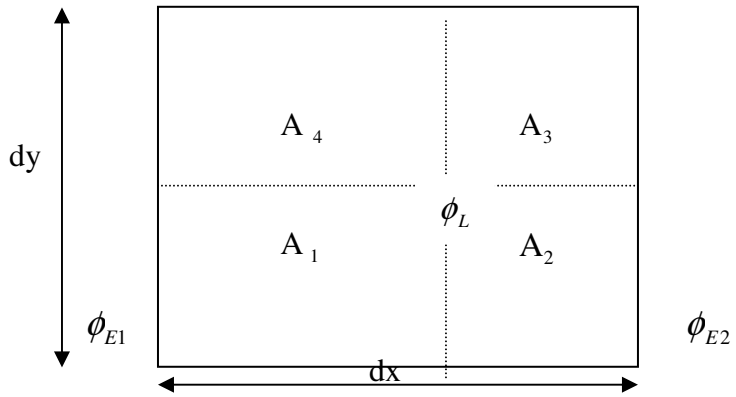

Figure 2-1. Interpolation scheme from Eulerian to Lagrangian and vice versa.

The interpolation scheme used for Lagrangian to Eularian Gridmaping reads

$$\phi_{E1} = \frac{\phi_L A_3}{dxdy}, \quad \phi_{E2} = \frac{\phi_L A_4}{dxdy}, \quad \phi_{E3} = \frac{\phi_L A_1}{dxdy}, \quad \phi_{E4} = \frac{\phi_L A_2}{dxdy}, \tag{2-24}$$

where, ϕ_L is the force acting on the bubbles and particles in the Lagrangian frame, and $\phi_{E1} \sim \phi_{E4}$ are the transmitted forces to the Eulerian grid nodes.

2.2.7 Geometry and Boundary Conditions

The present computational study was focused on a pseudo-two-dimensional bubble column with rectangular cross-section. Figure 2-2 shows the schematics of the bubble column, which was experimentally studied by Delnoij et al. (1997a). In their setup, bubbles rised through a 25cm wide, 130cm high and 2cm thick column from 14 uniformly spaced gas inlets located in the center of the column bottom surface. The distance between every two neighboring inlet was 4mm. In the simulations, identical geometry was used and neutrally buoyant particles were randomly distributed in the column at the initial time. Similar to the experiment, the continuous phase was assumed to be liquid water. The physical properties of water were kept fixed in the simulations, while the height of liquid level and the properties of particles and bubbles were varied for different cases. Table 2-1 summarizes the hydrodynamic properties of the dispersed phases for different cases studied.

The outflow condition for the liquid phase was assumed at the upper boundary of the column and no-slip boundary conditions were imposed on other walls of the column. Bubble-wall and particle-wall collisions were included in the model using a hard sphere collision model revised from the model developed by Hoomans et al. (1996) as described by equations (2-15)-(2-21), with m_a equals to infinite. The rotation of bubbles and particles, as well as, wall roughness effects was neglected. A restitution coefficient of 0.5 was used for both bubble-wall collision and particle-wall collision, while friction coefficients of 0.02 and 0.1 were assumed for bubble-wall collision and particle-wall collision, respectively.

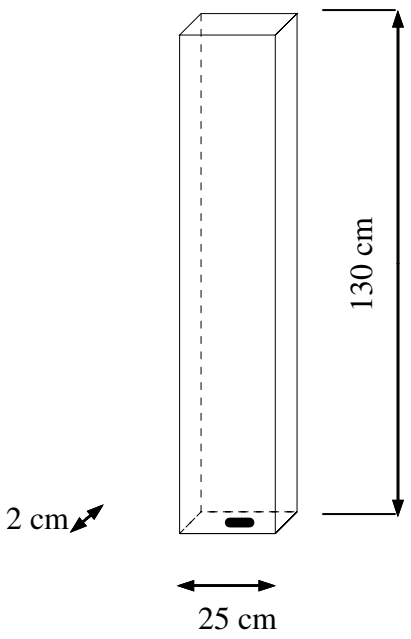

Figure 2-2. Schematics of the pseudo-two-dimensional bubble column.

Table 2-1. Hydrodynamic parameters for different cases

Case number	Bubble diameter mm	Superficial gas velocity mm/s	Bubble density kg/m^3	Particle diameter mm	Particle density kg/m^3
1	2.0	2.0	1.29	0.25	1000
2	2.0	2.0	1.29	-	-
3	1.5	0.844	1.29	0.25	1000

2.2.8 Free Surface Boundary Conditions

Proper modeling of liquid-gas free surface is important for accurate analysis of bubbly flows. The marker-and-cell (MAC) method (Harlow and Welch, 1965) was used to simulate the column free surface. The details of the MAC method were described by Griebel et al. (1998). They developed a time dependent computational model for analyzing two-dimensional single phase flow with free surface.

Neglecting the surface tension, density and viscosity of air, the boundary conditions on the free surface is givens as (Landau, 1959; Berger and Gastiaux, 1988):

$$(\boldsymbol{\tau}_f + p\mathbf{I})\cdot\mathbf{n} = 0 \qquad \text{(on the free surface)} \tag{2-25}$$

where $\boldsymbol{\tau}_f$ is the viscous stress tensor in liquid given by Equation (2-3) and $\mathbf{n} = (n_x\,\mathbf{i} + n_y\,\mathbf{j})$ is the unit normal to the free surface. ($\mathbf{i}$ and $\mathbf{j}$ are unit vectors in x and y directions.) For two-dimensional flows, the components of (2-25) in normal and tangential direction are given by

$$-p + 2\mu\left(n_x n_x \frac{\partial u}{\partial x} + n_x n_y\left(\frac{\partial u}{\partial y} + \frac{\partial v}{\partial x}\right) + n_y n_y \frac{\partial v}{\partial y}\right) = 0 \tag{2-26}$$

$$2 n_x m_x \frac{\partial u}{\partial x} + (n_x m_y + n_y m_x)\left(\frac{\partial u}{\partial v} + \frac{\partial v}{\partial x}\right) + 2 n_y m_y \frac{\partial v}{\partial y} = 0 \tag{2-27}$$

where $\mathbf{m} = (m_x\mathbf{i} + m_y\mathbf{j})$ is the unit vector tangent to the free surface.

2.2.9 Modeling Bubble-Free Surface Interaction

For a rising bubble approaching the free surface, Doubliez (1991) reported that for We < 0.28, the bubble breaks free into the free surface, while the bubble bounces for impacts at higher Weber numbers. Based on the work of Doubliez (1991), a simple model for interaction of bubbles with the free surface is used in this study. It is assumed that the bubbles that impact the column free surface with Weber number less than 0.28 will break free and leave the column, while bubbles impacting at higher Weber numbers will bounce using a hard sphere model. A Restitution coefficient of 0.2 was used for bubble-free surface collisions for We > 0.28.

2.2.10 Numerical Procedure

No current commercial codes can handle three phase flow problems using Eulerian-Lagrangian method. Therefore, a new computer code ELM3PF (Eulerian-Lagrangian Method for Three Phase Flow) for analysis of three phase flows was developed. In ELM3PF, the governing equations of the model were discretized using finite difference method in a structured equidistant staggered grid. The central and upwind (donor cell) discretization scheme was used for convective parts and an explicit time step was used

for time updating. The new code was written in C, and was based on NaSt2D code, which was a code for single-phase flows with free surface developed by Griebel et al. (1998). The new code (ELM3PF) has the capability of simulating unsteady, two dimensional three-phase liquid-gas-solid flows with free surface.

In ELM3PF, the pressure Poisson equations for liquid phase are solved using successive over-relaxation (SOR) method. A fixed time step, Δt, which typically is $0.001s$ is used for liquid phase calculation. The code calculates the liquid phase velocity field first. When the new liquid velocity field is obtained, the code evaluates, the minimum time for next collision, dt. Here, dt is the minimum time of all possible collisions including bubble-bubble collisions, particle-particle collisions, particle-bubble collisions, bubble-wall collisions and particle-wall collisions. If dt is smaller than Δt, the code computes bubble and particle velocities and positions over the time duration dt. The next collision process is then analyzed, and the corresponding discrete phase velocities after the collision are evaluated. The code then computes the next minimum time for collision and repeats this procedure until the accumulation of these dt's equals Δt. Thereafter the forces acting on the bubbles and particles are evaluated and transferred into the momentum equation for the liquid phase. The code then computes the new liquid velocity field. For a case that the minimum collision time dt is larger than Δt, the code compute the forces acting on the bubbles and particles, and transfer these forces into momentum equations for liquid phase and evaluates the new liquid velocity. Typically, 9940 bubbles and 1000 particles are used in this study. Initially particles are randomly distributed into the liquid. Initial bubble rising velocity is determined based on the given superficial gas velocity. CPU time requirement depends on the number of particles, bubbles and grid cells. For a typical number of bubbles and particles for a computational grid of 1500 cells, evaluation of one second transient behavior of the liquid-gas-solid three-phase flow requires about 4 hours CPU time on a SUN Ultra10 workstation.

2.2.11 Effect of Grid Size

In order to check the sensitivity of the simulation result on the grid size, the grid spacing was reduced by a factor of two from 1cm to 0.5cm. Comparison of the two cases

showed that the reduction of the grid size did not generate a noticeable difference in simulation results. Therefore, a grid spacing of 1cm was typically used.

2.3. RESULTS AND DISCUSSION:

2.3.1 Comparison with Experimental Data

We compared our model predictions with the experimental data of Delnoij, Kuipers and Swaaij (1997a). Their experiments were performed in a pseudo-two-dimensional bubble column. They measured the oscillation frequency of the bubble plumes in columns with five different aspect ratios for gas-liquid flows and found that a clear transition of the flow pattern occurs when the aspect ratio changes from 1 to 3. In a bubble column with an aspect ratio of 2.2, they used neutrally buoyant particles as tracer particles to visualize the liquid field. Figure 2-3 compares the present model predictions of the flow structure with the experimental data of Delnoij, et al. (1997a).

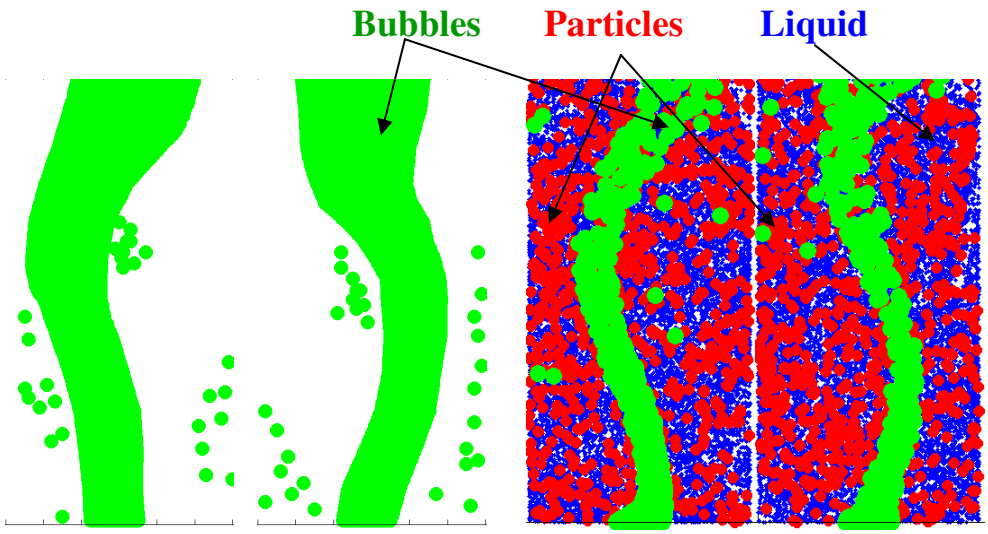

Figure 2-3. Flow structure in a three-phase bubble column with an aspect ratio of 2.2. Superficial gas velocity U_s = 2.0 mm/s, bubble size d_b = 2.0 mm.

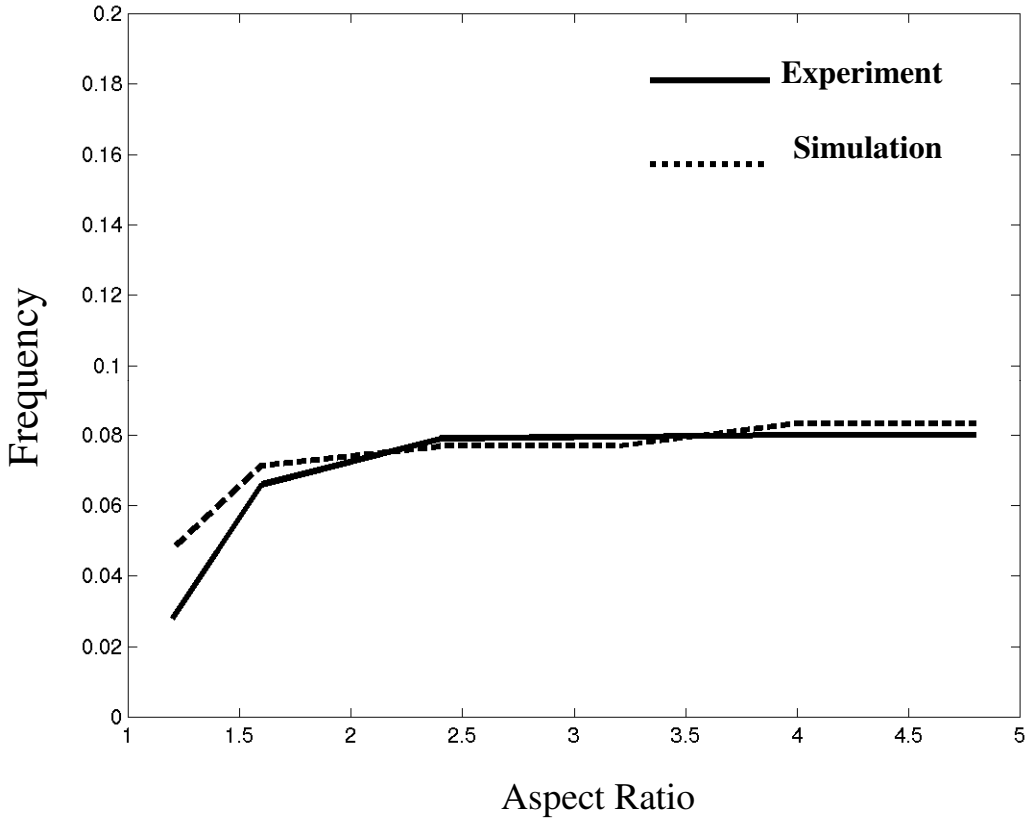

Figure 2-4. Comparison of the computed oscillation frequency of bubble plumes with the experimental data of Delnoij et al. (1997a).

Superficial gas velocity U_s = 2.0 mm/s, bubble size d_b = 2.0 mm.

The hydrodynamic parameters used in the simulation, which are identical to those of the experimental study, are listed in Table 2-1 (case 1). In Figure 3, the small dots show the liquid phase stream traces, while the small circles and the large circles show, respectively, the positions of the particles and bubbles. The model predictions appear to be in good agreement with the experimental data of Delnoij, et al. (1997a). The model not only predicts the proper S-shape path of the bubble plume, but also predicts the movements of large vortices and the oscillatory behavior of the bubble plume.

Delnoij et al. (1997a) performed a series of experiments on bubble columns with different aspect ratios and evaluated the corresponding quasi-steady frequencies of the

bubble plume oscillation. For conditions identical to the experiments, we performed a series of simulations for two-phase gas-liquid flows in the bubble column with different aspect ratios. Figure 2-4 compares the model predictions for the oscillation frequency of the bubble plumes with the experimental data of Delnoij et al. (1997a). The simulation parameters are listed in Table 2-1 (case 2). This figure shows good agreement of the model predictions for the bubble plume oscillation frequencies with the experimental data. Delnoij et al. (1997a) also performed a computer simulation that predicted the S-shape path of the bubble plumes, but their model had difficulty in predicting the evolution of the large vortical motions and the oscillatory behavior of the bubble plume in the column. Their model neglected the presence of free surface and bubble-bubble coalescence. The presently developed model includes the liquid free surface and can predict the movement of the large vortex and the oscillatory behavior of the bubble plume in the column. This implies that the column free surface has important consequences and has to be accounted for in the computational model. It appears that the fluctuations of free surface affect the motion of both the fluid phase and dispersed phases in the column.

2.3.2 Development of Transient Flow Structures

Figure 2-5 shows the snapshots of model predictions for the liquid stream traces, and the locations of bubbles and particles at times 1, 5, 9 and 13 seconds after initiation of the flow. The aspect ratio of the column is 2.2 and the values of other parameters used in the simulation are listed in Table 2-1 (case 1). The evolution of the flow structure in the bubble column can be seen from this figure. Figures 2-6, 2-7 and 2-8, respectively, show the corresponding bubble velocities, liquid velocities and particle velocities at different times. The transient characteristics of the three-phase flow are clearly seen from these figures. In the first 4 seconds, bubble plume rises rectilinearly along the centerline of the column, which generates two vortices behind the plume head as seen in Figures 2-5a and 2-7a. These vortices are symmetric in the first second after initiation of the flow, but as the bubble plume approaches the column free surface, the vortices become non-symmetric. Figure 2-7 also shows that on the liquid velocities generated by the counter rotating vortices in the bottom of the vessel point to the center of the column, which tends to move the bubbles inside toward the centerline; thus, the bubble plume shrinks in this

region. On the top, counter rotating vortices leads to liquid velocities pointing outward; this motion drags the bubbles toward the column walls. As a result, the head of the bubble plume expands, as seen more clearly in Figure 2-5. Figure 2-7d shows that when the bubble plume reaches the free surface of the column, staggered vortical flows in the column are formed. As a result, the bubble plume changes its path to S-shape that can be seen in Figure 2-5d. With the upward flow of the bubble plumes, these staggered vortices moves downward and result in an oscillation of the bubble plume as seen in Figure 2-5. Comparing Figures 2-5 and 2-7, shows that the evolution of the three-phase flow in the column is dominated by these time-dependent staggered vortices.

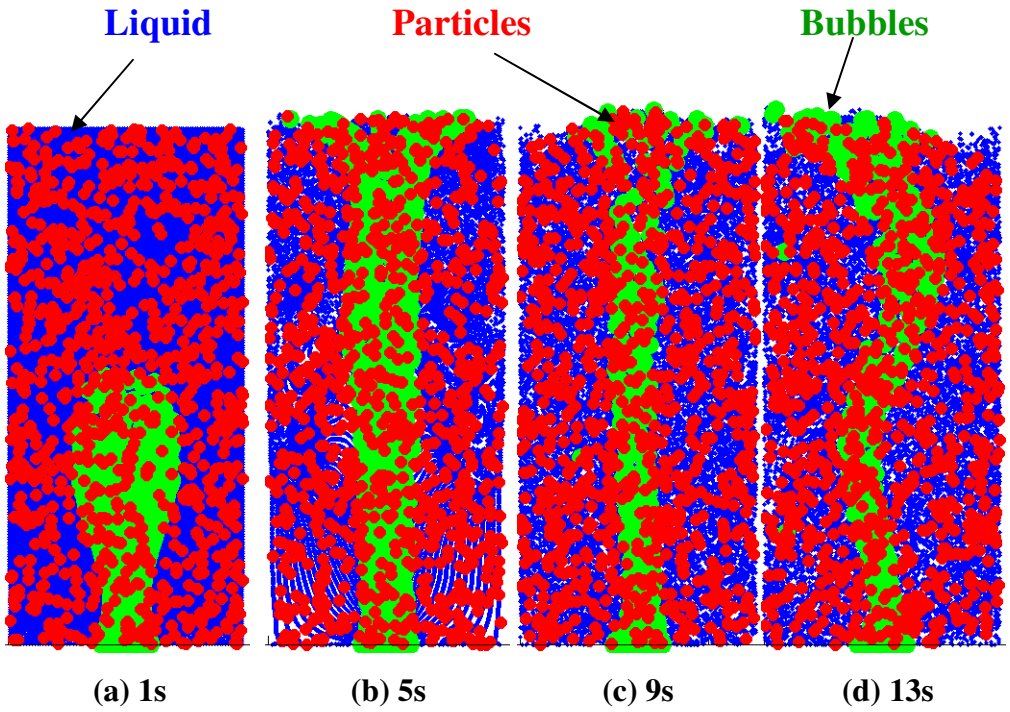

Figure 2-5. Computed flow structure of the gas-liquid-particle three-phase flow in a bubble column with an aspect ratio of 2.2. Superficial gas velocity U_s = 2.0 mm/s, bubble size d_b = 2.0 mm, particle size d_p = 0.25 mm.

Figures 2-5 and 2-7 show solid particles are concentrated mainly outside the large vortices in the regions with relatively high liquid velocities. This is, because of the centrifugal force that pushes the particles away form the center of the vortices. Some

particles are retained inside these staggered vortices, partly because of particle-particle collisions that decrease particle segregation.

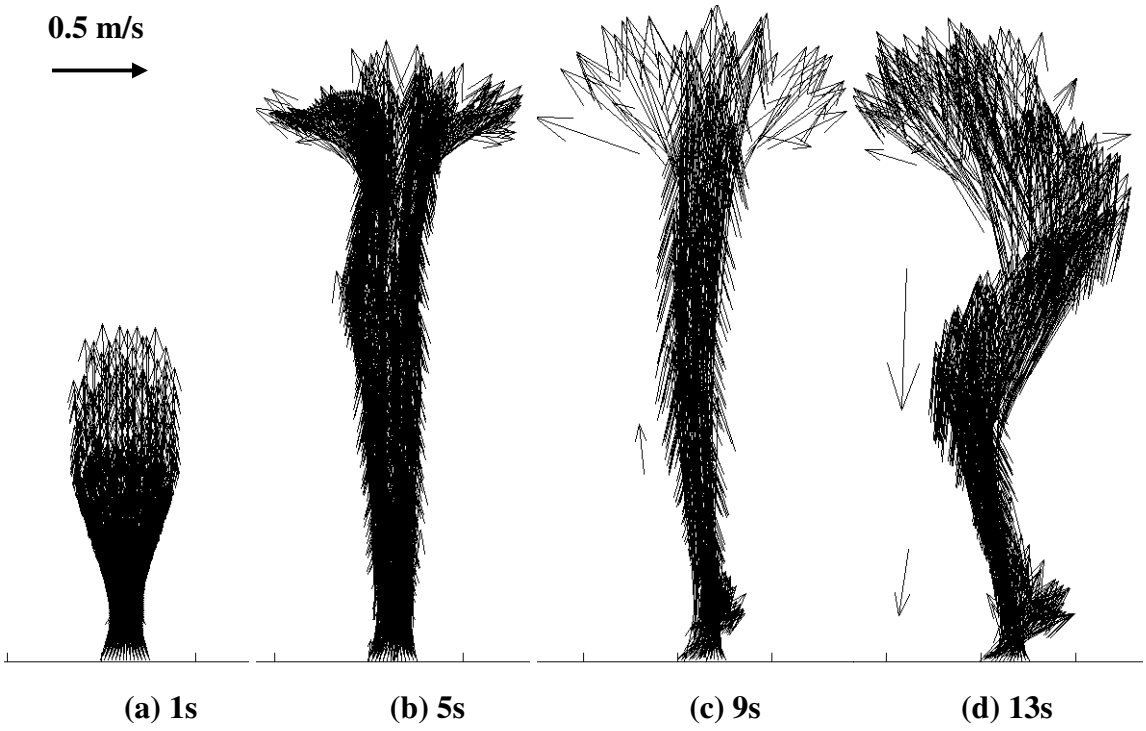

Figure 2-6. Computed snapshots of the bubble velocities of the gas-liquid-particle three-phase flow in a bubble column with an aspect ratio of 2.2. Superficial gas velocity U_s = 2.0 mm/s, bubble size d_b = 2.0mm, Particle size d_p = 0.25mm.

Comparison of Figures 2-5, 2-6 and 2-7 reveals another important feature of the three-phase flows in the column. It is seen that a number of bubbles are captured by the staggered vortices and move downward along with the vortices as shown in Figures 2-5d, 2-6d and 2-7d. In most cases, these captured bubbles are at some distance from the center of the vortices. Once those bubbles reach the bottom of the column, they turn upwards and move with the main bubble plume as seen in Figure 2-5c, 2-6c and 2-7c. Figures 2-5, 2-7 and 2-8, similarly show that particles are also captured by the vortices and are carried around by the time-dependent circulating motions. Comparing Figures 2-6, 2-7 and 2-8, also indicates that the bubble upward velocities are much larger than both particle and liquid, but bubble downward velocities are smaller than the other phases.

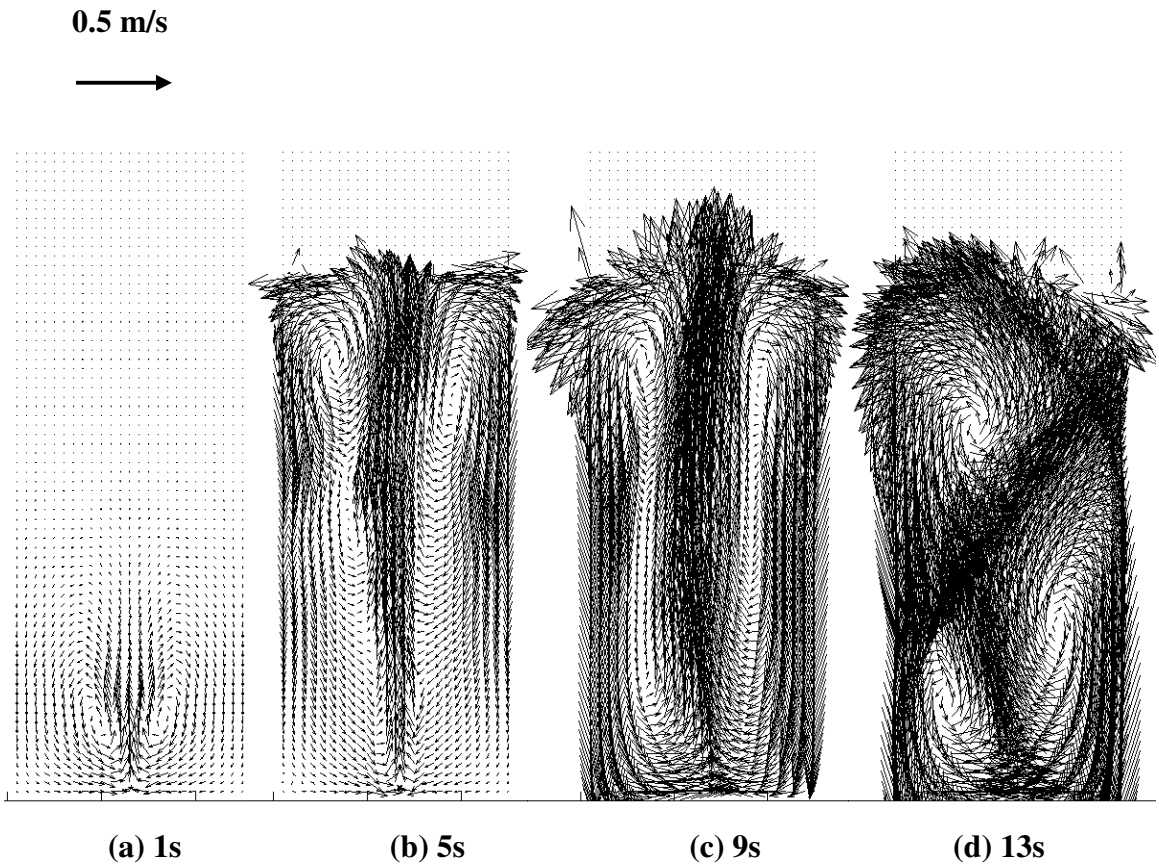

Figure 2-7. Computed snapshots of the liquid velocities of the gas-liquid-particle three-phase flow in a bubble column with an aspect ratio of 2.2. Superficial gas velocity U_s = 2.0 mm/s, bubble size d_b = 2.0mm, particle size d_p = 0.25mm.

As for the magnitudes of particle and liquid velocities, they are of the same order, with particle downward and upward velocities being generally smaller than that of liquid. In some regions, particle upward velocities can be slightly larger than liquid velocities. The differences between the liquid and particle velocities are, generally, very small.

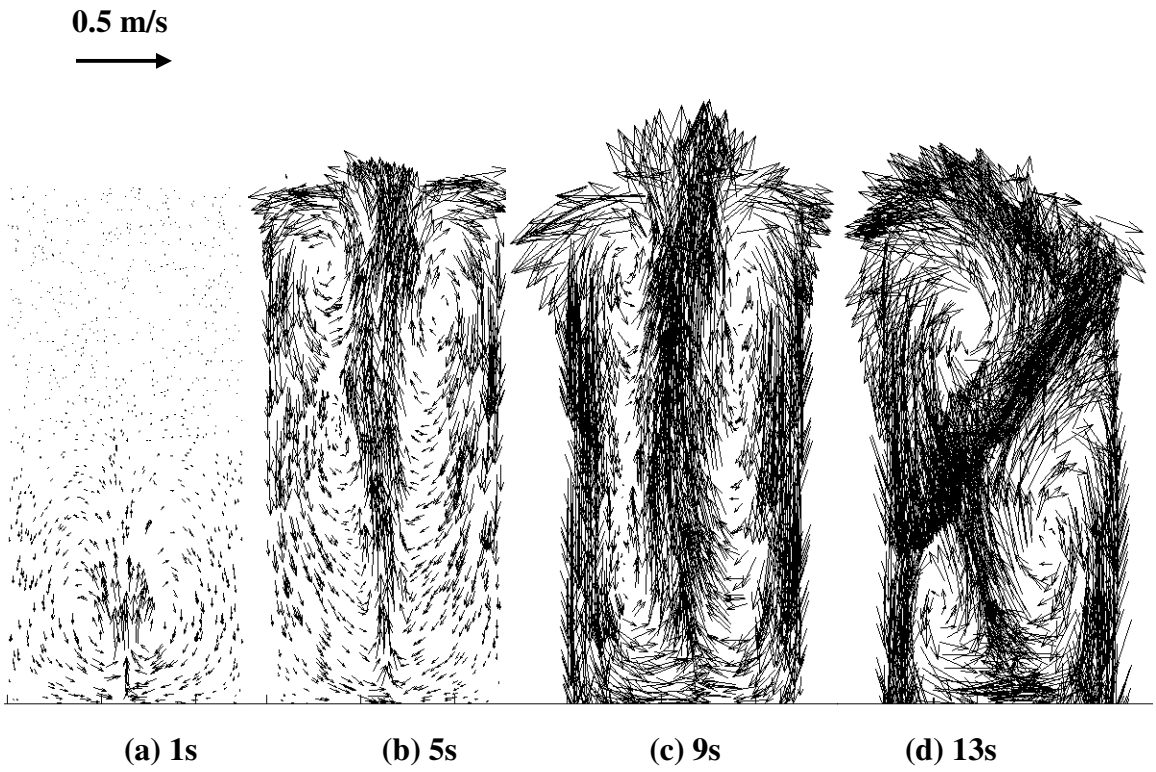

Figure 2-8. Computed snapshots of the particle velocities of the gas-liquid-particle three-phase flow in a bubble column with an aspect ratio of 2.2. Superficial gas velocity U_s = 2.0 mm/s, bubble size d_b = 2.0 mm, particle size d_p = 0.25 mm.

The reason for the observed velocity pattern can be explained by the effect of the buoyancy force of the bubbles, inertia of particles and viscosity of the liquid. The main driving force for the flow in the column is the rise of the bubbles due to the buoyancy effects. The bubbles then drag the liquid and the particles upwards along its time-evolving S-shape path. Thus, bubbles upward velocities in the column are naturally larger than both liquid and particle velocities.

In the regions outside the staggered vortices, where the liquid velocity is downward, the drag of liquid on the bubbles is also downward. The bubble buoyancy force, however, is upward, and thus the bubble can not follow the liquid closely. In this region the bubble velocities are smaller then both particle and liquid velocities.

The neutrally buoyant particles are generally being transported by the liquid, and thus the particle velocity is slightly smaller than the liquid. Occasionally particles with high velocities may entrain in low liquid velocity region. In these situations the particle local velocities may become slightly larger than the liquid phase.

Figure 2-9 shows the average velocities of the particles, bubbles and liquid at different sections across the bubble column. Here a space-time averaging method for time duration of 2 to 13 seconds was used. As expected, the bubble velocities are much larger than the particle and liquid velocities. The particle and the liquid velocities are of the same order. Along the center line of the column, all the three phase upward velocities increase with the height of the column, reaching their maximum values at the height of 0.4 m. The velocities then decrease with the height toward the free surface. Along the two side walls, the velocities are downward and the velocity magnitudes increase with the height of the column attaining their maximum values at about 0.45 m. Beyond this height, the velocities decrease toward the free surface. At the free surface the bubbles have positive net velocities as they leave the column. The horizontal component of the velocity shows that the liquid and the solid particles attain high outward velocities at the free surface. Figure 2-9 shows that the lower 2/3 height of the column, both upward velocities and downward velocities change slowly, while in the top 1/3 height of the column, the changes in velocity components are large. Figure 2-9 shows that the curves for the liquid and particle velocities are relatively smooth, while those for the bubbles are not. This is because of the statistical error to the relatively smaller number of samples for bubbles. The curves on the left side of Figure 2-9a indicate that a number of bubbles are captured by the downward moving vortices during the averaging time that the graph is generated.

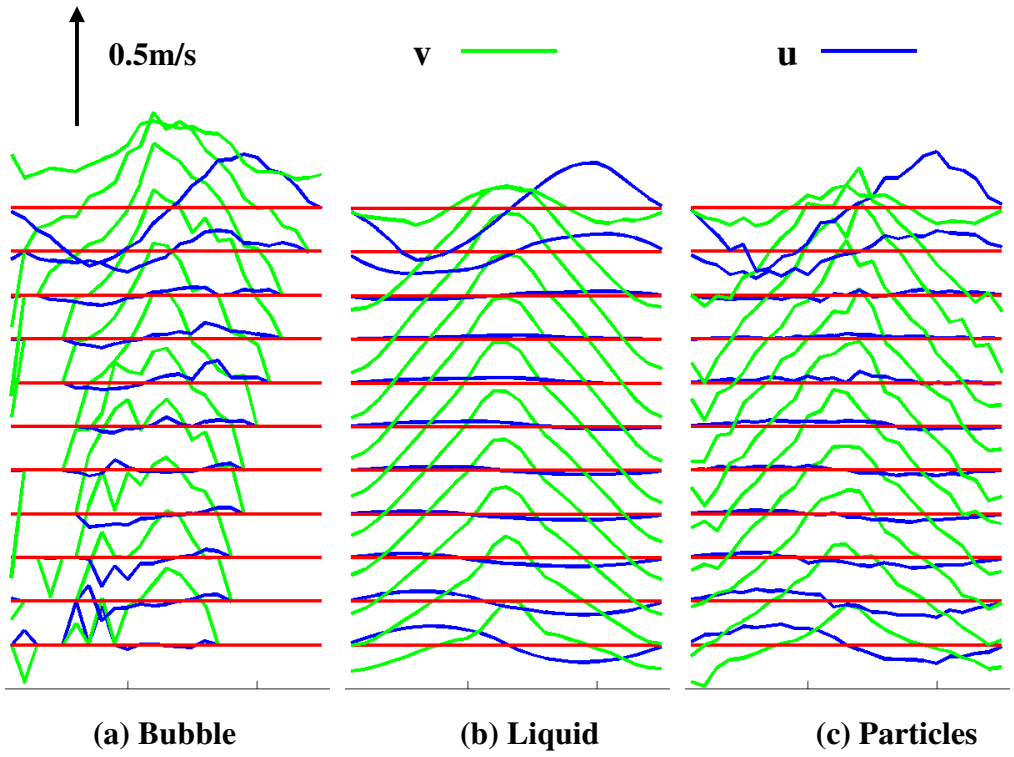

Figure 2-9. Average velocity profile of the bubbles, liquid and particles of the gas-liquid-particle three-phase flow in a bubble column with an aspect ratio of 2.2. Superficial gas velocity U_s = 2.0 mm/s, bubble size d_b = 2.0 mm, particle size d_p = 0.25 mm.

While for the simulations shown in Figures 2-6 to 2--9 particles are neutrally buoyant, particle inertia due to their finite size affect their motion characteristics. In the lower part of the column, liquid upward velocities are accelerating; thus, the particle upward velocities are slightly smaller than the liquid velocities due to particle inertia. In the upper part of the column, liquid upward velocities are decelerating, and thus the particle upward velocities are slightly larger than the liquid velocities. For the downward velocities, the trend is just opposite.

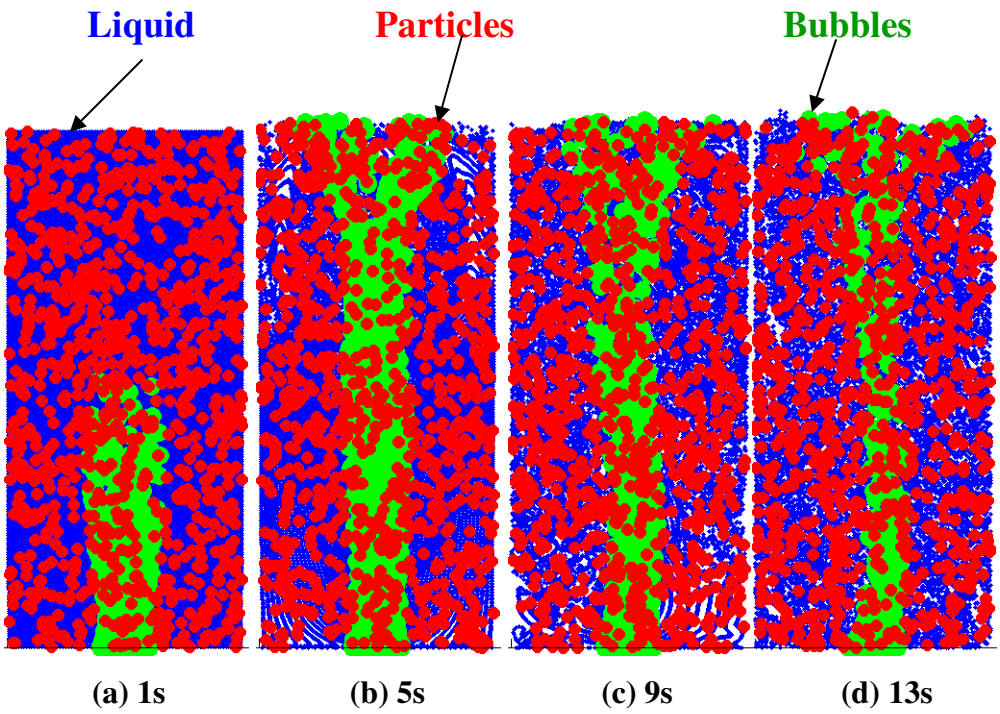

Figure 2-10. Computed flow structure of the gas-liquid-particle three-phase flow in a bubble column with an aspect ratio of 2.2. Superficial gas velocity U_s = 0.844 mm/s, bubble size d_b = 1.5 mm, particle size d_p = 0.25 mm.

2.3.3 Effect of Bubble Size on Gas-Liquid-Particle Flow

To study the effect of bubble size, a simulation was performed with the inlet bubble diameter being reduced to 1.5 mm. Other simulation parameters are listed in Table 2-1 (case 3). Figure 2-10 shows the snapshots of the flow structures of gas-liquid-particle three-phase flow with smaller bubbles. Figures 2-11, 2-12 and 2-13, respectively, show the corresponding velocities of bubbles, liquid, and particles.

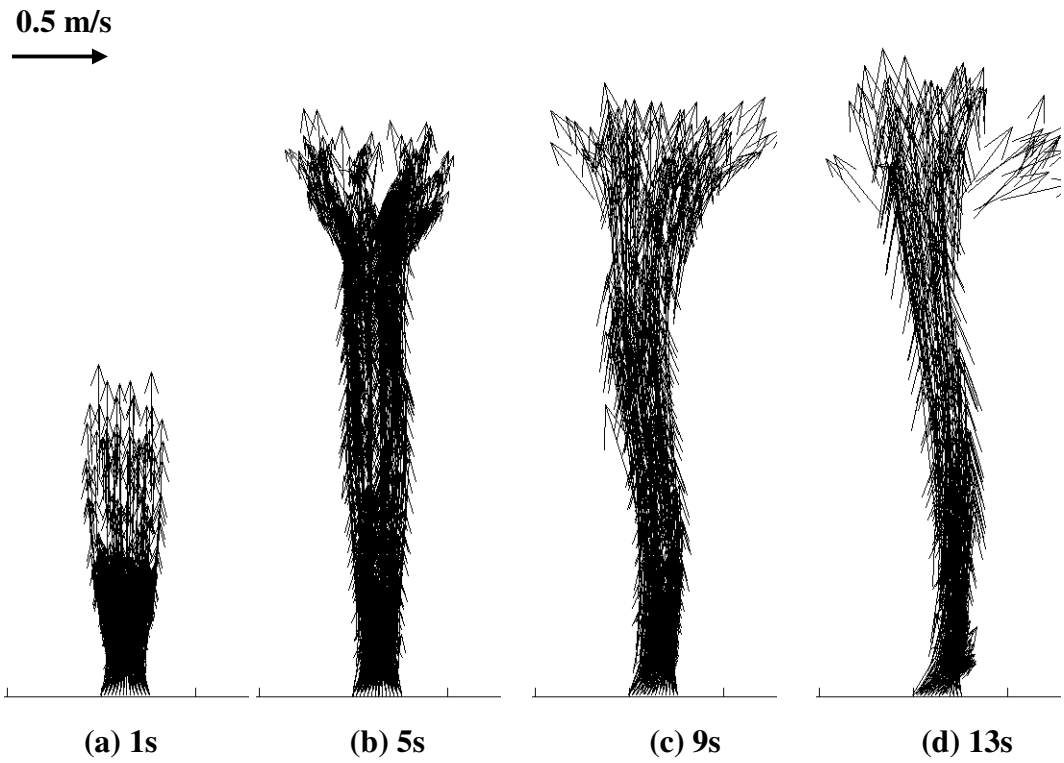

Figure 2-11. Computed snapshots of the bubble velocities of the gas-liquid-particle three-phase flow in a bubble column with an aspect ratio of 2.2. Superficial gas velocity U_s = 0.844 mm/s, bubble size d_b = 1.5 mm, particle size d_p = 0.25 mm.

Figure 2-10 and 2-12 show that solid particles are mainly located outside the large vortices and in the regions with high liquid velocities. Some particles are retained inside these staggered vortices perhaps due to particle-particle collisions. This observation is similarly to Figure 2-5 and 2-7 for larger size bubbles. Figure 2-11, 2-12 and 2-13 show bubble velocities are much larger than liquid and particle velocities, while liquid and particle velocities are of the same order, with particle downward and upward velocities being generally smaller than that of the liquid.

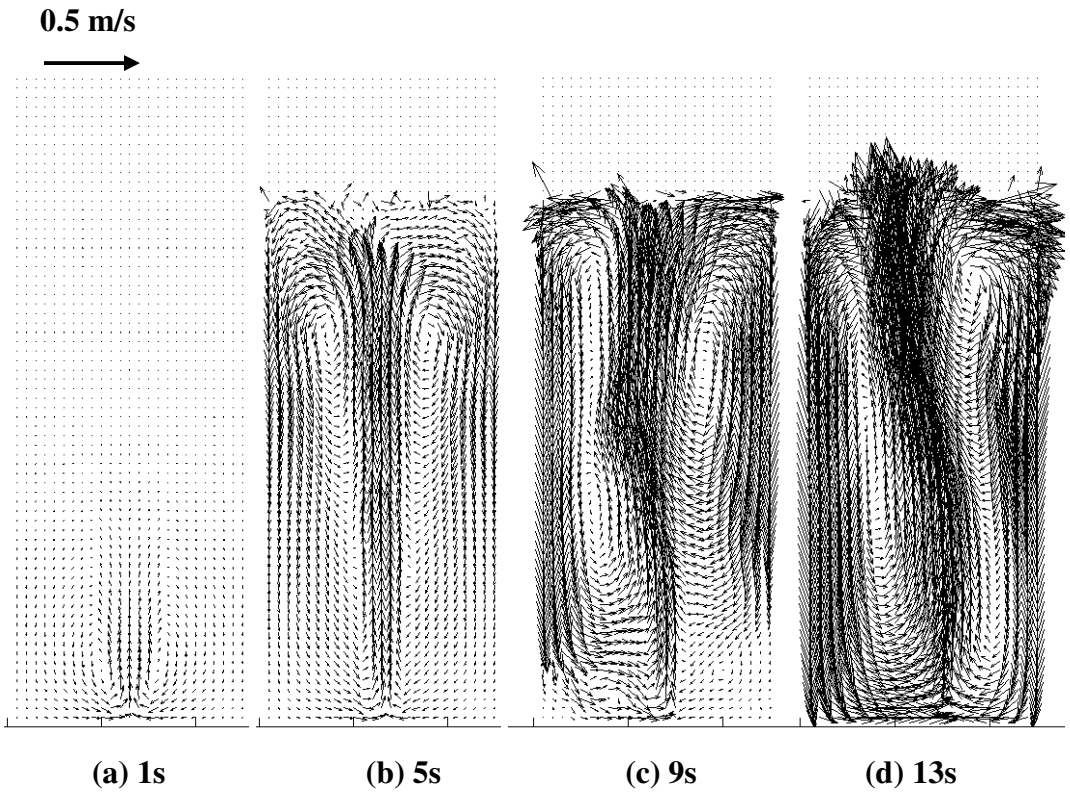

Figure 2-12. Computed snapshots of the liquid velocities of the gas-liquid-particle three-phase flow in a bubble column with an aspect ratio of 2.2. Superficial gas velocity U_s = 0.844 mm/s, bubble size d_b = 1.5 mm, particle size d_p = 0.25 mm.

Figures 2-10a and 2-10b show that the bubble plume rises rectilinearly along the centerline of the column in the first 5 seconds after initiation of the flow. Figure 2-10d shows one a slightly curved bubble plume shape but not S-shaped plume seen for larger bubbles. Figure 2-12b shows that at 5 seconds of the flow start up, the vortices formed are still symmetric, while the vortices generated by the 2mm bubble plume become non-symmetric as shown in Figure 2-7b. This implies that the flow patterns in the column seem to evolve at slower rate for 1.5 mm bubbles when compared to those for 2 mm bubbles. Clearly, compared to larger bubbles, small bubbles need more time to speed up the liquid to form the staggered vortices. Even when the staggered vortices have formed, they still need more time to become sufficiently strong to form the S-shape bubble plume in the column.

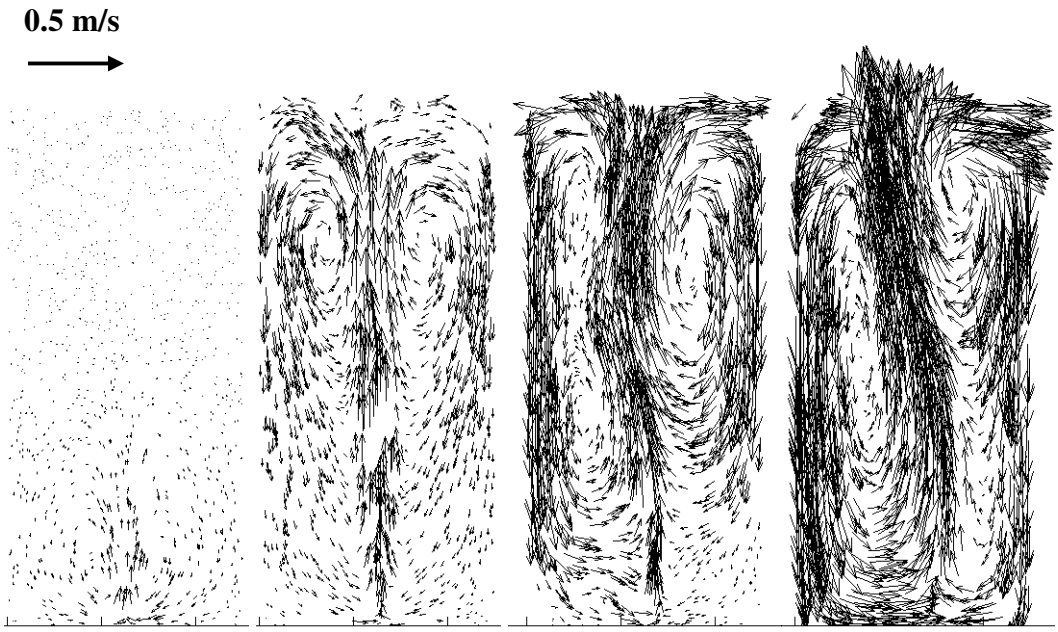

Figure 2-13. Computed snapshots of the particle velocities of the gas-liquid-particle three-phase flow in a bubble column with an aspect ratio of 2.2. Superficial gas velocity U_s = 0.844 mm/s, bubble size d_b = 1.5 mm, particle size d_p = 0.25 mm.

Compared with Figure 2-6, Figure 2-11 shows smaller bubble rising velocities. Furthermore, the bubble rising velocities increase slower with time. Since the liquid velocities are generated by the bubble motions and particles are transported by liquid, smaller bubble velocities will result in smaller liquid and particle velocities, as seen in Figures 2-12 and 2-13. Figure 11a also shows that the two vortices behind the plume head are much weaker than those in Figure 2-7a. As noted before, the expansion of the plume head is a result of outward liquid velocities on the top of the vortices; thus, weak liquid vortices result in a narrow plume head, as can be seen in Figure 2-10a. The liquid vortices in Figure 2-12 are also too weak to push the bubble plume to form into S-shape seen in Figure 2-5. Figures 2-10 and 2-11 also show that there are no isolated bubbles in the column. This is because the liquid generated vortices are not sufficiently strong to capture bubbles from the main babble plume. So although the bubble velocities will

determine the liquid velocities, the liquid velocities seem to have little effect on the shape of the bubble plume for small bubbles.

While in comparison with Figure 2-6a, Figure 2-11 shows smaller bubble rising velocities, Figure 2-5a and Figure 2-7a indicates that at the first second after initiation of flow, the height of the 2mm bubble plume and the 1.5mm bubble plume are almost same. That is, in the beginning the upward velocities of these two different size bubble plume are roughly the same. Nevertheless, the momentum transported to the liquid by 1.5mm bubbles is smaller compared to that for compared to 2mm bubbles. Thus, the liquid velocities are smaller, as seen from Figure 2-12a. In conclusion, compared to the three-phase flow with 2mm bubbles, the flow characteristics of the three-phase flow with 1.5 mm bubbles evolves slower, the bubble plume has lower oscillation frequency, and all phase velocities are smaller.

Figure 2-14 shows the average velocities of the particles, bubbles and liquid during the three-phase flows with 1.5 mm bubbles in the column. Similarly to the 2mm bubble case, it is seen that the bubble velocities are much larger than the particle and liquid velocities. The particle and the liquid velocities are of the same order. Along the center line of the column, all the three phase upward velocities increase with the height of the column and attain their maximum values at a height of about 0.4m. The velocities then decrease with further increase in height. Along the two side wall, the downward velocities of liquid and particles increase with the height of the column reaching their maximum values at about 0.45m, and then decrease toward the free surface. Figure 2-14 shows that the bubbles are concentrated in the bubble plume in the middle of the column and moving upward. Unlike for the case with 2 mm bubbles, there is no babble down ward velocity in this case. This is because no bubbles are captured by the downward moving vortices up to 13 seconds that the simulation was performed.

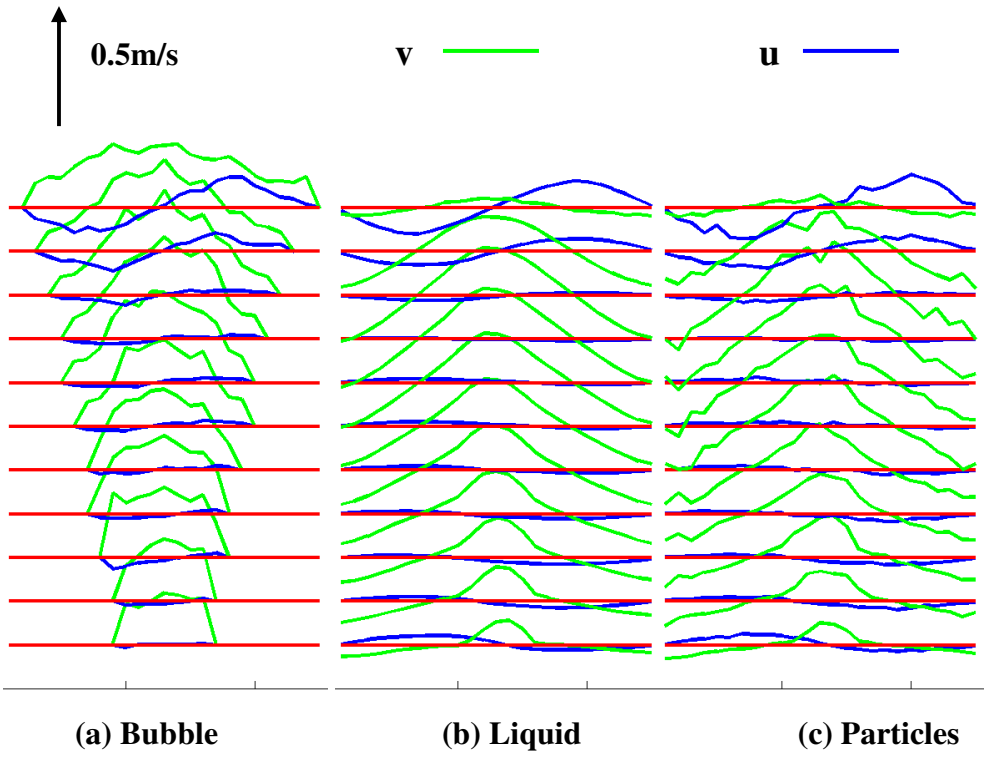

Figure 2-14. Average velocity profile of the bubbles, liquid and particles of the gas-liquid- particle three-phase flow in a bubble column with an aspect ratio of 2.2. Superficial gas velocity U_s = 0.844 mm/s, bubble size d_b = 1.5 mm, Particle size d_p = 0.25 mm.

2.4. CONCLUSIONS

In this study, an Eulerian-Lagrangian computational model for simulations of gas-liquid-solid flows in three–phase slurry reactors is presented. The two-way interactions between bubble-liquid and particle-liquid are included in the analysis. Particle-particle interactions and bubble-bubble interactions are accounted for by the hard sphere model approaches, and the bubble coalescence is also included in the model. The transient characteristics of three-phase flows are studied and the effects of bubble size on variation of flow patterns are discussed. On the basis of the presented results, the following conclusions are drawn:

1. The transient characteristics of the three-phase flow in the bubble column are dominated by time-dependent staggered vortices, which are generated near the free surface and move downwards.
2. The bubble plumes move along S-shape paths and exhibit an oscillatory behavior.
3. Highest particle concentrations occur in the region outside the staggered vortices, in the regions with high liquid velocities.
4. Most bubbles in the column form a main bubble plume, and only some bubbles are captured by the staggered vortices.
5. Bubble upward velocities are much larger than both particle and liquid velocities. The bubble downward velocities are, however, smaller than both particle and liquid velocities.
6. Bubble size has major effect on the characteristics of the three-phase flow. For the same number of bubbles, larger bubbles significantly increase the development of the flow characteristics. Compared to a column with small bubble, the column with large bubble has higher bubble, particle and liquid velocities and higher bubble plume oscillation frequency.
7. Bubble velocities determine liquid velocities, and liquid velocities can affect bubble plume shape depending on the size of the bubbles.

2.5 ACKNOWLEDGEMENT

The financial support by the Department of Energy of the United States is gratefully acknowledged.

2.6 NOMENCLATURE

$A_1 \sim A_4$	areas of small cells as shown in Figure 1, m^2
B, C	collision constants, 1/kg
C_D	drag coefficient, dimensionless
C_0	initial compression velocities, m/s^2
d_b	bubble diameter, m
d_d	discrete phase diameter, m

dt	minimum time for next collision, S
dx	grid size in x direction, m
dy	grid size in y direction, m
dz	grid size in z direction, m
e	restitution coefficient , dimensionless
f_d	coefficient used in drag coefficient calculation, dimensionless
$\mathbf{F_d}$	drag force, N
$\mathbf{F_b}$	buoyancy force, N
$\mathbf{F_l}$	Saffman force, N
$\mathbf{F_{vm}}$	virtual mass force, N
g	acceleration due to gravity force, m/s^2
I	unit matrix
I_a	moments of inertia of particle or bubble a, kgm^2
I_b	moments of inertia of particle or bubble b, kgm^2
m	tangent vector, dimensionless
m_a	mass of particle or bubble a, kg
m_b	mass of particle or bubble b, kg
m_d	discrete phase mass, kg
n	normal vector, dimensionless
P	momentum transferred from the discrete phase, N/kg
P	pressure, N/m^2
p_x	tangential components of the impulse, kgm/s
p_y	normal components of the impulse, kgm/s
R_a	radius of particle or bubble a , m
R_b	radius of particle or bubble b , m
Re	fluid phase Reynolds number, dimensionless
Re_d	discrete phase Reynolds number, dimensionless
s	sign of initial slip velocity , m/s

S_0 initial slip velocity, m/s

u_{a1}, v_{a1} velocities of particle or bubble a after the collision at collision coordinate, m/s

u_{a2}, v_{a2} velocities of particle or bubble a before the collision at collision coordinate, m/s

U_b bubble relative velocity, m/s

u_{bn}, v_{bn} velocities of particle or bubble b after the collision at collision coordinate, m/s

u_{bo}, v_{bo} velocities of particle or bubble b before the collision at collision coordinate, m/s

$\mathbf{u_d}$ discrete phase velocity, m/s

$\mathbf{u_f}$ fluid phase average velocity, m/s

V_d volume occupied by the discrete phase, m^3

V_{cell} volume of the grid cell, m^3

We weber number, dimensionless

Greek letters

α_d phase coefficient, dimensionless

ε_f liquid phase volume fraction, dimensionless

ϕ_L local liquid velocity, local liquid volume fraction or forces acting on the bubbles and particles for Lagrangian frame, m/s, dimensionless or N

$\phi_{E1} \sim \phi_{E4}$ liquid velocity, required forces or liquid volume fraction for Eulerian frame, m/s, N or dimensionless

ρ_f liquid phase density, kg/m^3

μ friction coefficient, dimensionless

μ_f liquid viscosity, $Pa \cdot s$

$\boldsymbol{\omega_f}$ liquid vorticity 1/s

ρ_d	discrete phase density, kg/ m^3
$\boldsymbol{\tau}_f$	fluid phase viscous stress tensor, N/m^2
λ_f	liquid bulk viscosity, kg/m/s
Δt	time step for liquid phase calculation, s
γ	Coefficient of surface tension, N/m

2.7 REFERENCES

Ahmadi, G. and Ma, D., 1990. A thermodynamical formulation for dispersed multiphase turbulent flows, Part I: Basic Theory. *Int. J. Multiphase Flow* **16**, pp. 323-340.

Abu-Zaid, S.and Ahmadi, G., 1992. A stress transport model for rapid granular flows in a rotating frame. *Int. J. Engng Sci*. **30** (10), pp.1483-1495.

Abu-Zaid, S. and Ahmadi, G., 1996. A rate dependent model for turbulent flows of dilute and dense two phase solid-liquid mixtures. *Powder Technology* **89**, pp. 45-56.

Andrews, M. J. and O'Rourke, P. J., 1996. The multiphase particle-in-cell (MP-PIC) method for dense particulate flows. *Int. J. Multiphase Flow* **22**, pp. 379-402.

Berger, M. and Gastiaux, B., 1988. Differential Geometry : manifolds, curves and surfaces. Spring-Verlag, New York.

Boisson, N. and Malin, M. R., 1996. Numerical prediction of two-phase flow in bubble Columns. *Intl. J. for Numerical Methods in Fluids* **23**, pp. 1289-1310.

Borchers, O., Busch, C., Sokolichin, A. and Eigenberger, G., 1999. Applicability of the stand k-ε turbulence model to the dynamic simulation of bubble, Part II: Comparison of detailed experiments and flow simulations. *Chem. Eng. Sci.* **54**, pp. 5927-5935.

Cao, J. F., and Ahmadi, G., 1995. Gas-particle two-phase turbulent flow in a vertical duct. Int. *J. Multiphase Flow*. **21** (6), pp.1203-1228.

Cao, J. F., and Ahmadi, G., 2000. Gas-particle two-phase turbulent flow in horizontal and inclined ducts. *Int. J. of Engineering Science* **38** , pp.1961-1981.

Delnoij, E., Kuipers, J. A. M. and van Swaaij, W. P.M., 1997a. Dynamic simulation of gas-solid two-phase flow: effect of column aspect ratio on the flow structure. *Chem. Eng. Sci.* **52**, pp. 3759-3772.

Delnoij, E., Lammers, F. A., Kuipers, J. A. M. and van Swaaij, W. P.M., 1997b. Dynamic

simulation of dispersed gas-solid two-phase flow using a discrete bubble model. *Chem. Eng. Sci*. **52**, pp. 1399-1562.

Devanathan, N., Dudukovic, M. P., Lapin, A. and Lubbert, A., 1995. Chaotic flow in bubble column reactors. *Chem. Engng Sci*. **50**, pp. 2661-2667.

Ding, J. and Gidaspow, D., 1990. A bubbling fluidization model using kinetic theory of granular flow, *AICHE J*. **36**, pp.523-538.

Doubliez, L., 1991. The drainage and rupture of a non-foaming liquid film formed upon bubble impact with a free surface. *Int. J. Multiphase Flow* **17**, pp. 783-803.

Fan, J., Zhang, X., Chen, L. and Cen, K.,1997. Numerical simulation and experimental study of two-phase flow in a vertical pipe. *Aerosol Sci. and Technology,* **27,** pp. 281-292.

Fan, J., Zheng, Y., Yao, J. and Cen, K., 2001. Direct simulation of particle dispersion in a three-dimensional temporal mixing layer. *Proc. R. Soc.* Lond. A **457**, pp. 2151-2166.

Fan, L.-S., 1989. Gas-Liquid-Solid Fluidization Engineering, Butterworths, Boston.

Gamwo, I.K., Halow, J.S., Gidaspow, D., and Mostofi, R., 2003. CFD Models for Methanol Synthesis Three-Phase Reactors: Reactor Optimization, Chemical Engineering Science **93**, pp. 103-112.

Gasche, H. E., Edinger, C., Kompel, H. and Hofmann, H., 1990. A fluid dynamically Based model of bubble column reactors. *Chem. Engng Technol*. **13**, pp. 341-349.

Gidaspow, D., Bahary, M. and Jayaswal, U. K.,1994. Hydrodynamic models for gas-liquid-solid fluidization. *Numerical Methods in Multiphase Flows*, FED **185**,ASME, New York, NY, pp. 117-124.

Grevskott, S., Sannas, B. H. , Dudukovic, M. P., Hjarbo, K. W. and Svendsen, H. F., 1996. Liquid circulation, bubble size distributions, and solids movement in two- and three-phase bubble columns, *Chem. Eng. Sci*. **51**, pp. 1703-1713.

Griebel, M., Dornseifer, T.and Neunhoeffer, T., 1998. Numerical Simulation in Fluid Dynamics: A practical introduction. The Society for Industrial and Applied Mathematics, Philadelphia, PA.

Grienberger, J. and Hofman, H. 1992, Investigations and modeling of bubble columns, *Chem. Engng Sci*. **47**, pp. 2215-2220.

Harlow, F. and Welch, J., 1965. Numerical calculation of time-dependent viscous

incompressible flow of fluid with free surface. *Phys. Fluid*, **8**, pp. 2182-2189.

Hillmer, G., Weismantel, L.and Hofmann, H., 1994. Investigations and modeling of slurry bubble columns. *Chem. Engng Sci.* **49**, pp. 837-844.

Hjertager, B. H. and Morud, K., 1993. Computational fluid dynamics simulation of bioreactors, in Bioreactor Performance (Edited by U. Mortensen and H. J. Noorman). Ideon, Lund.

Hjertager, B. H. and Morud, K., 1995. Computational fluid dynamics of bioreactors, *Mod. Indent. Control*. **16**, pp. 177.

Hoomans, B. P. B., Kuipers, J. A. M. and Briels, W. J., 1996. Discrete particle simulation of bubble and slug formation in a two-dimensional gas-fluidized bed: a hard-sphere approach. *Chem. Eng. Sci*. **51**, pp. 99-118.

Kvasnak, W. and Ahmadi, G., 1996. Deposition of ellipsoidal particles in turbulent duct Flows. *Chem. Eng. Sci*. **51**, pp. 5137-5148.

Krishna, R., Urseanu, M. I., van Baten, J. M., and Ellenberger, J., 1999. Influence of scale on the hydrodynamics of bubble columns operating in the churn-turbulent regime: experiments vs. Eulerian simulations. *Chem. Eng. Sci*. **54**, 4903-4911.

Landau, L., 1959. Course of theoretical physics /6. Fluid Mechanics. Pergamon Press, Oxford.

Lapin, A. and Lubbert, A., 1994. Numerical simulation of the dynamics of two phase gas-liquid flows in bubble columns. *Chem. Eng. Sci.* **49**, pp. 3661-3684.

Li, A., and Ahmadi, G., 1992. Dispersion and deposition of spherical particles from point sources in a turbulent channel flow. *Aerosol Sci. and Technol*. **16**, pp. 209-226.

Ma, D. and Ahmadi, G.,1990. A thermodynamical formulation for dispersed multiphase turbulent flows, Part II: Simple shear flows for dense mixtures. *Int. J. Multiphase Flow*, **16**, (2), pp. 341-351.

Mitra-Majumdar, D., Farouk, B. and Shah, Y. T., 1997. Hydrodynamic modeling of three-phase flows through a vertical column. *Chem. Eng. Sci*. **52**, pp. 4485-4497.

Mudde, R. F., and Simonin, O., 1999. Two- and three-dimensional simulations of a bubble plume using a two-fluid model. *Chem. Eng. Sci*. **54**, pp. 5061-5069.

Padial, N. TVanderHeyden, ., W. B., Rauenzahn, R. M. and Yarbo, S. L., 2000. Three-Dimensional simulation of a three-phase draft-tube bubble column. *Chem. Eng. Sci*.

55, 3261-3273.

Patankar, N. A. and Joseph, D. D., 2001a. Modeling and numerical simulation of particulate flows by the Eulerian-Lagrangian approach. *Int. J. Multiphase Flow* **27**, pp. 1659-1684.

Patankar, N. A. and Joseph, D. D., 2001b, Lagrangian numerical simulation of particulate Flows. *Int. J. Multiphase Flow* **27**, pp. 1685-1706.

Pfleger, D., Gomes, S., Gilbert, N. and Wagner, H.-G., 1999. Hydrodynamic simulations of laboratory scale bubble columns fundamental studies of the Eulerian-Eulerian modeling approach. *Chem. Eng. Sci.* **54**, pp. 5091-5099.

Pita, J. A. and Sandaresan, S., 1993. Developing flow of a gas-particle mixture in a vertical riser, *AICHE* J. **39**, pp. 541-552.

Ranade, V. V., 1992. Flow in bubble column: some numerical experiments. *Chem. Engng Sci.* **47**, pp. 1857-1869.

Sanyal, J., Vasquez, S., Roy, S., and Dudukovic, M. P., 1999. Numerical simulation of gas-liquid dynamics in cylindrical bubble column reactors. *Chem. Eng. Sci*. **54**, pp.5071-5083.

Sinclair, J. L. and Jackson, R., 1989. Gas-particle flow in a vertical pipe with particle-particle interactions. *AICHE J*. **35**, pp. 1473-1486.

Snider, D. M., O'Rourke, P. J. and Andrews, M. J., 1998. Sediment flow in inclined vessels calculated using a multiphase particle-in-cell model for dense particle flow. *Int. J. Multiphase Flow* **24**, pp. 1359-1382.

Sokolichin, A., Becker, S. and Eigenberger, G., 1993. Modellierung und numerische simulation von G/L Blasen-Stromungen. *Chem. Ing. Techn*. **66**, pp. 505-510.

Sokolichin, A. and Eigenberger, G., 1994. Gas-liquid flow in bubble columns and loop reactor: Part I. Detailed modeling and numerical simulation. *Chem. Eng. Sci.* **49**, pp. 5735-5746.

Sommerfeld, M. and Zivkovic, G., 1992. Recent advances in the numerical simulation of pneumatic conveying through pipe systems. *Computational Methods in Applied Sciences,* Ch. Hirsch (Editor), pp. 201-212.

Svendsen, H. F., Jakobsen, H. A. and Torvik, R., 1992. Local flow structures in internal loop and bubble column reactors. *Chem. Eng. Sci.* **47**, pp. 3297-3304.

Torvik, R. and Svendsen, H. F., 1990. Modeling of slurry reactors, A fundamental Approach. *Chem. Eng. Sci*. **45**, pp. 2325-2238.

Trapp, J. A. and Mortensen, G. A., 1993. A discrete particle model for bubble slug two phase flow. *J. Comp. Phys*. **107**, pp. 367-377.

Tsao H-K, Koch D.L. 1994. Collisions of slightly deformable, high Reynolds number bubbles with short-range repulsive forces. *Phys. Fluids 6:2591–605*

Tsao, Heng-Kwong and Koch, D. L., 1997, Observations of high Reynolds number bubbles interacting with a rigid wall. *Phys. Fluids* **9** (1), January, pp. 44-56.

Tsuji, Y., Kawaguchi, T. and Tanaka, T., 1993. Discrete particle simulation of two dimensional fluidized bed. *Powder Technol*. **77**, pp. 79-87.

Webb, C., Que, F. and Senior, P. R., 1992. Dynamic simulation of gas-liquid dispersion behavior in a 2-D bubble column using a graphics mini-supercomputer. *Chem. Eng. Sci.* **47**, pp. 3305-3312.

Wu, Y., Gidaspow, D., 2000. Hydrodynamic simulation of methanol synthesis in gas-liquid slurry bubble column reactors. *Chem. Eng. Sci*. **55**, pp. 573-587.

Xu, B. H. and Yu, A. B., 1997. Numerical simulation of the gas-solid flow in a fluidized bed by combing discrete particle method with computational fluid dynamics. *Chem. Eng. Sci.* **52**, pp. 2785-2809.

Zhang, J. P, 1999. Discrete phase simulation of bubble and particle dynamics in gas-liquid-solid fluidization systems. Ph.D. thesis, The Ohio State University.

Zhang, X., 1998, Study of gas-solid multiphase flow characteristics in impact rich/lean burners and curved ducts, Ph.D. dissertation, Zhejiang University, Hangzhou, Zhejiang, P. R. China.

Zhou, L., Yang, M. and Fan L., 2005. A second-order moment three-phase turbulence model for simulating gas–liquid–solid flows. *Chem. Eng. Sci*. **60**, pp. 647-653.

The content of this chapter is published in Chemical Engineering Science 60 (2005) 5089-5104.

CHAPTER 3. NUMERICAL SIMULATIONS OF LIQUID-GAS-SOLID THREE-PHASE FLOWS IN MICROGRAVITY

3.1 INTRODUCTION

Despite a number of related studies, the three-phase slurry reactor technology is far from being matured with many unresolved issues. In particular, the characteristics of the three-phase flows under microgravity conditions are poorly understood. Three-phase slurry reactors, however, is expected to be a key components of air revitalization and air purification devices critical to NASA's plan for long duration human space travel.

In this study the earlier developed computational model in Chapter 2 was used. While the study was focused on the zero gravity case, a sample case with normal gravity was also analyzed. The transient characteristics of three-phase flows were studied and the effects of gravity, bubble size and G-jitter acceleration under microgravity condition were analyzed.

3.2 GOVERNING EQUATIONS AND MODELS

Details of governing equations and model assumptions were described in Chapter 2. Particle-bubble interactions are included in the analysis by assuming the particles always go through the bubbles when Particle-bubble collision occurs. The particle environment fluid property parameters are then changed from liquid to gas parameters until the particles leave the bubbles, which means that using gas parameters to calculate the forces exerted on the particles, then these forces are coupled back to the bubbles it collide with. The effect of bubble-particle interface is not included in this study. The notations used here are also same as those used in Chapter 2.

In the present study a pseudo-two-dimensional bubble column with a rectangular cross-section is considered. Figure 3-1 shows the schematics of the bubble column. This column is similar as the one used in Chapter 2 (Figure 2-2), only difference is the height of this column is 75cm, not 130cm. The initial liquid level was assumed to be 55cm high, while the gravity as well as bubbles initial diameter were varied for different

cases. Table 3-1 summarizes the hydrodynamic properties of the dispersed phases for different cases studied. The study was focused on the comparison of the three-phase flows in the bubble column under microgravity and normal gravity conditions.

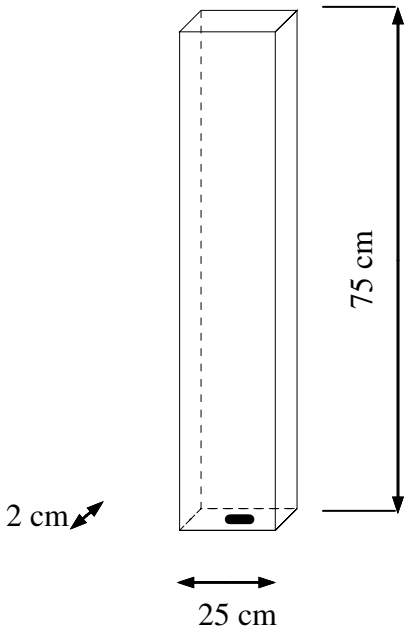

Figure 3-1. Schematics of the pseudo-two-dimensional bubble column.

Table 3-1. Hydrodynamic parameters for different cases

Case number	Bubble diameter mm	Superficial gas velocity mm/s	Bubble density kg/m^3	Particle diameter mm	Particle density kg/m^3	Gravity m/s^2
1	1.0	0.25	1.29	0.25	1000	-9.8
2	1.0	0.25	1.29	0.25	1000	0.0
3	3.0	6.75	1.29	0.25	1000	0.0
4	3.0	6.75	1.29	0.25	1000	G-jitter

3.3. RESULTS AND DISCUSSION:

3.3.1 Development of Transient Flow Structures with Normal Gravity

To study the effect of gravity on the flow characteristics, a sample reference case with normal gravity is first presented. The hydrodynamic parameters used in the simulation are listed in Table 3-1 (case 1). Figure 3-2 shows the snapshots of the model predictions for the liquid stream traces, and the locations of bubbles and particles at times of 1, 9, 22 and 30 s after initiation of the flow. In Figure 3-2, the small dots show the liquid phase stream traces, while the small circles and the large circles show, respectively, the positions of the particles and the bubbles. This figure shows the evolution of the flow structure in the bubble column. Figures 3-3, 3-4 and 3-5, respectively, show the corresponding bubble velocities, liquid velocities and particle velocities at different times. The transient characteristics of the three-phase flow can clearly be seen from these figures. In the first 22 s, bubble plume rises rectilinearly along the centerline of the column, which generates two vortices behind the plume head. These vortices are almost symmetric in the first 22 s, but with the further development of the bubble plume, the vortices become non-symmetric. As seen from Figure 3-4d, eventually staggered vortical flows form in the column. As a result, the bubble plume changes its path to S-shape that can be seen in Figure 3-2d. With the upward flow of the bubble plumes, these staggered vortices moves downward and result in an oscillation of the bubble plume. Figure 3-4 also shows that the liquid velocities generated by the counter rotating vortices in the bottom of the column point toward the center of the column. This tends to move the bubbles toward the centerline, and thus the bubble plume shrinks in this region. On the column top, however, opposite trend exists that drags the bubbles toward the column walls. As a result, the head of the bubble plume expands, as is seen in Figure 3-2. Comparing Figures 3-2 with 3-4, shows that the evolution of the three-phase flow in the column is controlled by these time-dependent staggered vortices.

Figures 3-2, 3-4 and 3-5 show solid particles are mainly concentrated in the region outside the large vortices. This is due to the effect of the centrifugal force that tends to move the particles away form the center of the vortices. Some particles are retained inside these staggered vortices, partly due to particle-particle collisions.

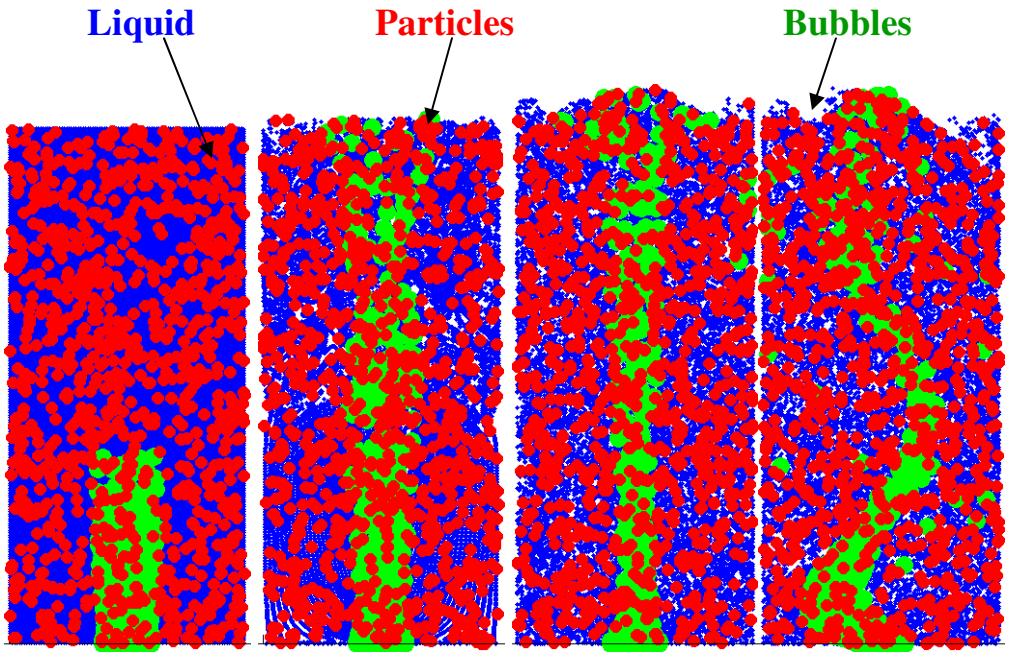

Figure 3-2. Computed flow structure of the gas-liquid-particle three-phase flow under normal gravity. Superficial gas velocity, U_s = 0.25mm/s, initial bubble size, d_b = 1.0 mm, particle size, d_p = 0.25 mm.

Figures 3-2, 3-3 and 3-4 reveal that a number of bubbles are captured by the staggered vortices and move with the vortices as is seen from Figures 3-2c, 3-2d, 3-3c, 3-3d, 3-4c and 3-4d. In general, these captured bubbles are at some distance from the center of the vortices. Similarly, Figures 3-2, 3-4 and 3-5 show that some particles are also captured by the vortices and are carried around by the time-dependent circulating motions. Comparison of Figures 3-3, 3-4 and 3-5 indicates that the bubble upward velocities are much larger than both particle and liquid velocities, but bubble downward velocities are smaller than the other phase velocities.

Figures 3-4 and 3-5 show that the magnitudes of particle and liquid velocities are of the same order, with particle downward and upward velocities being somewhat smaller than that of liquid. In some regions, however, particle upward velocities can be slightly

larger than the liquid velocities. In general, the differences between the liquid and particle velocities are very small.

The observed velocity characteristics of the three-phase flow can be explained by the effect of the bubble buoyancy force, particle inertia and liquid viscosity. The bubble buoyancy is the main driving force for the flow under normal gravity condition. The bubbles drag the liquid and the particles upwards along its time-evolving S-shape path. Thus, bubbles upward velocities in the column are larger than both liquid and particle velocities. While in the regions outside the staggered vortices, the liquid velocity is downward, the drag of liquid on the bubbles is also downward, but the bubble buoyancy

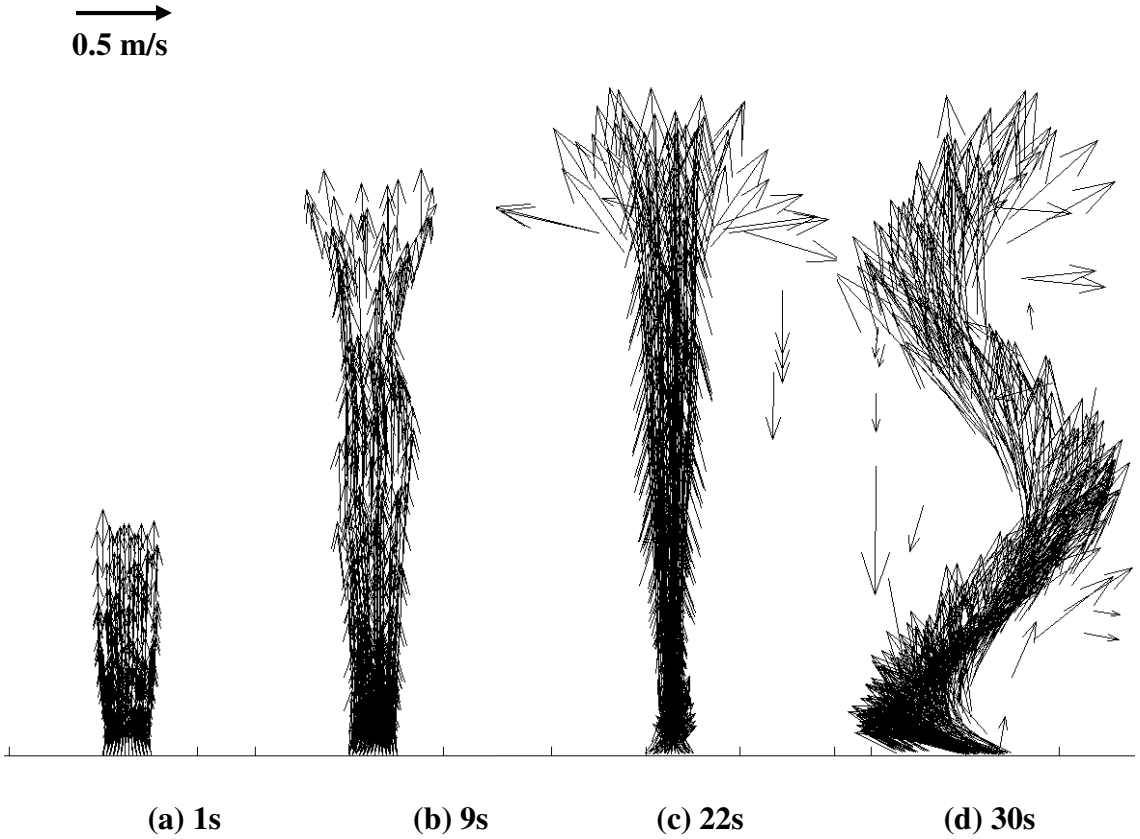

Figure 3-3. Computed snapshots of the bubble velocities of the gas-liquid-particle three-phase flow under normal gravity. Superficial gas velocity, U_s = 0.25 mm/s, initial bubble size, d_b = 1.0 mm, particle size, d_p = 0.25 mm.

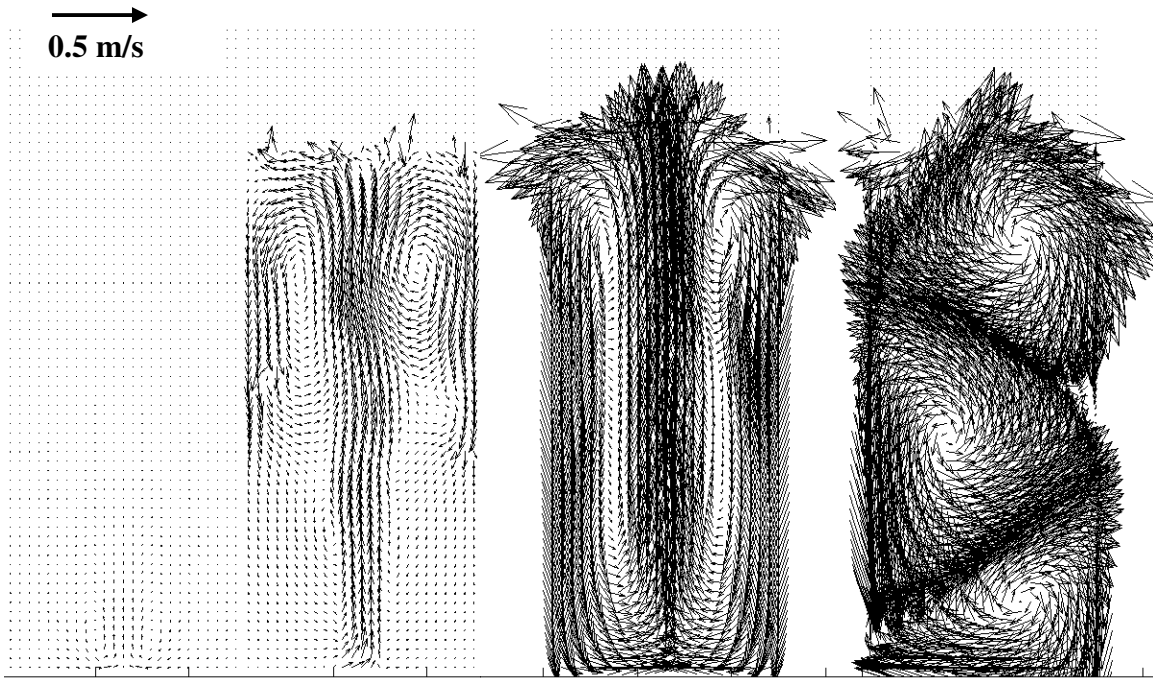

Figure 3-4. Computed snapshots of the liquid velocities of the gas-liquid-particle three-phase flow under normal gravity. Superficial gas velocity, U_s = 0.25 mm/s, initial bubble size d_b = 1.0 mm, particle size d_p = 0.25 mm.

force is upward; thus, the bubble can not follow the liquid closely. Therefore, in this region the bubble velocities are smaller then both particle and liquid velocities.

Because the neutrally buoyant particles are generally transported by the liquid, the particle velocity is slightly smaller than the liquid. However, particles with high velocities may entrain in low liquid velocity region; in these situations, the particle local velocities may become slightly larger than the liquid phase.

Figures 3-6 and 3-7, respectively, show average volume fractions of the bubbles and particles along the column height. Here, a and b, respectively, refer to the time period 5-20 s and 20-30 s. As expected, comparison of Figure 3-6a and 3-6b indicates that the bubble volume fraction increases with time. The reason is that with the evolution of the

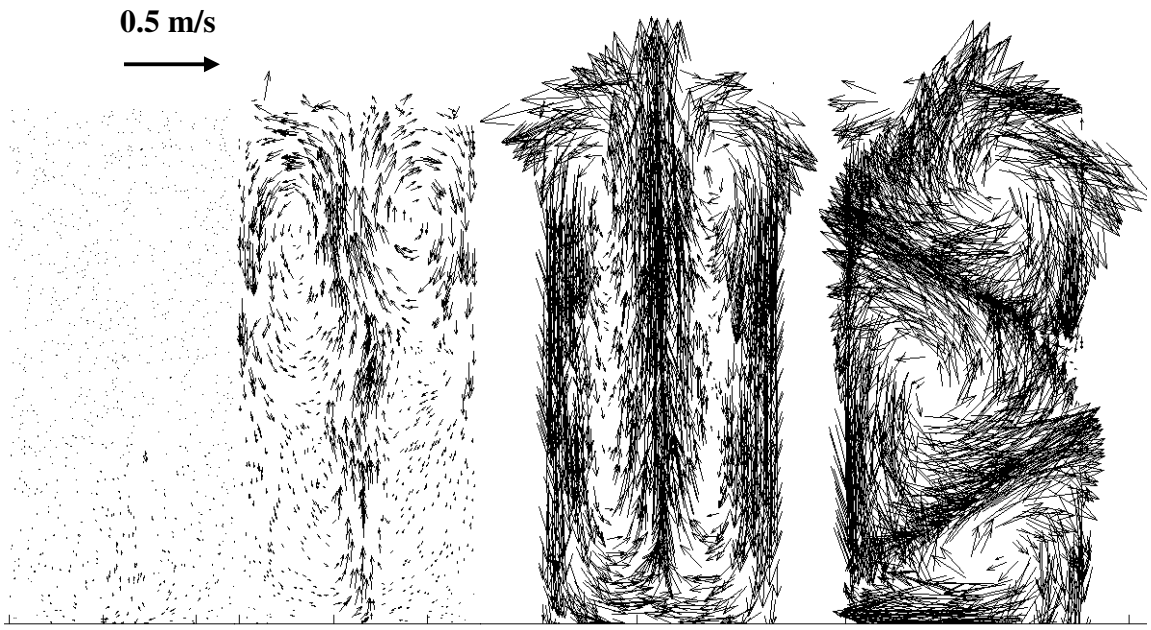

Figure 3-5. Computed snapshots of the particle velocities of the gas-liquid-particle three-phase flow under normal gravity. Superficial gas velocity, U_s = 0.25 mm/s, initial bubble size, d_b = 1.0 mm, particle size, d_p = 0.25 mm.

flow, the developed S-shape plume contains much more bubbles. Besides, the separated bubbles also make some contributions to the increase of the bubble volume fraction. Figure 3-6 also shows that, along the height of column, bubble volume fraction at the bottom are highest, it decreases from the bottom and reaches to its minimum value at about the two-third height of the column, and then increases toward the column top. This trend may be explained by variation of bubble upward velocity in the column. As seen from Figure 3-3c and 3-3d, bubble upward velocities increase along the column, attain its maximum at about two-third of the column height, and then decrease along the column height toward the free surface. A larger bubble upward velocity implies a shorter residence time, and leads to lower bubble volume fraction. Another reason for the observed bubble volume fraction profile could be the result of the presence of staggered vortices in the column.

Figure 3-7 shows the variation of the particle volume fraction in the column. For the time duration of 5-20 s, Figure 3-7a shows that the particle concentration is rough constant except for a relative high peak near the bottom of the column. As seen form Figures 3-4a and 3-4b, at the initial state of flow development, the liquid velocity near the bottom of the column is not very large. The particles are transported by the downward liquid velocities and collide with the bottom wall of the column. These particles lose their momentum and stay near the wall. As a result, the particle volume fraction in the region near the bottom wall is high. However, with the further development of the flow, the horizontal liquid velocities near the bottom wall become sufficiently high and move the near wall particles to the central part of the column. The particles are then captured by the upward flow generated by the bubble plume. As result for the 20-30 s time period the high particle volume fraction in the region near the bottom will disappears and Figure 3-7b shows a roughly uniform particle volume fraction along the column height.

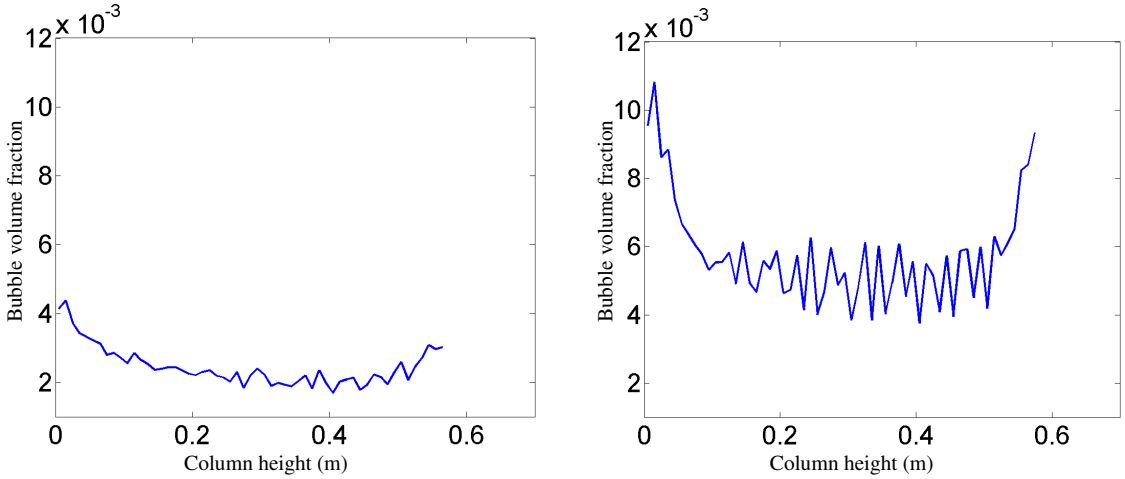

(a) (b)

Figure 3-6. Average volume fraction of the bubbles along the column height during gas-liquid-particle three-phase flows under normal gravity. Superficial gas velocity, U_s = 0.25 mm/s, initial bubble size d_b = 1.0 mm, particle size d_p = 0.25 mm. (a) Averaged over 5-20s (b) Averaged over 20-30s

Figures 3-8a and 3-8b, respectively, show the average Sauter mean diameter of the bubbles along the column height for time periods of 5-20 s and 20-30 s. These figures

indicate that the bubble diameter increases with the column height and the evolution of the flow. Clearly, the longer the bubbles stay, the higher the possibility they collide to

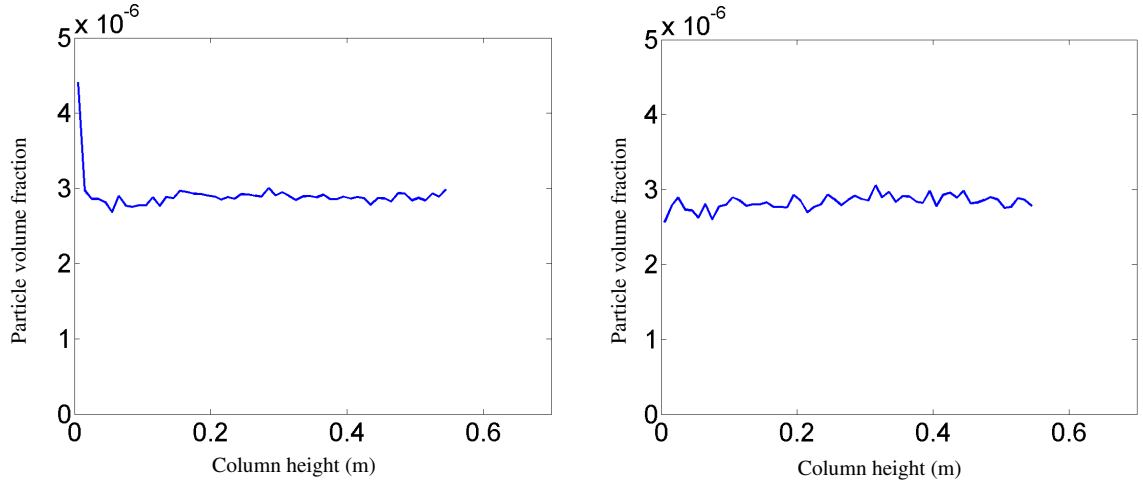

(a) (b)

Figure 3-7. Average volume fraction of the particles along the column height during gas-liquid-particle three-phase flow under normal gravity. Superficial gas velocity, U_s = 0.25 mm/s, initial bubble size d_b = 1.0 mm, particle size d_p = 0.25 mm. (a) Averaged over 5-20s (b) Averaged over 20-30s

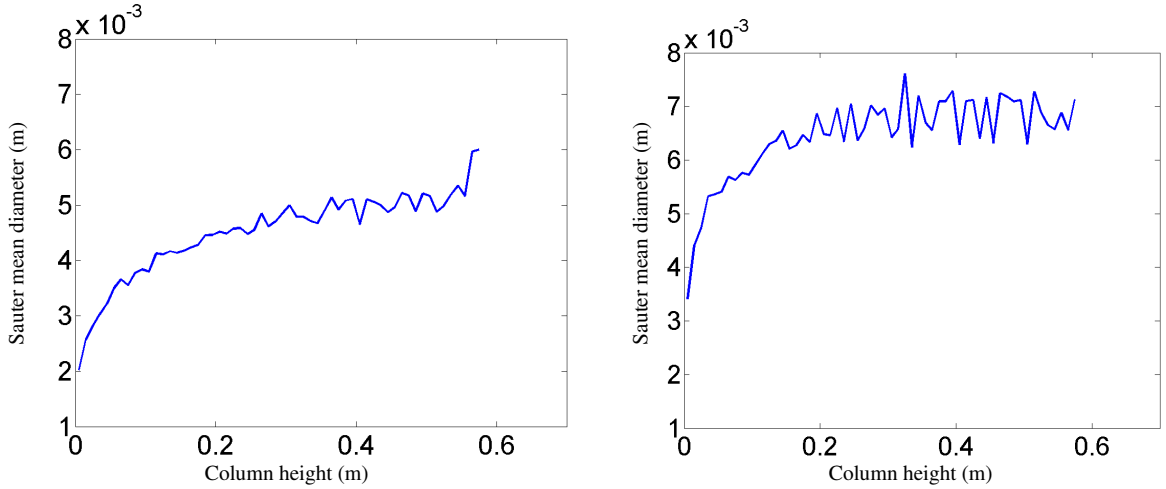

(a) (b)

Figure 3-8. Average Sauter mean diameter of the bubbles along the column height in the gas-liquid-particle three-phase flow under normal gravity. Superficial gas velocity U_s =

0.25 mm/s, initial bubble size d_b = 1.0mm, particle size d_p = 0.25 mm. (a) Averaged over 5-20s. (b) Averaged over 20-30s.

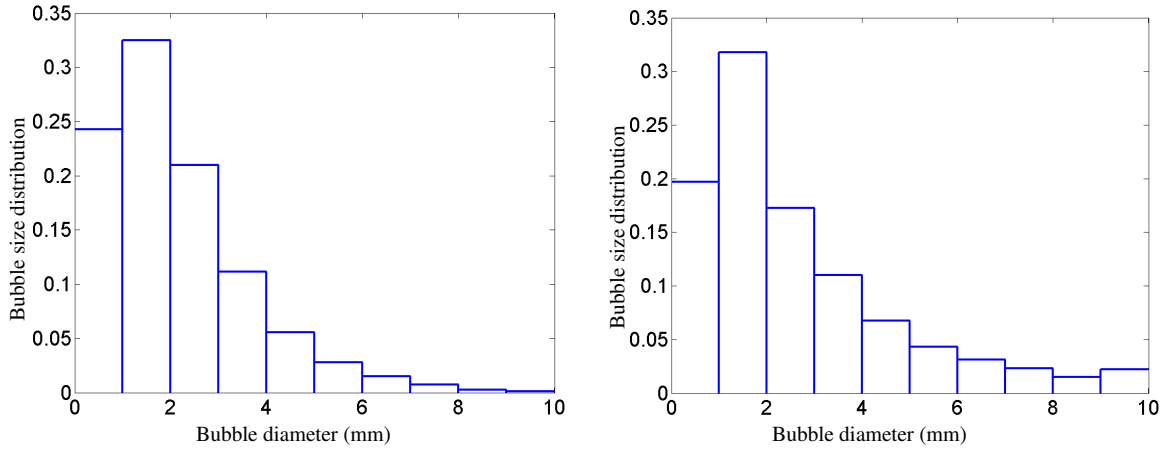

(a) (b)

Figure 3-9. Average bubble size distribution during the gas-liquid-particle three-phase flow under normal gravity in the entire column. Superficial gas velocity, U_s = 0.25 mm/s, initial bubble size, d_b = 1.0mm, particle size d_p = 0.25 mm. (a) Averaged over 5-20s. (b) Averaged over 20-30s.

each other and coalesce. So bubble diameter increases along the column height due to more bubble coalescence. The reason that the bubble diameter increases with the evolution of the flow is not only because that the developed S-shape plume keeps bubbles travel longer, therefore increase the chance of the bubble-bubble collisions and coalescences, but also because that the developed strong moving vortices will result in the strong disturbance and mixing of the bubbles, which will further result in more bubble-bubble collisions and coalescences.

Figures 3-9a and 3-9b show average bubble size distribution in the entire column from 5-20 s and 20-30 s, respectively. These figures show that the 1-2 mm bubbles have the largest number density and the number density decreases as the size increases. As noted before, the initial bubble diameter is 1mm, and due to bubble coalescence larger size bubbles are formed. Comparison of Figures 3-9a and 3-9b indicates that with the

time development of the flow, the number density of small bubbles decreases and the number density of large bubbles increases.

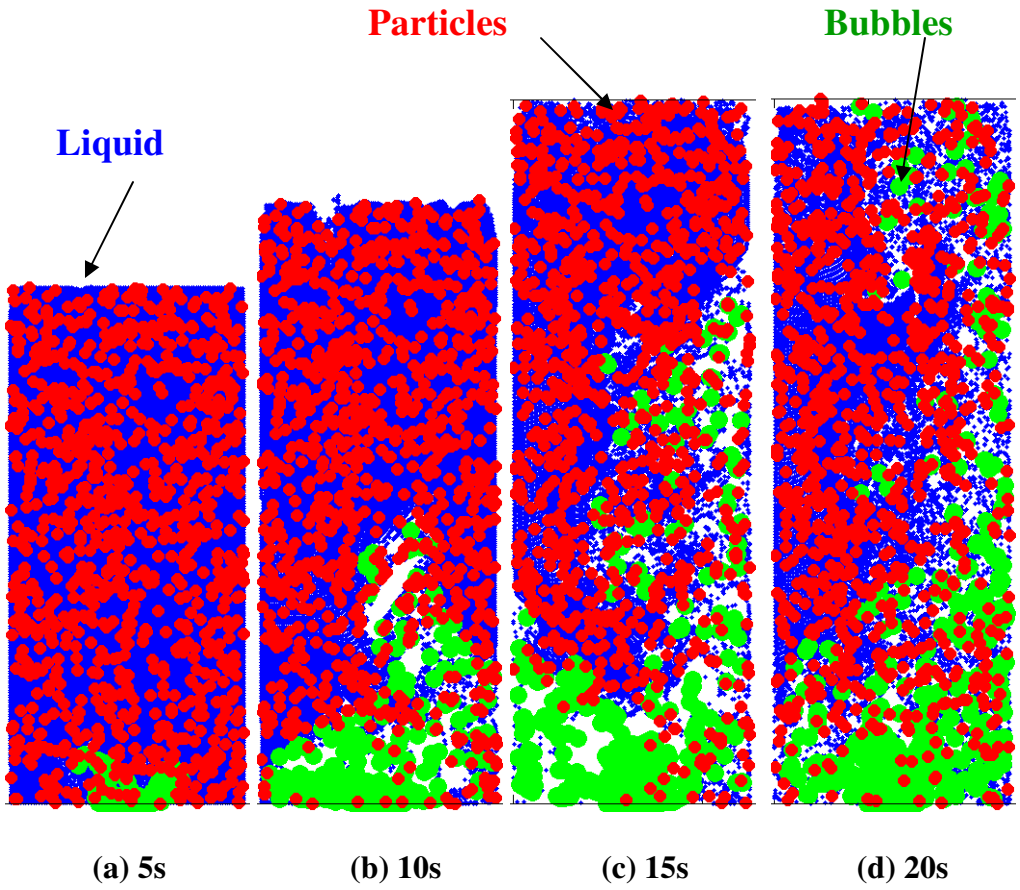

Figure 3-10. Computed flow structure of the gas-liquid-particle three-phase flows in zero-gravity. Superficial gas velocity U_s = 0.25 mm/s, initial bubble size, d_b =1.0 mm, particle size, d_p = 0.25 mm.

3.3.2 Development of Transient Flow Structures under Zero gravity Condition

Characteristics of the three-phase liquid-gas-solid flows under zero-gravity condition are studied in this section. The hydrodynamic parameters used in the simulation are listed in Table 3-1 (case 2). Figure 3-10 shows the snapshots of the model predictions for the liquid stream traces, and the locations of bubbles and particles at time of 5, 10, 15 and 20 s after initiation of the flow. Figures 3-11, 3-12 and 3-13, respectively, show the corresponding bubble velocities, liquid velocities and particle velocities. The transient characteristics and the development of the three-phase flow are clearly shown in these

figures. In the absence of gravity, there is no buoyancy force acting on the bubbles or the particles. Bubble motions are then due to the bubble initial injection momentum, bubble-bubble collisions, bubble-particle collisions, and liquid drag. Thus, compared to the flow with normal gravity, bubbles move very slowly in the column under zero-gravity condition.

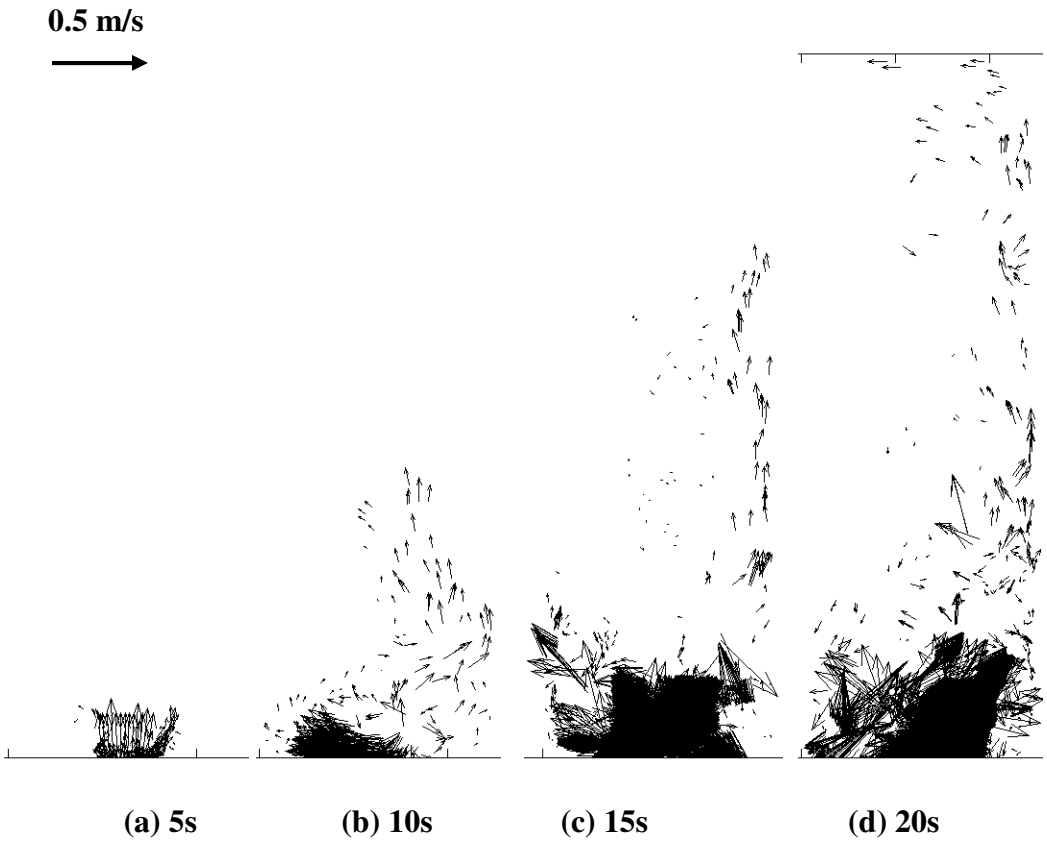

Figure 3-11. Computed snapshots of the bubble velocities of the gas-liquid-particle three phase flows in zero-gravity. Superficial gas velocity, U_s = 0.25 mm/s, initial bubble size, d_b =1.0mm, particle size, d_p = 0.25mm.

Unlike the case for normal gravity, Figure 3-10a shows that bubbles do not rise rectilinearly under zero-gravity condition. When bubbles enter the column, they quickly lose their initial momentum due to the liquid drag, and then accumulate at the bottom of the column due to lack of buoyancy force. After certain time when sufficient number of bubbles is accumulated, they begin to rise due to bubble-bubble collision and liquid

motion. Figures 3-11a and 3-12a show that the movements of the bubble clusters are along the liquid vertical path. Figures 3-10a and 3-13a show that particles are pushed away when the bubble clusters are raised. Figures 3-10b and 3-10c show significant increase of the liquid level in the column with time, which is the result of accumulation of large number bubbles in the column in zero-gravity condition. Figures 3-10b, 3-11b, and 3-12b show a plug flow behavior in the bubble column with the liquid above the bubble clusters moving with a roughly uniform velocity. When the bubble plume reaches the free surface, Figures 3-10d, 3-11d and 3-12d show that a large vortex is formed in the column. Figures 3-10 and 3-13 also show that particles are mainly located outside the bubble plume, with only a few particles retained inside the plume.

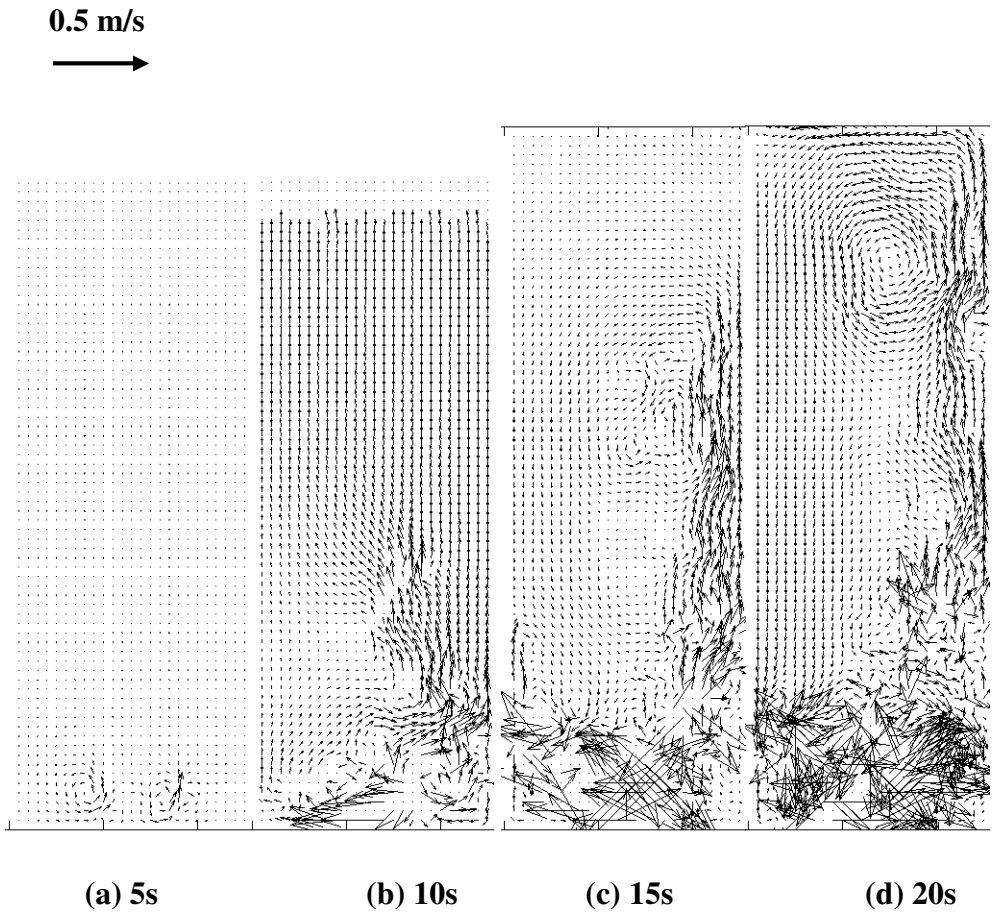

Figure 3-12. Computed snapshots of the liquid velocities of the gas-liquid-particle three-phase flow in zero-gravity. Superficial gas velocity, U_s = 0.25mm/s, initial bubble size d_b = 1.0mm, particle size, d_p = 0.25mm.

Comparison of Figures 3-11, 3-12 and 3-13 indicates that, except for the startup when the bubble upward velocities are much larger than both liquid and particle velocities, the velocities of bubbles, liquid and particles are of the same order under the zero-gravity condition, especially at the top of the column. At the bottom of the column, bubbles push the liquid and liquid transports the particles, so the bubble velocity is somewhat larger, and the particle velocity is a slightly smaller.

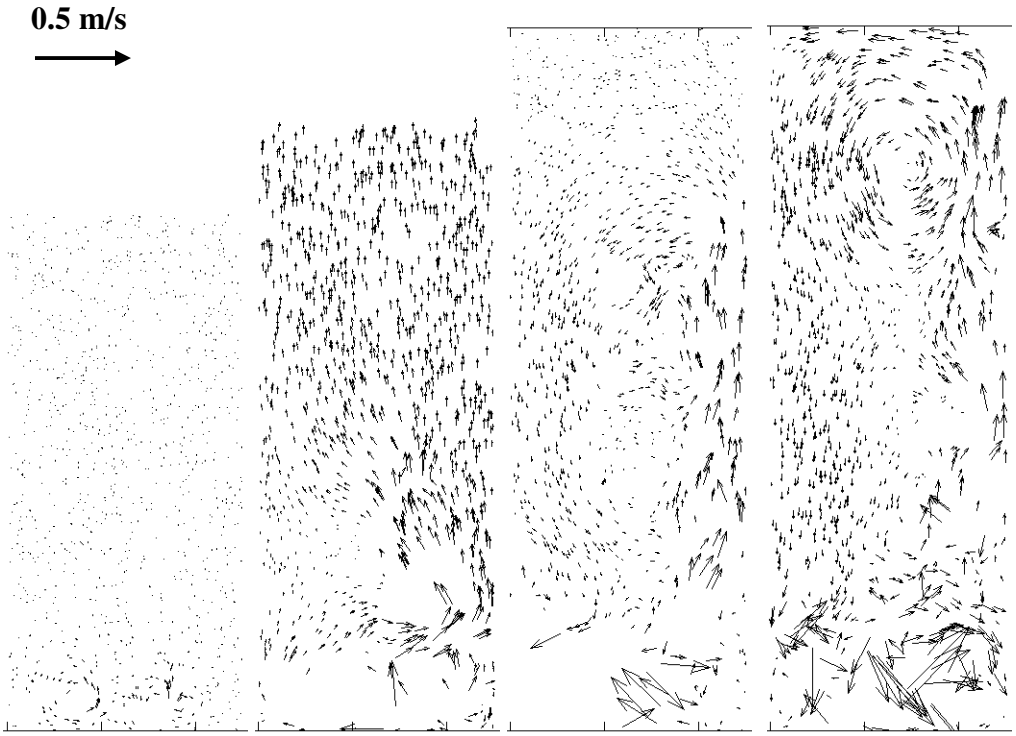

(a) 5s **(b) 10s** **(c) 15s** **(d) 20s**

Figure 3-13. Computed snapshots of the particle velocities of the gas-liquid-particle three-phase flow in zero-gravity. Superficial gas velocity, U_s = 0.25 mm/s, initial bubble size d_b = 1.0 mm, particle size d_p = 0.25 mm.

Comparing Figures 3-10, 3-11, 3-12 and 3-13, respectively, with Figures 3-2, 3-3, 3-4 and 3-5 for the normal gravity, shows the significant effect of gravity on the three-phase flow characteristics in the column. Clearly bubble rising velocity are very low due to the lack of buoyancy force. Also because of bubble accumulation in the column, liquid level in the column at zero-gravity is much higher than that of flow with normal

gravity. In addition, most particles are located outside the bubble plume, as a result, the mixing of different phases are much less when compared with that for flow with normal gravity. Thus, the interactions among the different phases are significantly reduced in zero-gravity condition. Compared to Figures 3-4 and 3-5, Figures 3-12 and 3-13 show that both liquid and particle velocities are smaller than those of the flow with normal gravity. In summary, compared with the flow in normal gravity, flow in zero-gravity has low phase velocity and phase mixing.

Figures 3-14 and 3-15, respective, show the average volume fractions of bubbles and particles along the column height during three-phase flows under zero-gravity condition. Here a and b, respectively, refer to the time averaging periods from 5 to 20 s and 18 to 21 s. The latter period refers to the duration that bubbles have reached the free surface. As seen from Figure 3-14a, due to the absence of buoyancy force, most bubbles are concentrated at the bottom of the column near the gas injection region. With the development of the flow, more new bubbles are injected into the bottom of the column; these new bubbles increase the liquid velocity and cause the earlier injected bubbles to move toward the top of the column. As a result, bubble volume fraction in the column increases with time, as seen in Figure 3-14.

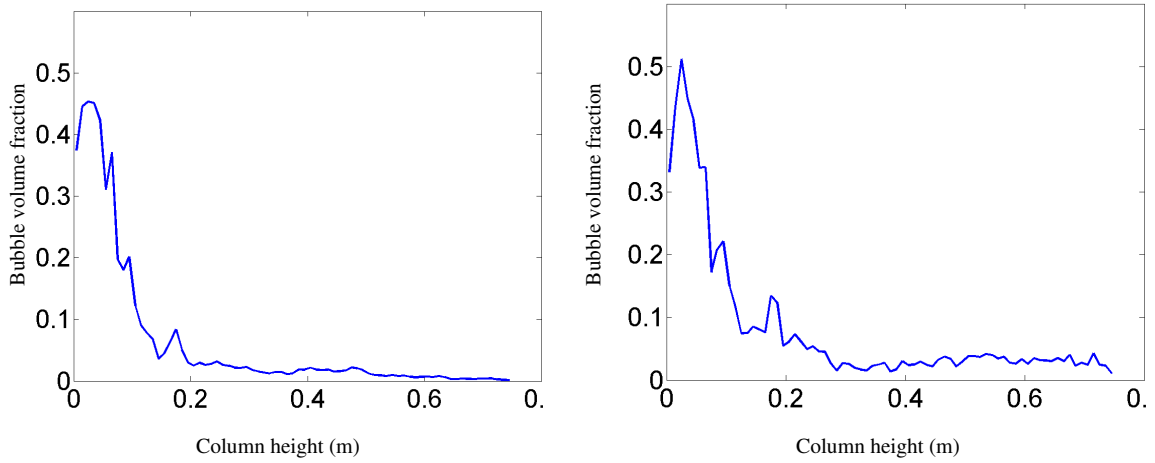

(a) (b)

Figure 3-14. Average volume fraction of the bubbles along the column height in the gas-liquid-particle three-phase flow in zero-gravity. Superficial gas velocity U_s = 0.25

mm/s, initial bubble size d_b = 1.0 mm, particle size d_p = 0.25 mm. (a) Averaged over 5-20s. (b) Averaged over 18-21s.

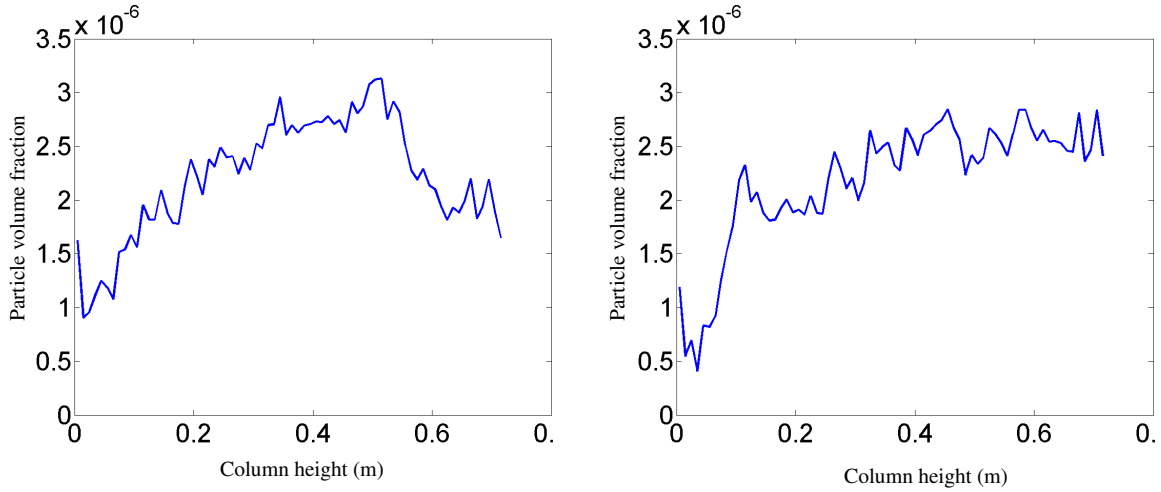

(a) (b)

Figure 3-15. Average volume fraction of the particles along the column height in the gas-liquid-particle three-phase flow in zero-gravity. Superficial gas velocity U_s = 0.25 mm/s, initial bubble size d_b = 1.0 mm, particle size d_p = 0.25 mm. a) Averaged over 5-20s. (b) Averaged over 18-21s.

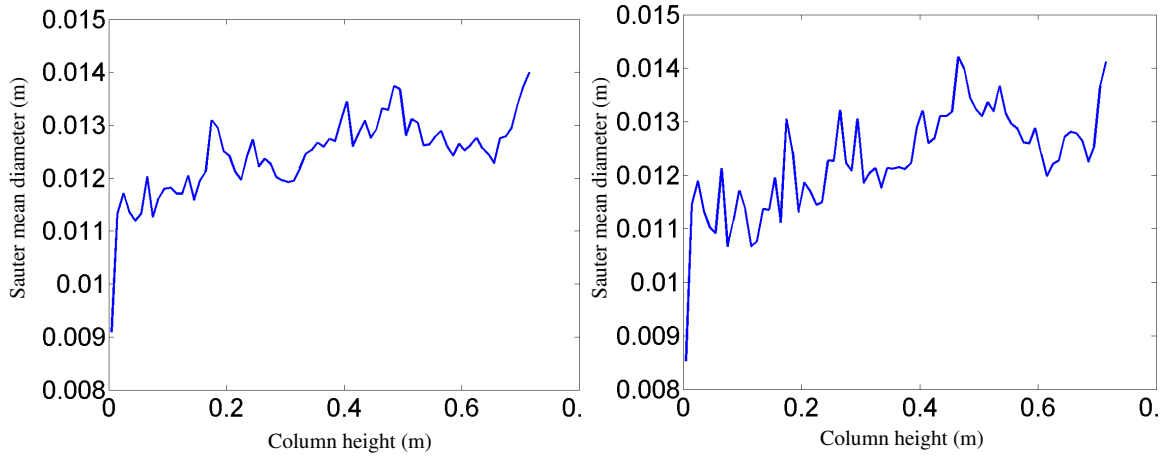

(a) (b)

Figure 3-16. Average Sauter mean diameter of the bubbles along the column height in the gas-liquid-particle three-phase flow in zero-gravity. Superficial gas velocity U_s = 0.25 mm/s, initial bubble size d_b = 1.0mm, particle size d_p = 0.25 mm. a) Averaged over

5-20s. (b) Averaged over 18-21s.

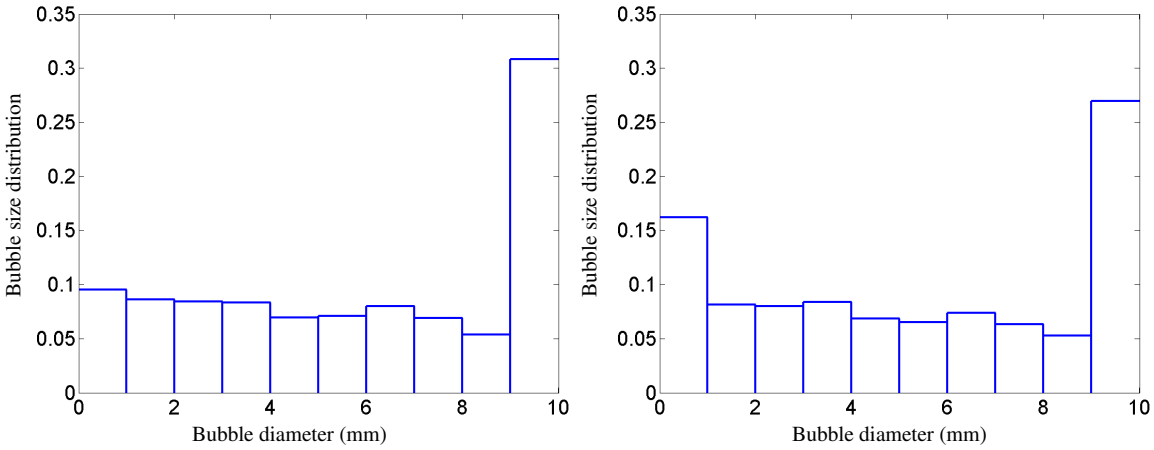

(a) (b)

Figure 3-17. Bubble size distribution during gas-liquid-particle three-phase flows in zero-gravity in the entire column. Superficial gas velocity, U_s = 0.25 mm/s, initial bubble size d_b = 1.0 mm, particle size d_p = 0.25 mm. (a) Averaged over 5-20s. (b) Averaged over 18-21s.

Figure 3-15a shows that most particles are concentrated in the middle part of the column. The particle volume fraction is low at the lower and the upper parts of the column. These low particle volume fractions are due to the gas injection in the lower part and the subsequent expansion of free surface in the upper part. When bubble plume reaches the free surface, as seen from Figure 3-15b, particle volume fraction increases along the height of the column. Comparing Figures 3-15a and 3-15b shows that particle volume fraction at the lower part of the column decreases at the latter time, indicates that more particles are pushed away by the bubble injection. The decrease of the maximum particle volume fraction in Figure 3-15b is the result of the rising level of liquid in the column.

Figures 3-16a and 3-16b show average Sauter diameter of the bubbles along the column height in the three-phase flow under zero-gravity condition, respectively, over time durations of 5-20 s and 18-21 s. These figures indicate that the Sauter mean

diameter of the bubbles increases along the height of the column, and the Sauter mean diameter of the bubbles in Figure 3-16b is larger than that in Figure 3-16a, which means that the Sauter mean diameter of the bubbles are proportional to the residence time of the bubbles in the column. The longer the bubbles residence time, the higher the possibility they collide with each other and coalesce. So due to bubble coalescence, bubble diameter not only increases along the column height, but also increases with time. But this is not the case for salt water. As mentioned in Chapter 2, Tsao and Koch (1994) pointed out that with presence of salts, the coalescence rate decreases significantly due to decreased critical Weber number. When two bubbles collide, it is more likely that they bounce back than coalesce even in microgravity.

Figures 3-17a and 3-17b, respectively, show average bubble size distributions in the entire column averaged over time durations of 5-20 s and 18-21 s during three-phase flows under zero-gravity condition. As seen from Figure 3-17a, due to the lack of buoyancy force, the 1 mm bubbles accumulate at the bottom of the column near the injectors. Thus, bubble-bubble collisions and coalescence increases, so that bubble sizes could become quite large. It is seen that the number density of bubbles with diameter larger than 9 mm is the highest. However, with the development of flow, more and more bubbles leave the bottom part and rise to the middle and top of the column, so the possibility of bubble-bubble collision and coalescence at the bottom become relatively low, thus the number density of large bubbles decreases and the number density of small bubbles increases, as show in Figure 3-17b. Figure 3-17a and b show that bubbles with diameter of 1 mm have the second largest amplitude in the distribution.

Compared with Figure 3-6, Figure 3-14 shows that the bubble distribution in zero-gravity is not as uniform as that in normal gravity. Similar trends are also observed for particles as shown in Figure 3-7 and Figure 3-15. These indicate again that the phase mixing in zero-gravity is not as effective as that in normal gravity. Comparison of Figures 3-16 and 3-8 shows that bubbles in zero-gravity are much larger than those in normal gravity. Compared with Figure 3-9, Figure 3-17 shows that larger bubbles are the majority, while large bubbles indicate the decrease of the contact area between bubble

and liquid, so once more, we get the conclusion that the flow in zero-gravity has low phase mixing which may result in lower chemical reaction productivity.

3.3.3 Effect of Bubble Size on Gas-Liquid-Particle Flow in Zero-gravity

To study the effect of bubble size on the flow characteristics in zero-gravity, the simulation was repeated with the inlet bubble diameter being increased to 3mm, and superficial velocity being increased to 6.75mm/s. This will maintain the same number of bubble injection at the inlet. Other simulation parameters are the same as listed in Table 3-1 (case 3). Figure 3-18a shows the flow structures at 6 s after initiation of the three-

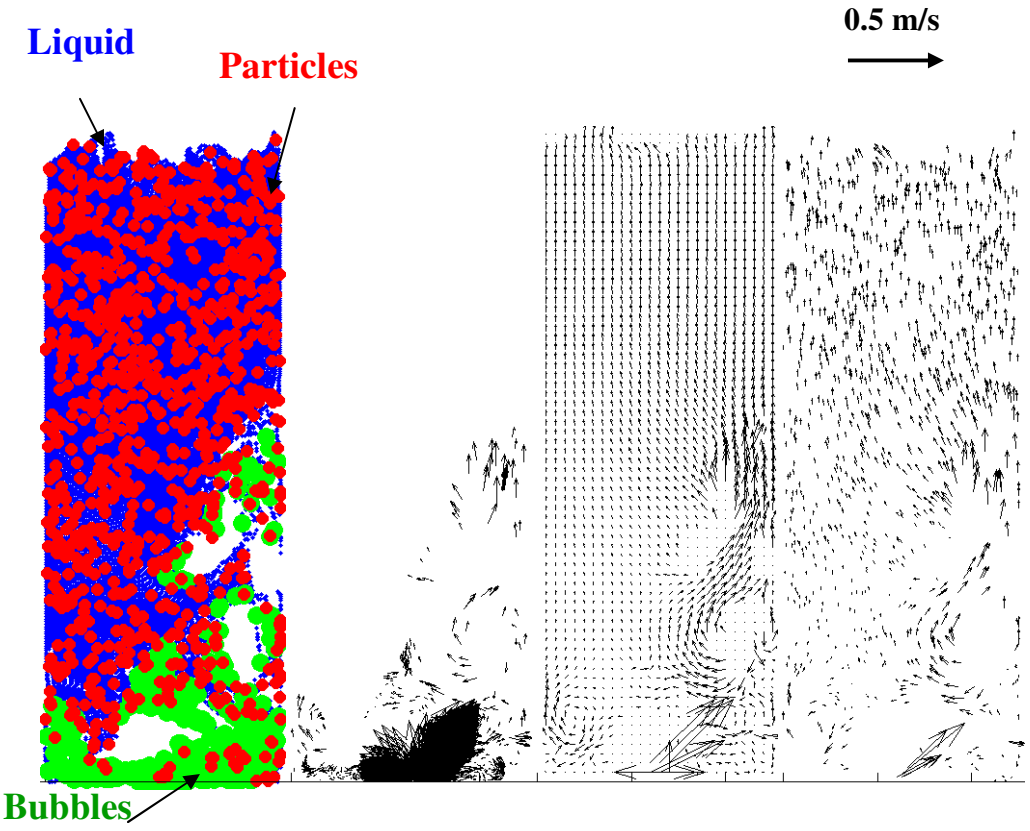

Figure 3-18. Computed flow structure and velocities of the gas-liquid-particle three-phase flow in zero-gravity. Superficial gas velocity U_s = 6.75 mm/s, initial bubble size d_b = 3.0 mm, particle size, d_p = 0.25 mm.

phase flow. Figures 3-18b, c and d, respectively, show the corresponding velocities of bubbles, liquid, and particles.

Compared to Figures 3-10a and 3-11a, Figures 3-18a and 3-18b show that larger bubbles have larger velocities for fixed number of injections; thus, bubble plume evolves faster than that with smaller inlet bubbles. Comparisons of Figure 3-12a and Figure 3-18c, as well as Figure 3-13a and Figure 3-18d, indicate that both liquid and particle velocity with larger inlet bubbles are higher than that with smaller inlet bubbles. The observed trends can be explained by bubble inertia and the momentum transferred among the three phases. Since the number of injected bubble are fixed, larger bubbles implies larger superficial velocity, which indicates that in the same time period more bubble momentum are introduced into the column and transferred to liquid and particle phases. Therefore, the liquid and particle velocities in the column are higher than those with smaller injected bubbles.

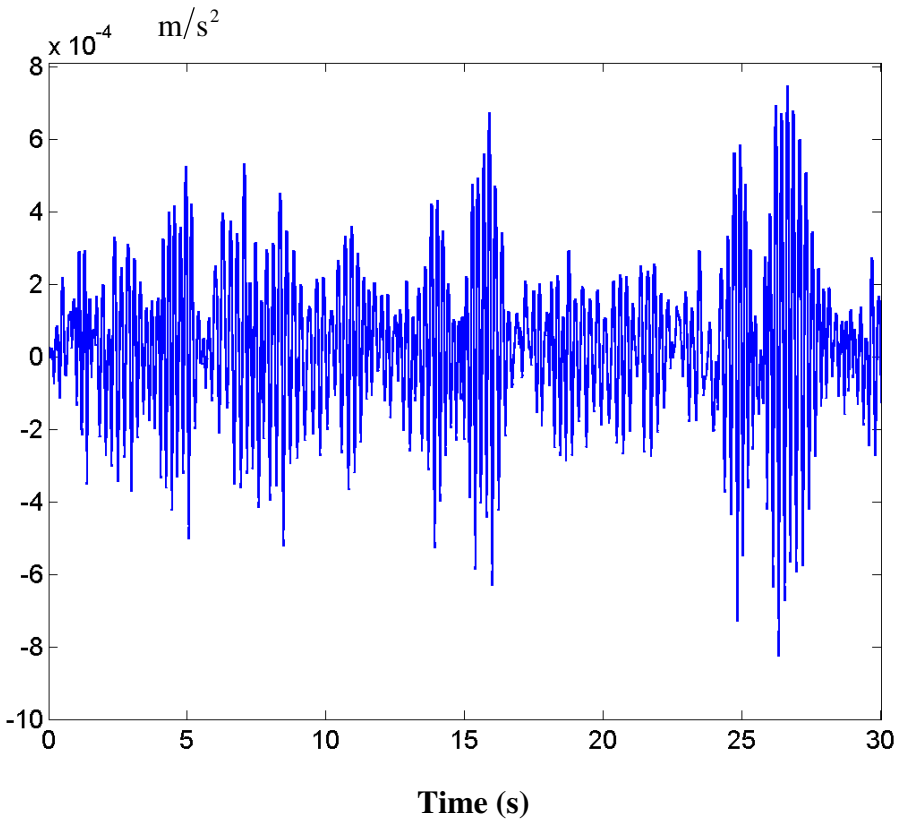

Figure 3-19. The variation of G-jitter acceleration with time from STS 51 data.

3.3.4 Effect of G-jitter Acceleration on Gas-Liquid-Particle Flow in Zero-gravity

To study the effect of G-jitter acceleration on the gas-liquid-particle three flow characteristics in zero-gravity, a simulation was performed under G-jitter acceleration from STS-51 Data by substituting G-jitter acceleration in all the three phases for normal gravity. The simulation parameters are listed in case 4 of Table 3-1. Figure 3-19 shows the variation of G-jitter acceleration with time from STS-51 data. It can be seen from Figure 3-19 that G-jitter acceleration is very small compared to the normal gravity. Figure 3-20a shows the flow structures at 6 s after initiation of the three-phase flow under G-jitter acceleration. Figures 3-20b, c and d, respectively, show the corresponding velocities of bubbles, liquid, and particles. Comparison between Figures 3-20 and 3-19 indicates the differences are small, which means the effect of G-jitter acceleration on the gas-liquid-particle three flows is small.

3.4. CONCLUSIONS

In this study, an Eulerian-Lagrangian computational model for simulations of gas-liquid-solid flows in microgravity is presented. The two-way coupling between bubble-liquid and particle-liquid are accounted for in the analysis. Interactions between particle-particle and bubble-bubble are included using the hard sphere model approach, and the bubble coalescence is also included in the model. The transient characteristics of three-phase flows in zero-gravity and microgravity are studied and the effects of gravity, bubble size and G-jitter acceleration on the characteristics of the flow are discussed. On the basis of the presented results, the following conclusions are drawn:

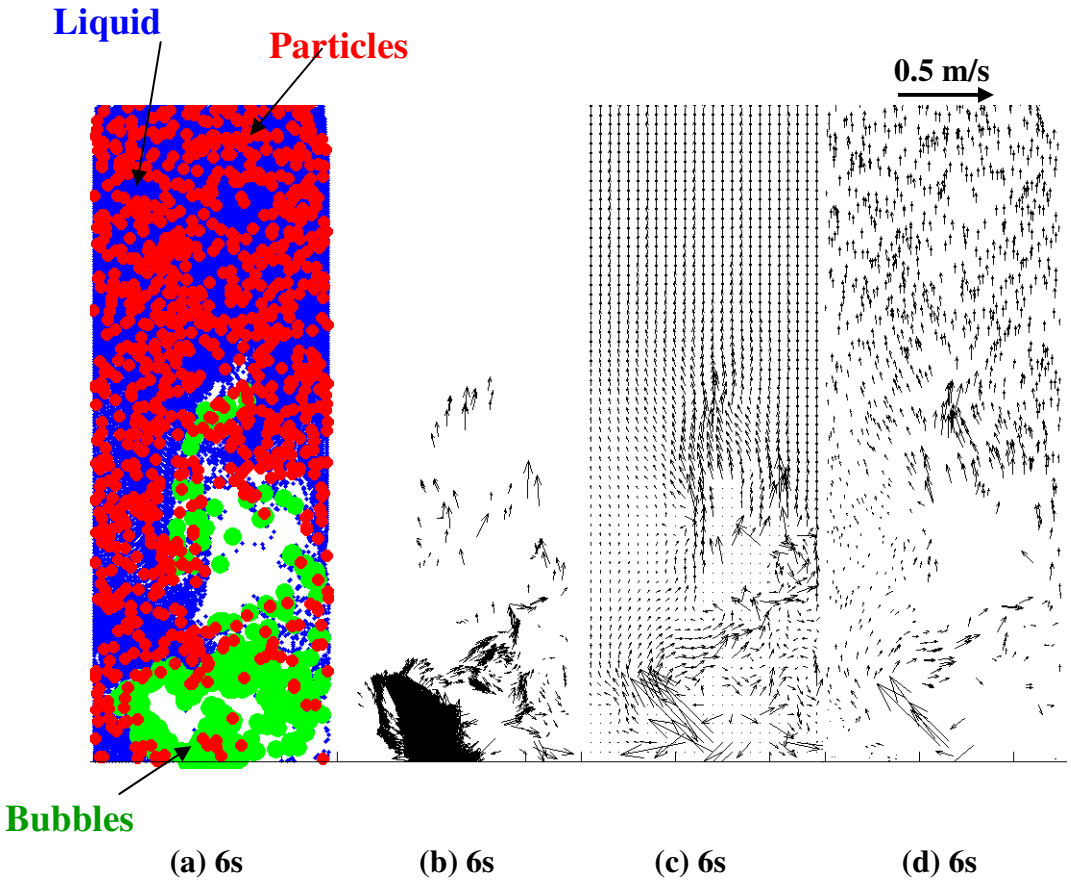

Figure 3-20. Computed flow structure of the gas-liquid-particle three-phase flow in zero-gravity with G-jitter. Superficial gas velocity U_s = 6.75 mm/s, initial bubble size d_b = 3.0 mm, particle size, d_p = 0.25 mm.

1. Gravity has magnificent influence on the transient characteristics of the flow in the bubble column. The three-phase flow in the bubble column with normal gravity are dominated by time-dependent staggered vortices, while in the flow without gravity, The sources for bubble motion are mainly bubble initial momentum, bubble-bubble collision and liquid transportation. Thus bubbles accumulate at the bottom of the column and move very slowly, and liquid level is much higher than that of the flow with normal gravity.

2. Particles are mainly located outside the bubble plume, only a few particles are retained inside the bubble plume. The flow in zero-gravity has low phase velocities and phase mixing.
3. The velocities of bubbles, liquid and particles are in the same order.
4. After bubble plume reaches the surface, particle volume fraction increases along the height of the column.
5. The Sauter mean diameter of the bubbles are proportional to the time the bubbles stay, bubble diameter not only increases along the column height, but also increases with time.
6. Due to more bubble-bubble collision and coalescence, bubbles can become very large, bubbles with diameter larger than 9 mm own largest quota in bubble size distribution in the whole column.
7. Bubble size has major effect on the flow. Larger bubbles have larger velocities, thus bubble plume evolves faster than that with smaller bubbles.
8. The effect of G-jitter acceleration on the gas-liquid-particle three flows is small.

3.5 ACKNOWLEDGEMENT

The financial support by the US Department of Energy is gratefully acknowledged.

The content of this chapter is partly presented in the 79th ACS Colloid and Surface Science Symposium, June 12-15, 2005, Potsdam, NY, USA.

CHAPTER 4. NUMERICAL SIMULATIONS OF LIQUID-GAS-SOLID THREE-PHASE FLOWS IN GRAVITY VARIATION

4.1 INTRODUCTION

Up to now, the effects of gravity variation on the characteristics of the three-phase flows are not well understood, which plays a key role on air revitalization and air purification devices critical to NASA's plan for long duration human space travel. In this chapter the earlier developed computational model was used and a sample case with normal gravity was also analyzed first, then the influences of the gravity variation on operation of the column were analyzed.

4.2 GOVERNING EQUATIONS AND MODELS

The detailed information on governing equations and model assumptions are described in Chapter 2. Bubble coalescence is accounted by assuming that two bubbles coalesce upon impact when the Weber number is less than 0.14, while they bounce for larger Weber numbers. Particles rising to the top surface of the liquid are treated in the analysis by assuming the particles always go through the free surface when Particle-free surface collision occurs. The particle environment fluid property parameters are then changed from liquid to gas parameters until the particles reenter the liquid due to gravity, which means that use gas parameters to calculate the forces exerted on the particles, but these forces are not coupled back to the free surface. Bubble-wall and particle-wall collisions were included in the model using a hard sphere collision model revised from the model developed by Hoomans et al. (1996) as described by equations (2-15)-(2-21), with m_a equals to infinite. A restitution coefficient of 0.5 was used for both bubble-wall collision and particle-wall collision, while friction coefficients of 0.02 and 0.1 were assumed for bubble-wall collision and particle-wall collision, respectively. The column used here is same as the one used in Chapter 3 (Figure 3-1). The initial liquid level was assumed to be 55cm high, while the gravity was varied for different cases as shown in Table 4-1. The hydrodynamic properties of the dispersed phases were also summarized in

Table 4-1. The study was focused on the comparison of the three-phase flows in the bubble column under 0.5g, 2g and normal gravity conditions.

Table 4-1. Hydrodynamic parameters for different cases

Case number	Bubble diameter mm	Superficial gas velocity mm/s	Bubble density kg/m^3	Particle diameter mm	Particle density kg/m^3	Gravity m/s^2
1	1.0	0.25	1.29	0.25	1000	-9.8
2	1.0	0.25	1.29	0.25	1000	-19.6
3	1.0	0.25	1.29	0.25	1000	-4.9

4.3 RESULTS AND DISCUSSION:

4.3.1 Development of Transient Flow Structures with Normal Gravity

To evaluate the effect of the gravity variation on the three-phase flow characteristics, a sample reference case with normal gravity is studied first. The hydrodynamic parameters for the simulation are listed in Table 4-1 (case 1). Figure 4-1 shows the snapshots of the predictions for the liquid stream traces, and the locations of bubbles and particles at time of 1, 8, 17 and 25 s after initiation of the flow. The small dots in Figure 4-1 show the liquid phase stream traces, while the small circles and the large circles show, respectively, the positions of the particles and bubbles. Figures 4-2, 4-3 and 4-4, respectively, show the corresponding velocities of bubbles, liquid and particles. The transient flow features are clearly described by these figures. Figure 4-1a, 4-1b and 4-1c show that bubble plume rises rectilinearly along the centerline of the column, which generates two vortices behind the plume head, as seen in Figure 4-3a, 4-3b and 4-3c, these vortices are almost symmetric, but with the evolution of the flow, the vortices become non-symmetric, eventually staggered vortical flows are formed, as shown by Figure 4-3d. Affected by these staggered vortices, the bubble plume changes its pattern to S-shape as seen in Figure 4-1d. With the upward pushing of the bubble plumes, the moving of these staggered vortices results in the oscillation of the bubble plume.

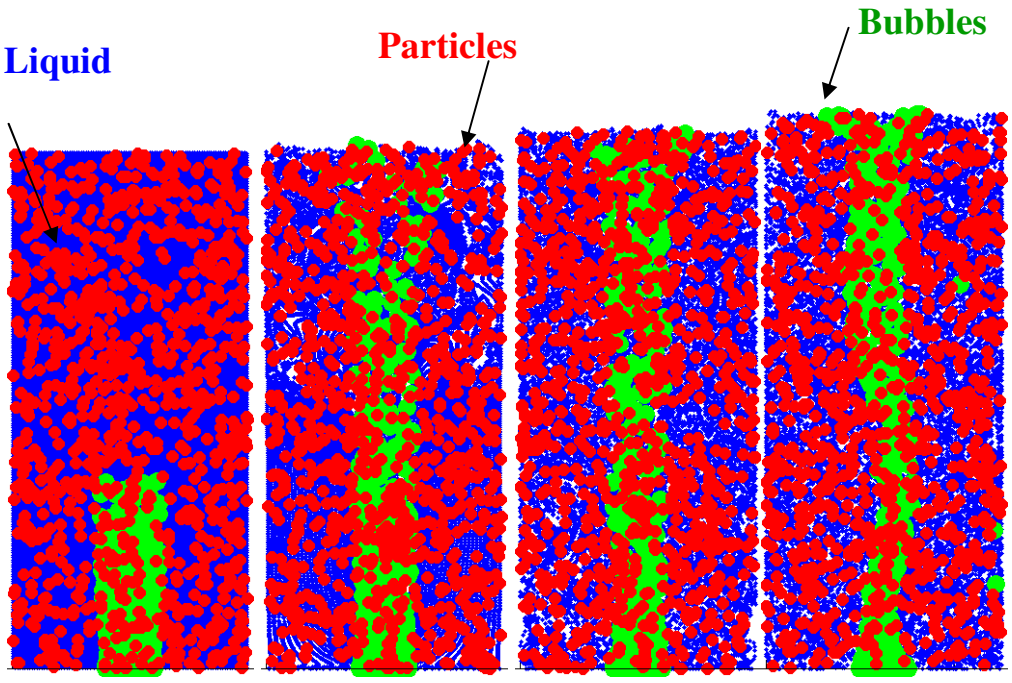

Figure 4-1. Computed flow structure of the gas-liquid-particle three-phase flow in normal gravity. Superficial gas velocity U_s = 0.25mm/s, initial bubble size d_b = 1.0 mm, particle size d_p = 0.25 mm.

Comparison of Figure 4-1 and Figure 4-3 shows that the evolution of the three-phase flow in the column is under the control of these time-dependent staggered vortices, the expand of the bubble plume on the top of the column and the shrink on the bottom is also a result of the vortices.

Figure 4-2b, 4-2c and 4-2d show the variation of bubble upward velocities along the column height. Bubble-bubble coalescences increase bubble size and buoyancy force, affected by the buoyancy force and liquid velocity, bubble upward velocities increase along the column height, attain the maximum at about 0.45m at 8s, 0.3m at 17s and 0.25m at 25s, respectively, then decrease along the column height because of the increasing liquid drag resulted from the low liquid upward velocity at the free surface region. Comparison of Figure 4-2b, 4-2c and 4-2d indicates that bubble maximum upward velocities increase with the time, while in other region of the column the

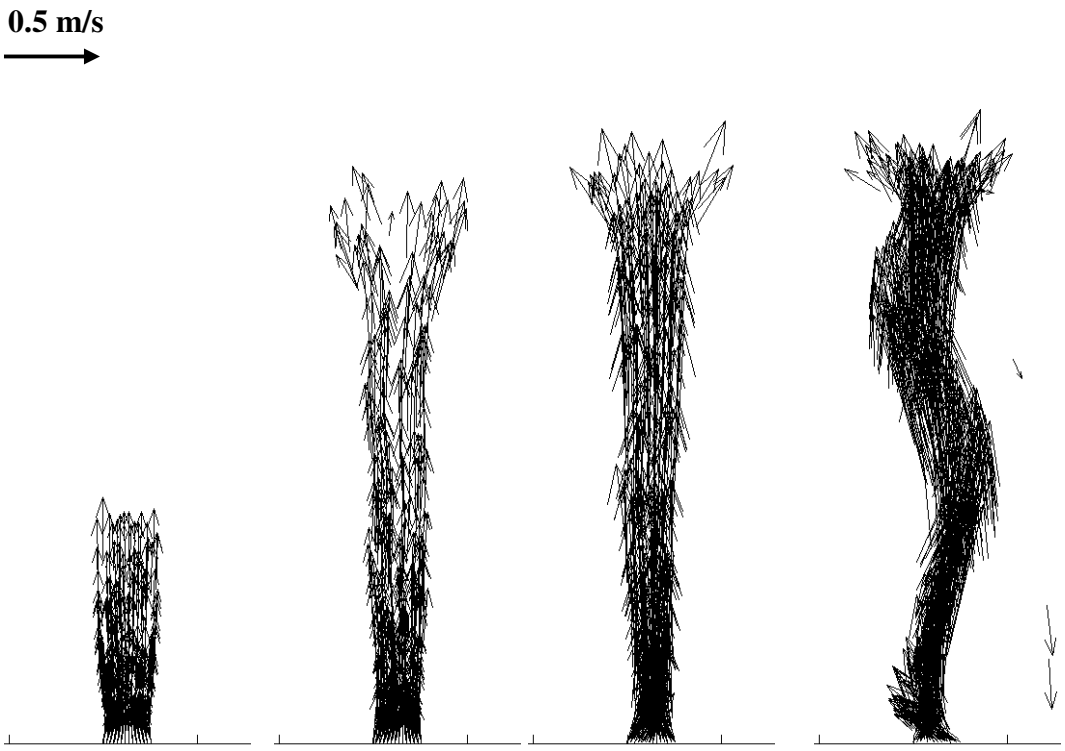

Figure 4-2. Computed snapshots of the bubble velocities of the gas-liquid-particle three-phase flow in normal gravity. Superficial gas velocity U_s = 0.25 mm/s, initial bubble size d_b = 1.0 mm, particle size d_p = 0.25 mm.

variation of bubble upward velocities with time is not as large as the increase of the maximum value, as a result, the differences of the bubble upward velocities along the column height increase with time, which may result in more bubble-bubble collision and coalescence.

Similarly, Figure 4-3 and Figure 4-4 show that the liquid and particle upward velocities increase along the column height, attain the maximum at about 0.4m at 8s, 0.25m at 17s and 0.2m at 25s, respectively, then decrease along the column height, these maximum upward velocities and the differences of these upward velocities along the column height increase with time thus there are more particle-particle collision with the

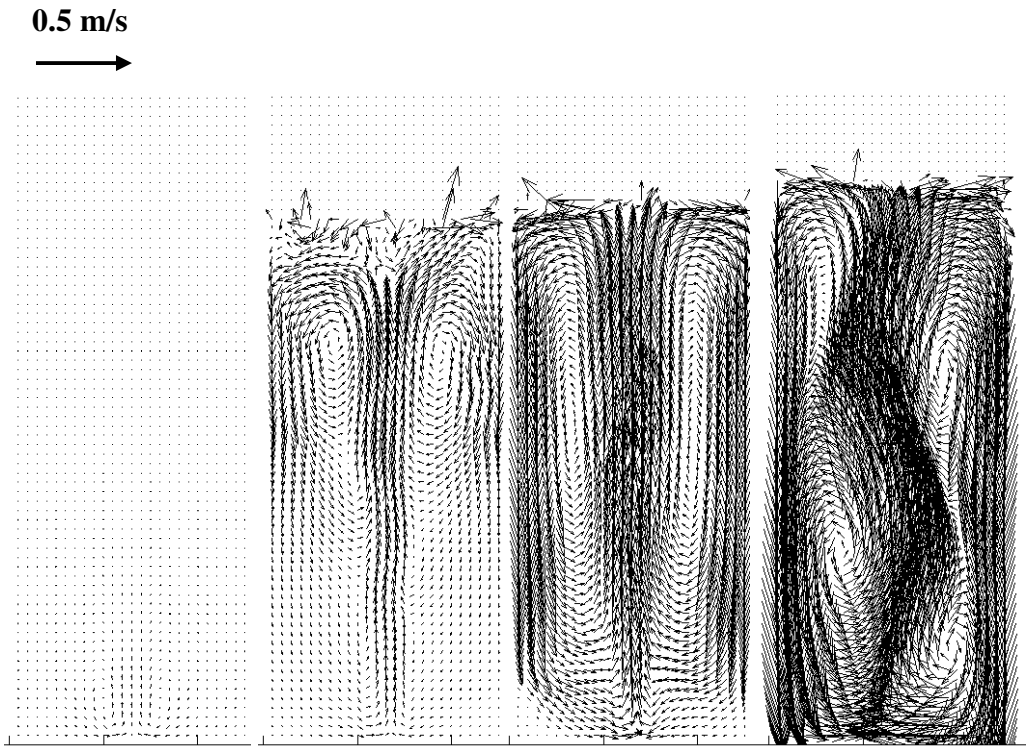

Figure 4-3. Computed snapshots of the liquid velocities of the gas-liquid-particle three-phase flow in normal gravity. Superficial gas velocity U_s = 0.25 mm/s, initial bubble size d_b = 1.0 mm, particle size d_p = 0.25 mm.

development of the flow. Figure 4-3 also implies that because of the liquid velocity distribution, the collision mode for discrete-phases is different in the top and low part of the column. Due to the effect of liquid vortices, bubbles and particles in the low part of the column are pushed toward the centerline, which will result in horizontal bubble-bubble and particle-particle collisions. In this region, particles and bubbles are in the acceleration process, particles or bubbles behind can not easily catch up those above them, so longitudinal collisions are scarce. While in the top part of the column, the liquid velocity will push the bubbles and particles toward the side wall of the column, so horizontal collisions are scarce. However, particles and bubbles in this region are in the deceleration process, so longitudinal collisions will play the major role. As for the bubble-particles collisions, because bubble upward velocities are in general larger than particle velocities, longitudinal collisions can happen along the full column height.

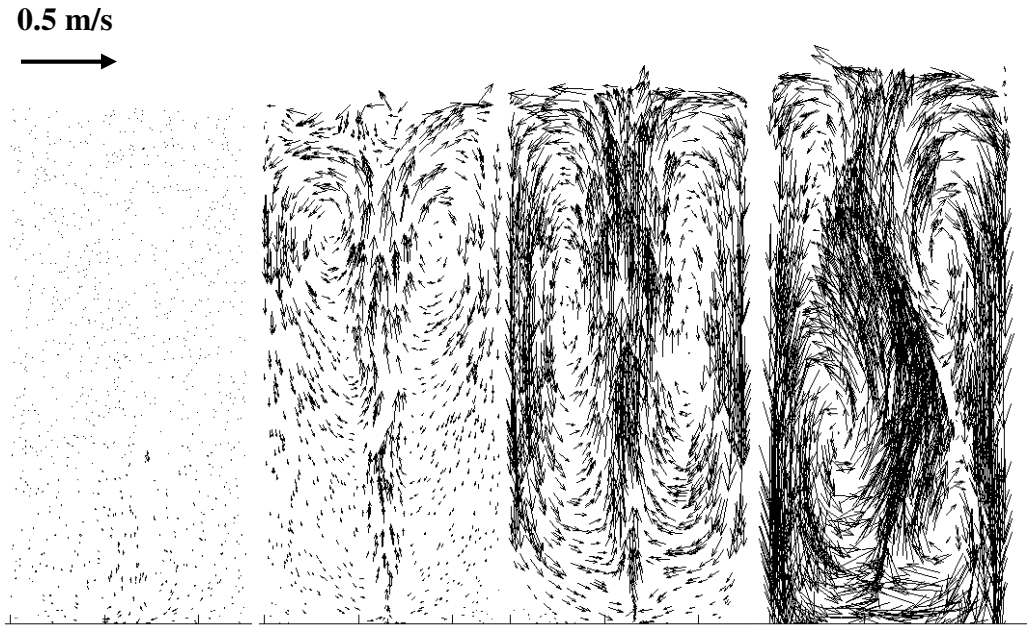

Figure 4-4. Computed snapshots of the particle velocities of the gas-liquid-particle three-phase flow in normal gravity. Superficial gas velocity U_s = 0.25 mm/s, initial bubble size d_b = 1.0 mm, particle size d_p = 0.25 mm.

With the evolution of the flow, the developed vortices not only result in the S-shape plume which keeps bubbles travel longer, therefore increase the chance of the bubble-bubble collisions and coalescences, but also result in the strong disturbance and mixing of the bubbles, which will further result in more bubble-bubble collisions coalescences.

The location difference between the maximum upward velocities of bubbles and those of liquid and particles implies a relaxation effect of the driving of bubbles to the liquid and particles.

Comparison of Figures 4-1, 4-3 and 4-4 indicates that due to the centrifugal force, particles are pushed away from the center of the vortices and concentrated in the region

outside the large vortices. Some particles are retained inside these staggered vortices, partly because of particle-particle collisions.

Figure 4-1d and Figure 4-2d reveals that a number of bubbles are captured by the staggered vortices and move with these vortices. In general, due to the centrifugal force, these captured bubbles are located at certain distance from the center of the vortices. Similarly, Figures 4-1, 4-3 and 4-4 also show that some particles are captured by the vortices and are carried around by the time-dependent circulating motions. Comparison of Figures 4-2, 4-3 and 4-4 shows the upward velocities of the bubble plume are much larger than both particle and liquid velocities, but downward velocities of the captured bubbles are smaller than the other phase velocities. The reason is that bubble upward buoyancy is the main driving force for the flow, so bubble upward velocities are much larger than both particle and liquid velocities. As for downward velocities of the captured bubbles, bubbles are pushed downward by liquid velocity, while the bubble buoyancy force is always upward, thus the bubble can not follow the liquid closely, therefore the bubble velocities are smaller then both particle and liquid velocities.

Figures 4-3 and 4-4 show that velocities of particles and liquid are in the same order, and their maximum upward velocities are in the same location. However, because particles are neutrally buoyant and are generally transported by the liquid, particle velocity is generally slightly smaller than the liquid velocities, but when particles with high velocities entrain in low liquid velocity region, the particle local velocities may become slightly larger than the liquid phase.

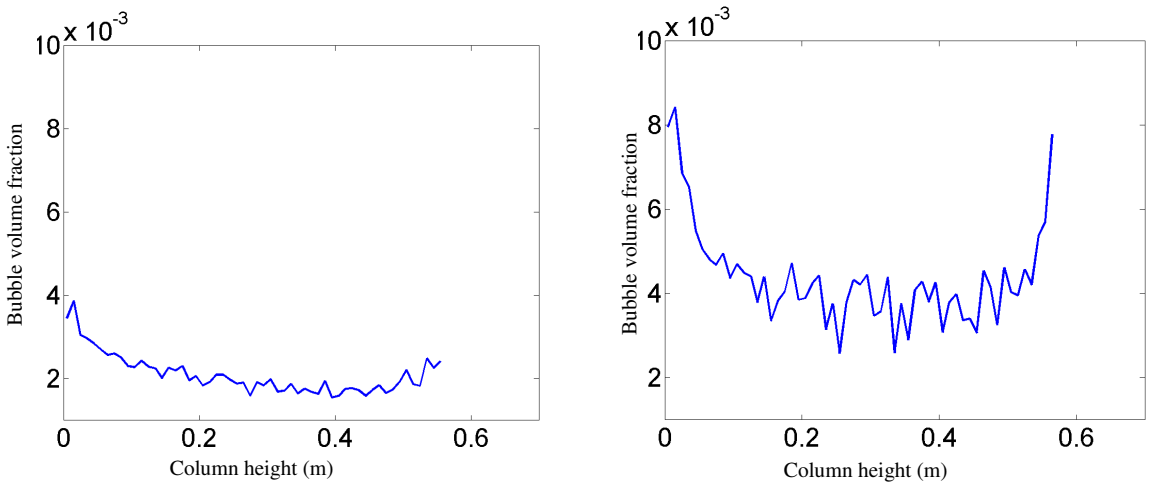

(a) (b)

Figure 4-5. Average volume fraction of the bubbles along the column height in the gas-liquid-particle three-phase flow in normal gravity. Superficial gas velocity U_s = 0.25 mm/s, initial bubble size d_b = 1.0 mm, particle size d_p = 0.25 mm. (a) 5-15s (b) 16-26s

Figures 4-5 and 4-6 show average volume fractions of the bubbles and particles along the column height, respectively, where (a) and (b) refer the time period from 5-15 s and 16-26 s, respectively. Figures 4-5a and 4-5b indicate that the highest bubble volume fraction is located at the bottom of the column; generally, it decreases along the height of column, attains the minimum at 0.4m and 0.25m, respectively, then increases along the height. These phenomena can be explained by two effects. First of all, as mentioned above, along the center line of the column, bubble upward velocities increase with the height of the column, reaching their maximum values at the height of about 0.4m and 0.25m, respectively, for different time duration. While maximum bubble velocities mean shortest bubble duration time and lowest bubble volume fraction. Secondly, as above mentioned, due to the liquid vortices, bubble plume shrinks in the middle of the column, and expands at the top of the column. So there are more spaces in the top for bubbles to stay, thus the average volume fraction of the bubbles can be higher in those regions. Comparison of Figure 4-5a and 4-5b shows that the bubble volume fraction increases with time, this is the result of S-shaped bubble plume and separate bubbles, which make the column contain more bubbles in the late development.

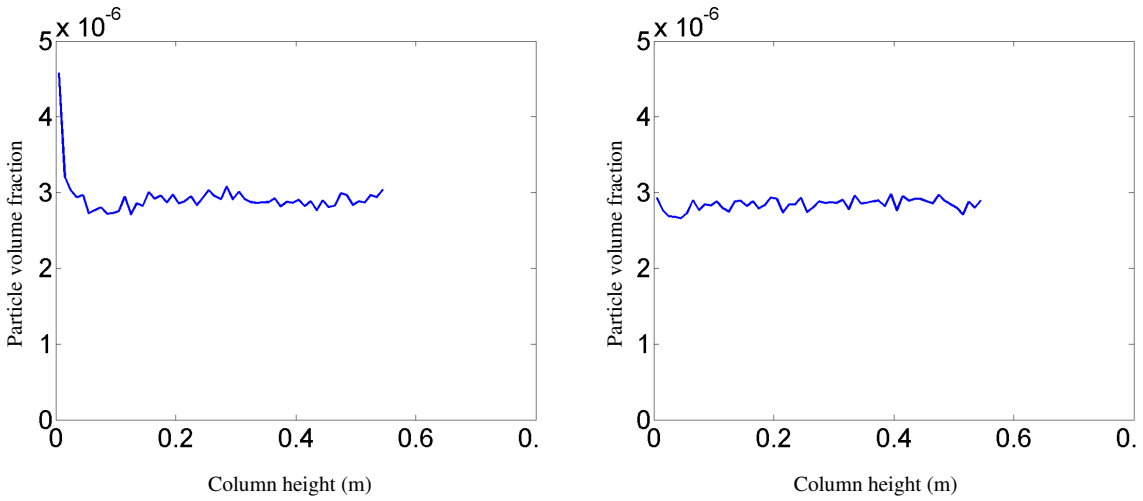

(a) (b)

Figure 4-6. Average volume fraction of the particles along the column height in the gas-liquid-particle three-phase flow in normal gravity. Superficial gas velocity U_s = 0.25 mm/s, initial bubble size d_b = 1.0mm, particle size d_p = 0.25 mm. (a) 5-15s (b) 16-26s

Figure 4-6a shows that particle volume fraction are very high at the bottom of the column. This can be explained by the distribution and evolution of the liquid velocities at the bottom. At the early development of the flow, liquid velocity is small, most particles are under the control of the downward liquid velocities, when the liquid with downward velocities push the particles to collide with the bottom wall, these particles will loss certain momentum and stay at the bottom, only particles near the narrow center region can rise up with the upward liquid. So particle volume fraction at the bottom wall is very high. However, with the evolution of the flow, liquid velocities increase. When the liquid vortices are very strong and horizontal liquid velocities in the bottom wall are big enough to push the near wall particle to the center and move them upwards with the bubble plume, high particle volume fraction at the bottom will not exist and particle volume fraction along the column height will become even, as shown by Figure 4-6b.

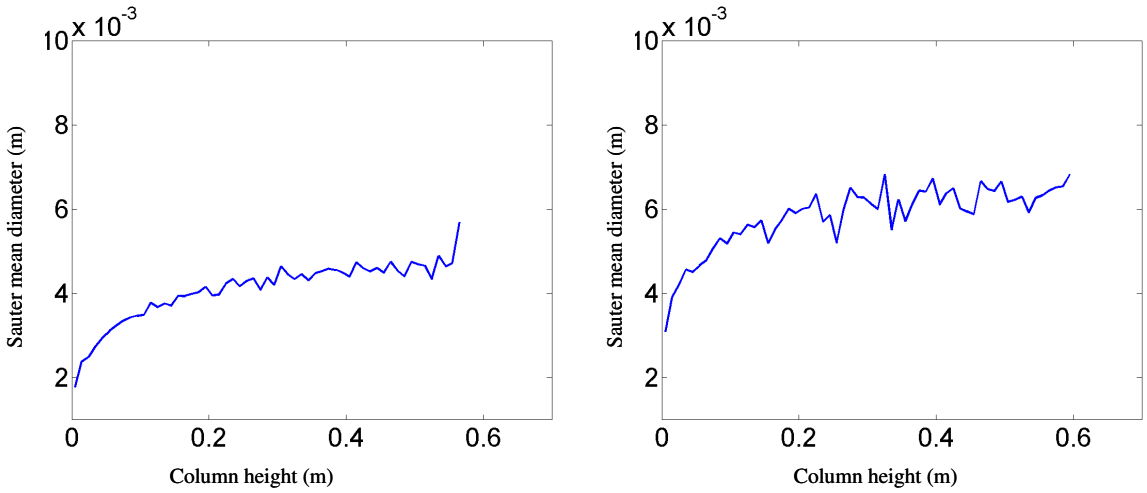

(a) (b)

Figure 4-7. Average Sauter mean diameter of the bubbles along the column height in the gas-liquid-particle three-phase flow in normal gravity. Superficial gas velocity U_s = 0.25 mm/s, initial bubble size d_b = 1.0mm, particle size d_p = 0.25 mm. (a) 5-15s (b) 16-26s

Figures 4-7a and 4-7b show average Sauter mean diameter of the bubbles along the column height from 5-15 s and 16-25 s, respectively. Because bubble-bubble coalescence will result in the increase of the bubble diameter, and the coalescence chance is proportional to the duration time of the bubbles, so bubble diameter increases with the column height, as seen from Figures4-7a and 4-7b. Comparison of Figures 4-7a and 4-7b show that bubble diameter increases with the evolution of the flow, due to more bubble coalescence. The dramatic increase of the bubble size at the free surface region in Figure 4-7a is the result of the rising free surface. At this region, due to bubble-bubble collisions, bubbles are larger, while there is no smaller bubble to balance those larger bubbles, so the average bubble size is lager.

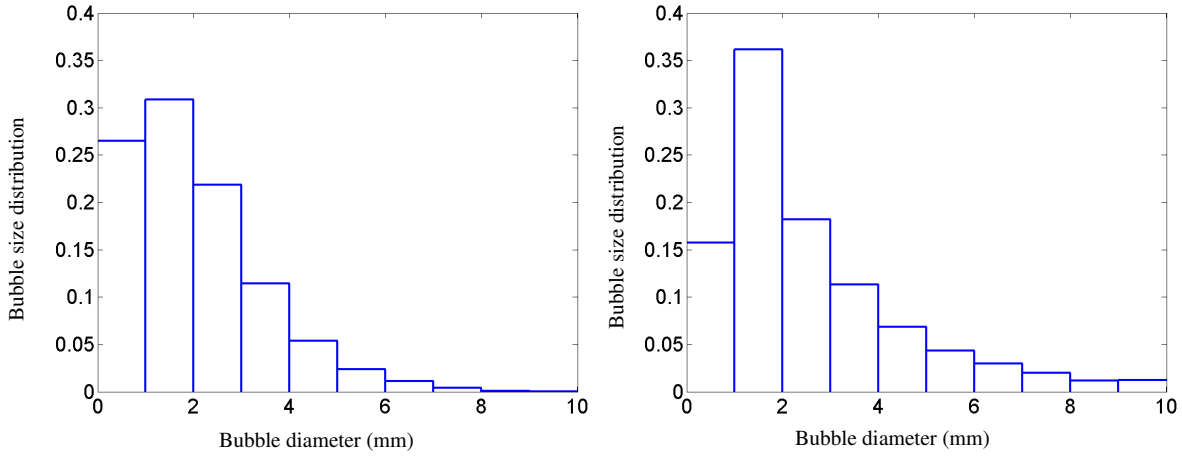

(a) (b)

Figure 4-8. Average bubble size distribution of the gas-liquid-particle three-phase flow in normal gravity in the entire column. Superficial gas velocity U_s = 0.25 mm/s, initial bubble size d_b = 1.0mm, particle size d_p = 0.25 mm. (a) 5-15s (b) 16-26s

Figures 4-8a and 4-8b show average bubble size distribution in the entire column from 5-15 s and 16-26 s, respectively. Though the bubble initial diameter is 1mm, due to bubble coalescence, bubbles between 1 and 2mm own largest quota. Comparison of Figures 4-8a and 4-8b shows that as mentioned above, with the evolution of the flow, there are more bubble coalescence, so the quota of small bubbles decreases and the quota of large bubbles increases.

4.3.2 Development of Transient Flow Structures in 2g Gravity

To study the effect of larger gravity on the three-phase flow, the characteristics of three-phase liquid-gas-solid flows under 2g gravity are studied in this section. The hydrodynamic parameters used in the simulation are listed in Table 4-1 (case 2). Figure 4-9 shows the snapshots of the model predictions for the liquid stream traces, and the locations of bubbles and particles at time of 1, 8, 17 and 25 s after the initiation of the flow. Figures 4-10, 4-11 and 4-12, respectively, show the corresponding velocities of bubbles, liquid and particles. These figures clearly demonstrated the transient characteristics and the evolution of the three-phase flow. In 2g gravity, the gravity force for all the three phases as well as the buoyancy force for both particles and bubbles is

twice of that in normal gravity condition. However, the liquid drag at the bubble is not related to the gravity, so compared to flow with normal gravity, bubbles can move faster in the column under 2g gravity condition.

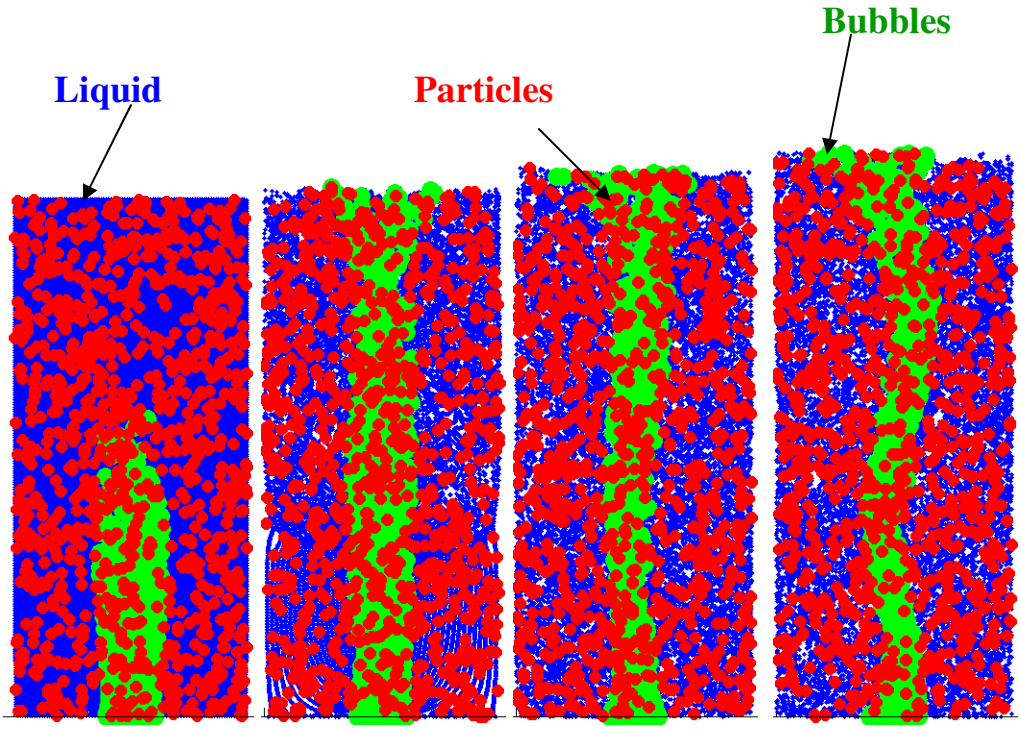

Figure 4-9. Computed flow structure of the gas-liquid-particle three-phase flow in 2g gravity. Superficial gas velocity U_s = 0.25 mm/s, initial bubble size d_b =1.0 mm, particle size d_p = 0.25 mm.

Similar to the flow with normal gravity, Figures 4-9a, 4-9b, 4-10a and 4-10b show that bubble plume rises rectilinearly along the centerline of the column; the vortices generated by the plume are almost symmetric at the early development of the flow, as seen in Figures 4-11a and 4-11b. But with the evolution of the flow, the vortices become non-symmetric as seen in Figure 4-11c, eventually staggered vortical flows are formed, as shown by Figure 4-11d, which changes the pattern of the bubble plume to S-shape as seen in Figure 4-9c, 4-9d, 4-10c and 4-10d, and the moving of these staggered vortices results in the oscillation of the bubble plume.

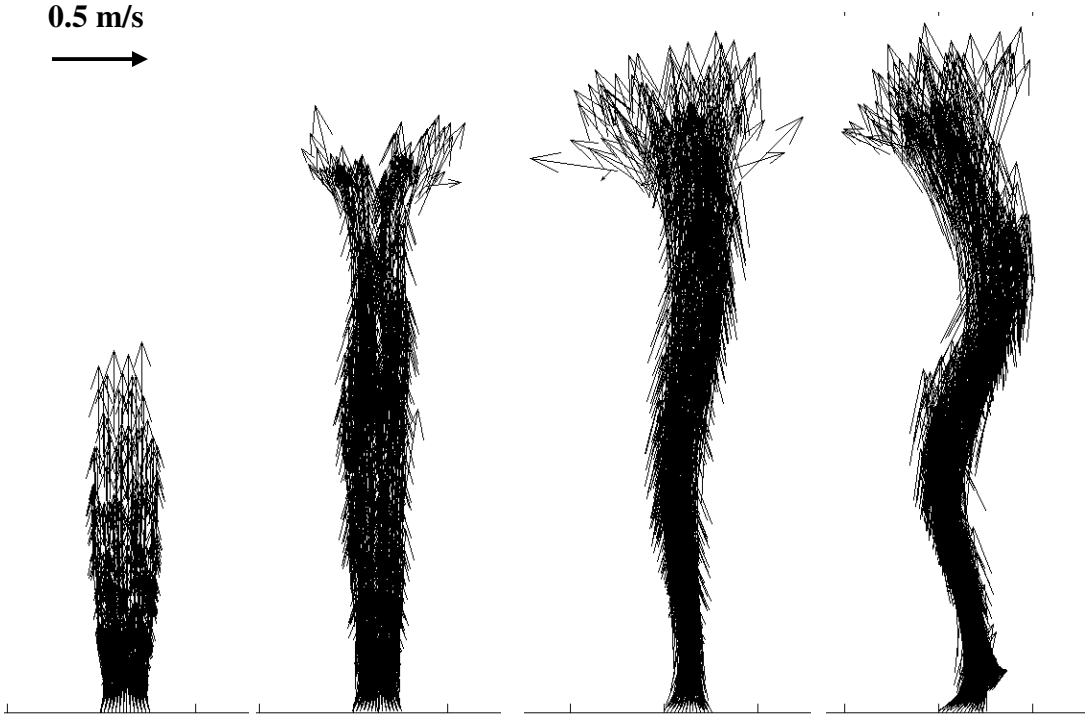

Figure 4-10. Computed snapshots of the bubble velocities of the gas-liquid-particle three-phase flow in 2g gravity . Superficial gas velocity U_s = 0.25 mm/s, initial bubble size d_b =1.0mm, Particle size d_p = 0.25mm.

Figure 4-10b, 4-10c and 4-10d show that the bubble upward velocities increase along the column height, attain the maximum at 0.45m, 0.5m and 0.45m, respectively, then decrease along the column height. The bubble maximum upward velocities as well as the differences of the bubble upward velocities along the column height increase with time, which may result in more bubble-bubble collision and coalescence.

Similarly, Figure 4-11b, 4-11c, 4-11d and Figure 4-12b, 4-12c, 4-12d show that the liquid and particle upward velocities increase along the column height, for liquid, all attain the maximum at 0.45m, for particles, at 0.45m, 0.4m, 0.4m respectively, then decrease along the column height. These maximum upward velocities and the differences

of these upward velocities along the column height increase with time; therefore there are more particle-particle collisions with the development of the flow.

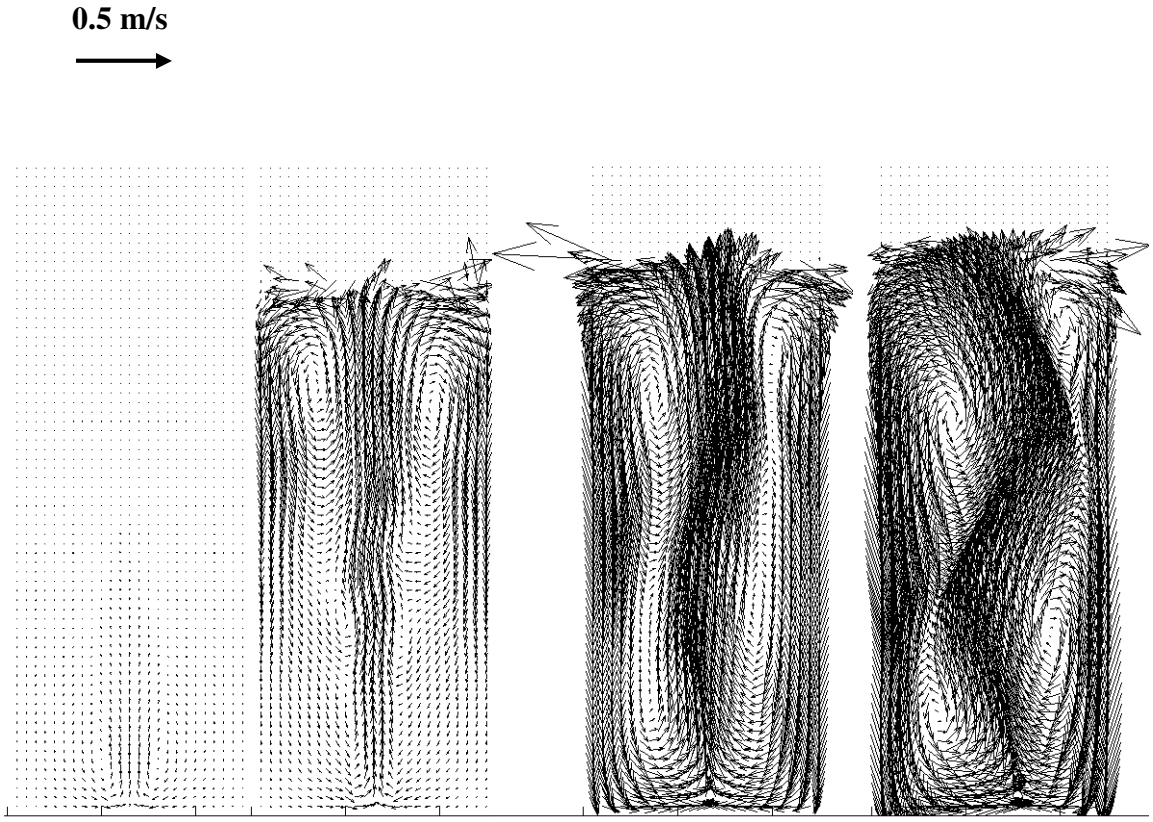

Figure 4-11. Computed snapshots of the liquid velocities of the gas-liquid-particle three-phase flow in 2g gravity. Superficial gas velocity U_s = 0.25mm/s, initial bubble size d_b = 1.0mm, particle size d_p = 0.25mm.

The location difference between the maximum upward velocities of bubbles, particles and liquid indicates that the relaxation effects exist not only at the driving of bubbles to the liquid, but also at the liquid transportation to particles.

Comparison of Figures 4-9, 4-11 and 4-12 indicates that most particles are concentrated outside the large vortices. Figures 4-11 and 4-12 show that velocities of particles and liquid are in the same order, with particle velocities being generally slightly

smaller than liquid velocity, but both are much smaller than bubble velocities shown in Figure 4-10.

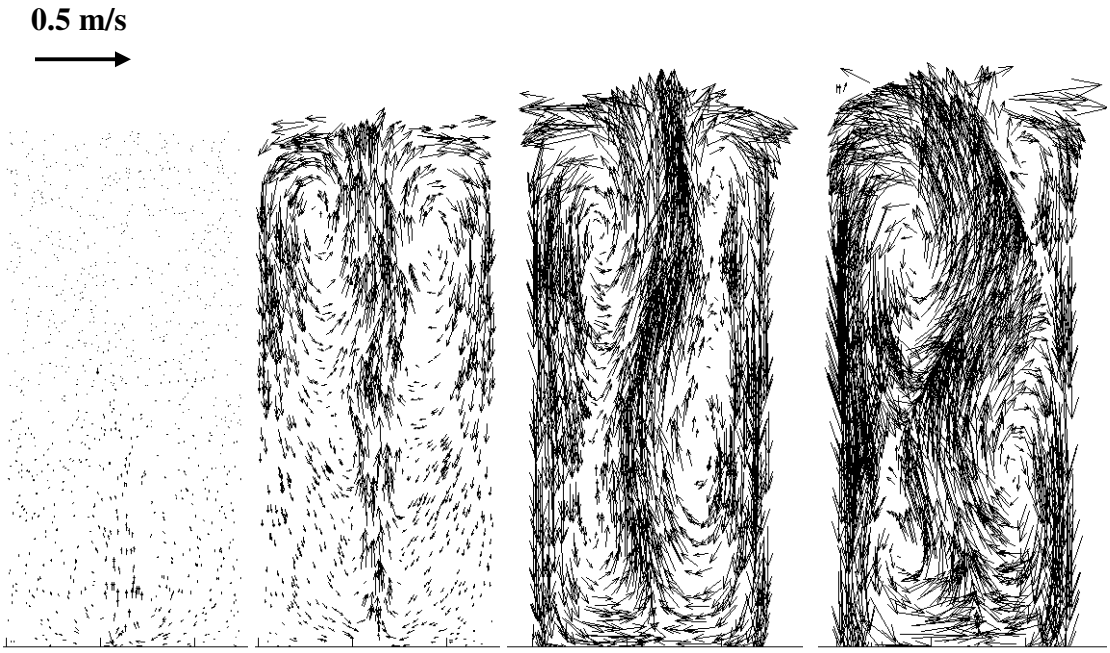

(a) 1s **(b) 8s** **(c) 17s** **(d) 25s**

Figure 4-12. Computed snapshots of the particle velocities of the gas-liquid-particle three-phase flow in 2g gravity. Superficial gas velocity U_s = 0.25 mm/s, initial bubble size d_b = 1.0 mm, particle size d_p = 0.25 mm.

Compared with Figure 4-1a, Figure 4-9a shows higher bubble plume position, which means bubbles under 2g gravity have larger rising velocities. Besides, compared with Figure 4-2, Figure 4-10 shows larger bubble-rising velocities too, which is a result of increased bubble buoyancy force in the flow under 2g gravity. Because bubble motion are the source of the three-phase bubbly flow, larger bubble-rising velocities will result in larger liquid and particle velocities as shown in Figures 4-11 and 4-12.

Compared with the rectilinear plume in Figure 4-1c, Figure 4-9c shows the bubble plume begins to oscillate at 17s, because of the effect of the non-symmetric liquid vortices as shown in Figure 4-11c, while in Figure 4-3c the liquid vortices are still

symmetric, which means due to the larger bubble-rising velocities, compared with the flow in normal gravity, the flow under 2g gravity develops fast.

Compared with Figure 4-2, Figure 4-10 also shows that there are more bubbles existing in the flow, since inlet bubble density are same, more bubbles means small bubble diameter and low bubble-bubble coalescence rate. This could be the result of larger bubble-rising velocities. Because larger bubble-rising velocities imply larger bubble longitudinal distances, which will decrease the bubble-bubble collision and coalescence rate. Besides, larger bubble-rising velocities also imply strong liquid vortices as shown in Figure 4-11, as a result, compared with Figure 4-3, Figure 4-11 shows larger horizontal liquid velocities at the bottom of the column, which point to the center of the column and will result in larger bubble relative velocities and larger Web numbers when bubbles in the left and right collide with each other. Collisions with larger Web numbers mean more bounce-back of the bubbles and less coalescence. Therefore, the diameter of bubbles is smaller while the number is lager in flow under 2g gravity.

Compared to flow under normal gravity as shown in Figures 4-1 and 4-2, there is no separate bubbles seen in Figure 4-9 and Figure 4-10. This could be the result of larger bubble-rising velocities too. Because the separate bubbles are the result of the drag of the liquid vortices, while larger bubble-rising velocities means larger bubble momentum and inertia, it is relatively difficult for liquid vortices to catch bubbles with large inertia from a strong bubble plume and forms separate bubbles.

Figures 4-13 and 4-14 show average volume fractions of the bubbles and particles along the column height under 2g gravity flow, respectively, where (a) and (b) refer the time period from 5-15 s and 16-26 s, respectively. Similar to the flow under normal gravity, Figures 4-13a and 4-13b show that the highest bubble volume fraction is located at the bottom of the column, it decreases along the height of column, attains the minimum at about 0.38m and 0.2m, respectively, then increases along the height; Comparison of Figure 4-13a and 4-13b shows that the bubble volume fraction increases with time; Figure 4-14a shows a high particle volume fraction at the bottom of the column, due to

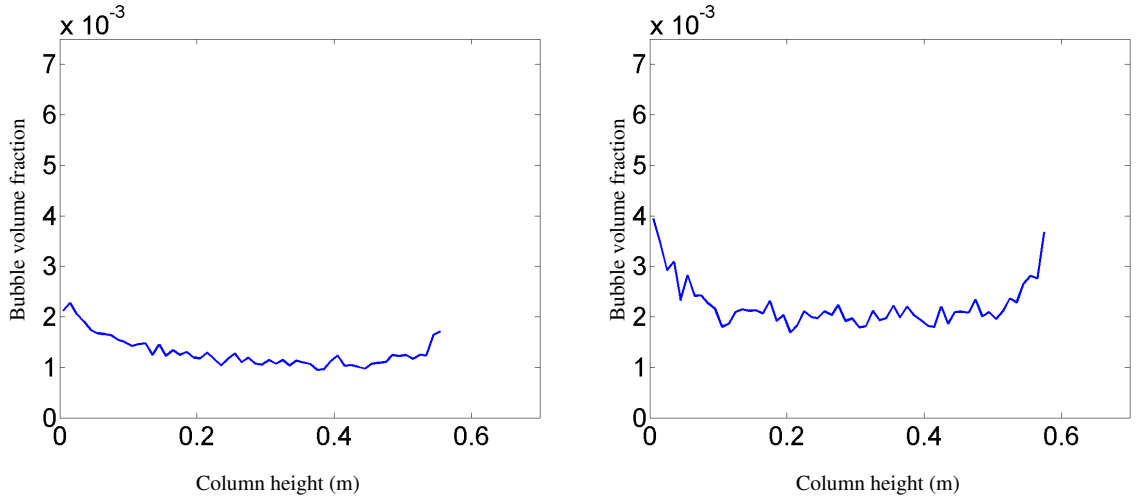

Figure 4-13. Average volume fraction of the bubbles along the column height in the gas-liquid-particle three-phase flow in 2g gravity. Superficial gas velocity U_s = 0.25 mm/s, initial bubble size d_b = 1.0mm, particle size d_p = 0.25 mm. (a) 5-15s (b) 16-26s

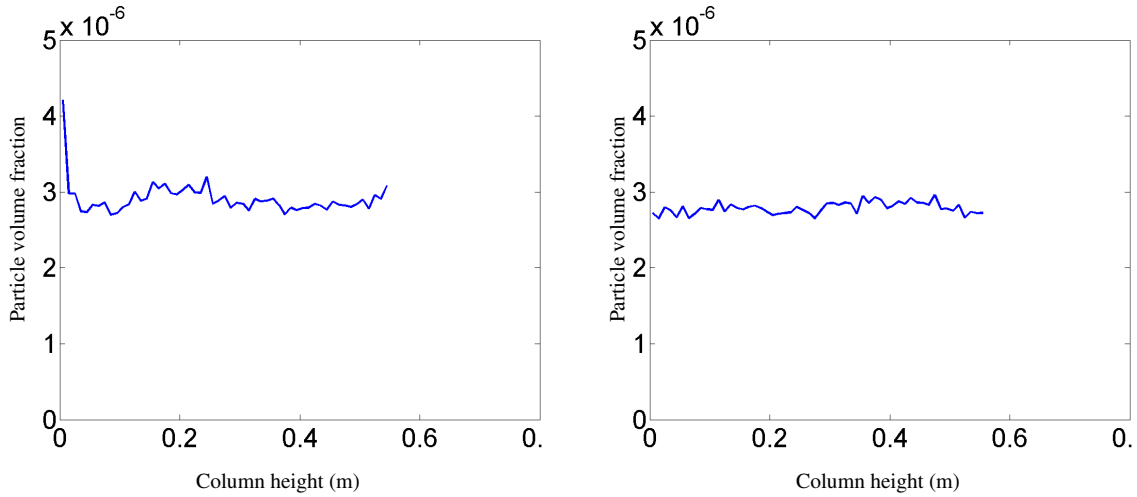

Figure 4-14. Average volume fraction of the particles along the column height in the gas-liquid-particle three-phase flow in 2g gravity. Superficial gas velocity U_s = 0.25 mm/s, initial bubble size d_b = 1.0mm, particle size d_p = 0.25 mm. (a) 5-15s (b) 16-26s

the liquid downward velocities which push the particles to the bottom wall at the early development of the flow, it disappears in Figure 4-14b as explained above. The small value at about 0.09m is the result of the multi-effect: particles are pushed up by liquid

with upward velocities which results in the second peak value at about 0.23m too; or particles are pushed down by that with downward velocities at the early development of the flow. The second small value at about 0.38m are the result of the high particle velocities in this region. However, all these features belong to the early development of the flow, which disappears in Figure 4-14b, because of the back and forth motion of the staggered vortices, which make the particle distribution uniform along the column height, like a revolving spoon mixing sugars within a cup of coffee. Compared with Figure 4-5, Figure 4-13 shows smaller value, due to higher bubble upward velocities under 2g gravity. Compared with Figure 4-6, Figure 4-14 shows similar shape, except that Figure 4-14a is much more bumpy, due to higher phase velocities under 2g gravity.

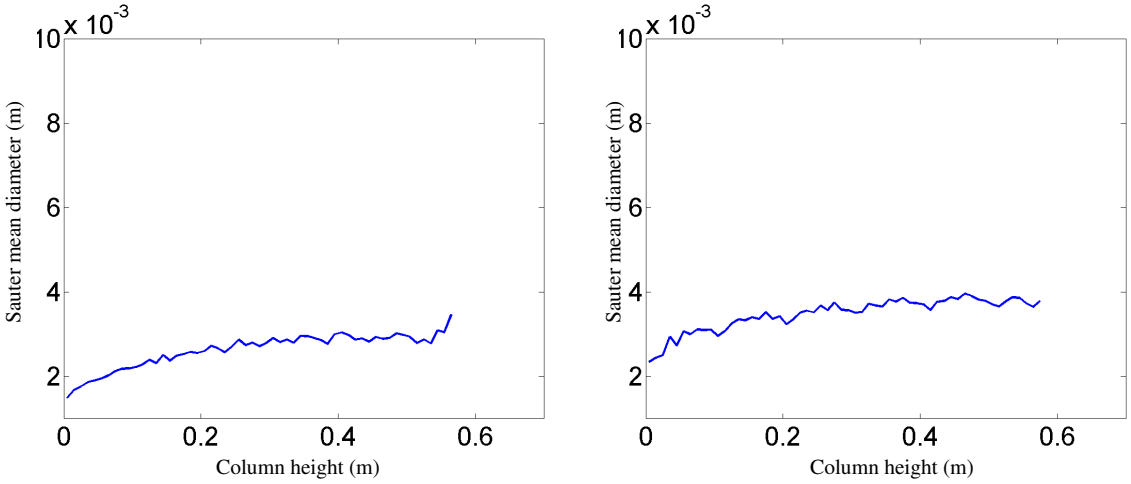

(a) (b)

Figure 4-15. Average sauter mean diameter of the bubbles along the column height in the gas-liquid-particle three-phase flow in 2g gravity. Superficial gas velocity U_s = 0.25 mm/s, initial bubble size d_b = 1.0mm, particle size d_p = 0.25 mm. (a) 5-15s (b) 16-26s

Figures 4-15a and 4-15b show average Sauter mean diameter of the bubbles along the column height under 2g gravity flow, from 5-15 s and 16-25 s, respectively. As mentioned above, due to bubble-bubble coalescence, bubble diameter increases with the column height and the evolution of the flow. Compared with Figure 4-7, Figure 4-15 shows much smaller value, due to less bubble-bubble coalescence under 2g gravity.

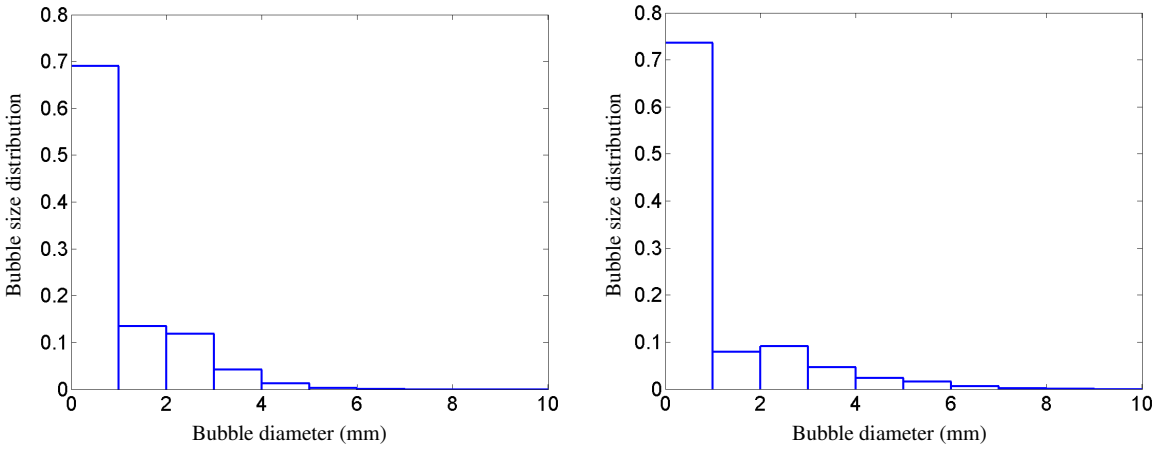

(a) (b)

Figure 4-16. Average bubble size distribution of the gas-liquid-particle three-phase flow in 2g gravity in the entire column. Superficial gas velocity U_s = 0.25 mm/s, initial bubble size d_b = 1.0mm, particle size d_p = 0.25 mm. (a) 5-15s (b) 16-26s

Figures 4-16a and 4-16b show average bubble size distribution in the entire column under 2g gravity flow from 5-15 s and 16-26 s, respectively. Comparison of Figures 4-16a and 4-16b shows that with the evolution of the flow, the quota of large bubbles with diameters of 3-7 mm increases due to bubble coalescence, which consumes the small bubbles with diameters of 1-3 mm. However, unlike the flow under normal gravity, Figure 4-16 shows that 1mm bubbles own largest quota, because of less bubble-bubble coalescence under 2g gravity. Besides, the quota of 1 mm bubbles increases with the evolution of the flow. The reason is that the developed strong liquid vortices result in larger horizontal liquid velocities at the bottom of the column, as mentioned above, which will result in larger bubble relative velocities for bubble-bubble collisions and less coalescence.

4.3.3 Development of Transient Flow Structures in 0.5g Gravity

To study the effect of smaller gravity on the three-phase flow, a study of the characteristics of three-phase liquid-gas-solid flows under 0.5g gravity is given in this section. The hydrodynamic parameters used in the simulation are listed in Table 4-1 (case 3). Figure 4-17 shows the snapshots of the simulations for the liquid stream traces,

and the locations of bubbles and particles at time of 1, 8, 17 and 25 s after the initiation of the flow. Figures 4-18, 4-19 and 4-20, respectively, show the corresponding velocities of bubbles, liquid and particles. These figures clearly described the transient characteristics and the evolution of the three-phase flow. In 0.5g gravity, the gravity force for all the three phases as well as the buoyancy force for both particles and bubbles is half of that in normal gravity condition, so compared to flow with normal gravity, bubbles move slowly in the column under 0.5g gravity condition.

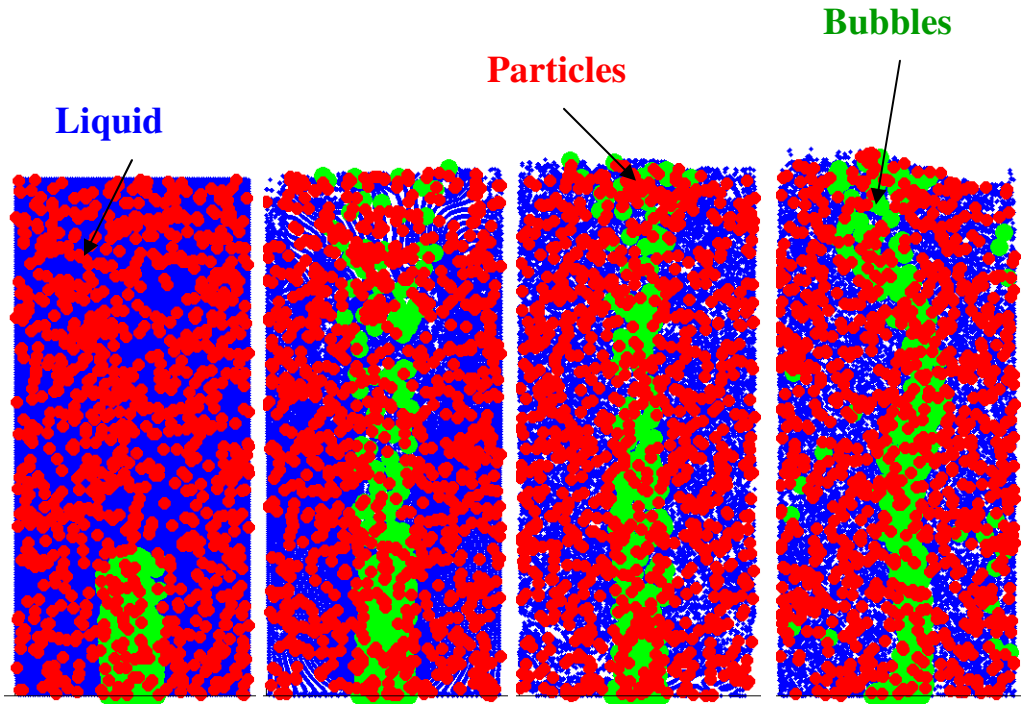

Figure 4-17. Computed flow structure of the gas-liquid-particle three-phase flow in 0.5g gravity. Superficial gas velocity U_s = 0.25 mm/s, initial bubble size d_b =1.0 mm, particle size d_p = 0.25 mm.

Similar to the flow with normal gravity, Figures 4-17, 4-18 and 4-19 show that at the 17s, bubble plume rises rectilinearly along the centerline of the column; the vortices generated by the plume are almost symmetric, as seen in Figures 4-19a, 4-19b and 4-19c. However, with the evolution of the flow, the vortices become non-symmetric and

eventually staggered vortical flows are formed, as shown by Figure 4-19d, which changes the pattern of the bubble plume to S-shape as seen in Figure 4-17d, and the moving of these staggered vortices controls the oscillation of the bubble plume.

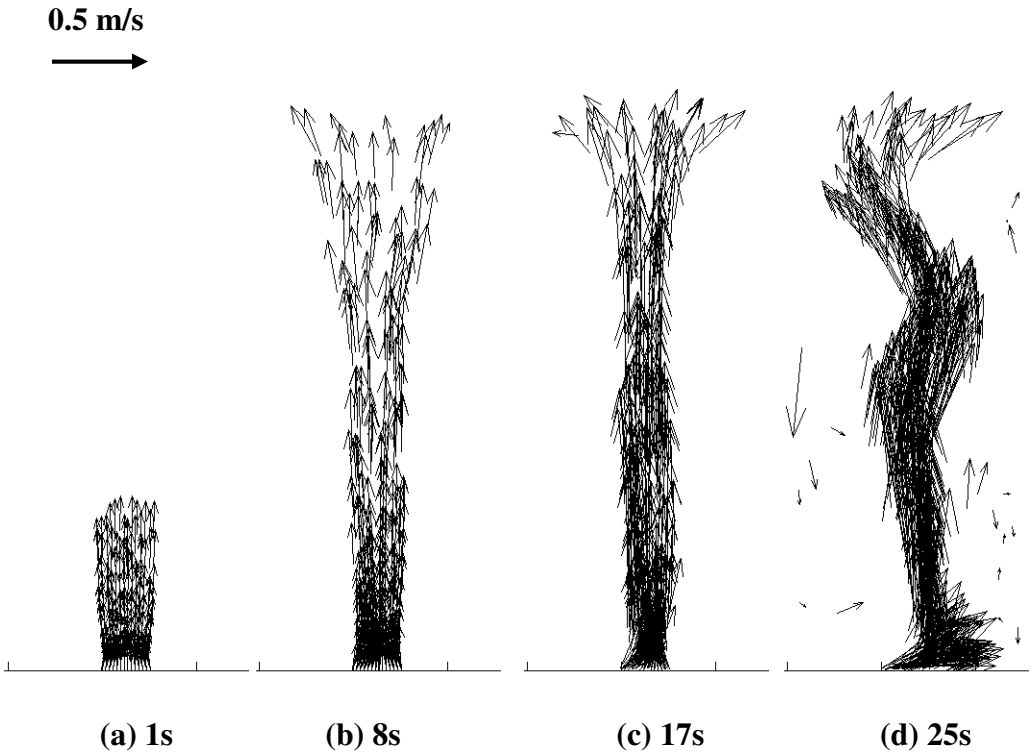

Figure 4-18. Computed snapshots of the bubble velocities of the gas-liquid-particle three phase flow in 0.5g gravity . Superficial gas velocity U_s = 0.25 mm/s, initial bubble size d_b =1.0mm, Particle size d_p = 0.25mm.

Figures 4-18, 4-19 and 4-20 show that the velocities of the bubbles, liquid and particles increase with the development of the flow. Besides, Figures 4-18 and 4-20 show that the maximum upward velocities of bubbles and particles as well as the differences of the bubble and particle upward velocities along the column height increase with the development of the flow too, which may implies more particle-particle and bubble-bubble collision and bubble-bubble coalescence.

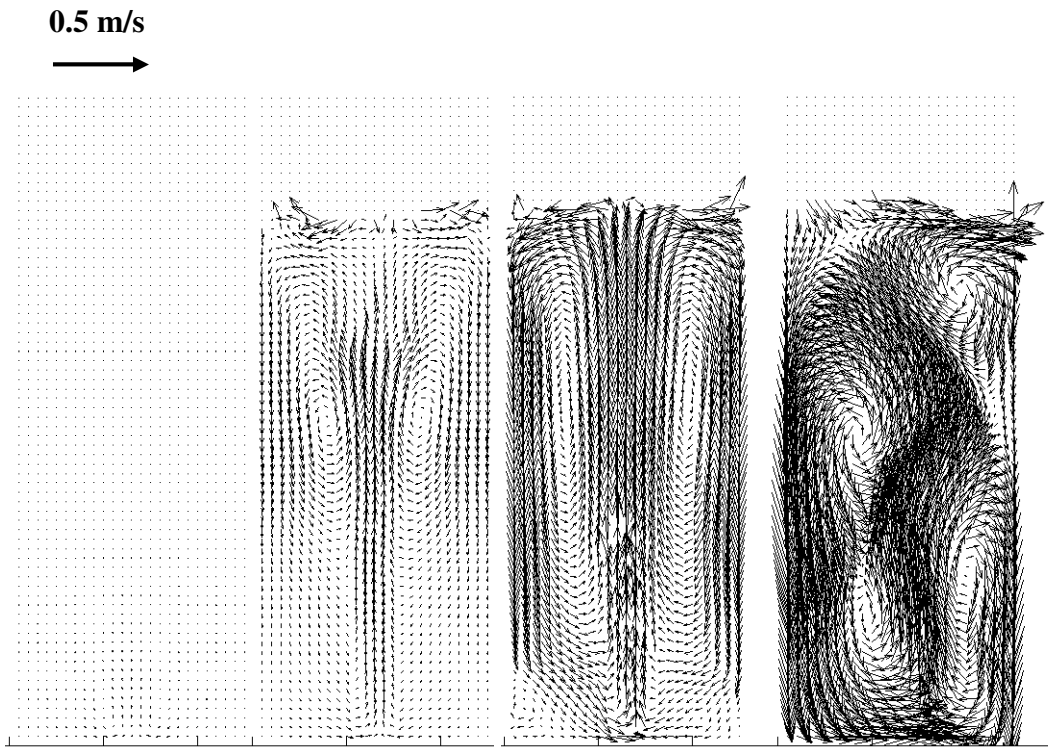

Figure 4-19. Computed snapshots of the liquid velocities of the gas-liquid-particle three-phase flow in 0.5g gravity. Superficial gas velocity U_s = 0.25mm/s, initial bubble size d_b = 1.0mm, particle size d_p = 0.25mm.

Figure 4-18b, 4-18c and 4-18d show that the bubble upward velocities increase along the column height, attain the maximum at 0.35m, 0.15m and 0.1m, respectively, then decrease along the column height. Figures 4-17d and 4-18d show many separate bubbles, moving with liquid vortices.

Similarly, Figure 4-19b, 4-19c, 4-19d and Figure 4-20b, 4-20c, 4-20d show that the liquid and particle upward velocities increase along the column height, for liquid, attain the maximum at 0.35m, 0.4m and 0.1m respectively; for articles, at 0.35m, 0.4m and 0.15m respectively, then decrease along the column height.

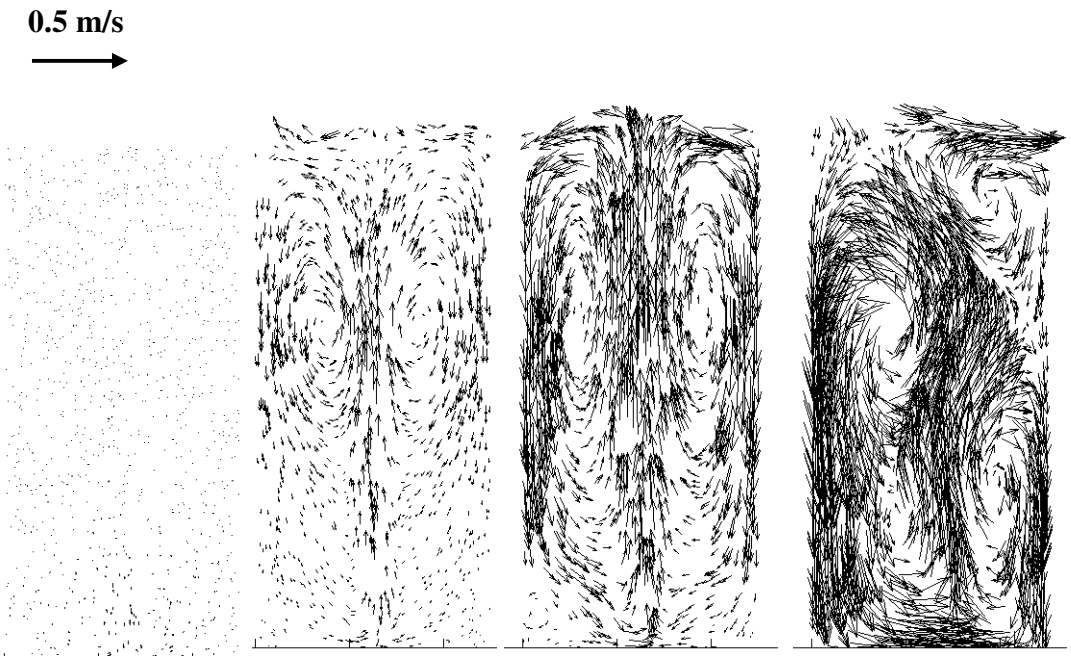

Figure 4-20. Computed snapshots of the particle velocities of the gas-liquid-particle three-phase flow in 0.5g gravity. Superficial gas velocity U_s = 0.25 mm/s, initial bubble size d_b = 1.0 mm, particle size d_p = 0.25 mm.

The obviously locations difference between the maximum upward velocities of bubbles, particles and liquid indicate once more that the relaxation effects exist at both the driving of bubbles to the liquid and the liquid transportation to particles.

Comparison of Figures 4-17, 4-19 and 4-20 indicates that most particles are concentrated outside the large vortices. Figures 4-19 and 4-11 show that velocities of particles and liquid are in the same order, while particle velocities are generally slightly smaller than liquid velocity, but both are smaller than bubble velocities shown in Figure 4-18.

Compared with Figure 4-1a, Figure 4-17a shows lower bubble plume position, which means bubbles under 0.5g gravity have smaller rising velocities, as can be seen by comparison of Figure 4-18 with Figure 4-2, due to decreased bubble buoyancy force.

Because bubble motion are the source of the three-phase bubbly flow, smaller bubble-rising velocities will result in smaller liquid and particle velocities as shown in Figures 4-19 and 4-20. Therefore, compared with flow under normal gravity, flow under 0.5g gravity develops slowly.

Compared with Figure 4-2, Figure 4-18 shows less bubbles in the flow, at the condition of same inlet bubble density, less bubbles means larger bubble diameter and higher bubble-bubble coalescence rate. This could be explained by the smaller bubble-rising velocities. Under 0.5g gravity, smaller bubble-rising velocities imply smaller bubble longitudinal distances, while will increase the bubble-bubble collision and coalescence rate. Besides, smaller bubble-rising velocities also mean weak liquid vortices as shown in Figure 4-19, as a result, compared with Figure 4-3, Figure 4-19 shows smaller horizontal liquid velocities at the bottom of the column, which point to the center of the column and will result in smaller bubble relative velocities and smaller Web numbers when bubbles in the left and right collide with each other. Collisions with smaller Web numbers mean less bounce-back of the bubbles and more coalescence. Thus, the diameter of bubbles is larger while the number is smaller in flow under 0.5g gravity.

Compared to flow under normal gravity as shown in Figures 4-1 and 4-2, there are more separate bubbles seen in Figure 4-17 and Figure 4-18. This could be explained by the smaller bubble-rising velocities too. Because smaller bubble-rising velocities mean smaller bubble momentum and inertia, it is much more easy for liquid vortices to catch bubbles from the bubble plume with smaller inertia and forms separate bubbles.

Figures 4-21 and 4-22 show average volume fractions of the bubbles and particles along the column height under 0.5g gravity flow, respectively, where (a) and (b) refer the time period from 5-15 s and 16-26 s, respectively. Similar to the flow under normal gravity, Figures 4-21a and 4-21b show that the highest bubble volume fraction is located at the bottom of the column, it decreases along the height of column, attains the minimum at about 0.4m and 0.28m, respectively, where correspondingly to the maximum bubble velocities, then increases along the height; Comparison of Figure 4-21a and 4-21b shows

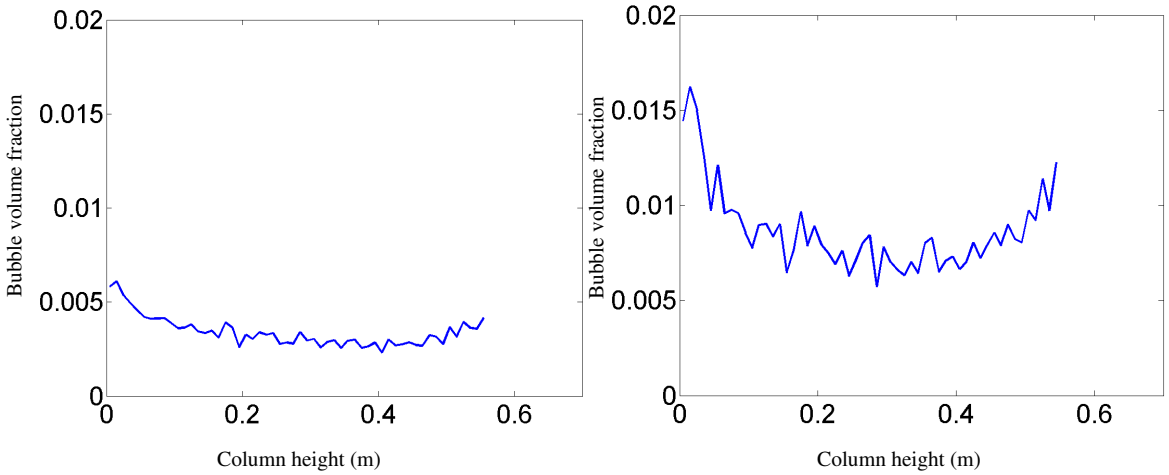

(a) (b)

Figure 4-21. Average volume fraction of the bubbles along the column height in the gas-liquid-particle three-phase flow in 0.5g gravity. Superficial gas velocity U_s = 0.25 mm/s, initial bubble size d_b = 1.0mm, particle size d_p = 0.25 mm. (a) 5-15s (b) 16-26s

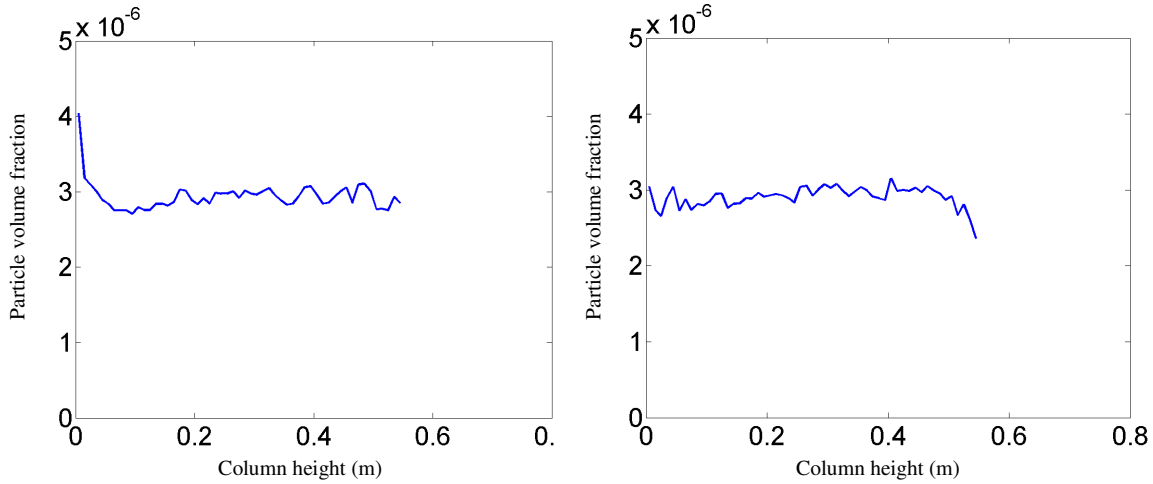

(a) (b)

Figure 4-22. Average volume fraction of the particles along the column height in the gas-liquid-particle three-phase flow in 0.5g gravity. Superficial gas velocity U_s = 0.25 mm/s, initial bubble size d_b = 1.0mm, particle size d_p = 0.25 mm. (a) 5-15s (b) 16-26s

that the bubble volume fraction increases with the evolution of the flow; Figure 4-22a shows a high particle volume fraction at the bottom of the column, due to the liquid downward velocities at the early development of the flow, it disappears in Figure 4-22b

as explained above. Figure 4-22b shows a small value at the top of the column, which could be the effect of the uneven free surface, generated by the disturbing of large bubbles and staggered liquid vortices. When the free surface is slant, the average volume fractions of particles will decrease. Compared with Figure 4-5, Figure 4-21 shows much larger value, due to smaller bubble upward velocities under 0.5g gravity. Compared with Figure 4-6, Figure 4-22 shows similar shape, Figure 4-22b shows a decreased value at the free surface region, as mentioned above, due to disturbing of large bubbles and liquid vortices under 0.5g gravity.

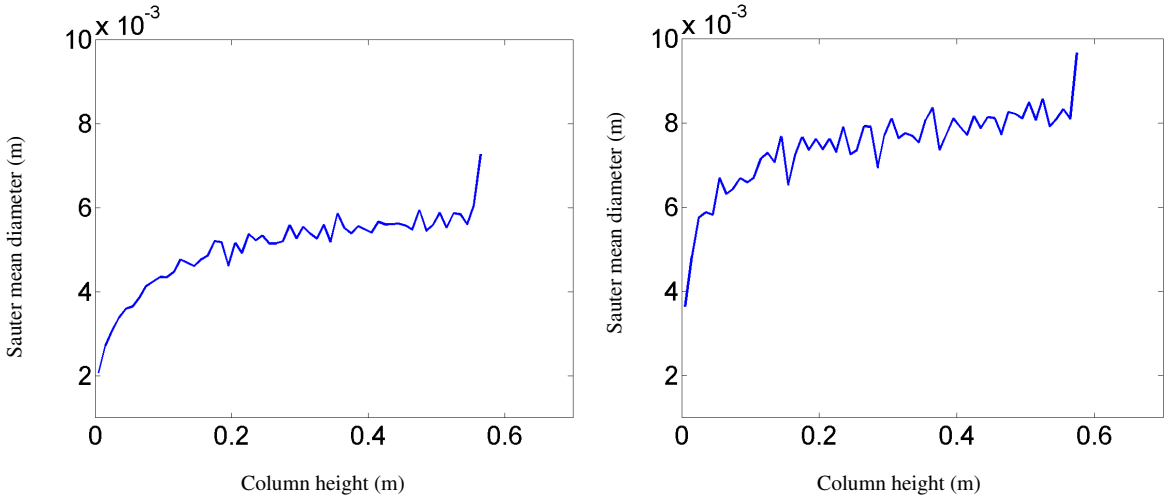

Figure 4-23. Average sauter mean diameter of the bubbles along the column height in the gas-liquid-particle three-phase flow in 0.5g gravity. Superficial gas velocity U_s = 0.25 mm/s, initial bubble size d_b = 1.0mm, particle size d_p = 0.25 mm. (a) 5-15s (b) 16-26s

Figures 4-23a and 4-23b show average Sauter mean diameter of the bubbles along the column height under 0.5g gravity flow, from 5-15 s and 16-25 s, respectively. As mentioned above, due to bubble-bubble coalescence, bubble diameter increases with the column height and the development of the flow. Compared with Figure 4-7, Figure 4-23 shows much larger value, due to more bubble-bubble coalescence under 0.5g gravity.

Figures 4-24a and 4-24b show average bubble size distribution in the entire column under 0.5g gravity flow from 5-15 s and 16-26 s, respectively. Comparison of Figures 4-24a and 4-24b shows that with the evolution of the flow, the quota of large bubbles

increases due to bubble coalescence. Compared with the flow under normal gravity, Figure 4-24 shows that the quota of large bubbles increase, because of more bubble-bubble coalescence under 0.5g gravity.

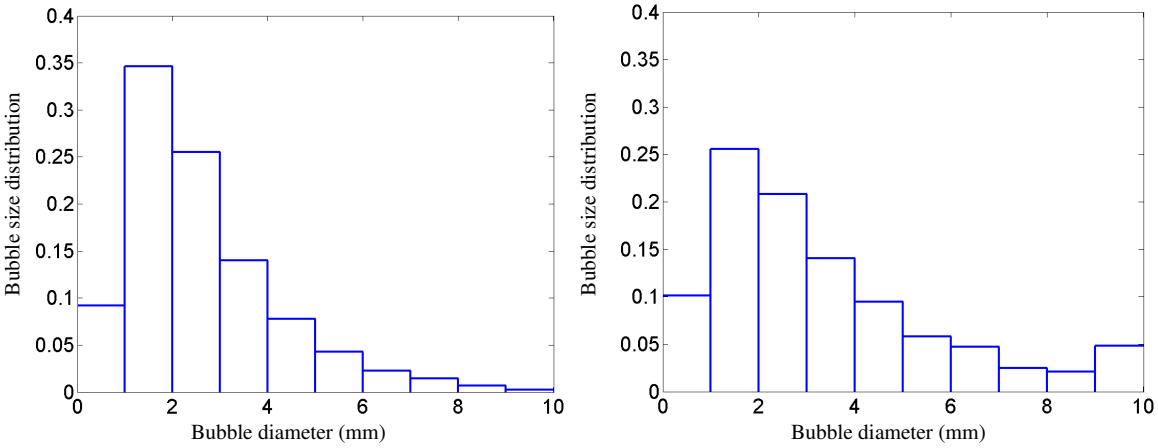

Figure 4-24. Average bubble size distribution of the gas-liquid-particle three-phase flow in 0.5g gravity in the entire column. Superficial gas velocity U_s = 0.25 mm/s, initial bubble size d_b = 1.0mm, particle size d_p = 0.25 mm. (a) 5-15s (b) 16-26s

4.4 CONCLUSIONS

Numerical simulations of gas-liquid-solid flows in different gravity were performed by an Eulerian-Lagrangian approach. The two-way coupling between bubble-liquid and particle-liquid are accounted for in the study. Interactions between particle-particle and bubble-bubble are included using the hard sphere model approach, and the bubble coalescence is also included in the model. The transient characteristics of three-phase flows in different gravity are studied and the effects of gravity are discussed. On the basis of the presented results, we have the following conclusions:

1. The three-phase flow in the bubble column are dominated by time-dependent staggered vortices, Particles are mainly located outside the bubble plume. The velocities of liquid and particles are in the same order, with particle velocity being generally slightly smaller than the liquid velocities, but both smaller than bubble velocities.

2. The location of the maximum upward velocities of bubbles, particles and liquid can be different, because of the relaxation effects at the driving of bubbles to the liquid, and the liquid transportation to particle.
3. The bubble volume fraction increases with the evolution of the flow. The highest bubble volume fraction is located at the bottom of the column.
4. The Sauter mean diameter of the bubbles are proportional to the time the bubbles stay. Due to bubble-bubble coalescence, bubble diameter not only increases along the column height, but also increases with development of the flow.
5. Because of increased bubble buoyancy force in the flow under high gravity, the phase velocities are larger than that of the flow under low gravity, therefore, the flow under high gravity develop fast. However, due to less bubble-bubble collision and coalescence, bubbles in the high gravity flow are smaller.
6. There are less separate bubbles in the flow with high gravity, due to high inertia of the bubble plume.
7. Bubble volume fraction is smaller in the flow with high gravity, because of the high bubble velocities

4.5 ACKNOWLEDGEMENT

The financial support by the US Department of Energy is gratefully acknowledged.

The content of this chapter is partly presented in the International Conference on Multiphase Flow, 9.-13. July, 2007. Leipzig,Germany.

CHAPTER 5. EFFECTS OF CAPILLARY FORCE AND SURFACE DEFORMATION ON PARTICLE REMOVAL IN TURBULENT FLOWS

5.1 INTRODUCTION

Micro-particle adhesion and removal are of great concern in semiconductor, pharmaceutical and xerographic industries. Particle adhesion force per unit mass increases sharply as the particle size decreases; therefore, it is very difficult to remove particles with diameter smaller than 1μm from surfaces (Ranade (1987) and Mittal (1988)).

The topic of particle adhesion and removal has been reviewed by Corn (1966), Krupp (1967), Visser (1972), Tabor (1977), Bowling (1985) and Berkeley (1980). For particles under dry conditions, the van der Waals force makes the major contribution to the particle adhesion to a surface. Bradley (1932) and Derjaguin (1934) considered the effect of contact deformation on particle adhesion. Johnson, Kendall and Roberts (1971) developed the so-called JKR adhesion model to include the effects of the surface energy and surface deformation. Kendall (1975) studied rolling friction and adhesion between smooth solids. Using the Hertzian profile assumption and including the effects of surface energy, Derjaguin, Muller and Toporov (1975) developed a particle adhesion theory, which now is referred to as the DMT model. Maugis and Pollock (1984) developed a particle adhesion model allowing for plastic deformation. Other adhesion models have been developed by Tsai, Pui and Liu (1991) and Maugis (1995). More recent studies of particle adhesion were reported by Quesnel et al. (2001) and Kendall (2001).

There has been much debate on the validity of the JKR and DMT models. Muller et al. (1980, 1983) studied the range of application of the JKR and DMT models using a Lennard-Jones potential and suggested that, for a system with high Young's modulus, low surface energy, and small-diameter particles, the DMT model applies; in contrast, for a system with low Young's modulus, high surface energy, and large-diameter particles, the JKR model is more suitable.

Particle resuspension was studied by a number of researchers. Corn (1965) and Corn and Stein (1965) measured the re-entrainment of particles from plane surfaces, and also noted the importance of surface roughness and relative humidity. Punjrath and Heldman (1972) studied the particle resuspension mechanisms by a series of wind tunnel experiments. Gillett et al. (1974), Makhonko and Rabotnova (1982) and Garland (1983) reported the results of their studies concerning particle resuspension from soil and grass surfaces. Healy (1977), Sehmel (1980), Smith et al. (1982), Hinds (1982) and Nicholson (1988) reviewed the resuspension processes. Particle detachment mechanisms in turbulent flows were studied by Cleaver and Yates (1973). More recent models of particle resuspension processes were reported by Reeks and Hall (1988), Wen and Kasper (1989), Wang (1990), Masironi and Fish (1967), Tsai et al. (1991), Soltani and Ahmadi (1994, 1995a, 1995b, 1999) and Ibrahim et al. (2003). The influence of relative humidity on adhesion was discussed by Podczeck et al. (1997), Busnaina and Elsawy (2001) and Tang and Busnaina (2001). Zimon (1982) and Taheri and Bragg (1992), respectively, reported their experiments for particle resuspension in dry and humid air conditions. The experiments of Zimon (1982) were carried out with humidity less than 10%. Taheri and Bragg (1992), however, performed their experiments at a normal room temperature and humidity, and their results agree well with the prediction by Soltani and Ahmadi (1994) for particle resuspension in moist air. Recently, Ibrahim et al. (2003, 2004) also measured particle resuspension in both dry and humid air conditions. Their experiments were conducted at a humidity of 25±3% for dry condition and 67% for humid condition. Direct atomic force microscopy (AFM) measurement of adhesion force was performed by Gotzinger and Peukert (2003a, 2003b). More recently, Ahmadi et al. (2007) studied particle adhesion and detachment in turbulent flows including the effect of capillary forces using the JKR adhesion theory, rolling, and sliding detachment models.

In this study, a new model for rolling detachment of spherical particles in the presence of capillary forces for both elastic and plastic surface deformations is developed. An effective thermodynamic work of adhesion model is used to account for the effects of capillary force for hydrophilic materials. The maximum adhesion resistance moments are evaluated using the JKR and the DMT models for elastic surface

deformation and the Maugis-Pollock model is used for the plastic surface deformation. The turbulence burst/inrush model is used for evaluating the near-wall velocity field. The potential for rolling detachment of spherical particles is studied and the critical shear velocities for detaching particles of various sizes are evaluated, and the results are compared with those obtained in the absence of the capillary force. It is shown that the capillary force significantly increases the particle adhesion and decreases the opportunity for resuspension. The model predictions for glass particles on glass and steel substrates are compared with the available experimental data for dry and humid air conditions.

5.2 ADHESION MODELS

In this section, a brief summary of the adhesion models used in this study is presented.

5.2.1 JKR Model

In the Johnson-Kendall-Roberts (1971) (JKR) model the effects of surface energy and deformation of an elastic sphere in contact with an elastic half-space are included. Accordingly, a finite contact area forms and the radius of the contact circle, a, is given as

$$a^3 = \frac{d}{2K}\left[P + \frac{3}{2}W_A\pi d + \sqrt{3\pi W_A dP + \left(\frac{3\pi W_A d}{2}\right)^2}\right] \tag{5-1}$$

where

$$K = \frac{4}{3}\left[\frac{1-\nu_1^2}{E_1} + \frac{1-\nu_2^2}{E_2}\right]^{-1} \tag{5-2}$$

is the composite Young's modulus. Here, d is the particle diameter, P is the applied normal load, and ν_i and E_i are, respectively, the Poisson ratio, and the Young modulus of material i (i=1 or 2). In Equation (5-1), W_A is the thermodynamic work of adhesion.

According to the JKR model, the pull-off force, F_{po}, needed to detach a particle is given by:

$$F_{po}^{JKR} = \frac{3}{4}\pi W_A d \tag{5-3}$$

At the moment of separation, the contact radius is given by

$$a = \frac{a_o}{4^{1/3}} = \left(\frac{3\pi W_A d^2}{8K}\right)^{\frac{1}{3}} \tag{5-4}$$

where a_o is the contact radius at zero applied load given as

$$a_o = \left(\frac{3\pi W_A d^2}{2K}\right)^{\frac{1}{3}} . \tag{5-5}$$

5.2.2 DMT Model

In the Derjaguin-Muller-Toporov (1975) (DMT) model the detachment force is given by

$$F_{Po}^{DMT} = \pi W_A d \tag{5-6}$$

which is 4/3 times the JKR force given by Equation (5-3). The contact radius at zero external force is given as

$$a_0 = \left(\frac{\pi W_A d^2}{2K}\right)^{\frac{1}{3}} \tag{5-7}$$

which comes from Hertz's contact theory. The DMT model predicts that at the moment of separation, the contact radius is reduced to zero.

5.2.3 Maugis-Pollock Model

While the JKR and the DMT models assume elastic deformation, the Maugis-Pollock (1984) model takes into account the plastic deformation of the particle and the substrate. The corresponding contact radius is given as

$$a = \sqrt{\frac{P + \pi W_A d}{\pi H}} \tag{5-8}$$

where H is the hardness of the material. For glass-steel combination, because the hardness of the steel is in the range of that of the glass, the hardness of the steel is used. The hardness can be estimated as

$$H = 3Y \tag{5-9}$$

Here Y is the yield stress of the material.

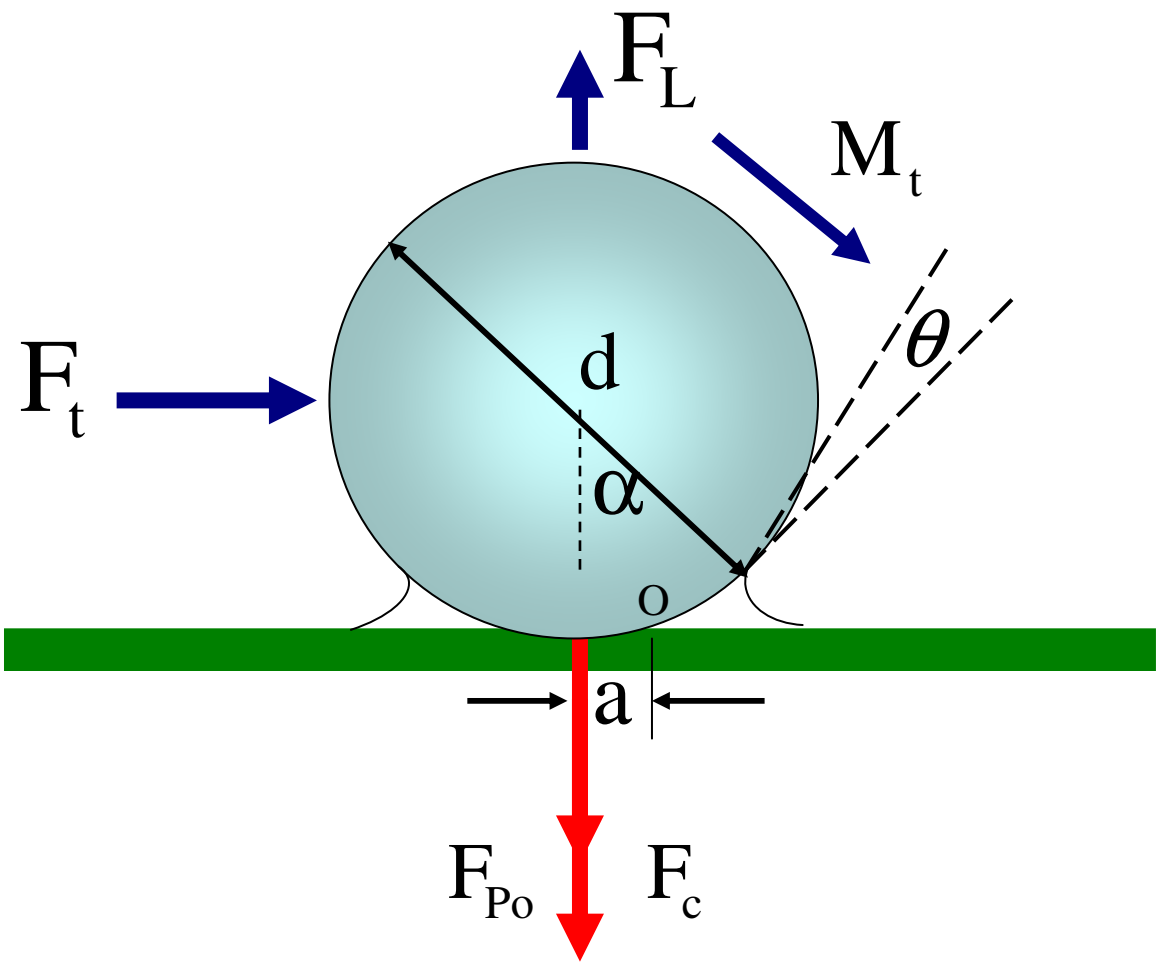

Figure 5-1. Geometric features of a spherical particle attached to a surface with capillary.

5.3 CAPILLARY FORCE AND EFFECTIVE THERMODYNAMIC WORK OF ADHESION

5.3.1 Capillary Force

In humid air, water vapor condenses in the small spaces between bodies in contact; as a result, for hydrophilic materials, a meniscus is formed around the particle-substrate contact area as shown in Figure 5-1. The curvature of the surface of the meniscus is determined by the Kelvin equation. The surface tension as well as the pressure force due to reduced Laplace pressure originating from the curvature of the surface of the meniscus form the so-called capillary force. Therefore, an additional capillary force, beyond the van der Waals force is exerted, which significantly enhances the adhesion between the particle and the substrate. The capillary force is determined by the surface tension of water σ (=0.0735 N/m, at room temperature), the particle diameter d, the wetting angle θ and the angle α as shown in Figure 5-1. That is,

$$F_c = 2\pi\sigma d[\sin\alpha \sin(\theta+\alpha) + \cos\theta] \tag{5-10}$$

The first term in Equation (5-10) is due to the surface tension force and the second term is the result of the sub-ambient pressure in the liquid meniscus. The angle α is normally very small, and for small values of wetting angle θ, the expression for the capillary force becomes (Ranade, 1987; Busnaina and Elsawy, 2001)

$$F_c = 2\pi\sigma d. \tag{5-11}$$

In order to include the effect of capillary force in adhesion models, we assume that the particles are deposited on the surface under dry condition and then a liquid meniscus forms due to vapor condensation on the particle-substrate contact. Thus, a superposition of van der Waals and capillary forces may be assumed. The total force needed to lift-off the particle then is, $F_{po} + F_c$, where F_{po} is the pull-off force for overcoming the van der Waals adhesion, which is a function of thermodynamic work of adhesion W_A. The

presence of capillary force enhances the surface energy of the materials; therefore, it is reasonable to account for the combined effect of van der Waals adhesion and capillary force with an increased effective thermodynamic work of adhesion W_A^e. Note that the effective thermodynamic work of adhesion will depend on the adhesion model used.

5.3.2 Effective Thermodynamic Work of Adhesion

To evaluate the effective thermodynamic work of adhesion for the JKR model, the effective pull-off force must be balanced with the combined effect of van der Waals pull-off force and the capillary force. That is,

$$\frac{3}{4}\pi W_A^{eJKR} d = \frac{3}{4}\pi W_A d + 2\pi\sigma d \tag{5-12}$$

where W_A^{eJKR} is the effective work of adhesion for the JKR model. It then follows that,

$$W_A^{eJKR} = W_A + \frac{8\sigma}{3} \tag{5-13}$$

The expression for the contact radius is then given by Equation (5-1) with W_A being replaced by W_A^{eJKR}.

The effective thermodynamic work of adhesion for the DMT and the Maugis-Pollock models can be similarly obtained. That is,

$$W_A^{eDMT} = W_A^{eMP} = W_A + 2\sigma \tag{5-14}$$

The corresponding approximate expression for the effective contact radius as estimated from the DMT model is given as

$$a_e^3 \approx \frac{d}{2k}\left(P + \pi W_A^{eDMT} d\right) \tag{5-15}$$

For the Maugis-Pollock model, the effective contact radius is given as

$$a_e = \sqrt{\frac{P + \pi W_A^{eMP} d}{\pi H}} \tag{5-16}$$

5.4 DETACHMENT MODELS

Particles can be detached from a surface by three mechanisms: rolling, sliding and lifting. Wang (1990) and Soltani and Ahmadi (1994, 1995) pointed out that the removal of smooth spherical particles was more easily achieved by the rolling motion, rather than by sliding and lifting. Therefore, in this work, only rolling detachment is discussed.

5.4.1 Rolling Detachment Model

Ziskind et al. (1997) described a model for rolling detachment of a sphere from a surface. In their model, the detachment occurs when the hydrodynamic moment exceeds the maximum adhesion resistance moment evaluated for the JKR and DMT models for elastic surface and particle deformations. Here the approach is extended to include the effect of capillary force as well as the effect of plastic surface deformation.

Figure 5-1 shows a spherical particle attached to a planar surface in a fluid flow. Note that the lift force, which is very small, is neglected in the present analysis. In humid air, a meniscus is formed at the particle-substrate contact. Here it is assumed that the particle was deposited before the meniscus formation. The particle will be detached when the moment of the hydrodynamic force about the point "O" (which is located at the rear perimeter of the contact circle) overcomes the maximum adhesion resistance moment due to combined adhesion force and the capillary force. That is,

$$M_t + F_t\left(\frac{d}{2} - \alpha_o\right) \geq (P \cdot a)_{Max}. \tag{5-17}$$

In Equation (5-17) F_t is the fluid drag force, α_o is the overlap (relative approach) between the particle and surface, M_t is the hydrodynamic moment about the center of the particle, $(P \cdot a)_{Max}$ is the maximum adhesion resistance moment due to combined adhesion force and the capillary force. In most practical cases,,α_o is very small compared to d/2, therefore α_o can be neglected and Equation (5-17) becomes

$$M_t + F_t \frac{d}{2} \geq (P \cdot a)_{Max} \tag{5-18}$$

For developing a particle rolling detachment model, the corresponding maximum adhesion resistance moment need to be evaluated. In the subsequent section, the JKR and DMT adhesion models are used for elastic surface deformations, while the Maugis-Pollock adhesion model is used for plastic surface deformation, and the corresponding adhesion resistance moments are evaluated.

5.5 MAXIMUM ADHESION RESISTANCE

5.5.1 Maximum Adhesion Resistance for the JKR Model

Equation (5-1) in nondimensional form may be restated as

$$a^{*3} = 1 - P^* + \sqrt{1 - 2P^*} \tag{5-19}$$

where the nondimensional applied normal load and contact radius are defined as

$$P^* = -\frac{P}{\frac{3}{2}\pi W_A d} \tag{5-20}$$

$$a^* = \frac{a}{\left(\frac{3\pi W_A d^2}{4K}\right)^{\frac{1}{3}}} \tag{5-21}$$

The corresponding nondimensional moment about the point "O" (Figure 5-1) is given as

$$M^{*JKR} = P^* a^* = P^* (1 - P^* + \sqrt{1 - 2P^*})^{1/3} \tag{5-22}$$

To find the maximum resistance moment, the derivative of Equation (5-22) with respect to P^* is set equal to zero. The nondimensional applied load and nondimensional contact radius at the maximum moment are given as

$$P^*\big|_M = \frac{15}{32} \quad \text{and} \quad a^*\big|_M = \left(\frac{25}{32}\right)^{1/3} \tag{5-23}$$

The corresponding nondimensional maximum moment then becomes

$$M_{Max}^{*JKR} = 0.432 \tag{5-24}$$

or in dimensional form,

$$M_{Max}^{JKR} = 2.707 \frac{W_A^{4/3} d^{5/3}}{K^{1/3}} \tag{5-25}$$

Note that Ziskind et al. (1997) reported a slightly different value of 0.42 for the nondimensional maximum moment. Similarly, to include the effects of capillary force, the corresponding maximum moment then becomes

$$M_{Max}^{JKR} = 2.707 \frac{W_A^{e4/3} d^{5/3}}{K^{1/3}} \tag{5-26}$$

5.5.2 Maximum Adhesion Resistance for the DMT Model

For the DMT model, the approximate expression for the contact radius in nondimensional form is given as

$$a^{*3} = \left(\frac{a^3}{3\pi W_A d^2 / 4K} \right) = \frac{2}{3} - P^* \tag{5-27}$$

The corresponding nondimensional moment about the point "O" (Figure 5-1) due to the applied normal load is given as

$$M^{*DMT} = P^* a^* = P^* \left(\frac{2}{3} - P^*\right)^{1/3} \tag{5-28}$$

The nondimensional applied load and the nondimensional contact radius at the maximum resistance moment are then given by

$$P^*\big|_M = \frac{1}{2} \qquad a^*\big|_M = \left(\frac{1}{6}\right)^{1/3} \tag{5-29}$$

The nondimensional maximum moment then is given as

$$M_{Max}^{*DMT} = 0.275 \tag{5-30}$$

or

$$M_{Max}^{DMT} = 1.725 \frac{W_A^{4/3} d^{5/3}}{K^{1/3}} \tag{5-31}$$

Similarly, to include the effects of capillary force, the corresponding maximum moment becomes,

$$M_{Max}^{DMT} = 1.725 \frac{W_A^{e4/3} d^{5/3}}{K^{1/3}} \tag{5-32}$$

Comparing the nondimensional maximum moment due to the applied normal load for the JKR and DMT models, it follows that

$$M_{Max}^{*JKR} = 1.57\, M_{Max}^{*DMT} \tag{5-33}$$

Ziskind et al. (19) reported $M_{Max}^{*DMT} = 0.28$ and $M_{Max}^{*JKR} = 1.5\, M_{Max}^{*DMT}$. The slight differences between the values reported in (1997) and the values in Equations (5-24), (5-30) and (5-33) are due the approximate estimates used by Ziskind et al. They read the maximum moments from figures, which may not be accurate. While the differences are small, the presently reported values are more accurate.

5.5.3 Maximum Adhesion Resistance for the Maugis-Pollock Model

From Equation (5-8), the corresponding moment about the point "O" (Figure 5-1) due to the applied load is given as

$$M^{MP} = -Pa = -P\sqrt{\frac{P + \pi W_A d}{\pi H}} \tag{5-34}$$

Evaluating the maximum value of the moment given by (5-34) it follows that

$$P\big|_M = -\frac{2}{3}\pi W_A d \qquad \text{and} \qquad a\big|_M = \sqrt{\frac{W_A d}{3H}} \tag{5-35}$$

and the maximum resistance moment is given as

$$M_{Max}^{MP} = \frac{2\pi (W_A d)^{3/2}}{3\sqrt{3H}} \tag{5-36}$$

Similarly, including the effects of capillary force, the corresponding maximum moment becomes

$$M_{Max}^{MP} = \frac{2\pi (W_A^e d)^{3/2}}{3\sqrt{3H}} \tag{5-37}$$

5.5.4 The Regime of the Maximum Adhesion Resistance Moment Theory

The maximum resistance moment theory is based on the JKR, DMT and Maugis-Pollock models; therefore, the regime of the maximum resistance moment theory is the same as that of the corresponding adhesion model on which it is based.

5.6 HYDRODYNAMIC FORCES AND TORQUES

The near-wall turbulent flow structure including burst and inrush processes have major effects on the particle detachment process (Soltani and Ahmadi (1994, 1995b)). Here, peak near-wall velocity during turbulent burst/inrush and the corresponding hydrodynamic forces and torques are briefly outlined.

5.6.1 Burst/Inrush Model

The maximum instantaneous streamwise velocity experienced locally near the wall during the turbulent burst/inrush is given in wall units as (1994, 1995b)

$$u_M^+ = 1.72y^+. \tag{5-38}$$

where,

$$u_M^+ = \frac{u_M}{u^*}, \qquad y^+ = \frac{yu^*}{\nu}. \tag{5-39}$$

Here, u* is the shear velocity, ν is the kinematic viscosity of air and u_M is the maximum velocity at a distance of y from the wall. The corresponding fluid velocity at the mass center of a particle attached to a wall may be obtained from Equation (5-38). i.e.,

$$u_M^+ = 0.86d^+, \tag{5-40}$$

where d^+ is the nondimensional particle diameter defined as

$$d^+ = \frac{du^*}{\nu}. \tag{5-41}$$

In this case, the drag force acting on the particle becomes

$$F_t = \frac{4.38\pi\rho d^2 u^{*2}}{C_c}, \tag{5-42}$$

where ρ is the density of the air and the Cunningham factor is given as (1964, 1977)

$$C_c = 1 + Kn\,[1.257 + 0.4\exp(-1.1/Kn)]\ . \tag{5-43}$$

Here the Knudsen number is defined as

$$Kn = \frac{2\lambda}{d}, \tag{5-44}$$

where λ is the mean free path of air.

The corresponding moment of the hydrodynamic force acting on the particle is given as

$$M_t = \frac{1.62\pi\rho u^{*2}\, d^3}{C_c}, \tag{5-45}$$

where the effect of the Cunningham correction factor is also included.

The lift force acting on the particle is very small compared to the adhesion and capillary forces and, therefore, is neglected in the present analysis.

5.7 PARTICLE DETACHMENT

Soltani and Ahmadi (1994) evaluated the minimum critical shear velocity for removing different size particles in the absence of the capillary force. Recently, Ahmadi et al. (2007) studied the effect of the presence of capillary force on particle adhesion and detachment in turbulent flows. They used a simplified version of moment detachment with the use of the JKR model as well as sliding detachment model. In this section, the results for accurate rolling detachment model for both elastic and plastic deformations are presented. The critical shear velocities for particle removal in humid air are evaluated with the use of the JKR, the DMT and the Maugis-Pollock models.

Using the expression for the hydrodynamic drag and torque in Equation (5-18), the critical shear velocity for rolling detachment of spherical particles including the capillary force is given as

$$u_c^{*2} = \frac{M_{Max}}{3.81\pi\rho d^3/C_c} \tag{5-46}$$

where M_{Max} is the maximum adhesion resistance moment. The critical shear velocity for particle detachment according to the JKR, DMT and Maugis-Pollock models can be evaluated by substituting, respectively, the expressions for the maximum resistance moment from Equations (5-26), (5-32) and (5-37) into Equation (5-46) for M_{Max}.

Table 5-1. Material properties for different combinations

Material combination	E (10^{10} Pa)	A (10^{-20} J)	W_A (10^{-3} J/m^2)	ρ_p (10^3 kg/m^3)	ν_i	H (10^7 Pa)
Polystyrene-polystyrene	0.28	6.37	10.56	1.05	0.33	6.59
Calcium carbonate-calcium carbonate	3.5	10.1	16.7	2.71	0.27	250
Glass-glass	6.9	8.5	14.1	2.18	0.2	490-665.4
Glass-steel	_	_	150	_	_	646.8

E: Young's modulus of material A: Hamaker constant

W_A : thermodynamic work of adhesion ρ_p : density of material

ν_i : Poisson's ratio of material i H: hardness of material

5.8 RESULTS

In this section the results concerning detachment of particles of different sizes and various materials from substrates of various materials are presented. The material properties for polystyrene, calcium carbonate, glass and steel that were used in this study are listed in Table 5-1. All these materials discussed here are hydrophilic materials. Most

of the results are presented in term of critical shear velocity, u_c^*, which is the minimum shear velocity needed for detaching a particle from the substrate.

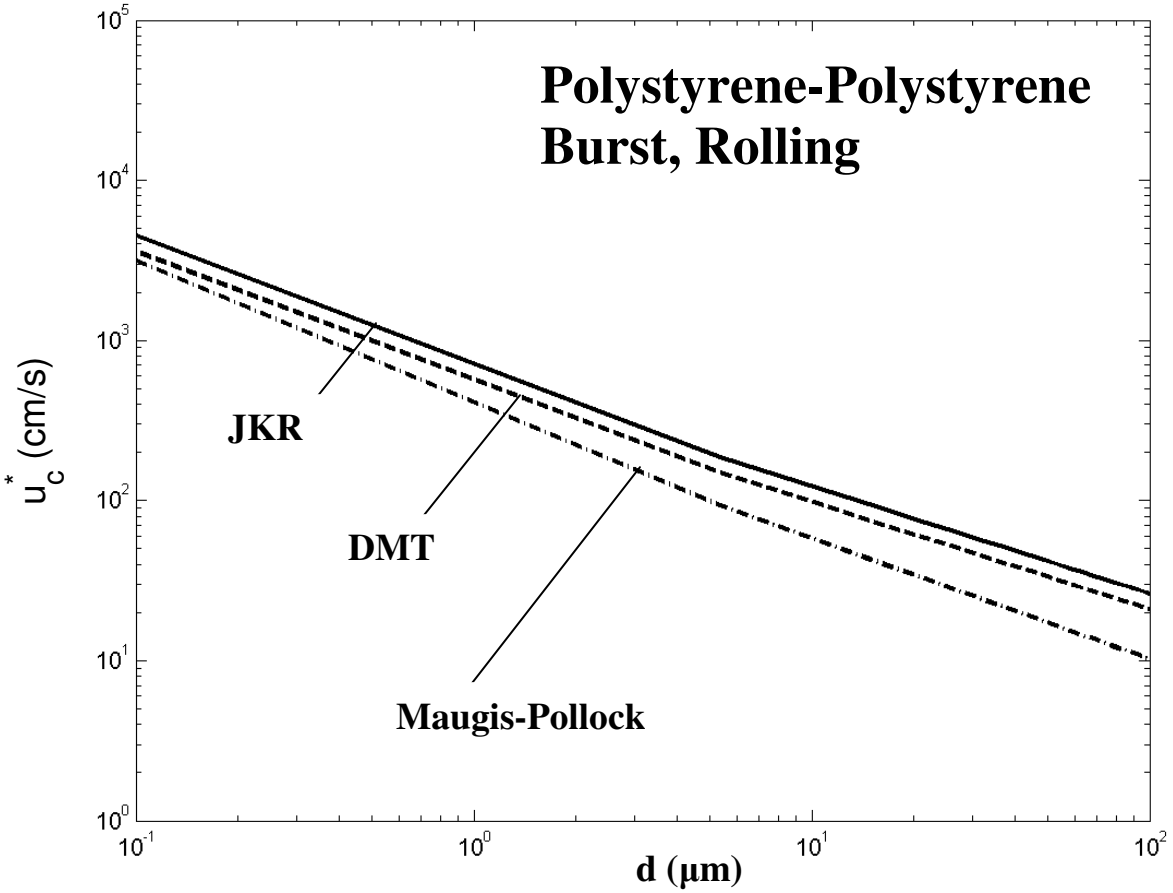

Figure 5-2. Variation of the critical shear velocities with the particle diameter as predicted by the burst model using different adhesion models for resuspension of polystyrene particles from a polystyrene substrate without capillary effects.

Variations of u_c^* with particle diameter as predicted by different adhesion models for the rolling detachment of polystyrene particles from a polystyrene substrate for dry and humid air conditions are shown, respectively, in Figures 5-2 and 5-3. Here the near-wall velocity during the burst/inrush of turbulent flow was used in the analysis. Figure 5-2 shows that the critical shear velocity decreases with the increase of the particle diameter. That is, as expected small particles are more difficult to remove than the larger ones. Figure 5-2 also shows that the critical shear velocity as predicted by the JKR adhesion

model is the largest. The predicted critical shear velocity by the DMT model is only slightly less than that by the JKR model. The predicted value by the Maugis-Pollock model, which accounts for plastic deformation, is lower than those by the JKR and the DMT models for elastic deformation. The differences are small for smaller particles, but become relatively large for larger particles.

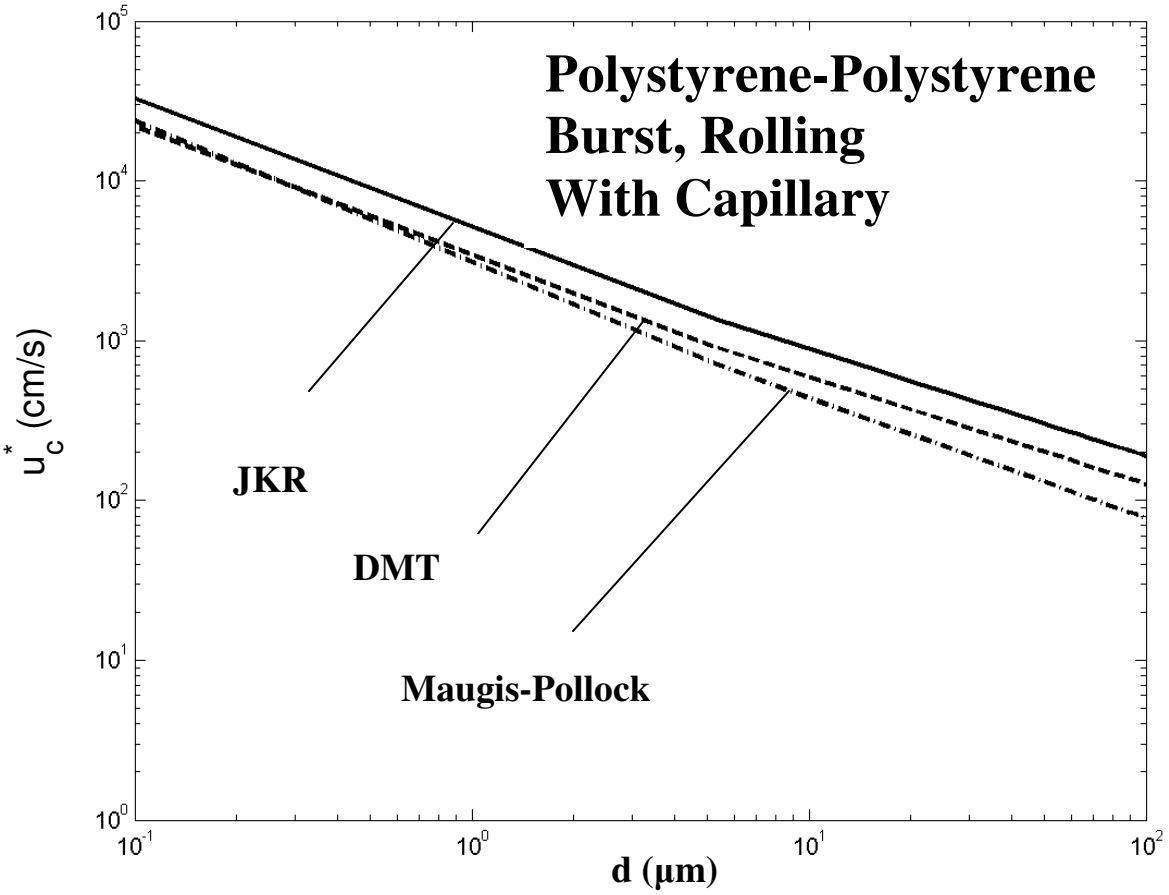

Figure 5-3. Variation of the critical shear velocities with the particle diameter as predicted by the burst model using different adhesion models for resuspension of polystyrene particles from a polystyrene substrate with capillary effects.

These differences are due to the variations of the maximum adhesion resistance moments for the JKR, the DMT and the Maugis-Pollock models. Equation (5-33) shows that this maximum moment for the JKR adhesion model is 1.57 times that by the DMT model. For particles larger than 0.1 micrometer, the maximum adhesion resistance

moment predicted by the Maugis-Pollock theory is smaller than those obtained from the JKR and DMT models. For example, for 1 micrometer polystyrene particle at polystyrene substrate, the maximum moment for plastic surface deformation (Maugis-Pollock theory) is 0.518 times that for elastic surface deformation as predicted by the DMT model. Therefore, the critical shear velocities obtained from the Maugis-Pollock theory are the lowest among the three adhesion models. Because plastic deformation could occur at the polystyrene-polystyrene contact, the prediction of the Maugis-Pollock theory is expected to give more accurate results in this case.

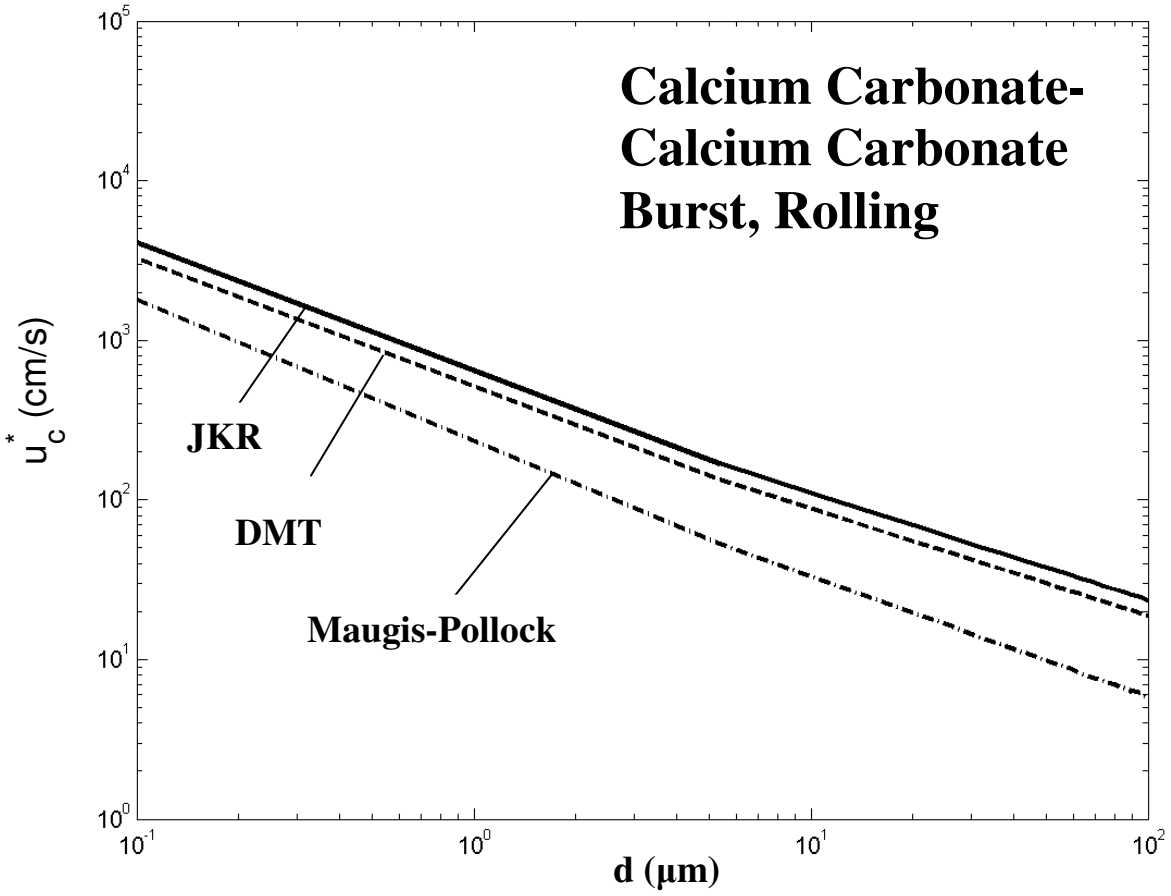

Figure 5-4. Variation of the critical shear velocities with the particle diameter as predicted by the burst model using different adhesion models for resuspension of calcium carbonate particles from a calcium carbonate substrate without capillary effects.

The minimum particle size calculated in this study is 0.1 μm. It is not a good idea to

use the present model for nano particles. The reason is that the mean free path of air is 0.07 μm, which is 70nm, flow in this range can not be treated as a continuous phase. For flow on nano particles, it is more like air molecules bombard nano particles. A discrete element method may be a better option for this case.

Figure 5-3 displays the variation of the critical shear velocity with particle size when the air is humid and the effect of capillary force becomes important. The trends are similar to those observed in Figure 5-2. The critical shear velocity decreases with the increase of the particle diameter. The model predictions from the JKR model are slightly higher than those from the DMT model. The predictions from the Maugis-Pollock model

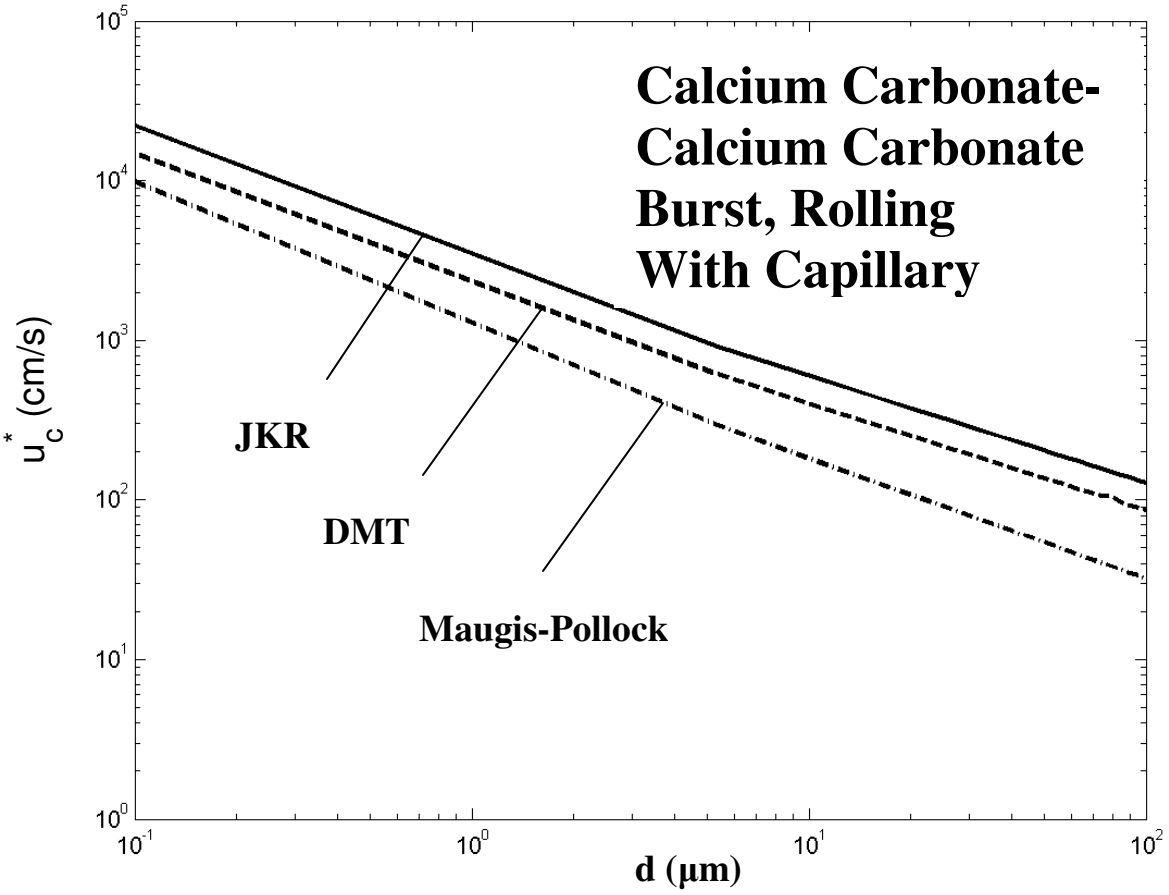

Figure 5-5. Variation of the critical shear velocities with the particle diameter as predicted by the burst model using different adhesion models for resuspension of calcium carbonate particles from a calcium carbonate substrate with capillary effects.

for u_c^* are the lowest for large particles, but slightly higher than those from the DMT model for small particles. Figure 5-3 shows higher critical shear velocities compared to results presented in Figure 5-2. This implies that the presence of capillary force significantly increases the critical shear velocity for particle rolling removal.

Figures 5-4 and 5-5 show the variations of the critical shear velocity with particle diameter for rolling detachment of calcium carbonate particles from a calcium carbonate substrate. Here the burst/inrush near-wall velocity model and different adhesion models under dry and humid air conditions were used. These figures show that the critical shear velocity decreases with the increase of the particle diameter, and the presence of capillary force dramatically increases the critical shear velocity for particle removal. Figures 5-4 and 5-5 also show that the model predictions from the JKR model are slightly higher than those from the DMT model, and the predictions from the Maugis-Pollock model for the critical shear velocity are the lowest.

5.8.1 Comparison with Experimental Data

This section compares the model predictions with the experimental data of Taheri and Bragg (1992) and Zimon (1982) as well as Ibrahim et al. (2003, 2004). The experiment of Taheri and Bragg was concerned with the resuspension of glass particles from a smooth glass surface under normal room temperature and humidity for a range of air velocities between 2 and 130 m/s. Their result agrees well with the prediction by Soltani and Ahmadi (1995) for particle resuspension in moist air, which implies the existence of the capillary force. The experiments of Zimon (1982) were for the entrainment of glass particles from a steel substrate with humidity less than 10%, which can be considered as dry air condition. Ibrahim et al. (2003) reported experimental data for the detachment of glass and steel particles from a glass substrate at a humidity of 25±3%, which is considered as dry air condition in this study. In their subsequent work, Ibrahim et al. (2004) experimentally studied the detachment of steel particles from a glass substrate under a humidity of 67%, which is humid air condition.

Figure 5-6 shows the comparison of the experimental data of Taheri and Bragg

(1992) and Ibrahim et al. (2003) with the predicted critical shear velocity for rolling detachment of glass particles from a glass substrate by the burst/inrush resuspension model and different adhesion models under dry and humid air conditions. Figure 5-6 shows that the simulated critical shear velocity displays a trend similar to those in Figures 5-4 and 5-5. That is, the critical shear velocity decreases with the increase of the particle diameter, and the presence of capillary force dramatically increases the critical shear velocity for particle removal. Furthermore, the model predictions for the JKR theory are slightly higher than those for the DMT theory, and the predictions from the Maugis-Pollock model lead to the lowest critical shear velocities.

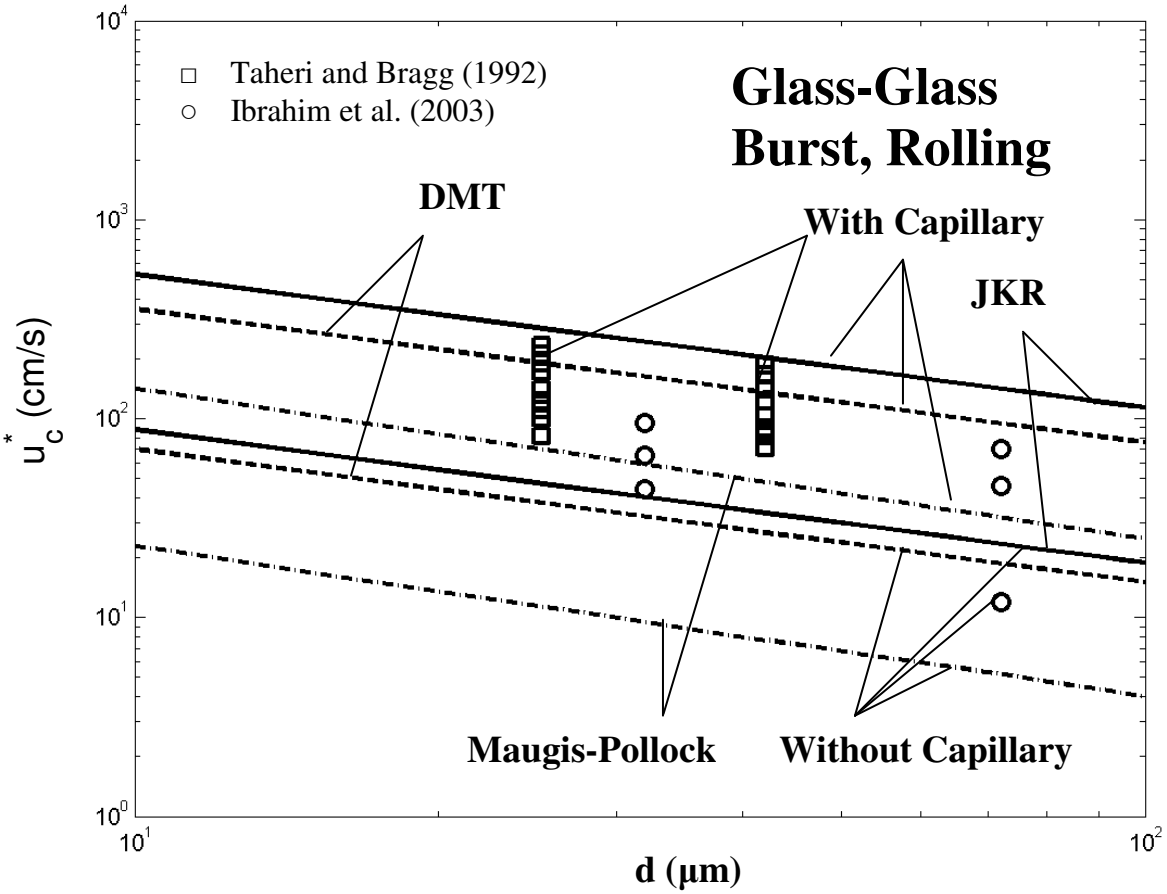

Figure 5-6. Comparison of the critical shear velocities as predicted by the burst model using different adhesion models with the experimental data of Taheri and Bragg (1992) (□) as well as Ibrahim et al. (2003) (○) for resuspension of glass particles from a glass substrate.

Figure 5-6 also shows that the predicted critical shear velocities from the JKR and DMT models with capillary force agree very well with the experimental data of Taheri and Bragg (1992) under humid air condition. In addition, these model predictions in the absence of capillary force are in good agreement with the experimental data of Ibrahim et al. (2003) for dry air condition. It is also seen that the predicted critical shear velocity from the Maugis-Pollock model with capillary force is somewhat lower than the experimental data. As noted before, the Maugis-Pollock model accounts for the plastic deformation at the particle-surface contact, but glass-glass contact is perhaps better modeled with an elastic deformation model such as the JKR or DMT theory.

Figure 5-6 also shows that the distance between the model predictions with and without capillary force are roughly the same for different diameters. That is, for particles of the same material with different diameters, the capillary effect increases the critical shear velocity by the same amount. In addition, the distances between the curves predicted by different models with or without capillary forces are almost the same. This implies that the increase in adhesion force by the capillary effect is independent of the adhesion model.

Muller et al. (1980, 1983) pointed out, JKR are suitable for low Young's modulus, high surface energy and large particles. DMT are suitable for high Young's modulus, low surface energy and small particles. Figure 5-6 shows that for glass-glass combination without capillary effect, both the predictions from the JKR and DMT match the experimental date, with the predictions from the JKR match the experimental date a little bit better. But in general, they are both fine.

Figure 5-7 shows the comparison of the experimental data of Zimon (1982) and Ibrahim et al. (2003, 2004) with the predicted critical shear velocity for rolling detachment of particles by the burst/inrush resuspension model and different adhesion models under both dry and humid air conditions. The experimental data of Zimon (1982) were for detachment of glass particles from a steel substrate under dry air condition, while the experimental data of Ibrahim et al. (2003) were for detachment of steel particles

from a glass substrate under dry air condition. The experimental data of Ibrahim et al. (2004) shown in this figure were for detachment of steel particles from a glass substrate under humid air condition. Figure 5-7 displays trends similar to those seen in Figures 5-4 to 5-6. The critical shear velocity decreases with the increase of particle diameter, and the presence of capillary force dramatically increases the critical shear velocity. The model predictions from the JKR theory are also slightly higher than those from the DMT theory, and prediction from the Maugis-Pollock model is the lowest.

Figure 5-7 shows that the predicted critical shear velocities from the JKR and DMT models without capillary force are higher than the experimental data of Zimon (1982) and Ibrahim et al. (2003) under dry air condition. Similar deviations are observed between the JKR and DMT model predictions with capillary force with the experimental data of Ibrahim et al. (2004) under humid air condition. Soltani and Ahmadi (1995a, 1999) have suggested that small surface roughness that reduces the effective adhesion force significantly is the reason for these discrepancies. Figure 5-7 shows that the predictions from the Maugis-Pollock model with and without capillary force are in the range of the experimental data of Zimon (1982) and Ibrahim et al. (2004). This suggests that the inclusion of plastic deformation at the interface could also improve the model prediction. Because JKR and DMT models are for elastic materials, Maugis-Pollock model is for plastic materials. This also implies thst Glass-steel could be a plastic combination. We, however, believe that the surface roughness is the main cause for the discrepancy between the model prediction and experimental data.

Figure 5-7 shows that the capillary force increases the critical shear velocity by roughly the same amount, irrespective of the particle size and the adhesion model used. This trend is similar to that observed in Figure 5-6. Comparison of Figures 5-6 and 5-7 indicates that the increase in critical shear velocity varies for different materials. This is because that capillary force is a function of only particle diameter, and adhesion force is a function of materials properties as well as particle diameter. Thus, the relative importance of the capillary force changes for different materials. Capillary force is more important for glass particles on a glass substrate when compared with that for glass

particle on a steel substrate.

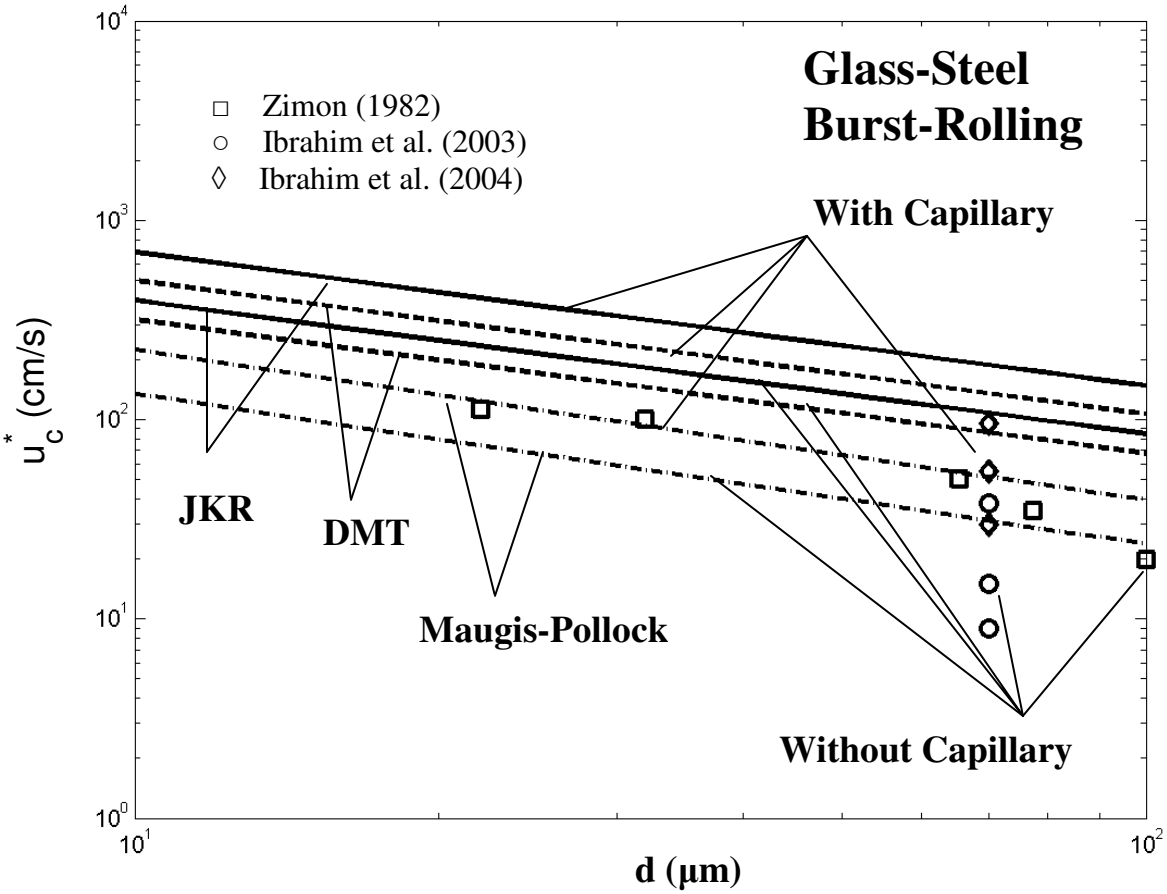

Figure 5-7. Comparison of the critical shear velocities as predicted by the burst model using different adhesion models with the experimental data of Zimon (1982) (□) for resuspension of glass particles from a steel substrate, and Ibrahim et al. (2003) (○) as well as Ibrahim et al. (2004) (◊) for resuspension of steel particles from a glass substrate.

5.8.2. Comparison with Earlier Model

This section compares the new model predictions with those from the earlier model of Ahmadi et al. (2007) where the effect of capillary forces was simply added to the moment balance equation. Figure 5-8 compares the critical shear velocities as predicted by these models for resuspension of polystyrene particles from a polystyrene substrate. In the absence of capillary force, Figure 5-8 shows that the predicted critical shear velocities are the same. When the capillary force is present, however, the critical shear velocities

predicted by the earlier model (2007) are smaller than those obtained from the present maximum adhesion resistance moment model. That is, the earlier simplified model under-estimates the critical shear velocities for particle detachment in the presence of capillary forces.

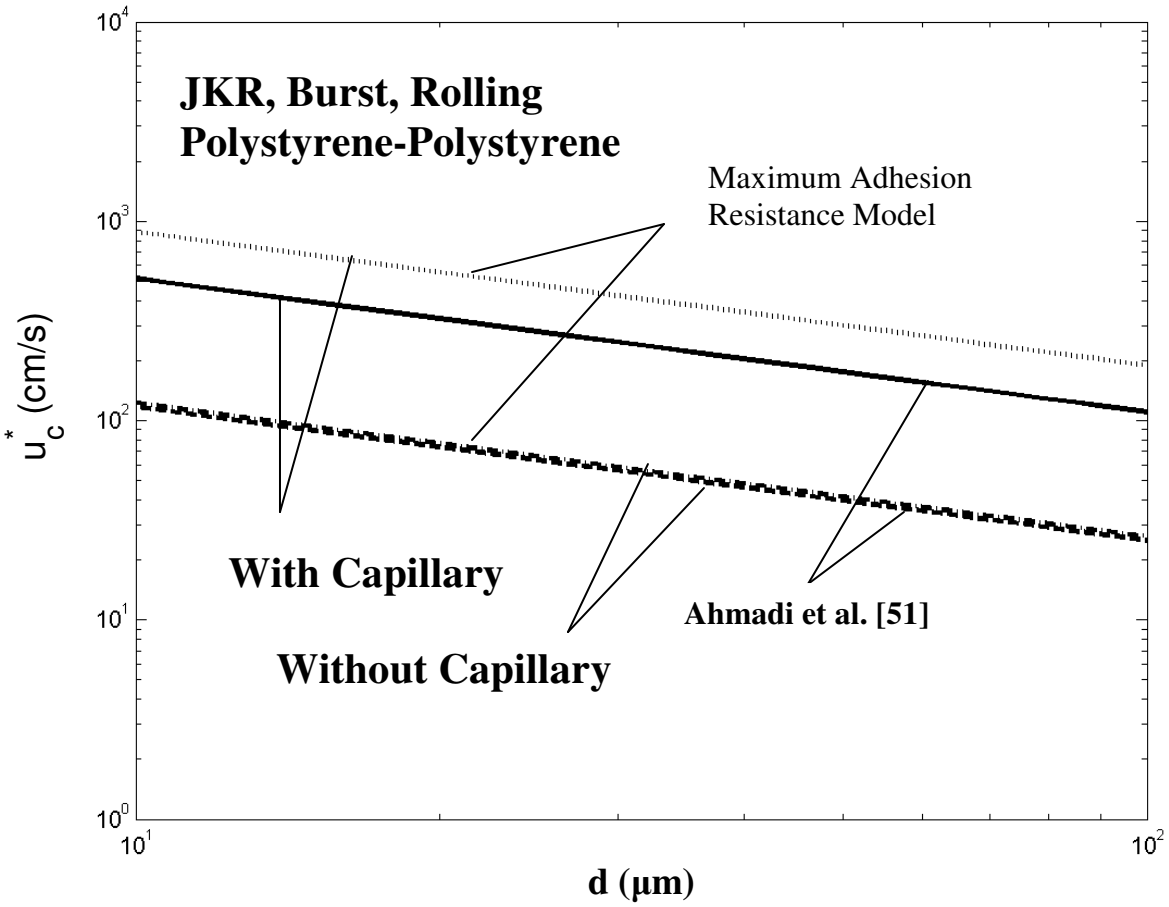

Figure 5-8. Comparison of the critical shear velocities as predicted by the maximum adhesion resistance model with the model of Ahmadi et al. (2007) for resuspension of polystyrene particles from a polystyrene substrate.

5.9 CONCLUSIONS

Particle resuspension including the effect of capillary force using different adhesion theories and a new rolling detachment model in turbulent flows is studied. The effect of capillary force for hydrophilic materials is included in the model with the use of an effective thermodynamic work of adhesion. Analytical expressions for the maximum

moment due to the applied normal load and the critical shear velocity for particle rolling removal are obtained and the results are presented and compared with the available experimental data. Based on the presented results the following conclusions are drawn:

- The capillary effect significantly increases the critical shear velocity for particle detachment.
- For elastic deformation at the interface, the critical shear velocity predicted by the JKR adhesion model is somewhat higher than that predicted by the DMT model.
- The Maugis-Pollock model that accounts for the plastic surface deformation leads to the lowest critical shear velocity for particle removal for the materials studied in the present work.
- For the particles of the same material with different diameters, the capillary effect increases the critical shear velocity by about the same order.
- The relative importance of the capillary force varies depending on the particle and substrate materials. The capillary effect is more important for glass particles on a glass substrate when compared with glass particles on a steel substrate.
- The model predictions are in good agreement with the available experimental data.

5.10 Acknowledgements

The financial support of the Environmental Protection Agency (EPA) and the NYSTAR Center of Excellence at Syracuse University is gratefully acknowledged.

5.11 Nomenclature

A	Hamaker constant
a	contact radius, m
a_e	contact radius with capillary force, m
$a\|_M$	contact radius reached at the maximum adhesion resistance moment, m
a_o	contact radius at zero applied load, m
a^*	nondimensional contact radius
$a^*\|_M$	nondimensional contact radius at the maximum adhesion resistance moment
C_c	Cunningham factor

d	particle diameter, m
d^+	nondimensional particle diameter
E_i	Young modulus of material i, N/m^2
F_c	capillary force, N
F_L	lift force, N
F_{po}	pull-off force, N
F_{Po}^{DMT}	pull-off force evaluated by DMT model, N
F_{po}^{JKR}	pull-off force evaluated by JKR model, N
F_t	drag force, N
H	hardness of material, Pa
K	composite Young's modulus, N/m^2
Kn	Knudsen number
M_{Max}	maximum adhesion resistance moment due to the applied normal load, N·m
M_t	hydrodynamic moment, N·m
M_{Max}^{DMT}	maximum resistance moment evaluated by DMT model, N·m
M^{*DMT}	nondimensional resistance moment evaluated by DMT model, N·m
M_{Max}^{*DMT}	nondimensional maximum resistance moment evaluated by DMT model, N·m
M_{Max}^{JKR}	maximum resistance moment evaluated by JKR model, N·m
M^{*JKR}	nondimensional resistance moment evaluated by JKR model, N·m
M_{Max}^{*JKR}	nondimensional maximum resistance moment evaluated by JKR model, N·m
M^{MP}	resistance moment evaluated by Maugis-Pollock model, N·m
M_{Max}^{MP}	maximum resistance moment evaluated by Maugis-Pollock model, N·m
P	applied normal load, N
P^*	nondimensional applied normal load
$P\|_M$	applied normal load at the maximum adhesion resistance moment, N
$P^*\|_M$	nondimensional applied normal load at the maximum adhesion resistance moment

$(P\cdot a)_{Max}$ maximum adhesion resistance moment, N·m

u_c^* minimum shear velocity needed for detaching a particle from the substrate, m/s

u_M^+ nondimensional maximum gas velocity at the mass center of the particle

u_M maximum gas velocity at the mass center of the particle

u^* shear velocity, m/s

W_A thermodynamic work of adhesion, J/m^2

W_A^e effective thermodynamic work of adhesion, J/m^2

W_A^{eJKR} effective thermodynamic work of adhesion for JKR model, J/m^2

W_A^{eDMT} effective thermodynamic work of adhesion for DMT model, J/m^2

W_A^{eMP} effective thermodynamic work of adhesion for Maugis-Pollock model, J/m^2

Y yield stress of the material, Pa

y^+ nondimensional distance from the wall

y distance from the wall, m

z_o minimum separation distance, m

Greek letters

α half particle-liquid contact angle, rad

α_o overlap between the particle and surface, m

θ wetting angle, rad

λ mean free path of air, m

ν kinematic viscosity of air, m^2/s

ν_i Poisson's ratio of material i

ρ density of air, kg/m^3

ρ_p density of particle and substrate material, kg/m^3

σ surface tension of water, N/m

5.12 REFERENCES

Ahmadi, G., Guo, S. and Zhang, X., Particulate Sci. Technol., **25**: 1-18, (2007).

Bowling, R. A., J. Electrochem. Soc. **132**, 2208-2219 (1985).

Berkeley, R. C. W., *Microbial Adhesion to Surfaces*, pp. 93-113, Ellis Horwood, New York (1980).

Bradley, R. S., Philos. Mag., **13**, 853-862. (1932).

Busnaina, A.A., and Elsawy, T., In: *Particle Adhesion: Applications and Advances,* Quesnel, D.J., Rimai, D.S. and Sharpe, L.H. (Eds.), Taylor and Francis, New York, pp. 391-409, (2001).

Cleaver, J. W. and Yates, B., J. Colloid Interface Sci. **44**, 464-474 (1973).

Corn, M., J. Air Pollution Control Assoc. **11**, 566-575 (1965).

Corn, M. and Stein, F., J. Am. Ind. Hyg. Assoc. **26**, 325-336 (1965).

Corn, M., in *Aerosol Science*, C. N. Davies (Ed.), p. 359, Academic Press, New York (1966).

Derjaguin, B. V., Muller, V. M. and Toporov, Yu. P., J. Colloid Interface Sci. **53**, 314 -326 (1975).

Derjaguin, B. V., Kolloid Zhur. **69**, 155-164 (1934).

Friedlander, S. K., *Smoke, Dust and Haze*, John Wiley, New York (1977).

Fuchs, N. A., *The Mechanics of Aerosols*, MacMillan, New York (1964).

Garland, J. A., in: *Precipitation Scavenging, Dry Deposition and Resuspension*, Pruppacher, H. R., Semonin, R. G. and Slinn, W. G. N. (Eds.) Vol. 2, pp. 1087-1097, Elsevier, Amsterdam (1983).

Gillett, D. A., Blifford, I. H. and Fryrear, D. W., J. Geophys. Res. **79**, 4068-4075 (1974).

Gotzinger, M. and Peukert, W., Powder Technol., **130**, 102-109 (2003a).

Gotzinger, M. and Peukert, W., Powder Technol., **135-136**, 82-91 (2003b).

Healy, J. W., in: *Transuranics in Natural Environments*, White, M. G. and Dunaway, P. B. (Eds.) pp. 211-222, U.S. Energy Research & Development Administration, Las Vegas, NV (1977).

Hinds, W. C., Aerosol Technology: *Properties, Behavior, and Measurement of Airborne Particles*, John Wiley and Sons, New York (1982).

Ibrahim, A.H., Dunn, P.F. and Brach, R.M., J. Aerosol Sci. **34**, 765-782 (2003).

Ibrahim, A. H., Dunn, P. F. and Brach, R. M., J. Aerosol Sci., **35**, 805-821 (2004).

Johnson, K. L., Kendall K. and Roberts, A. D.,Proc. Royal. Soc. Lond. A 324, 301-313 (1971).

Kendall, K., Wear, **33**, 351-358 (1975).

Kendall, K., *Molecular Adhesion and Its Applications: The Sticky Universe,* Kluwer Academic/ Plenum Publishers, New York (2001).

Krupp, H., Adv. Colloid Interface Sci. **1**, 111-140 (1967).

Leighton, D. and Acrivos, A., J. Appl. Math. Phys., **36**, 174-178 (1985).

Makhonko, K. P. and Rabotnova, F. A., Pure Appl. Geophys. **120**, 54-66 (1982).

Masironi, L. A. and Fish, B. R., in: *Surface Contamination*, Fish, B. R. (Ed.), pp. 55-59, Pergamon Press, Oxford (1967).

Maugis, D. and Pollock, H. M., Acta Metall. **32**, 1323 (1984).

Maugis, D., J. Colloid Interface Sci. **150**, 243-169 (1995).

Mittal, K. L. (Ed.), *Particles on Surfaces: Detection, Adhesion and Removal*, Volumes 1 -3, Plenum Press, New York (1988, 1989, 1991).

Muller, V. M., Yushenko, V. S. and Derjaguin, B. V., J. Colloid Interface Sci. **77**, 91 -101 (1980).

Muller, V. M., Yushenko, V. S. and Derjaguin, B. V., J. Colloid Interface Sci. **92**, 92 -101 (1983)

Nicholson, K. W., Atmospheric Environment, **22**, 2639-2651 (1988).

Podczeck, F., Newton, J. M. and James, M. B., J. Colloid Interface Sci. **187**, 484–491 (1997).

Punjrath, J. S. and Heldman, D. R., J. Aerosol Sci. **3**, 429-440 (1972). Quesnel, D.J., Rimai, D.S. and Sharpe, L.H. (Eds.), *Particle Adhesion: Applications and Advances,* Taylor and Francis, New York (2001).

Ranade, M. B., Aerosol Sci. Technol. **7**, 161-176 (1987).

Reeks, M.W. and Hall, D., J. Fluid Eng. **110**, 165-171 (1988).

Sehmel, G. A., Environment Intl. **4**, 107-127 (1980).

Smith, W. J., Whicker, F. W. and Meyer, H. R., Nuclear Safety, **23**, 685-699 (1982).

Soltani, M. and Ahmadi, G. J., Adhesion Sci. Technol., **8**, 763-785 (1994).

Soltani, M. and Ahmadi, G., J. Adhesion, **51**, 105-123 (1995a).

Soltani, M. and Ahmadi, G., Physics Fluid A, **7**, 647-657 (1995b).

Soltani, M. and Ahmadi, G., J. Adhesion Sci. Technol. **13**, 325-355 (1999).

Tabor, D., J. Colloid Interface Sci. **58**, 2-13 (1977).

Taheri, M. and Bragg, G.M., Aerosol Sci. Technol., **15**, 15-20 (1992).

Tang, J. and Busnaina, A.A., In: *Particle Adhesion: Applications and Advances,* Quesnel, D.J., Rimai, D.S. and Sharpe, L.H. (Eds.), Taylor and Francis, New York, pp. 411-419, (2001).

Tsai, C. J., Pui, D. Y. H. and Liu, B. Y. H., J. Aerosol Sci. **22**, 737-764 (1991).

Tsai, C. J., Pui, D. Y. H. and Liu, B. Y. H., Aerosol Sci. Technol. **15**, 239-255 (1991).

Visser, J., Adv. Colloid Interface Sci. **3**, 331-363 (1972).

Wang, H. C., Aerosol Sci. Technol. **13**, 386-396 (1990).

Wen, H. Y. and Kasper, G., J. Aerosol Sci. **20**, 483-498 (1989).

Zimon, A. D., *Adhesion of Dust and Powder*, Consultants Bureau, New York (1982).

Ziskind, G., Fichman M. and Gutfinger, C., J. Aerosol Sci. **28**, 623-634, (1997).

The content of this chapter is published in J. Adhesion Sci. Technol., Vol. 21, No. 16, pp. 1589-1611 (2007)

CHAPTER 6. EFFECTS OF ELECTROSTATIC AND CAPILLARY FORCES AND SURFACE DEFORMATION ON PARTICLE DETACHMENT IN TURBULENT FLOWS

6.1 INTRODUCTION

Fine particle adhesion and removal from surfaces have attracted considerable attention due to their numerous applications in semiconductor, pharmaceutical and xerographic industries. Despite numerous studied, effects of electrostatic and capillary forces on particle adhesion and removal are not fully understood.

For charged particles in the presence of an electric field, the electrostatic forces strongly affect the particle transport, as well as adhesion and detachment. Donald [1,2], Donald and Watson [3], and Lee and Ayala [4] showed a strong dependence of the adhesion force on charges carried by the toner particles even in the absence of an imposed external electric field. Donald and Watson [5] developed a model to include the effect of an electric field on particle adhesion in the xerographic processes. Goel and Spencer [6] analyzed the effect of the electrostatic and van der Waals forces on the adhesion of toner particles. They concluded that for large particles (about 15 μm), the electrostatic imagine force dominates the particle adhesion, while for small particles (about 5 μm), the van der Waals force become the dominant force.

Hays [7,8] studied the detachment of charged toner particles under an electric field and suggested that the large adhesion force was due to the electrostatic imagine force of "patchy" charges that were concentrated on particle asperities. Lee and Jaffe [9] reported the effect of electrostatic forces on the adhesion of toner particles in xerographic printers. Mizes [10] quantified the relative contributions of nonelectrostatic and electrostatic forces to the net particle adhesion force. He concluded that under large electric fields (2 to 8 V/μm), the electrostatic contributions dominated the nonelectrostatic effects. Soltani and Ahmadi [11] studied rough particle detachment with electrostatic forces in turbulent flows. Their predictions agreed well with the experimental results by Hays [7,8] and Mizes [10]. Feng and Hays [12] performed a finite-element analysis of the electrostatic

force on a uniformly charged dielectric sphere resting on a dielectric-coated electrode in a detaching electric field. Masashi and Manabu [13] measured particle adhesion force using the electric field detachment method. They found that the adhesion force increased with time elapsed after the particles are placed on substrate. Hays and Sheflin [14] performed electric field detachment measurements on ion-charged toner for different charge levels and found that the adhesion of ion-charged toner is less than that of triboelectrically charged toner. They suggested that the enhanced electrostatic adhesion of triboelectrically charged toner is attributed to a non-uniform surface charge distribution.

Hinds [15] reviewed the work on the particle resuspension processes. More recent studies on models of particle resuspension processes were provided by Soltani and Ahmadi [16-19] and Ibrahim et al. [20]. For particles in humid air, the capillary force significantly affects the detachment of the particles. The effect of relative humidity on adhesion was studied by Podczeck et al. [21], Busnaina and Elsawy [22] and Tang and Busnaina [23]. Zimon [24] and Taheri and Bragg [25] performed experiments on particle resuspension in dry and humid air conditions. The experiments of Zimon [24] were conducted with humidity less than 10%. Taheri and Bragg [25] carried out their experiments under the condition of normal room temperature and humidity, their results agree well with the simulation result by Soltani and Ahmadi [16] for moist particle resuspension. Ibrahim et al. [20,26] measured particle resuspension in both dry and humid air conditions. Their experiments were performed at a humidity of 25±3% for dry condition and 67% for humid condition. Direct atomic force microscopy (AFM) measurement of adhesion force was reported by Gotzinger and Peukert [27,28]. Recently, Ahmadi et al. [29] studied particle adhesion and detachment in turbulent flows including the effect of capillary forces.

In this study, the rolling detachment of spherical particles in the presence of capillary and electrostatic forces for both elastic and plastic surface deformations was studied. An effective thermodynamic work of adhesion model was used to account for the effects of capillary and electrostatic forces for hydrophilic materials. The maximum adhesion

resistance moments were evaluated using the JKR and the DMT models for elastic surface deformation, while the Maugis-Pollock model was used for the plastic surface deformation. The turbulence burst/inrush model was used for evaluating the near-wall velocity field. The rolling detachment of spherical particles was studied and the critical shear velocities for detaching particles of various sizes were evaluated. The results were compared with those obtained in the absence of the electrostatic force and the capillary force. It was shown that the capillary and electrostatic forces significantly affected the particle adhesion and the opportunity for resuspension. The model predictions for resuspension of glass particles from a glass substrate with an average Boltzmann charge distribution were compared with the available experimental data.

6.2 ADHESION MODELS

The adhesion models used in this study are similar as that used in Chapter 5, the detailed information can be found in Section 5.2.

6.3 CAPILLARY FORCE, ELECTROSTATIC FORCE AND EFFECTIVE THERMODYNAMIC WORK OF ADHESION

6.3.1 Capillary Force

In this section, the introduction on capillary force is briefly presented. The detailed information about capillary force can be found in Chapter 5, Section 5.3.1.

As shown in Figure 6-1, for hydrophilic materials in humid air, the capillary force is determined by the surface tension of water σ (=0.0735 N/m, at room temperature), the particle diameter d, the wetting angle θ and the angle α as shown in Figure 6-1. That is:

$$F_c = 2\pi\sigma d[\sin\alpha \sin(\theta+\alpha) + \cos\theta)] \tag{6-1}$$

The angle α is normally very small, therefore for small values of wetting angle θ, the expression for the capillary force becomes:

$$F_c = 2\pi\sigma d. \quad (6\text{-}2)$$

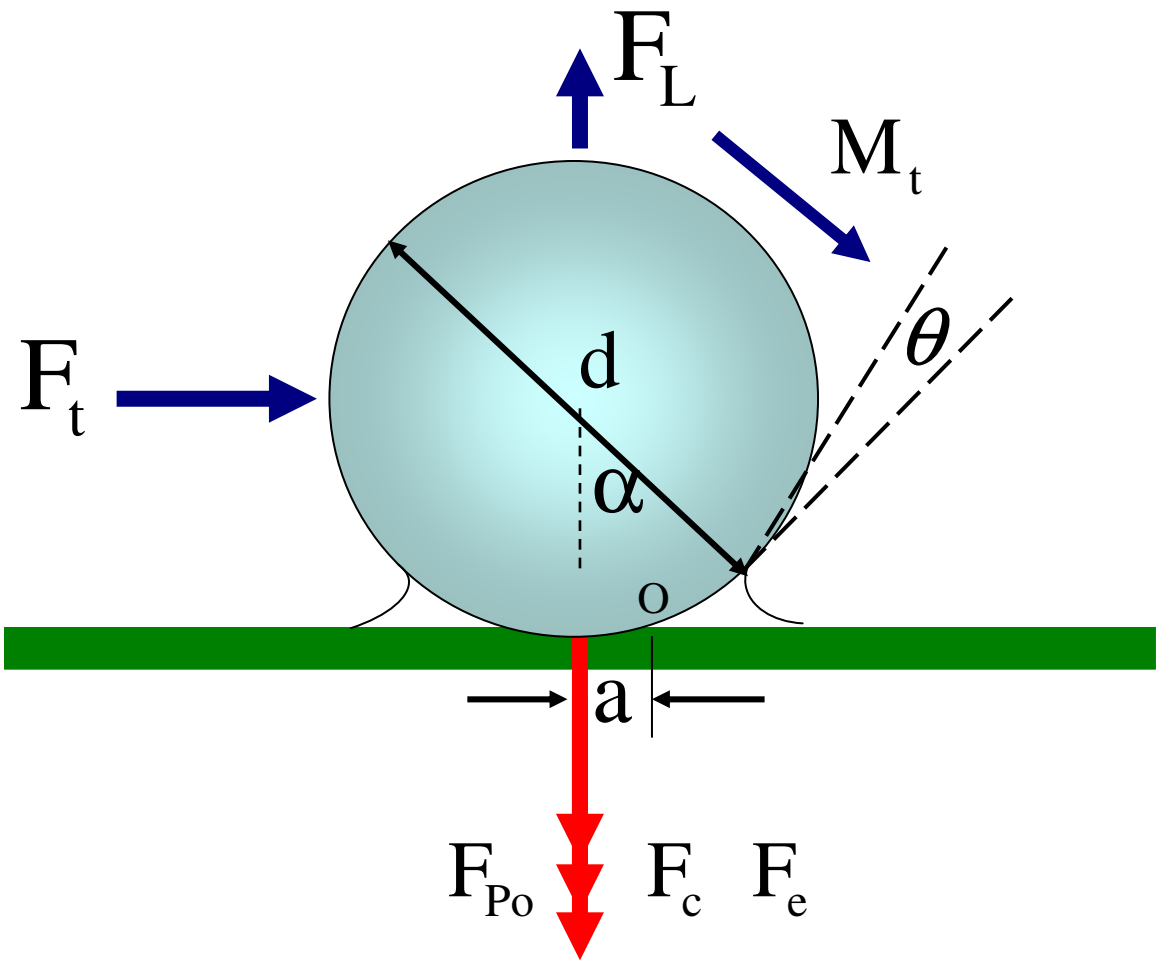

Figure 6-1. Geometric features of a spherical particle attached to a surface with capillary.

6.3.2 Charge Distribution

An aerosol particle rarely has zero charge due to the high ion concentration in the atmosphere. Particles smaller than 0.1 μm in diameter do not contain a charge naturally [30]. The number of natural charge increases with particle size. Particles can be charged through different mechanisms based on corresponding ionic atmosphere conditions. There are three different charge distributions outlined hereafter.

6.3.2.1 Boltzmann charge distribution

Boltzmann charging occurs for small particles in a bipolar ionic atmosphere. For particles larger than 0.1μm at normal condition, the average number of absolute charges per particle can be approximated by [31]

$$|n| = 2.37\sqrt{d}\,, \tag{6-3}$$

where d is given in μm. Therefore the average number of positive or negative charges per particle is $|n|/2$ [11].

6.3.2.2 Diffusion charge distribution

Diffusion charging occurs when uncharged particles obtain charges by diffusion of charged unipolar gaseous ions to their surfaces through random collisions between ions and particles. For a particle of diameter d_c during diffusion charging time t, the approximate number of obtained charges n is given as [15]

$$n = \frac{d_c kt}{2e_c^{\,2}} \ln\left[1 + \frac{\pi d \bar{c}_i e_c^{\,2} N_i t}{2kT}\right], \tag{6-4}$$

where $\bar{c}_i = 2.4\times10^4$ cm/s is the mean thermal speed of the ions, d_c is particle diameter in cm, $e_c = 4.8\times10^{-10}$ stC (electrostatic units) is the electronic unit charge in cgs units, N_i is the ion concentration, $k = 1.38\times10^{16}$ ergs/K is the Boltzmann constant, and T is the temperature of the gas. In the subsequent analysis, a typical value of $N_i t \approx 10^8$ ion$\cdot$s/cm^3 is used.

6.3.2.3 Field charge distribution

For particles in an electric field, the particles acquire charges due to collisions with ions which are moving along the lines of force that intersect the particle surfaces. This process is known as field charging. After a sufficient time for a given charging condition, the saturation number of charges n acquired by the particle of diameter d is given as [15]

$$n = \left[\frac{3\varepsilon}{\varepsilon + 2}\right]\left[\frac{E_c d_c^{\,2}}{4e_c}\right], \tag{6-5}$$

where ε is the dielectric constant of the particle, E_c is the electric field strength in cgs units. Equations (6-4) and (6-5) are expressed in cgs units. Field charging is the dominant mechanism for particles larger than 1μm and diffusion charging is the dominant one for particles less than 1μm.

6.3.3 Electrostatic Force

For a charged particle resting on a conducting substrate in the presence of an applied electric field, the electrostatic force acting on the particle is given as [11]

$$F_e = qE + \frac{q^2}{16\pi\varepsilon_0 y^2} + \frac{qEd^3}{16y^3} + \frac{3\pi\varepsilon_0 d^6 E^2}{128 y^4} \qquad (6\text{-}6)$$

Where $\varepsilon_0 = 8.859\times10^{-12}$ amp •s /V•m is the permittivity (dielectric constant of free space). d is the particle diameter, E is the electric field strength, and q is the total electrical charge on the particle, which is given as [11]

$$q = ne \qquad (6\text{-}7)$$

where $e = 1.6\times10^{-19}$ C is the electronic unit charge in mks units. n is the number of units of charge. In equation (6-6), y is the distance of the particle from the surface, which is approximately half d, so equation (6-6) becomes

$$F_e = qE + \frac{q^2}{4\pi\varepsilon_0 d^2} + \frac{qE}{2} + \frac{3\pi\varepsilon_0 d^2 E^2}{8} \qquad (6\text{-}8)$$

The first term on the right-hand side of equation (6-8) is the Coulomb force. The second term is the image force. The third term is the dielectrophoretic force on the induced dipole due to the gradient of the field from the image charge. The forth term is the polarization force due to the interaction of the induced dipole and its image. The Coulomb and dielectrophoretic forces can be either toward or away from the substrate, depending on the charges carried by the particles. While the image and polarization forces are always toward the substrate.

In most cases of this study, the particles and substrates are made of the same material, so the electrical double layer force is neglected. This force is caused by

the contact potential and becomes important when the particle and the substrate are made of two different materials with a high level of contact potential or when particles are smaller than 10 μm.

In order to include the effects of capillary and electrostatic forces in adhesion models, we assume that the particles without any charge are deposited on the substrate under dry condition, then an electric field is applied and particles get charged, at the same time a liquid meniscus forms due to vapor condensation on the particle-substrate contact. Therefore, a superposition of van der Waals, capillary and electrostatic forces may be assumed. The total force needed to lift-off the particle then is, $F_{po} + F_c + F_e$, where F_{po} is the pull-off force for overcoming the van der Waals adhesion, which is a function of thermodynamic work of adhesion W_A. The presence of capillary force enhances the surface energy of the materials; while the electrostatic forces can increase or decrease the surface energy, depending on the charges carried by the particles; therefore, it is reasonable to account for the combined effect of van der Waals adhesion, capillary and electrostatic forces with an effective thermodynamic work of adhesion W_A^e. This effective thermodynamic work of adhesion is variable with the adhesion model used.

6.3.4 Effective Thermodynamic Work of Adhesion

To evaluate the effective thermodynamic work of adhesion for the JKR model, the effective pull-off force must be balanced with the combined effect of van der Waals pull-off force, the capillary and electrostatic forces. That is,

$$\frac{3}{4}\pi W_A^{eJKR} d = \frac{3}{4}\pi W_A d + F_c + F_e \tag{6-9}$$

where W_A^{eJKR} is the effective work of adhesion for the JKR model. F_c and F_e are given by equations (6-2) and (6-8). It then follows that,

$$W_A^{eJKR} = W_A + \frac{8\sigma}{3} + \frac{2qE}{\pi d} + \frac{q^2}{3\pi^2\varepsilon_0 d^3} + \frac{\varepsilon_0 d E^2}{2} \tag{6-10}$$

The corresponding approximate expression for the effective contact radius is then given

by Equation (5-1) with W_A being replaced by W_A^{eJKR}.

The effective thermodynamic work of adhesion for the DMT and the Maugis-Pollock models can be obtained in a similar way. That is,

$$W_A^{eDMT} = W_A^{eMP} = W_A + 2\sigma + \frac{1.5qE}{\pi d} + \frac{q^2}{4\pi^2\varepsilon_0 d^3} + \frac{3\varepsilon_0 dE^2}{8} \tag{6-11}$$

The corresponding effective contact radius as estimated from the DMT model is given as

$$a_e^3 \approx \frac{d}{2k}\left(P + \pi W_A^{eDMT} d\right) \tag{6-12}$$

For the Maugis-Pollock model, the corresponding effective contact radius is given as

$$a_e = \sqrt{\frac{P + \pi W_A^{eMP} d}{\pi H}} \tag{6-13}$$

6.4 DETACHMENT MODELS

As mentioned in Section 5.4, the detachment of smooth spherical particles is more easily achieved by the rolling motion, rather than by sliding and lifting. Therefore, only rolling detachment is discussed in this study.

6.4.1 Rolling Detachment Model

The rolling detachment approach used here is similar to that used in Section 5.4.1, but the approach used here is extended to include the effect electrostatic forces.

Figure 6-1 shows a spherical particle attached to a planar surface in a fluid flow. The lift and gravity forces, which are very small, are neglected in this study. In humid air, a meniscus is formed at the particle-substrate contact. Here it is assumed that the particle without any charge are deposited on the substrate under dry condition, then an electric field is applied and particles get charged, at the same time a liquid meniscus forms on the particle-substrate contact. The particle will be detached when the moment of the

hydrodynamic force about the point "O" (which is located at the rear perimeter of the contact circle) overcomes the maximum adhesion resistance moment due to combined adhesion, capillary and electrostatic forces. That is,

$$M_t + F_t(\frac{d}{2} - \alpha_o) \geq (P \cdot a)_{Max}. \tag{6-14}$$

Where F_t is the fluid drag force, α_o is the overlap (relative approach) between the particle and surface, M_t is the hydrodynamic moment about the center of the particle, $(P \cdot a)_{Max}$ is the maximum adhesion resistance moment due to combined adhesion, capillary and electrostatic forces. In most practical cases, α_o can be neglected and Equation (6-14) becomes

$$M_t + F_t \frac{d}{2} \geq (P \cdot a)_{Max} \tag{6-15}$$

6.5 MAXIMUM ADHESION RESISTANCE

To develop a particle rolling detachment model, the corresponding maximum adhesion resistance moment need to be evaluated. In this study, the JKR and DMT adhesion models are used for elastic surface deformations, while the Maugis-Pollock adhesion model is used for plastic surface deformation. Using a similar approach as developed in Section 5.5, one can obtain the maximum adhesion resistance moment for different adhesion models.

For the JKR model without capillary and electrostatic forces

$$M_{Max}^{JKR} = 2.707 \frac{W_A^{4/3} d^{5/3}}{K^{1/3}} \tag{6-16}$$

For the JKR model with capillary and electrostatic forces

$$M_{Max}^{JKR} = 2.707 \frac{W_A^{eJKR\,4/3} d^{5/3}}{K^{1/3}} \tag{6-17}$$

For the DMT model without capillary and electrostatic forces

$$M_{Max}^{DMT} = 1.725 \frac{W_A^{4/3} d^{5/3}}{K^{1/3}} \tag{6-18}$$

For the DMT model with capillary and electrostatic forces

$$M_{Max}^{DMT} = 1.725 \frac{W_A^{eDMT\,4/3} d^{5/3}}{K^{1/3}} \tag{6-19}$$

For the Maugis-Pollock model without capillary and electrostatic forces

$$M_{Max}^{MP} = \frac{2\pi (W_A d)^{3/2}}{3\sqrt{3H}} \tag{6-20}$$

For the Maugis-Pollock model with capillary and electrostatic forces

$$M_{Max}^{MP} = \frac{2\pi (W_A^{eMP} d)^{3/2}}{3\sqrt{3H}} \tag{6-21}$$

Note that from a similar process in Chapter 5, one has

$$M_{Max}^{*JKR} = 1.57\, M_{Max}^{*DMT} \tag{6-22}$$

6.6 HYDRODYNAMIC FORCES AND TORQUES

As mentioned in Section 5.6, the particle detachment process is strongly affected by the near-wall turbulent flow structure. This flow structure includes burst and inrush processes. The peak near-wall velocity during turbulent burst/inrush and the corresponding hydrodynamic forces and torques are listed as Equations (5-38) to (5-45) in Chapter 5, Section 5.6. The lift force acting on the particle is very small compared to the adhesion, capillary and electrostatic forces and therefore is neglected in this work.

6.7 PARTICLE DETACHMENT

In this section, the critical shear velocities for particle removal in humid air with capillary and electrostatic force are evaluated with the use of the JKR, the DMT and the Maugis-Pollock models. Substituting the expression for the hydrodynamic drag and torque into Equation (6-15), the critical shear velocity for rolling detachment of spherical particles including the capillary and electrostatic force is obtained as:

$$u_c^{*2} = \frac{M_{Max}}{3.81\pi\rho d^3 / C_c} \tag{6-23}$$

where M_{Max} is the maximum adhesion resistance moment. The critical shear velocity for particle detachment according to the JKR, DMT and Maugis-Pollock models can be

evaluated by substituting, respectively, the expressions for the maximum resistance moment from Equations (6-17), (6-19) and (6-21) into Equation (6-2) for M_{Max}.

Table 6-1. Material properties for different combinations

Material combination	E $(10^{10}\ Pa)$	A $(10^{-20}\ J)$	W_A $(10^{-3}\ J/m^2)$	ρ_p $(10^3\ kg/m^3)$	ν_i	H $(10^7\ Pa)$
Polystyrene-polystyrene	0.28	6.37	10.56	1.05	0.33	6.59
Glass-glass	6.9	8.5	14.1	2.18	0.2	490-665.4
Glass-steel	_	_	150	_	_	646.8
Polystyrene-nickel	_	_	23.65	_	_	_

E: Young's modulus of material A: Hamaker constant

W_A : thermodynamic work of adhesion ρ_p : density of material

ν_i : Poisson's ratio of material i H: hardness of material

6.8 RESULTS

6.8.1 Force and Charge Analysis

In this section the results for the average Boltzmann, the saturation and fixed 20 μC/g charge distributions are given. The results for the electrostatic, capillary and pull-off forces are also presented and discussed. The material properties for polystyrene, glass, nickel and steel that were used in this work are listed in Table 6-1. Two electric fields are presented in the study, 5000 kV/m and 10000kV/m.

Figure 6-2 shows the variation of the average Boltzmann charge distribution with the particle diameter. It is seen that average Boltzmann charge increase with the increase of the particle diameter. Figure 6-3 shows the variation of the saturation and fixed 20 μC/g

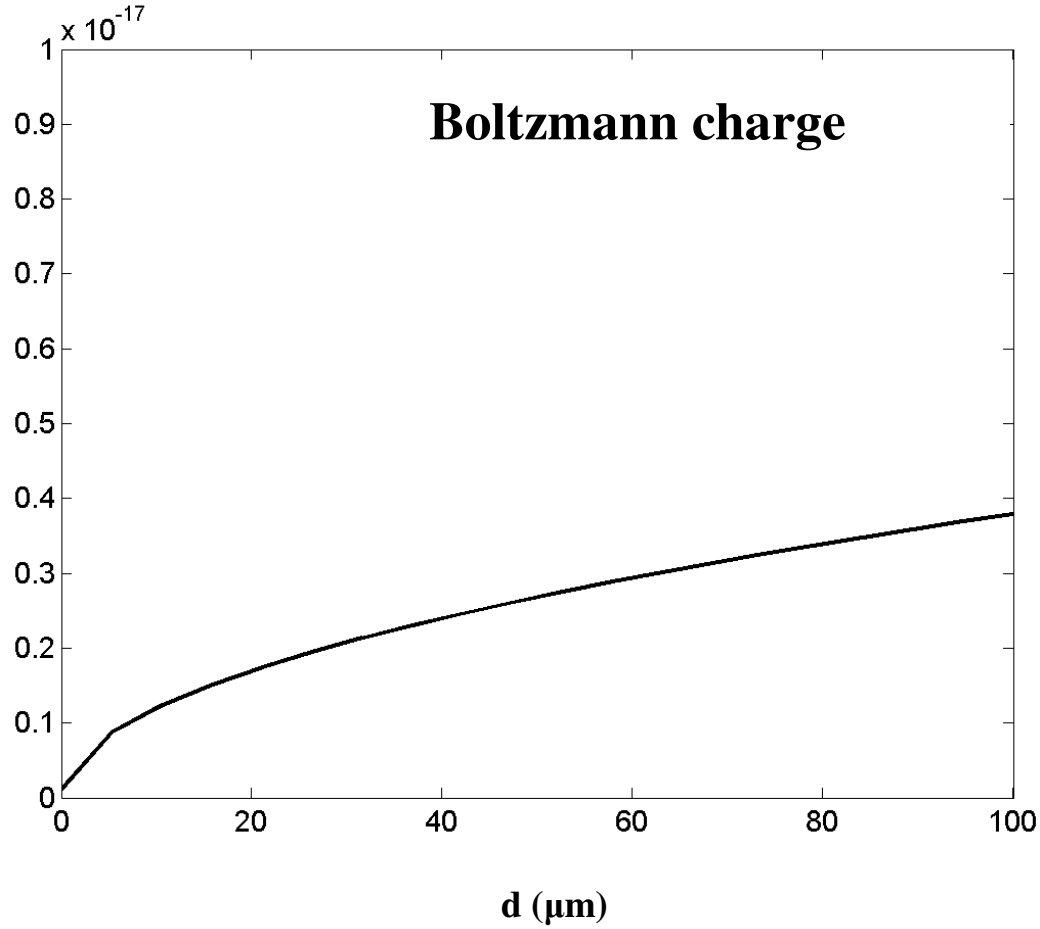

Figure 6-2. Variation of the average Boltzmann charge distribution with the particle diameter.

charge distributions with the particle diameter for polystyrene particles. Figure 6-3 shows similar trend as in that in Figure 6-2. The saturation and fixed 20 µC/g charge distributions increase with the increase of the particle diameter. The saturation charge distribution in an electric field of 5000 kV/m is about half of that in 10000kV/m. For particles smaller than 25µm, 20 µC/g charge distribution is smaller than the saturation charge distributions. However, for particles larger than 50µm, 20 µC/g charge distribution is larger than the saturation charge distributions. Compared to Figure 6-2, Figure 6-3 shows that the saturation and fixed 20 µC/g charge distributions are much higher than the average Boltzmann charge distribution.

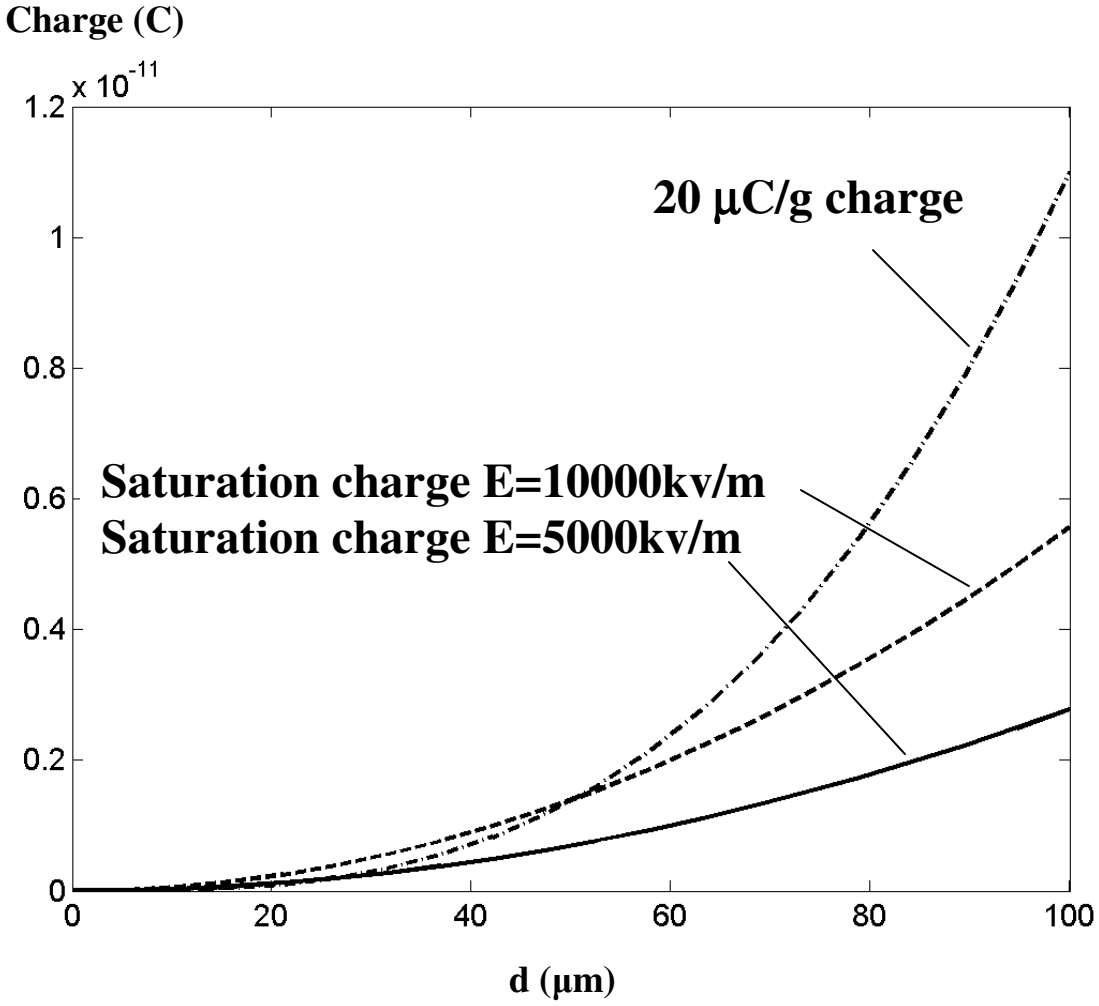

Figure 6-3. Variation of the saturation and fixed 20 μC/g charge distribution with the particle diameter for polystyrene particles.

Figure 6-4 shows the variation of the combined Coulomb forces (Coulomb force and dielectrophoretic force) with the particle diameter for polystyrene particles carrying different charges in an electric field of 10000kV/m. It is seen that the combined Coulomb forces increase with the increase of the particle diameter. For particles carrying average Boltzmann charge, the combined Coulomb forces are much smaller than those of particles carrying saturation and fixed 20 μC/g charges. The reason is that the average Boltzmann charge distribution is much smaller than the saturation and fixed 20 μC/g charge distributions, as mentioned above. Figure 6-4 also shows that corresponding to the amount of charges carried by the particles, for particles smaller than 50μm, the

combined Coulomb forces for particles carrying fixed 20 μC/g charge distribution are smaller than those of particles carrying saturation charge distributions; But for particles larger than 50μm, the combined Coulomb forces for particles carrying fixed 20 μC/g charge distribution are larger than those of particles carrying saturation charge distributions.

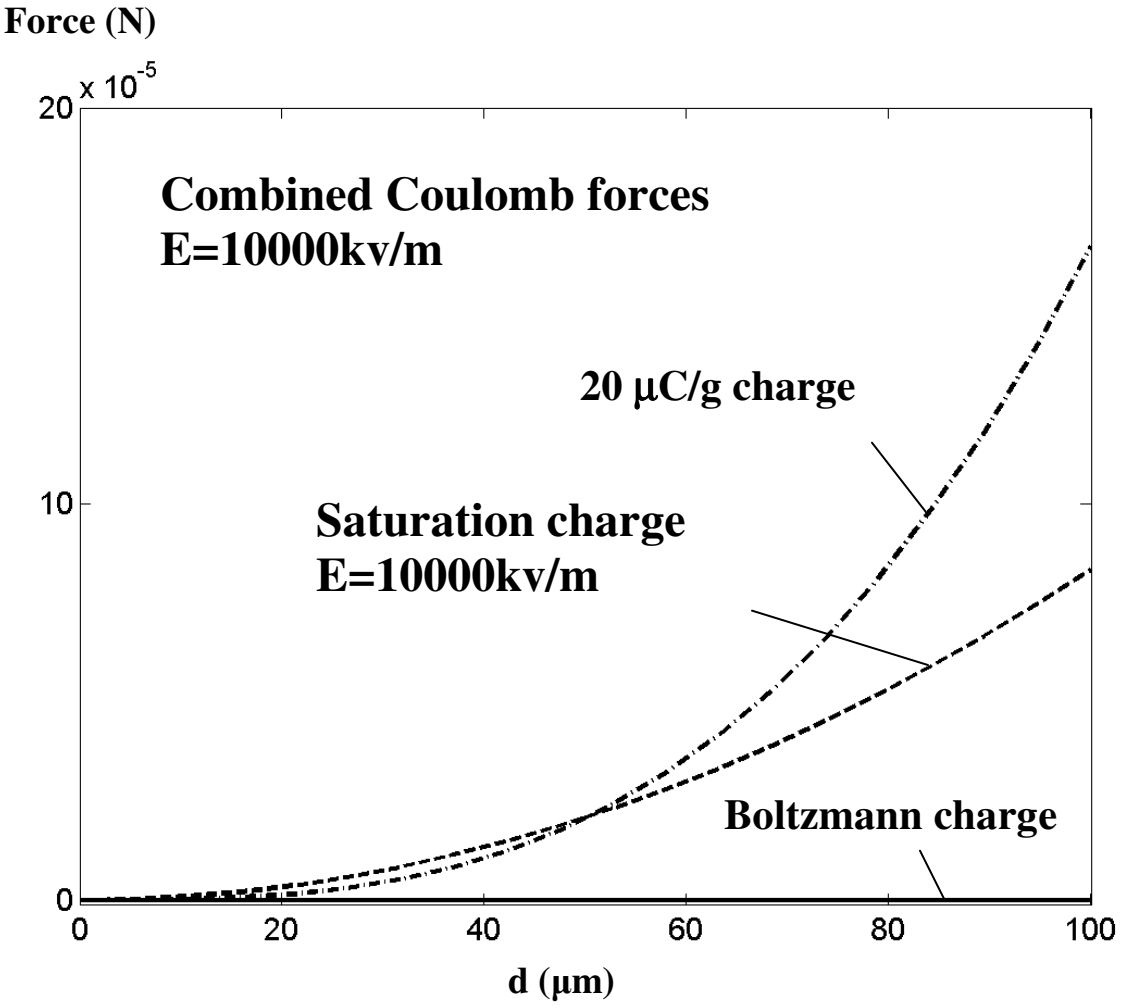

Figure 6-4. Variation of the combined Coulomb forces with the particle diameter for polystyrene particles carrying different charges in an electric field of 10000kV/m.

Figure 6-5 shows the variation of the imagine forces with the particle diameter for polystyrene particles carrying different charges. Similar to the trend in Figure 6-4, Figure 6-5 shows that the imagine forces increase with the increase of the particle diameter. For

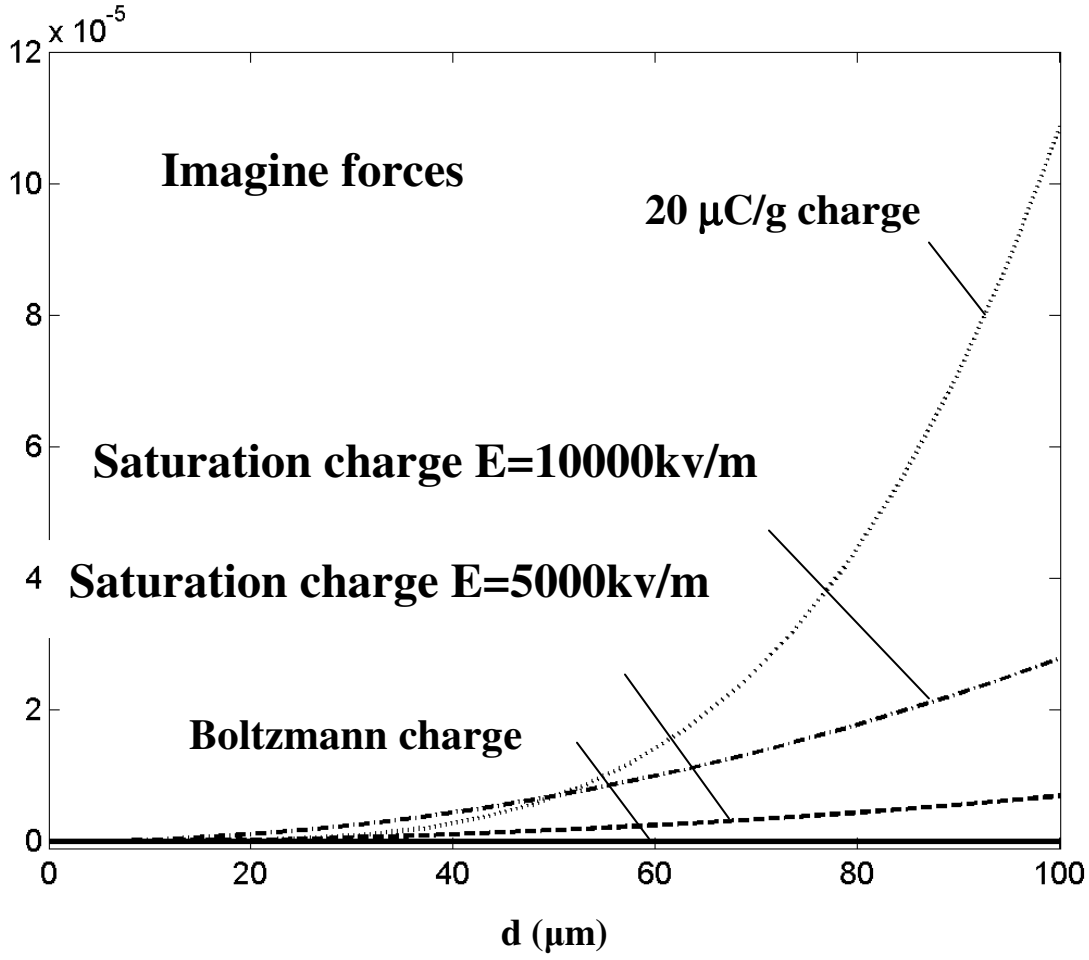

(a)

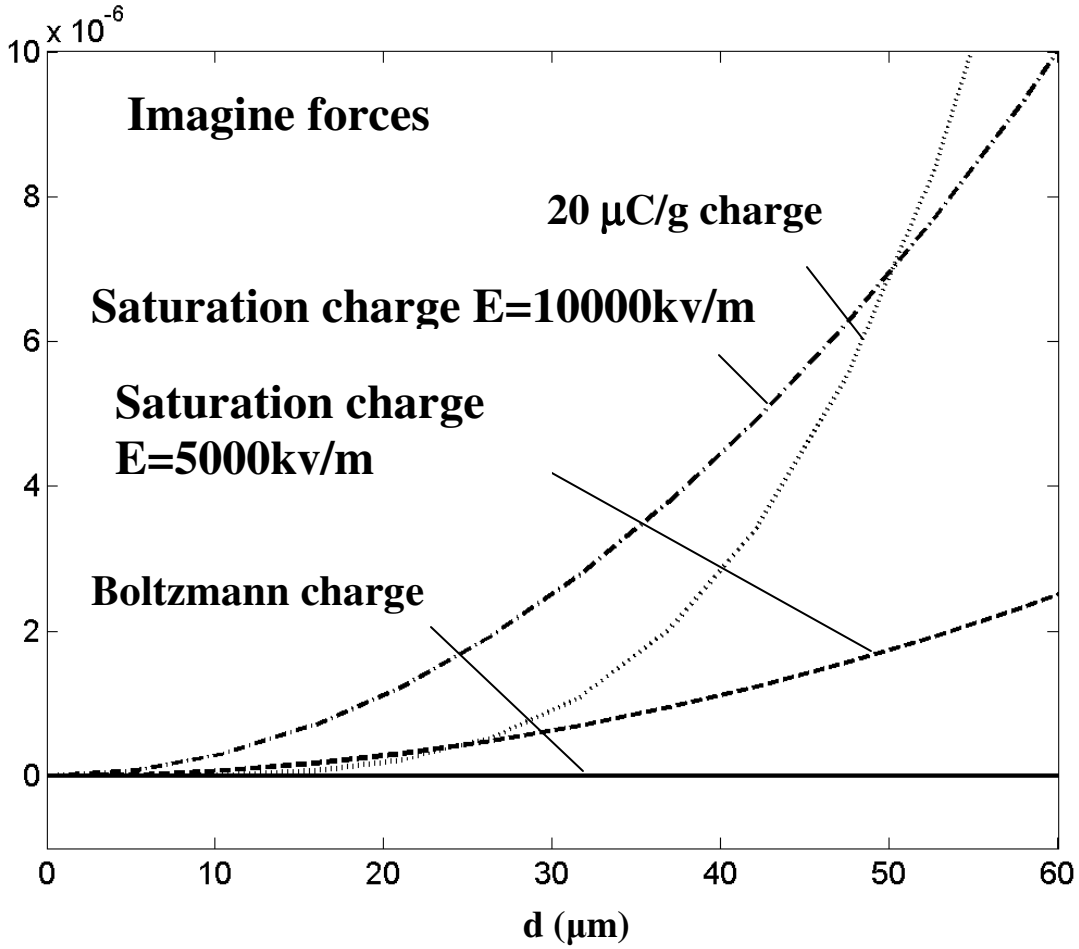

(b)

Figure 6-5. Variation of the imagine forces with the particle diameter for polystyrene particles carrying different charges.

particles carrying average Boltzmann charge, the imagine forces are much smaller than those of particles carrying saturation and fixed 20 μC/g charges. The reason is that in general, the average Boltzmann charge distribution is much smaller than the saturation and fixed 20 μC/g charge distributions. Figure 6-5 also shows that for particles smaller than 25μm, the imagine forces for particles carrying fixed 20 μC/g charge distribution are smaller than those of particles carrying saturation charge distributions; But for particles larger than 50μm, the imagine forces for particles carrying fixed 20 μC/g charge distribution are larger than those of particles carrying saturation charge distributions. It is also seen from Figure 6-5 that the imagine forces for particles carrying the saturation

charge distribution in an electric field of 5000 kV/m are smaller than that in 10000kV/m. Compared to Figure 6-4, Figure 6-5 shows that the imagine forces are smaller than the combined Coulomb forces.

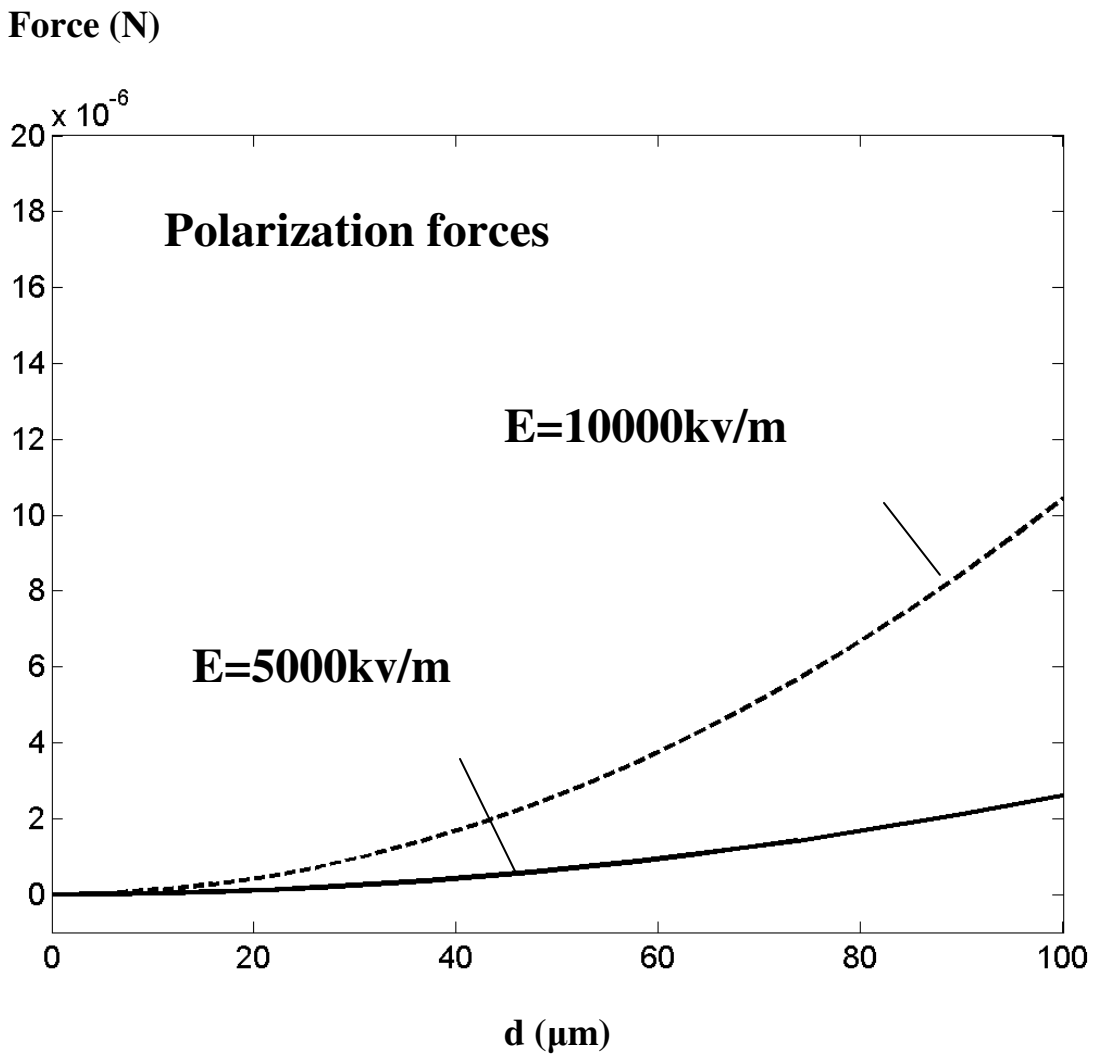

Figure 6-6. Variation of the polarization forces with the particle diameter for polystyrene particles in different electric fields.

Figure 6-6 shows the variation of the polarization forces with the particle diameter for polystyrene particles in different electric fields. Similar to Figure 6-5, Figure 6-6 shows that the polarization forces increase with the increase of the particle diameter; the polarization forces for particles in an electric field of 5000 kV/m are smaller than that in

10000kV/m. Compared to Figures 6-4 and 6-5, Figure 6-6 shows that the polarization forces are smaller than the imagine forces and combined Coulomb forces for particles carrying the saturation and fixed 20 μC/g charge distribution but larger than the imagine forces and combined Coulomb forces for particles carrying the average Boltzmann charge distribution.

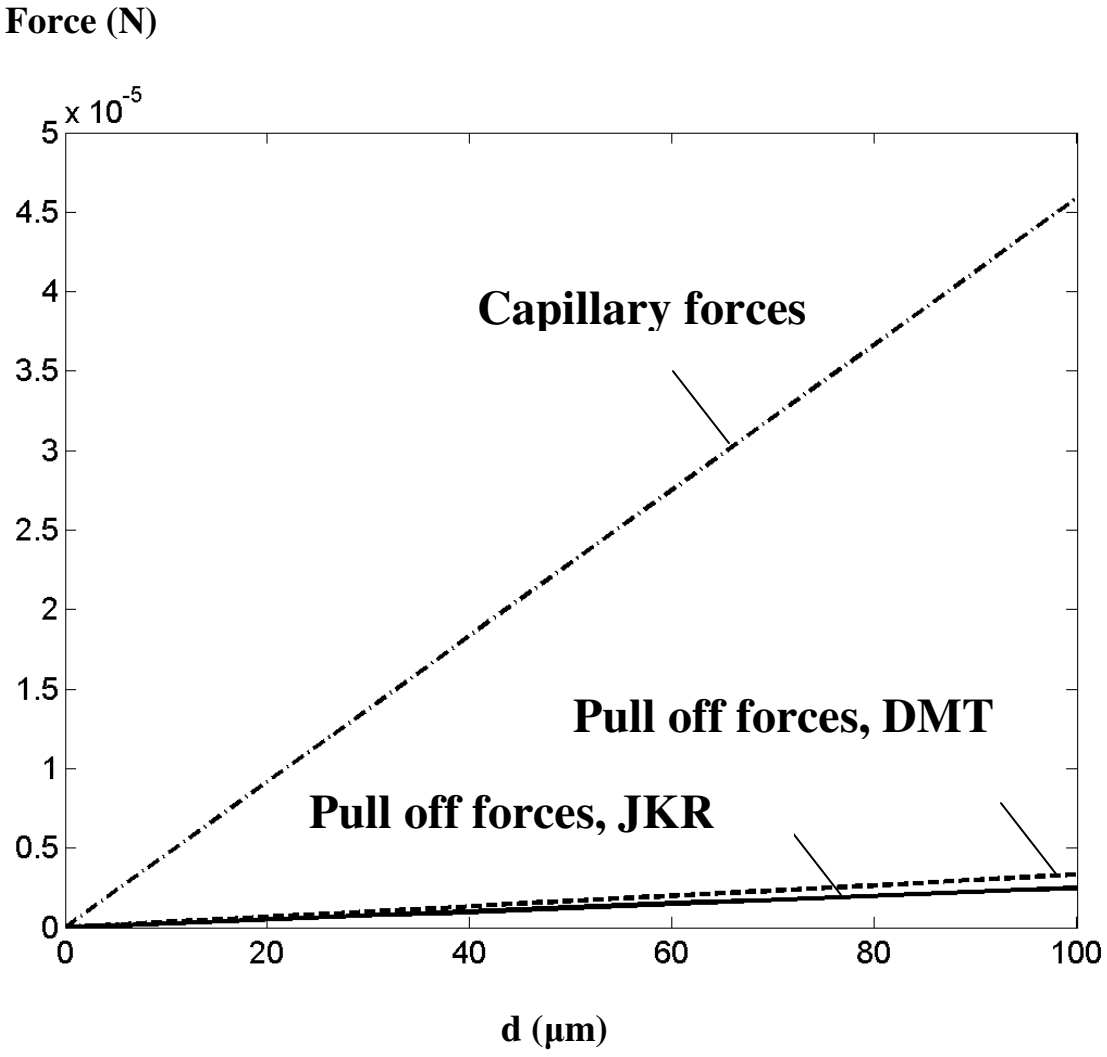

Figure 6-7. Variation of the capillary and pull-off forces with the particle diameter for resuspension of polystyrene particles from a polystyrene substrate.

Figure 6-7 shows the variation of the capillary and pull-off forces with the particle diameter for resuspension of polystyrene particles from a polystyrene substrate. It can be

seen from Figure 6-7 that the capillary and pull-off forces increase with the increase of the particle diameter, and capillary forces are much larger than the pull-off forces. . Compared to Figures 6-4, 6-5 and 6-6, Figure 6-7 shows that the capillary forces can be smaller than the combined Coulomb forces for particles carrying the saturation and fixed 20 μC/g charge distribution, also can be smaller than the imagine forces for particles carrying the fixed 20 μC/g charge distribution, but can be larger than the polarization forces, also can be are larger than the imagine forces for particles carrying the saturation and Boltzmann charge distribution.

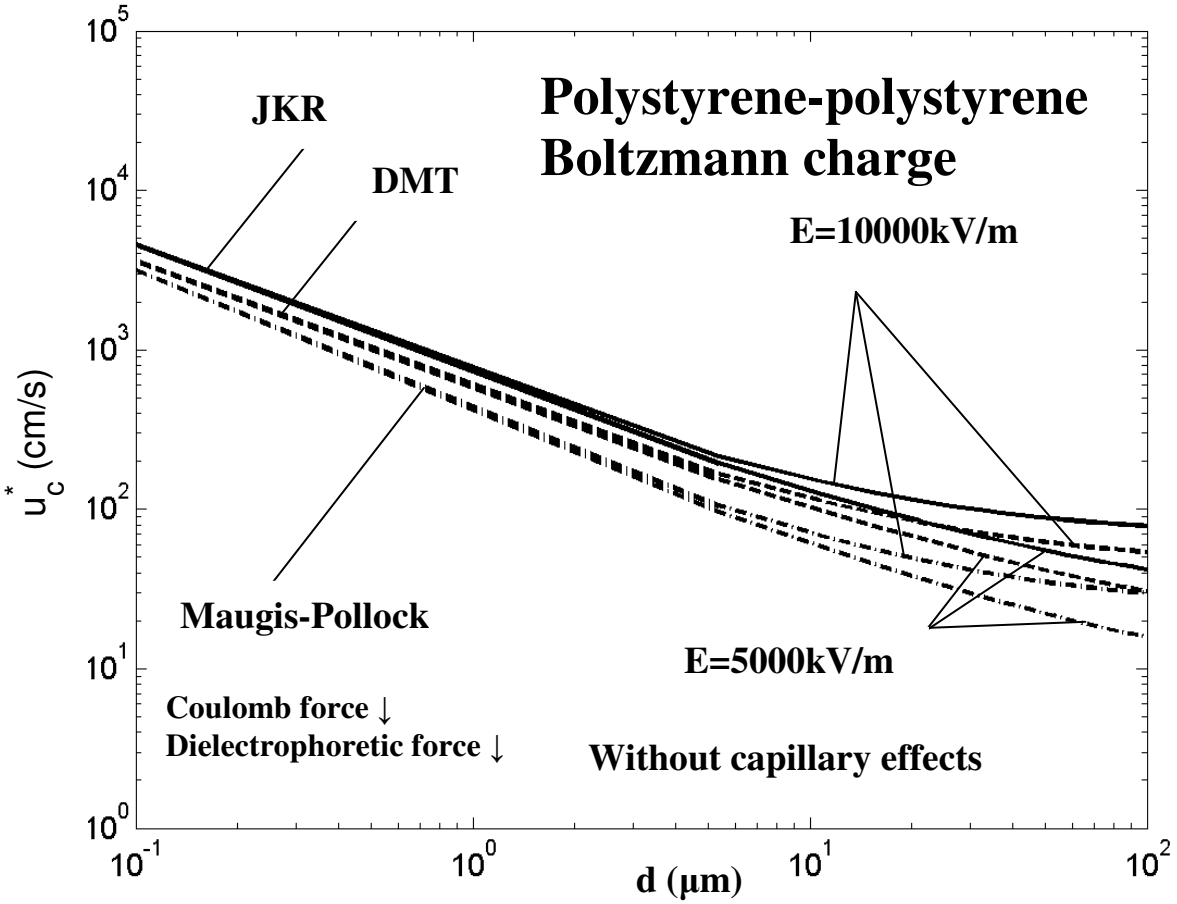

Figure 6-8. Variation of the critical shear velocities with the particle diameter as predicted by different adhesion models for resuspension of polystyrene particles with an average Boltzmann charge distribution from a polystyrene substrate in the presence of different electric fields without capillary effects. Coulomb force and dielectrophoretic force are directed towards the substrate.

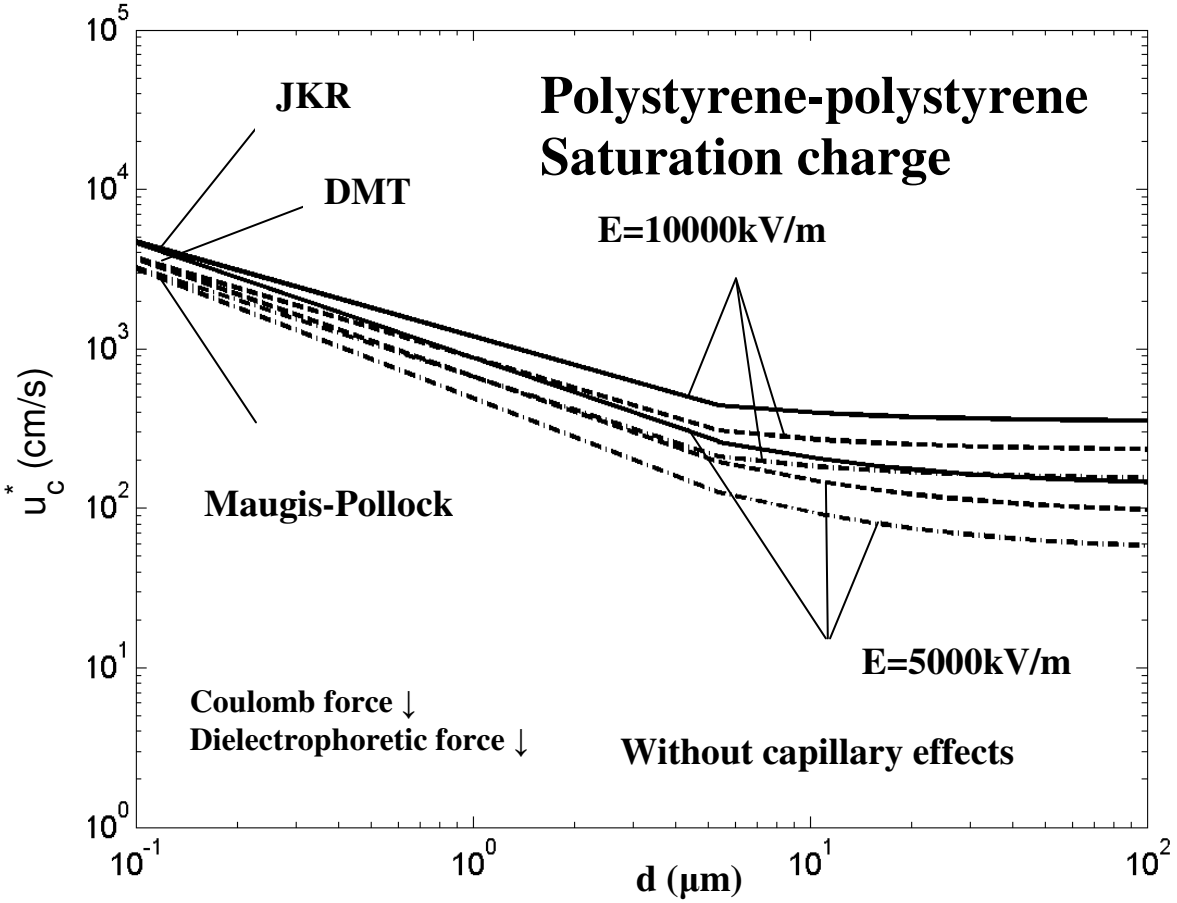

Figure 6-9. Variation of the critical shear velocities with the particle diameter as predicted by different adhesion models for resuspension of polystyrene particles with saturation charge distribution from a polystyrene substrate in the presence of different electric fields without capillary effects. Coulomb force and dielectrophoretic force are directed towards the substrate.

6.8.2 Critical Shear Velocity Analysis

In this section the results for detachment of particles of different sizes and various materials from substrates of various materials are presented and discussed. All results are presented in term of critical shear velocity, u_c^*, which is the minimum shear velocity needed to remove a particle from the substrate. Here for the particles in the turbulent flow, the near-wall velocity during the burst/inrush of turbulent flow was used in the analysis.

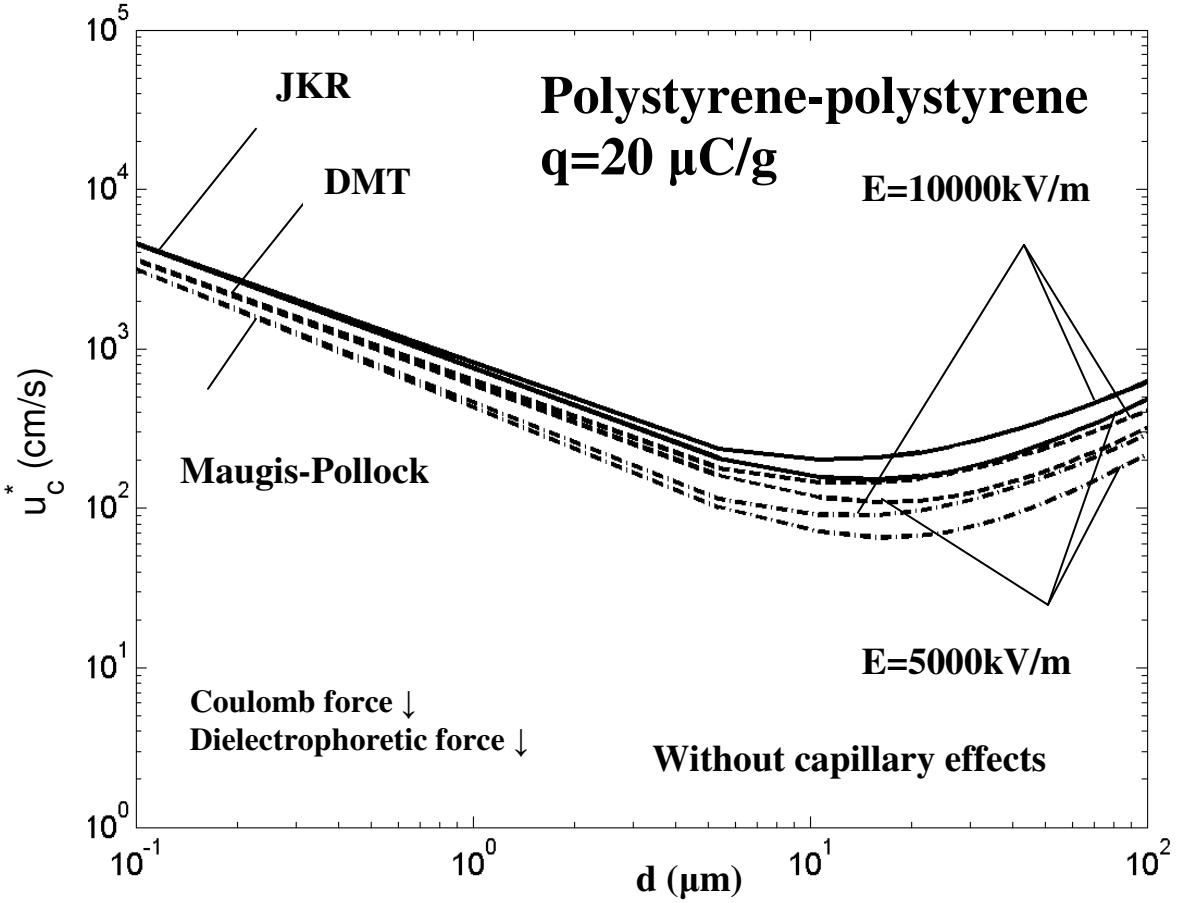

Figure 6-10. Variation of the critical shear velocities with the particle diameter as predicted by different adhesion models for resuspension of polystyrene particles with 20 µC/g charge distribution from a polystyrene substrate in the presence of different electric fields without capillary effects. Coulomb force and dielectrophoretic force are directed towards the substrate.

Figures 6-8, 6-9 and 6-10 show the variations of u_c^* with particle diameter as predicted by different adhesion models in different electric fields for the rolling detachment of polystyrene particles with Boltzmann charge, saturation charge and fixed 20µC/g charge respectively from a polystyrene substrate for dry conditions. Here Coulomb force and dielectrophoretic force are directed towards the substrate. Figure 6-8 shows that the critical shear velocity decreases with the increase of the particle diameter.

That is, as expected small particles are more difficult to remove than the larger ones. Figure 6-8 also shows that the critical shear velocity as predicted by the JKR adhesion model is the largest. The predicted critical shear velocity by the DMT model is less than that by the JKR model. The predicted value by the Maugis-Pollock model, which accounts for plastic deformation, is lower than those by the JKR and the DMT models for elastic deformation. The differences are small for smaller particles, but become relatively large for larger particles. As mentioned in Chapter 5, these differences are due to the variations of the maximum adhesion resistance moments for the JKR, the DMT and the Maugis-Pollock models. Figure 6-8 also shows that the critical shear velocities in an electric field of 5000 kV/m are lower than those in 10000kV/m. The reason is that the electrostatic forces increase with the increase of electric field intensity. The differences are small for smaller particles, but become large for larger particles. The reason is larger particles carry more charges, as seen from equations (6-3) and (6-5), though imagine force for Boltzmann charge decrease with the increase of the particle diameter, however, overall, the electrostatic forces still increases with the increase of the particle diameter, as shown by equation (6-8).

Figures 6-9 and 6-10 show similar trend as that in Figure 6-8. The critical shear velocity predicted by the JKR adhesion model is the largest, and the predicted value by the Maugis-Pollock model is lower than those by the JKR and the DMT models; The differences are small for smaller particles, but become relatively large for larger particles; The critical shear velocities in an electric field of 5000 kV/m are lower than those in 10000kV/m; For Figure 6-9, the differences are small for smaller particles, but become large for larger particles. While for Figure 6-10, though the differences are small for smaller particles, and become large for larger particles. However, for particles larger than 30μm, the differences become smaller again. The reason is for a fixed charge of 20 μC/g, if particles are larger than 30μm, the imagine forces can become comparable to or larger than the combined Coulomb and dielectrophoretic forces, while imagine forces are independent of electric fields. Therefore, electric fields have less effect on large particles where imagine forces are larger or comparable to the combined Coulomb and dielectrophoretic forces. Figure 6-9 shows that the critical shear velocity decreases with

the increase of the particle diameter. Compared to Figure 6-8, Figure 6-9 shows higher shear velocities. The reason is the electrostatic forces acting on particles with a saturation charge are much higher than those with an average Boltzmann charge. Figure 6-10 shows that for small particles, the critical shear velocity decreases with the increase of the particle diameter; for large particles, the critical shear velocity increases with the increase of the particle diameter due to higher level of charges that large particles obtained for a fixed charge of 20 μC/g. Compared to Figure 6-8, Figure 6-10 shows higher shear velocities for large particles. For small particles, shear velocities in Figures 6-8 and 6-10 are almost same. Compared to Figure 6-9, Figure 6-10 shows higher shear velocities for large particles and lower shear velocities for small particles. This is because for a fixed charge of 20 μC/g, the amount of charges on a particle is proportional to its mass; small particles have less charge, as less as those with Boltzmann charge distribution, but less than those with saturation charge distribution. Large particles have a much higher level of charge compared to those of Boltzmann charge distribution and saturation charge distribution. So for small particles, shear velocities in Figures 6-8 and 6-10 are almost same, while Figure 6-10 shows lower shear velocities than those of Figure 6-9. For large particles, Figure 6-10 shows higher shear velocities than those of both Figures 6-8 and 6-9.

Figures 6-11, 6-12 and 6-13 show the variations of u_c^* with particle diameter as predicted by different adhesion models in the presence of capillary effects and different electric fields for the rolling detachment of polystyrene particles with Boltzmann charge, saturation charge and fixed 20μC/g charge respectively from a polystyrene substrate. Here Coulomb force and dielectrophoretic force are directed towards the substrate. The trends are similar to those observed in Figures 6-8, 6-9 and 6-10. Figure 6-11 shows that the critical shear velocity decreases with the increase of the particle diameter. The model predictions from the JKR model are slightly higher than those from the DMT model. The predictions from the Maugis-Pollock model for u_c^* are the lowest for large particles, but slightly higher than those from the DMT model for small particles. Compared to results presented in Figure 6-8, Figure 6-11 shows higher critical shear velocities. This implies that the presence of capillary force significantly increases the critical shear velocity for particle rolling removal. Figure 6-11 also shows that the critical shear velocities in an

electric field of 5000 kV/m are lower than those in 10000kV/m, but the differences are relatively smaller compared to results presented in Figure 6-8. Because the Figures are in logarithmic coordinate, this does not mean that the absolute values of the differences are smaller. This means that when Coulomb force and dielectrophoretic force are directed towards the substrate, the relative effects of the electrostatic forces decrease in the presence of capillary effects.

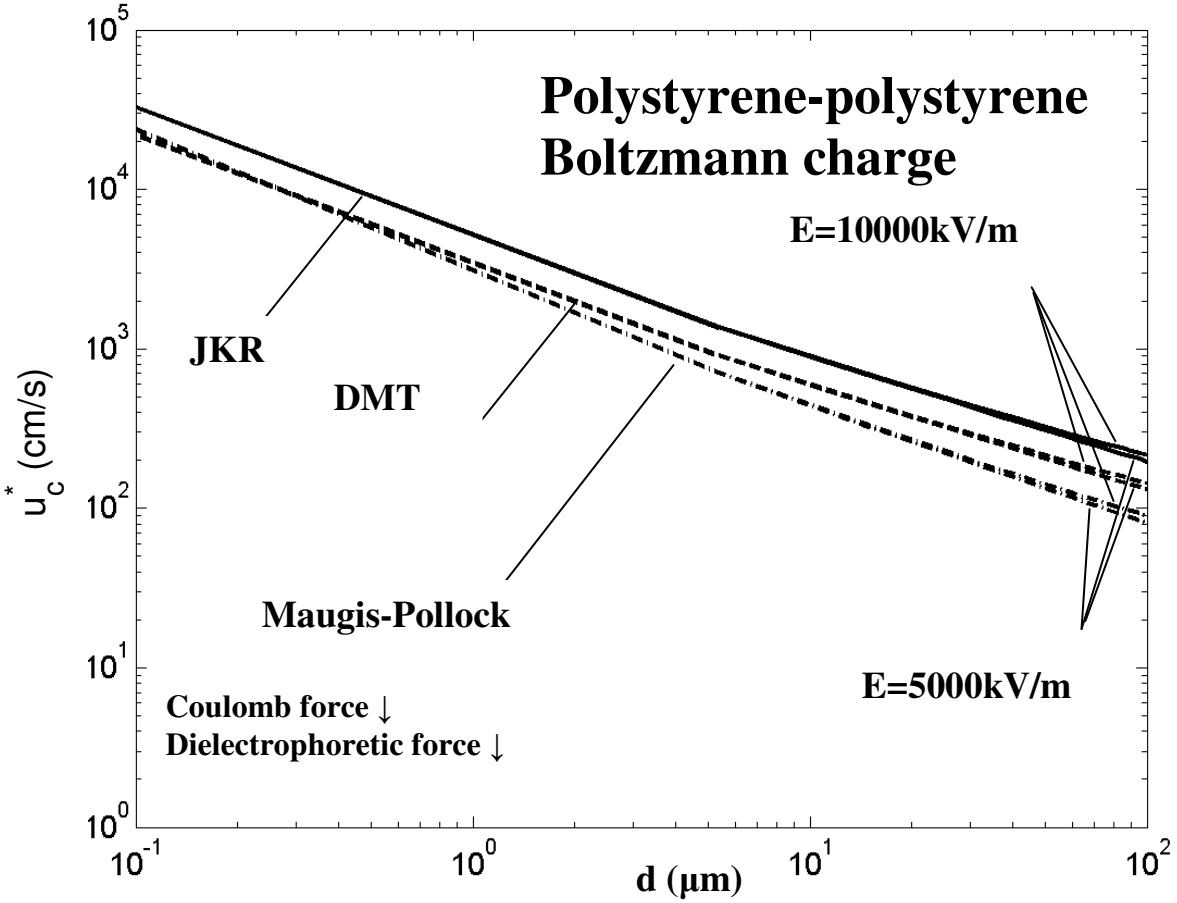

Figure 6-11. Variation of the critical shear velocities with the particle diameter as predicted by different adhesion models for resuspension of polystyrene particles with an average Boltzmann charge distribution from a polystyrene substrate in the presence of capillary effects and different electric fields. Coulomb force and dielectrophoretic force are directed towards the substrate.

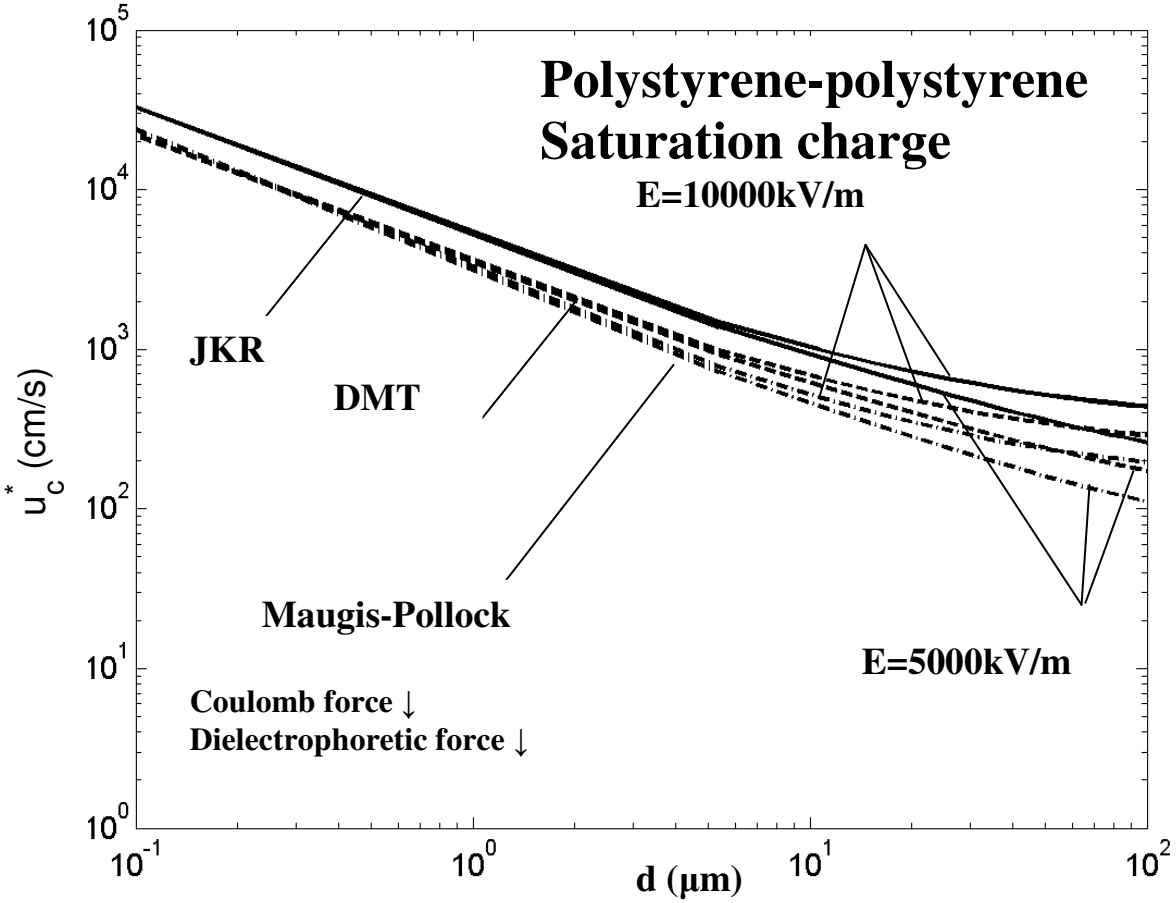

Figure 6-12. Variation of the critical shear velocities with the particle diameter as predicted by different adhesion models for resuspension of polystyrene particles with saturation charge distribution from a polystyrene substrate in the presence of capillary effects and different electric fields. Coulomb force and dielectrophoretic force are directed towards the substrate.

Figure 6-12 shows that the critical shear velocity decreases with the increase of the particle diameter. Compared to Figure 6-11, Figure 6-12 shows higher shear velocities. Figure 6-13 shows that for small particles, the critical shear velocity decreases with the increase of the particle diameter; for large particles, the critical shear velocity increases with the increase of the particle diameter due to higher level of charges that large particles obtained for a fixed charge of 20 μC/g. Compared to Figure 6-11, Figure 6-13

shows higher shear velocities for large particles. For small particles, shear velocities in Figures 6-11, 6-12 and 6-13 are almost same. Compared to Figure 6-12, Figure 6-13 shows higher shear velocities for large particles and lower shear velocities for smaller particles.

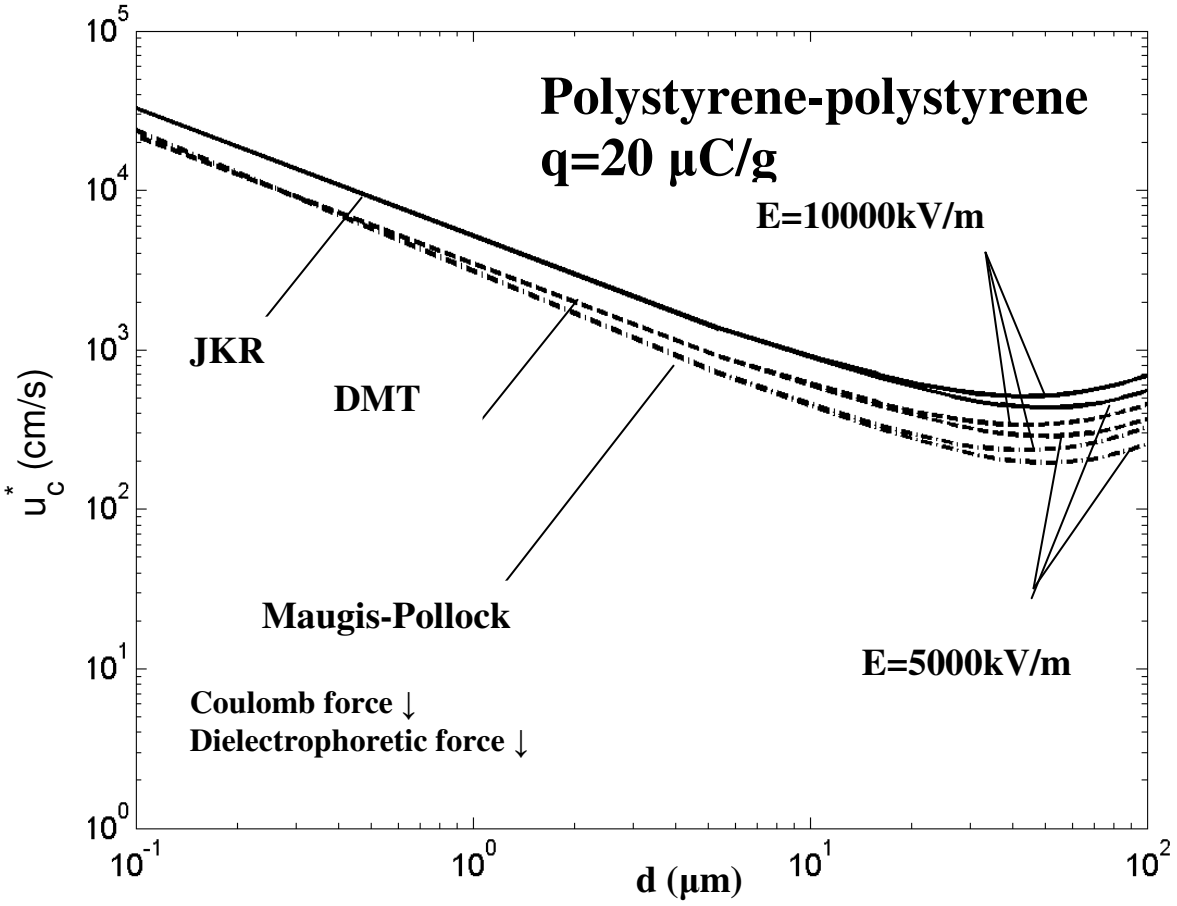

Figure 6-13. Variation of the critical shear velocities with the particle diameter as predicted by different adhesion models for resuspension of polystyrene particles with 20 µC/g charge distribution from a polystyrene substrate in the presence of capillary effects and different electric fields. Coulomb force and dielectrophoretic force are directed towards the substrate.

Similar to Figure 6-11, Figures 6-12 and 6-13 also show that the model predictions from the JKR model are slightly higher than those from the DMT model. The predictions

from the Maugis-Pollock model for u_c^* are the lowest for large particles, but slightly higher than those from the DMT model for small particles. Compared to results presented in Figures 6-9 and 6-10, Figures 6-12 and 6-13 show higher critical shear velocities, which means that the presence of capillary force significantly increases the critical shear velocity for particle rolling removal. Figures 6-12 and 60-13 also shows that the critical shear velocities in an electric field of 5000 kV/m are lower than those in 10000kV/m, the differences are small for smaller particles, but become large for larger particles. But the differences are relatively smaller compared to results presented in Figures 6-9 and 6-10, which means that the relative effects of the electrostatic forces decrease in the presence of capillary effects. However, compared to Figure 6-10, for particles larger than 30μm, the differences in Figure 6-13 do not become smaller again. The reason is same, in the presence of capillary effects, the relative effects of the electrostatic forces are decreased. Same reason can explain that for small particles, Figure 6-9 shows higher shear velocities than those in Figures 6-8 and 6-10, while shear velocities in Figures 6-11, 6-12 and 6-13 are almost same.

Figures 6-14, 6-15 and 6-16 show the variations of u_c^* with particle diameter as predicted by different adhesion models in the presence of capillary effects and different electric fields for the rolling detachment of glass particles with Boltzmann charge, saturation charge and fixed 20μC/g charge respectively from a glass substrate. Here Coulomb force and dielectrophoretic force are directed towards the substrate. The trends are similar to those observed in Figures 6-11, 6-12 and 6-13. Figure 6-14 shows that the critical shear velocity decreases with the increase of the particle diameter. The model predictions from the JKR model are higher than those from the DMT model. The predictions from the Maugis-Pollock model are the lowest. Figure 6-14 also shows that the critical shear velocities in an electric field of 5000 kV/m are lower than those in 10000kV/m. Compared to Figure 6-11, Figure 6-14 shows lower critical shear velocities. This implies that for particles with Boltzmann charge distribution, detaching glass particles from a glass substrate is easier than detaching polystyrene particles from a polystyrene substrate. Figure 6-15 shows that the critical shear velocity decreases with the increase of the particle diameter. Compared to Figure 6-14, Figure 6-15 shows higher

shear velocities for large particles. Figure 6-16 shows that for small particles, the critical shear velocity decreases with the increase of the particle diameter; For large particles, the critical shear velocity increases with the increase of the particle diameter due to higher level of charges that large particles obtained for a fixed charge of 20 μC/g. Compared to Figure 6-14, Figure 6-16 shows higher shear velocities for large particles. Compared to Figure 6-15, Figure 6-16 shows higher shear velocities for large particles and slightly lower shear velocities for smaller particles. For much smaller particles, shear velocities in Figures 6-14, 6-15 and 6-16 are almost same.

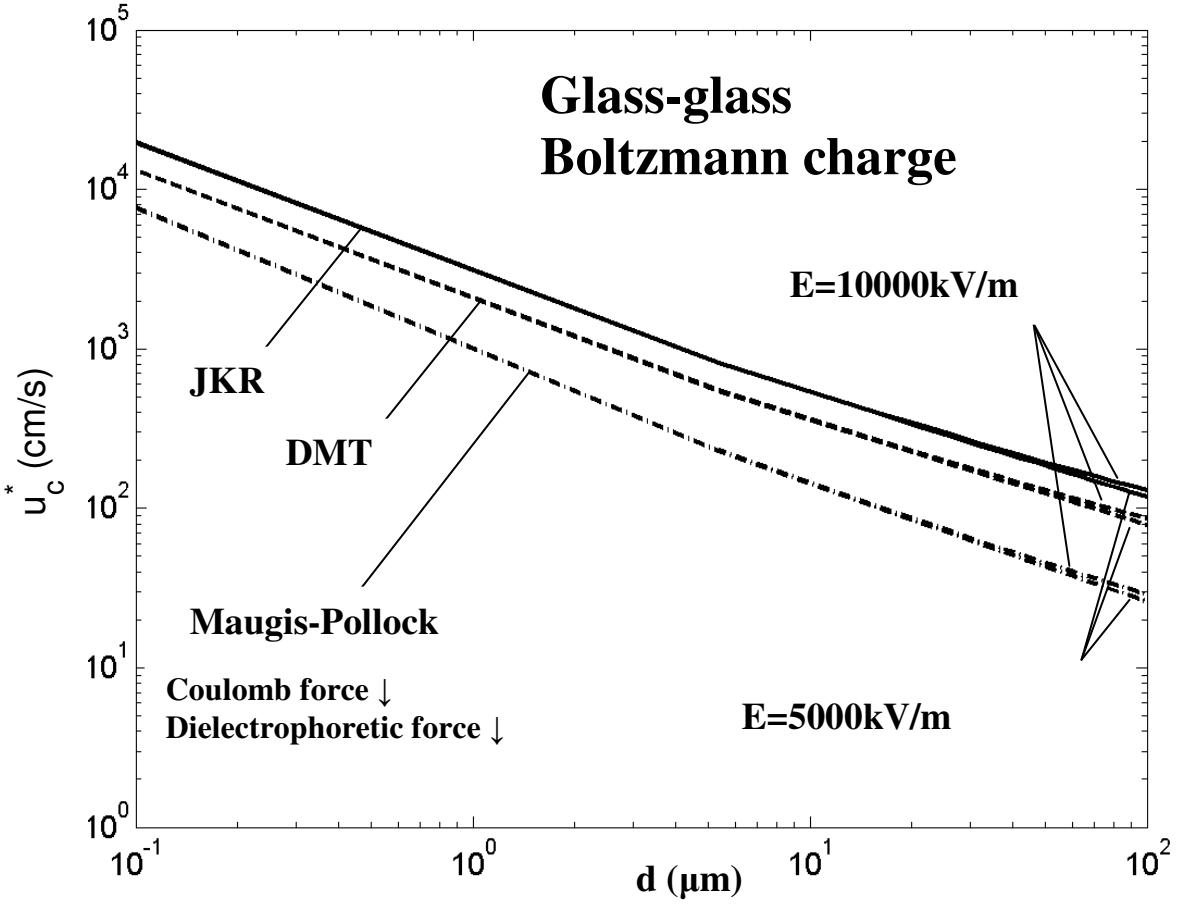

Figure 6-14. Variation of the critical shear velocities with the particle diameter as predicted by different adhesion models for resuspension of glass particles with an average Boltzmann charge distribution from a glass substrate in the presence of capillary effects and different electric fields. Coulomb force and dielectrophoretic force are directed towards the substrate.

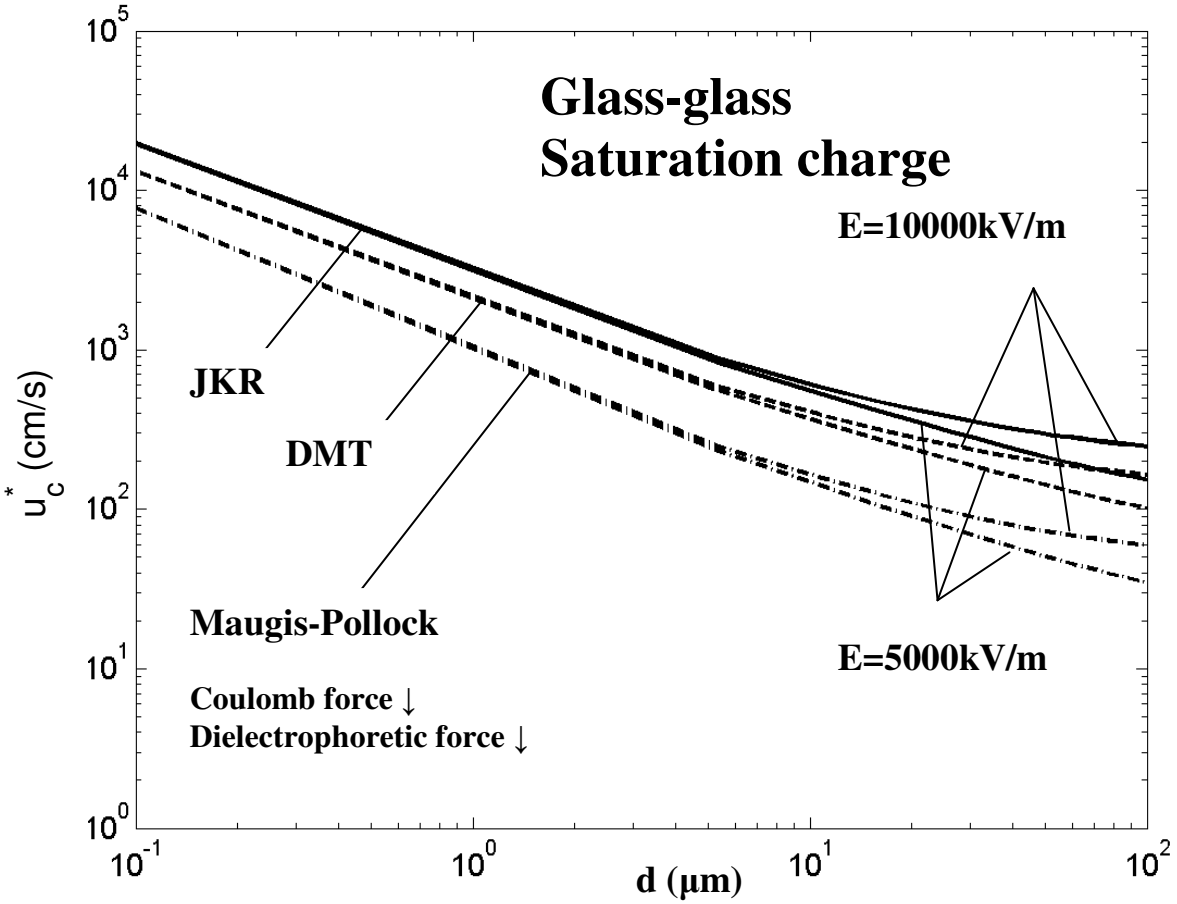

Figure 6-15. Variation of the critical shear velocities with the particle diameter as predicted by different adhesion models for resuspension of glass particles with saturation charge from a glass substrate in the presence of capillary effects and different electric fields. Coulomb force and dielectrophoretic force are directed towards the substrate.

Similar to Figure 6-14, Figures 6-15 and 6-16 also show that the model predictions from the JKR model are higher than those from the DMT model. The predictions from the Maugis-Pollock model are the lowest. Compared to Figure 6-12, Figure 6-15 shows lower critical shear velocities. This implies that for particles with saturation charge distribution, detaching glass particles from a glass substrate is easier than detaching polystyrene particles from a polystyrene substrate. Compared to Figure 6-13, for Maugis-Pollock model, Figure 6-16 shows lower critical shear velocities. While for JKR and DMT models, Figure 6-16 shows lower critical shear velocities for small particles, but

slightly higher critical shear velocities for large particles. Because glass is basically an elastic material, JKR and DMT models may be more suitable. This implies that for small particles with fixed 20μC/g charge distribution, detaching glass particles from a glass substrate is easier than detaching polystyrene particles from a polystyrene substrate, for big particles, detaching glass particles from a glass substrate can be a little difficult than detaching polystyrene particles from a polystyrene substrate, but there is no big difference.

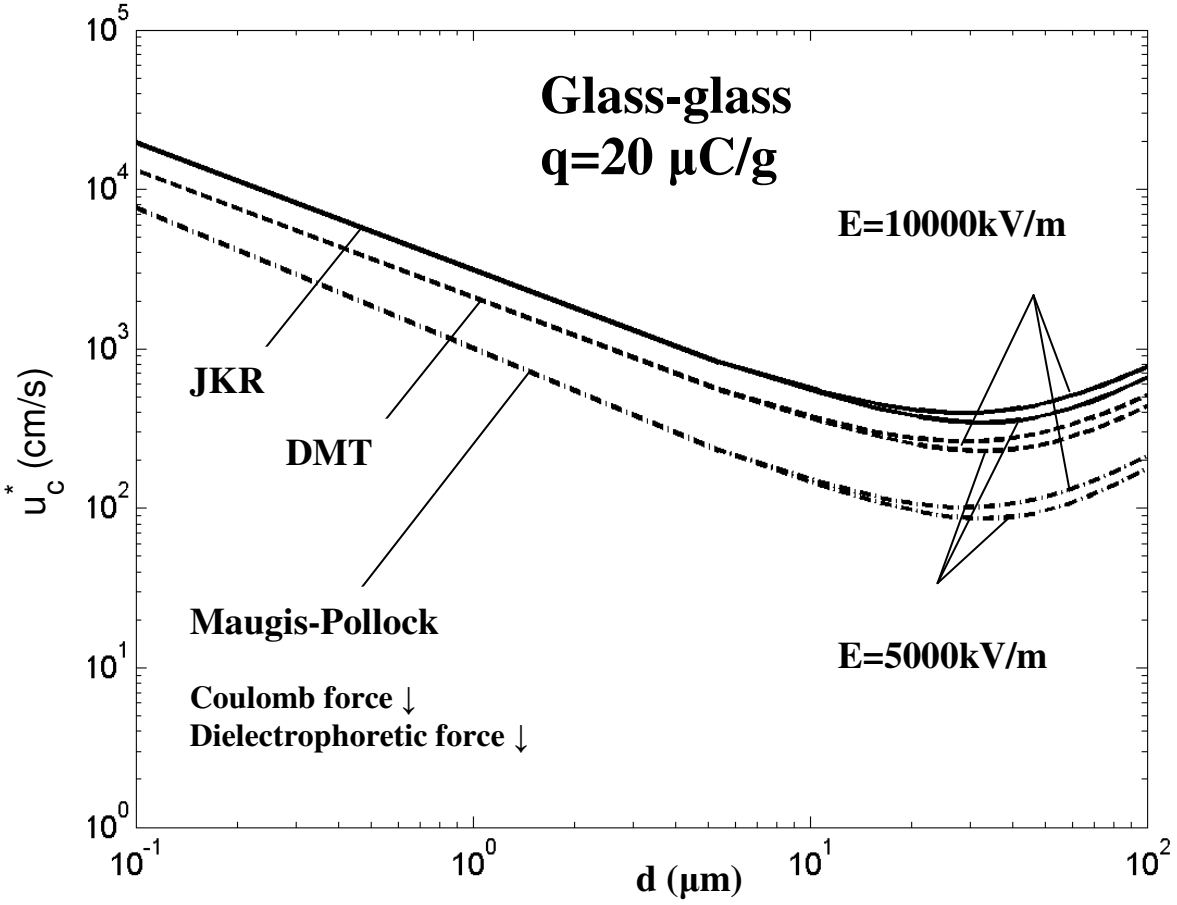

Figure 6-16. Variation of the critical shear velocities with the particle diameter as predicted by different adhesion models for resuspension of glass particles with 20 μC/g charge from a glass substrate in the presence of capillary effects and different electric fields. Coulomb force and dielectrophoretic force are directed towards the substrate.

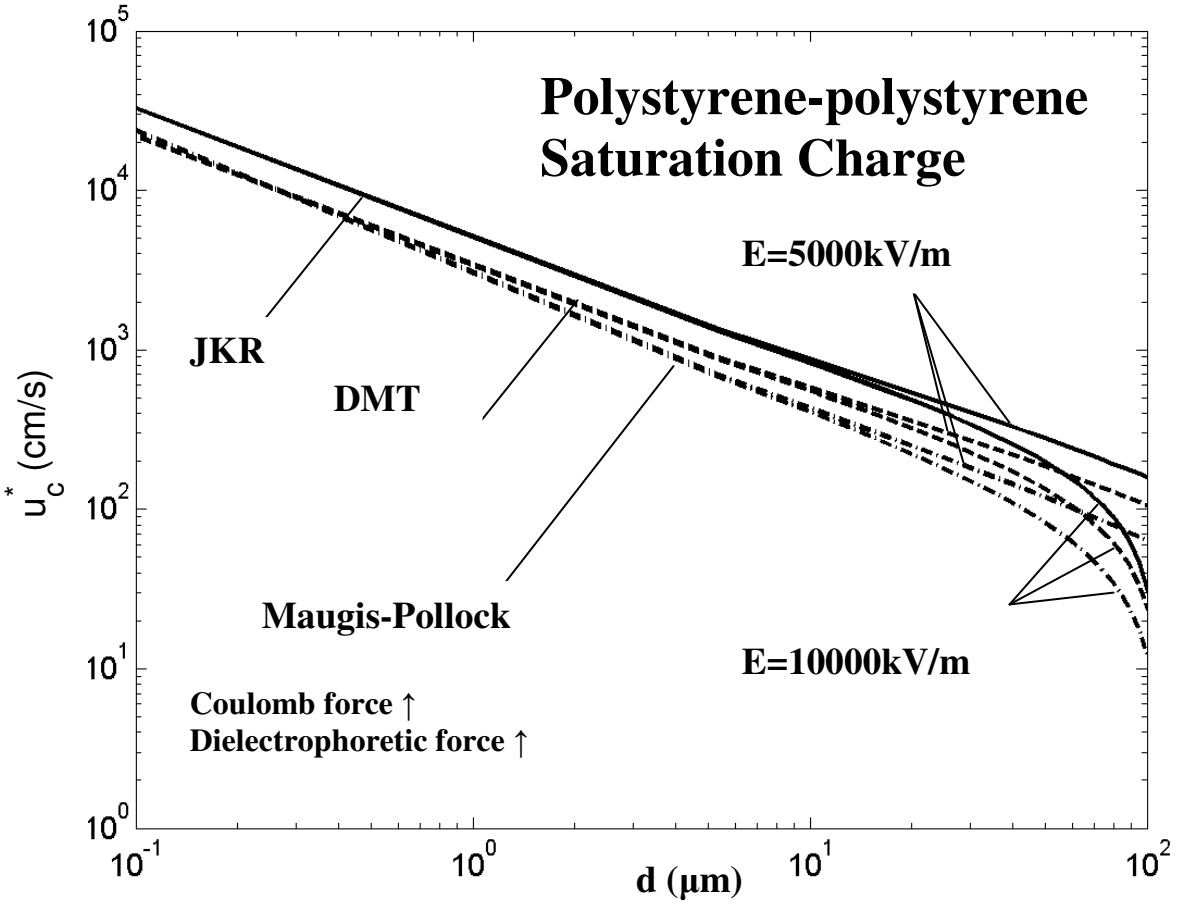

Figure 6-17. Variation of the critical shear velocities with the particle diameter as predicted by different adhesion models for resuspension of polystyrene particles with saturation charge distribution from a polystyrene substrate in the presence of capillary effects and different electric fields. Coulomb force and dielectrophoretic force are directed away from the substrate.

Figures 6-17 and 6-18 show the variations of u_c^* with particle diameter as predicted by different adhesion models in the presence of capillary effects and different electric fields for the rolling detachment of polystyrene particles with saturation charge and fixed 20μC/g charge respectively from a polystyrene substrate. Here Coulomb force and dielectrophoretic force are directed away from the substrate. Figure 6-17 shows that the critical shear velocity decreases with the increase of the particle diameter. The model predictions from the JKR model are slightly higher than those from the DMT model. The

predictions from the Maugis-Pollock model for u_c^* are the lowest for large particles, but slightly higher than those from the DMT model for small particles. Compared to results presented in Figure 6-12, Figure 6-17 shows lower critical shear velocities for large particles, especially in an electric field of 10000 kV/m. This implies that in the presence of capillary force, when directed away from the substrate and under a strong electric field, Coulomb force and dielectrophoretic force significantly decrease the critical shear velocity for large particle rolling removal. Figure 6-17 also shows that the critical shear velocities in an electric field of 5000 kV/m are higher than those in 10000kV/m, but the differences are relatively larger compared to results presented in Figure 6-12, where Coulomb force and dielectrophoretic force are directed towards the substrate. This means that the relative effects of the electrostatic forces increase when Coulomb force and dielectrophoretic force are directed away from the substrate.

Figure 6-18 shows that the critical shear velocity in an electric field of 5000 kV/m decreases with the increase of the particle diameter for small particles, but slightly increase for large particles. While in an electric field of 10000kV/m, the critical shear velocity decreases with the increase of the particle diameter. The model predictions from the JKR model are slightly higher than those from the DMT model. The predictions from the Maugis-Pollock model for u_c^* are the lowest for large particles, but slightly higher than those from the DMT model for small particles. Compared to results presented in Figure 6-13, Figure 6-18 shows lower critical shear velocities for large particles, especially in an electric field of 10000 kV/m. This implies that in the presence of capillary force, when directed away from the substrate especially under a strong electric field, Coulomb force and dielectrophoretic force significantly decrease the critical shear velocity for large particle rolling removal. Figure 6-18 also shows that the critical shear velocities in an electric field of 5000 kV/m are higher than those in 10000kV/m, but the differences are relatively larger compared to results presented in Figure 6-13, where Coulomb force and dielectrophoretic force are directed towards the substrate. This means that the relative effects of the electrostatic forces increase when Coulomb force and dielectrophoretic force are directed away from the substrate.

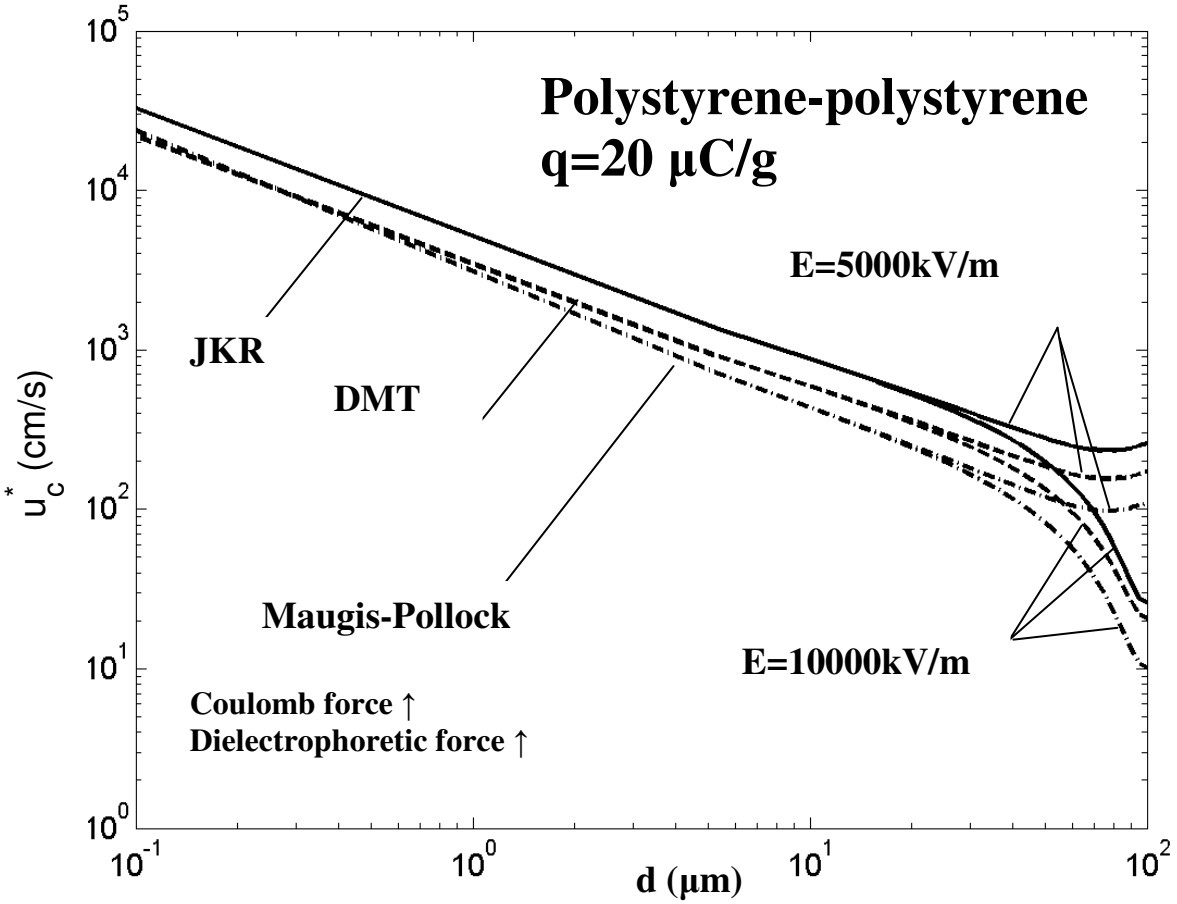

Figure 6-18. Variation of the critical shear velocities with the particle diameter as predicted by different adhesion models for resuspension of polystyrene particles with 20 μC/g charge distribution from a polystyrene substrate in the presence of capillary effects and different electric fields. Coulomb force and dielectrophoretic force are directed away from the substrate.

Figures 6-19 and 6-20 show the variations of u_c^* with particle diameter as predicted by different adhesion models in the presence of capillary effects and different electric fields for the rolling detachment of glass particles with saturation charge and fixed 20μC/g charge respectively from a glass substrate. Here Coulomb force and dielectrophoretic force are directed away from the substrate. Figure 6-19 shows that the critical shear velocity decreases with the increase of the particle diameter. The model predictions from the JKR model are higher than those from the DMT and Maugis-Pollock

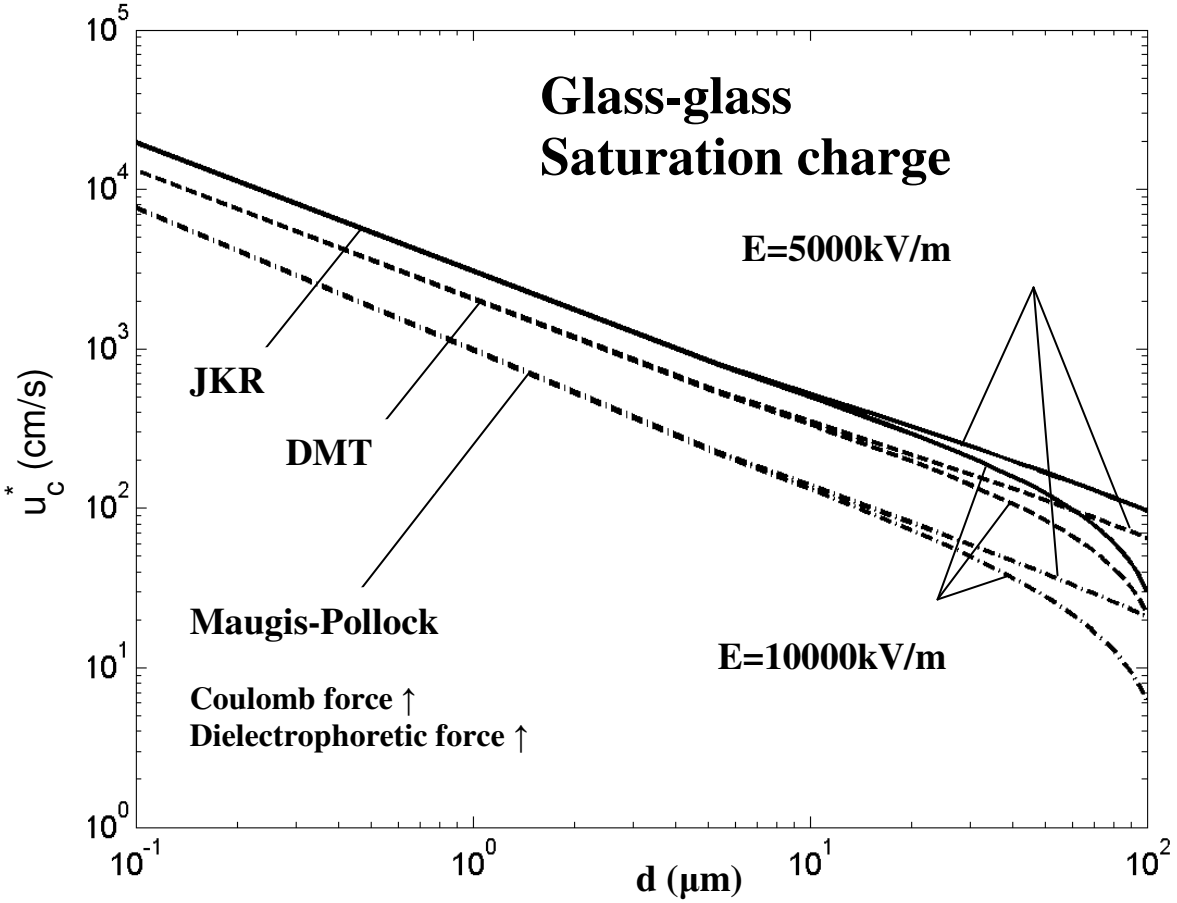

Figure 6-19. Variation of the critical shear velocities with the particle diameter as predicted by different adhesion models for resuspension of glass particles with saturation charge from a glass substrate in the presence of capillary effects and different electric fields. Coulomb force and dielectrophoretic force are directed away from the substrate.

models. The predictions from the Maugis-Pollock model for u_c^* are the lowest. Compared to results presented in Figure 6-15, Figure 6-19 shows lower critical shear velocities for large particles, especially in an electric field of 10000 kV/m. This implies that in the presence of capillary force, when directed away from the substrate and under a strong electric field, Coulomb force and dielectrophoretic force significantly decrease the critical shear velocity for large particle rolling removal. Figure 6-19 also shows that the

critical shear velocities in an electric field of 5000 kV/m are higher than those in 10000kV/m, but the differences are relatively larger compared to results presented in Figure 6-15, where Coulomb force and dielectrophoretic force are directed towards the substrate. This means again that the relative effects of the electrostatic forces increase when Coulomb force and dielectrophoretic force are directed away from the substrate.

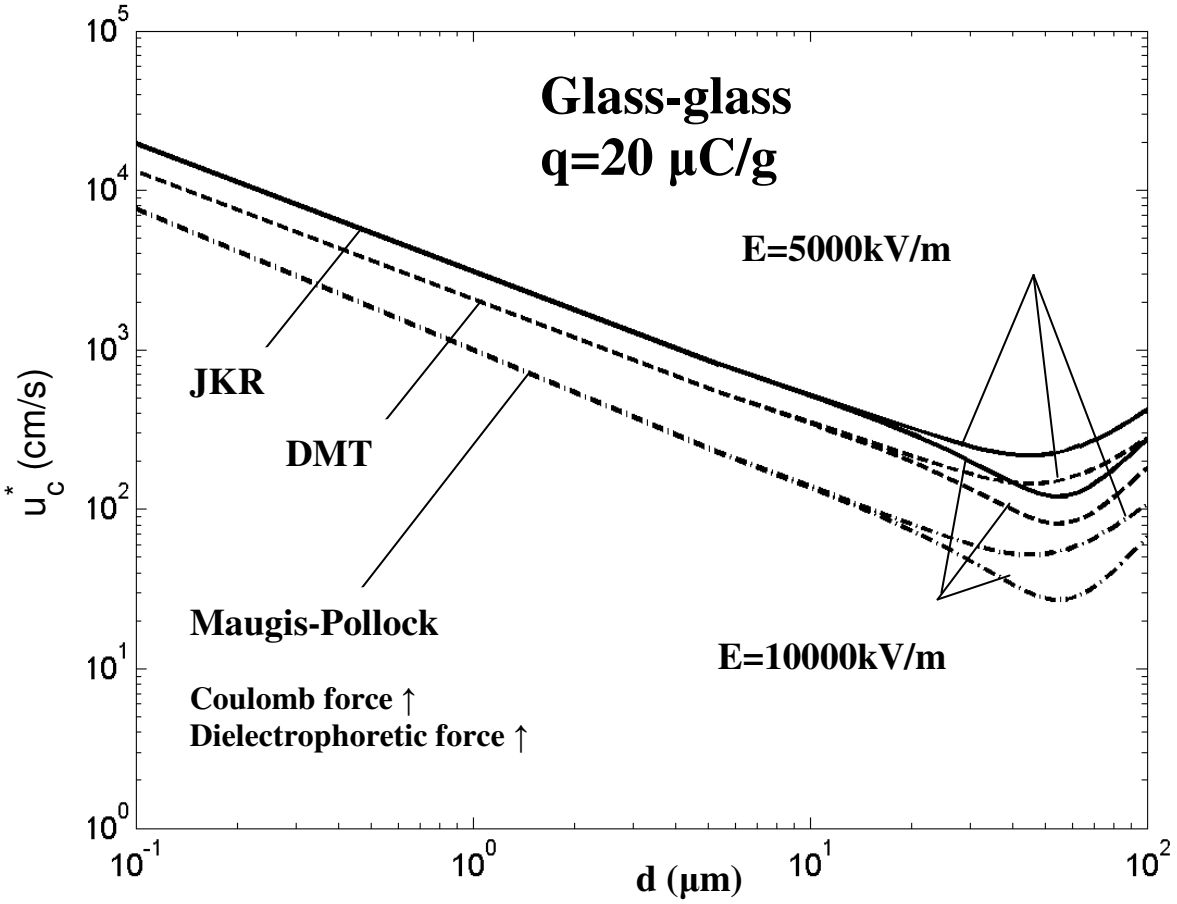

Figure 6-20. Variation of the critical shear velocities with the particle diameter as predicted by different adhesion models for resuspension of glass particles with 20 µC/g charge from a glass substrate in the presence of capillary effects and different electric fields. Coulomb force and dielectrophoretic force are directed away from the substrate.

Figure 6-20 shows that the critical shear velocity decreases with the increase of the particle diameter for small particles, but increase for large particles. The model

predictions from the JKR model are slightly higher than those from the DMT and Maugis-Pollock models. The predictions from the Maugis-Pollock model for u_c^* are the lowest. Compared to results presented in Figure 6-16, Figure 6-20 shows lower critical shear velocities for large particles, especially in an electric field of 10000 kV/m. This implies that in the presence of capillary force, when directed away from the substrate especially under a strong electric field, Coulomb force and dielectrophoretic force significantly decrease the critical shear velocity for large particle rolling removal. Figure 6-20 also shows that the critical shear velocities in an electric field of 5000 kV/m are higher than those in 10000kV/m, but the differences are relatively larger compared to results presented in Figure 6-16, where Coulomb force and dielectrophoretic force are directed towards the substrate. This means again that the relative effects of the electrostatic forces increase when Coulomb force and dielectrophoretic force are directed away from the substrate.

Figure 6-21 shows the variations of u_c^* with particle diameter as predicted by different adhesion models in the presence of capillary effects and different electric fields for the rolling detachment of glass particles with saturation charge from a steel substrate. Here Coulomb force and dielectrophoretic force are directed away from the substrate. Figure 6-21 shows that the critical shear velocity decreases with the increase of the particle diameter. The model predictions from the JKR model are higher than those from the DMT and Maugis-Pollock models. The predictions from the Maugis-Pollock model for u_c^* are the lowest. Compared to results presented in Figure 6-19, Figure 6-21 shows higher critical shear velocities.

Figure 6-21 also shows that the critical shear velocities in an electric field of 5000 kV/m are slightly higher than those in 10000kV/m, but the differences are relatively smaller compared to the results presented in Figure 6-19. This means that in the presence of capillary force, when Coulomb force and dielectrophoretic force are directed away from the substrate and under an electric field, the relative effects of the electrostatic forces are material dependent. The effect for rolling detachment of glass particles with

saturation charge from a steel substrate is smaller than that for rolling detachment of glass particles with saturation charge from a glass substrate.

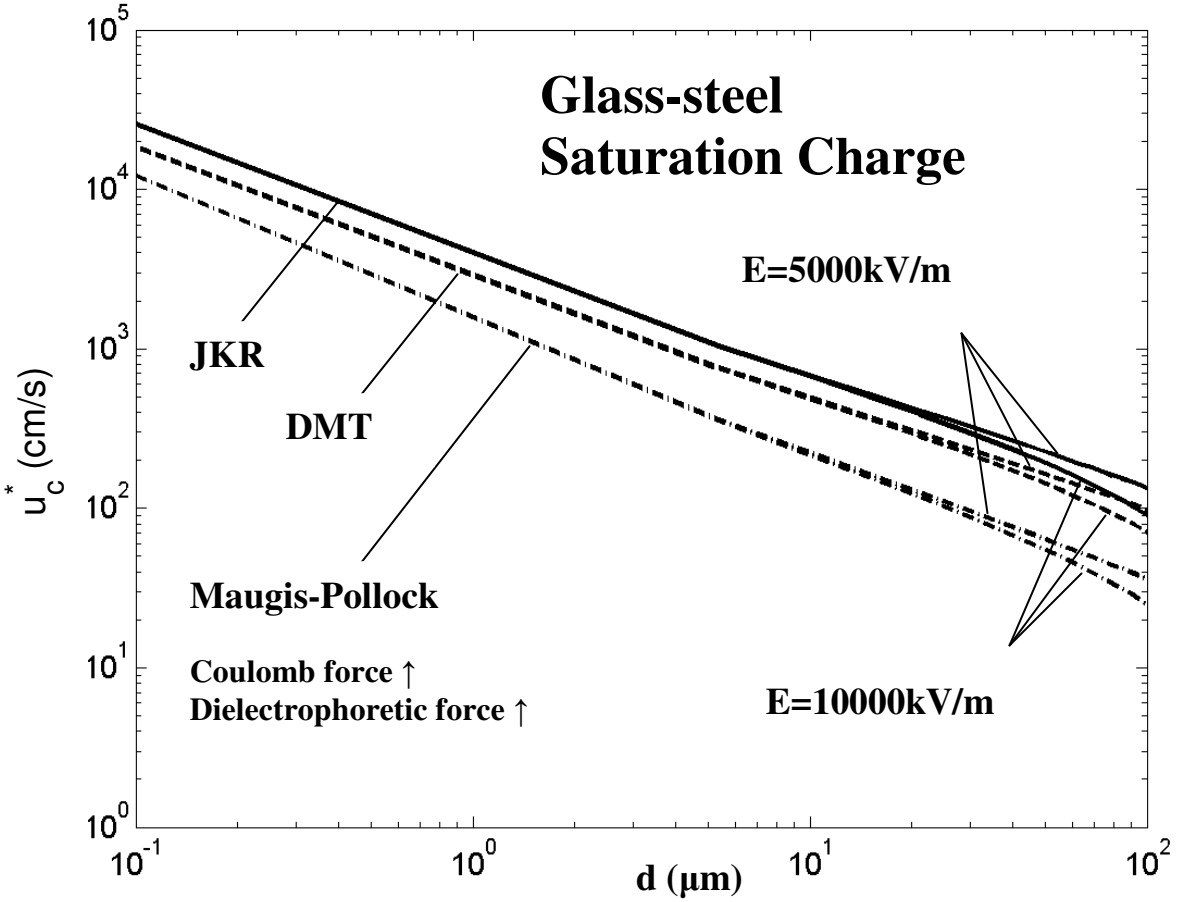

Figure 6-21. Variation of the critical shear velocities with the particle diameter as predicted by different adhesion models for resuspension of glass particles with saturation charge from a steel substrate in the presence of capillary effects and different electric fields. Coulomb force and dielectrophoretic force are directed away from the substrate.

Figure 6-22 shows the variations of critical shear velocities with particle diameter as predicted by different adhesion models for the rolling detachment of polystyrene particles from a polystyrene substrate with or without capillary effects in the condition without electrostatic forces. It can be seen from Figure 6-22 that the critical shear velocity decreases with the increase of the particle diameter. For both case with or without capillary effects, the model predictions from the JKR model are higher than those from

the DMT and Maugis-Pollock models; For the case without capillary effects, the predictions from the Maugis-Pollock model for u_c^* are the lowest; While for the case with capillary effects, the predictions from the Maugis-Pollock model for u_c^* are the lowest for large particles, but slightly higher than those from the DMT model for small particles. It can be also seen from Figure 6-22 that capillary effects significantly increase the critical shear velocity. Comparing the three lines without the capillary effects in Figure 6-22 with those in Figures 6-8, 6-9 and 6-10 show that the electrostatic forces only have major effects on the increases of the critical shear velocity for large particle detachment.

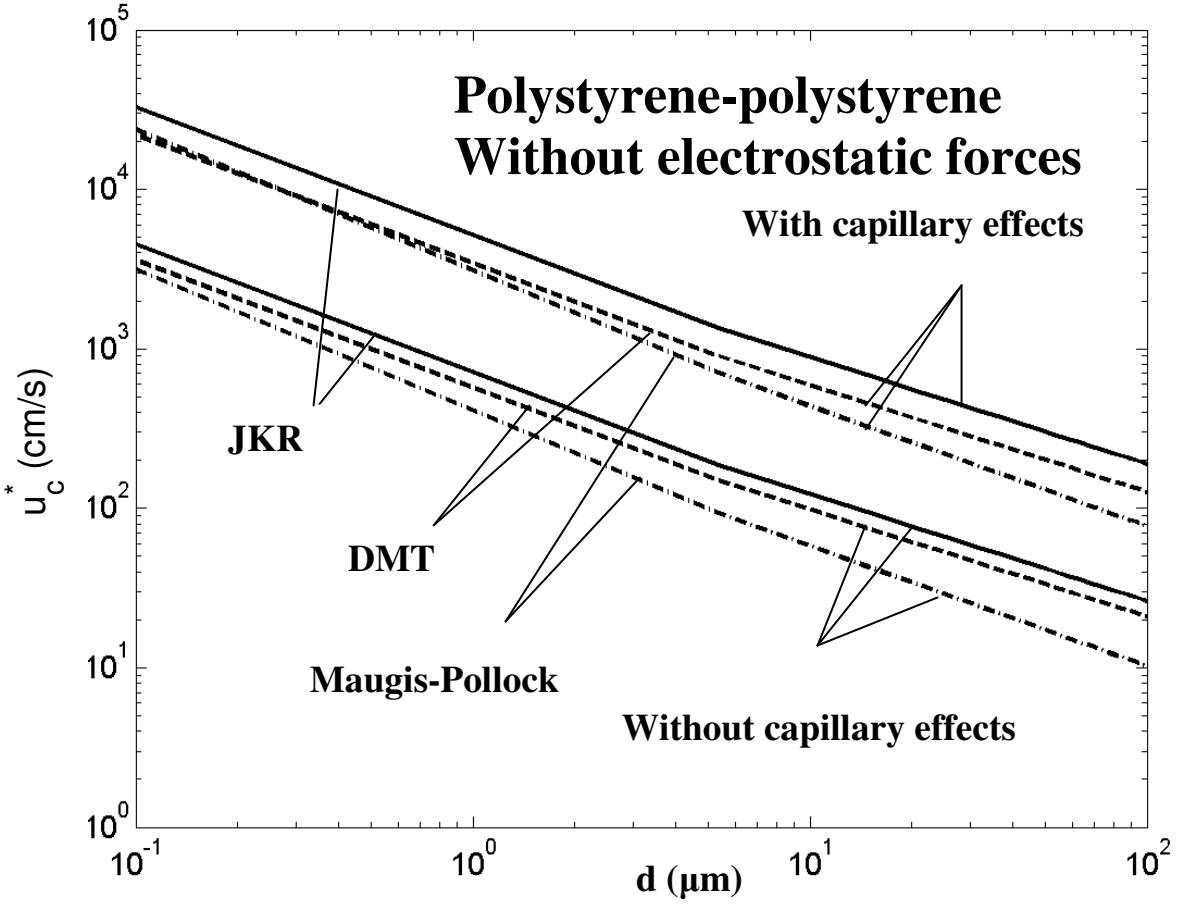

Figure 6-22. Variation of the critical shear velocities with the particle diameter as predicted by different adhesion models for resuspension of polystyrene particles from a polystyrene substrate without electrostatic effects.

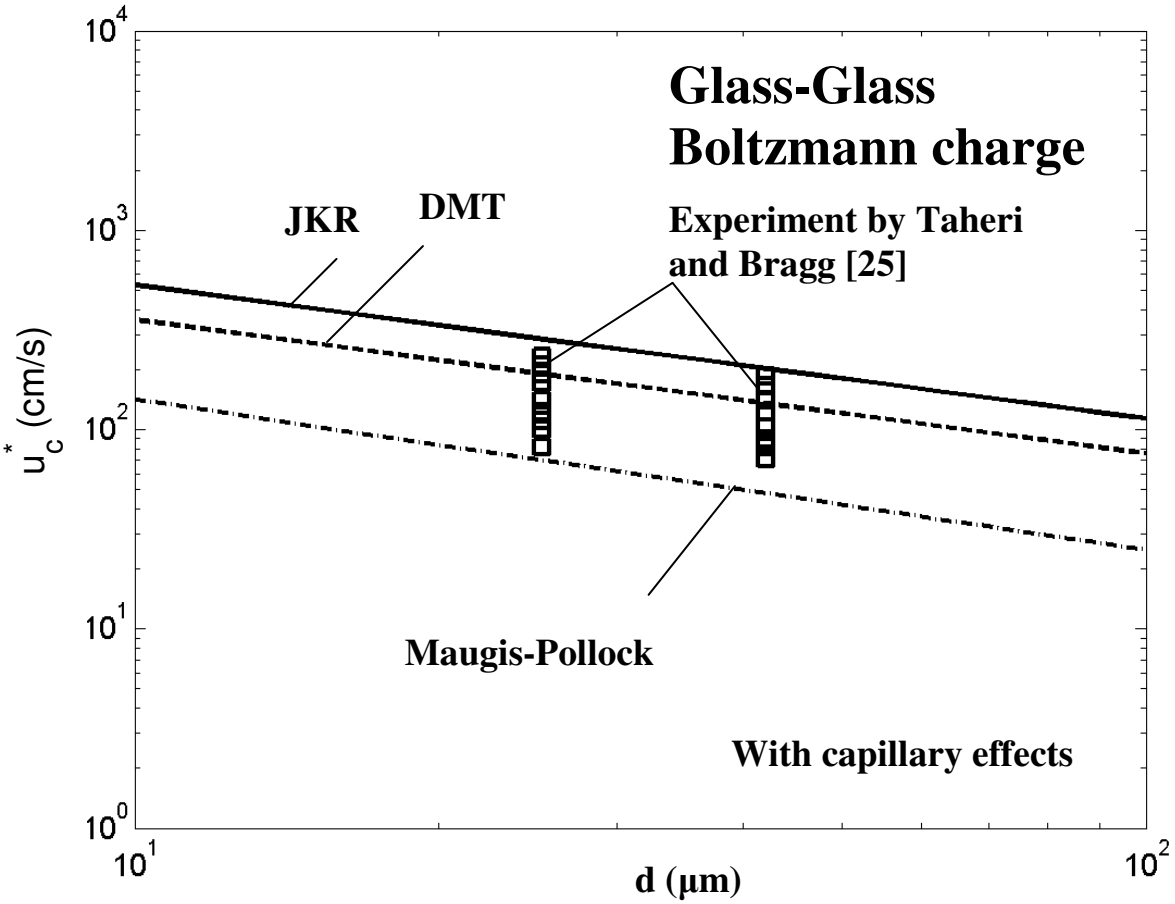

Figure 6-23. Comparison of the critical shear velocities as predicted by different adhesion models with the experimental data of Taheri and Bragg [25] (□) for resuspension of glass particles with an average Boltzmann charge distribution from a glass substrate in the presence of capillary effects.

6.8.3 Comparison with Experimental Data

This section compares the model predictions with the experimental data of Taheri and Bragg [25] and Hays [7]. The experiment of Taheri and Bragg was concerned with the resuspension of glass particles from a smooth glass surface under normal room temperature and humidity for a range of air velocities between 2 and 130 m/s. Their result agrees well with the prediction by Soltani and Ahmadi [18] for particle resuspension in moist air, which implies the existence of the capillary force. The experiments of Hays [7] studied the electrical detachment of charged 13 μm toner particles under an electric field

from a nickel carrier bead with an average charge of $3\times10^{-14}C$, where the Coulomb force and dielectrophoretic force are directed away from the substrate, therefore, for toner particles carry different charges, there are corresponding critical electric detachment fields under which the particle electrostatic forces exactly balance the adhesion forces and thus particles can get detached.

Figure 6-23 shows the comparison of the critical shear velocities as predicted by different adhesion models with the experimental data of Taheri and Bragg [25] (□) for resuspension of glass particles with an average Boltzmann charge distribution from a glass substrate in the presence of capillary effects. It can be seen from Figure 6-23 that the critical shear velocity decreases with the increase of the particle diameter, and the model predictions for the JKR theory are slightly higher than those for the DMT theory, and the predictions from the Maugis-Pollock model lead to the lowest critical shear velocities. It also can be seen that the predicted critical shear velocities from the JKR and DMT models with capillary force agree very well with the experimental data of Taheri and Bragg [25] under humid air condition, while the predicted critical shear velocity from the Maugis-Pollock model with capillary force is somewhat slightly lower than the experimental data. The reason is the Maugis-Pollock model accounts for the plastic deformation at the particle-surface contact, but glass-glass contact is maybe better modeled with an elastic deformation model such as the JKR or DMT theory.

Figure 6-24 shows the comparison of the critical electric detachment fields for 13 μm particles by JKR model with the experimental data of Hays [7] for toner (PSL) particles on a nickel carrier bead without flow and capillary effects. It can be seen from Figure 6-24 that the critical electric detachment fields increases with the increase of the charges carried by the particles. The reason is that Coulomb force and dielectrophoretic force are related to amount of charges and electric field, while imagine force is related to the square of amount of charges. When the charges increase, imagine force toward the substrate increases much fast than Coulomb force and dielectrophoretic force do, therefore, an increased electric field is need to increase Coulomb force and dielectrophoretic force further to balance the imagine force. Though polarization force is

related to the square of the electric field, but polarization force is too small to play an important role. Figure 6-24 shows that the predicted electric detachment fields from the JKR model are higher than the experimental data. The reason is that the toner particles are not smooth particles, the coarse surface roughness of the toner particles will decrease the particle adhesion force and therefore decrease the electric detachment fields.

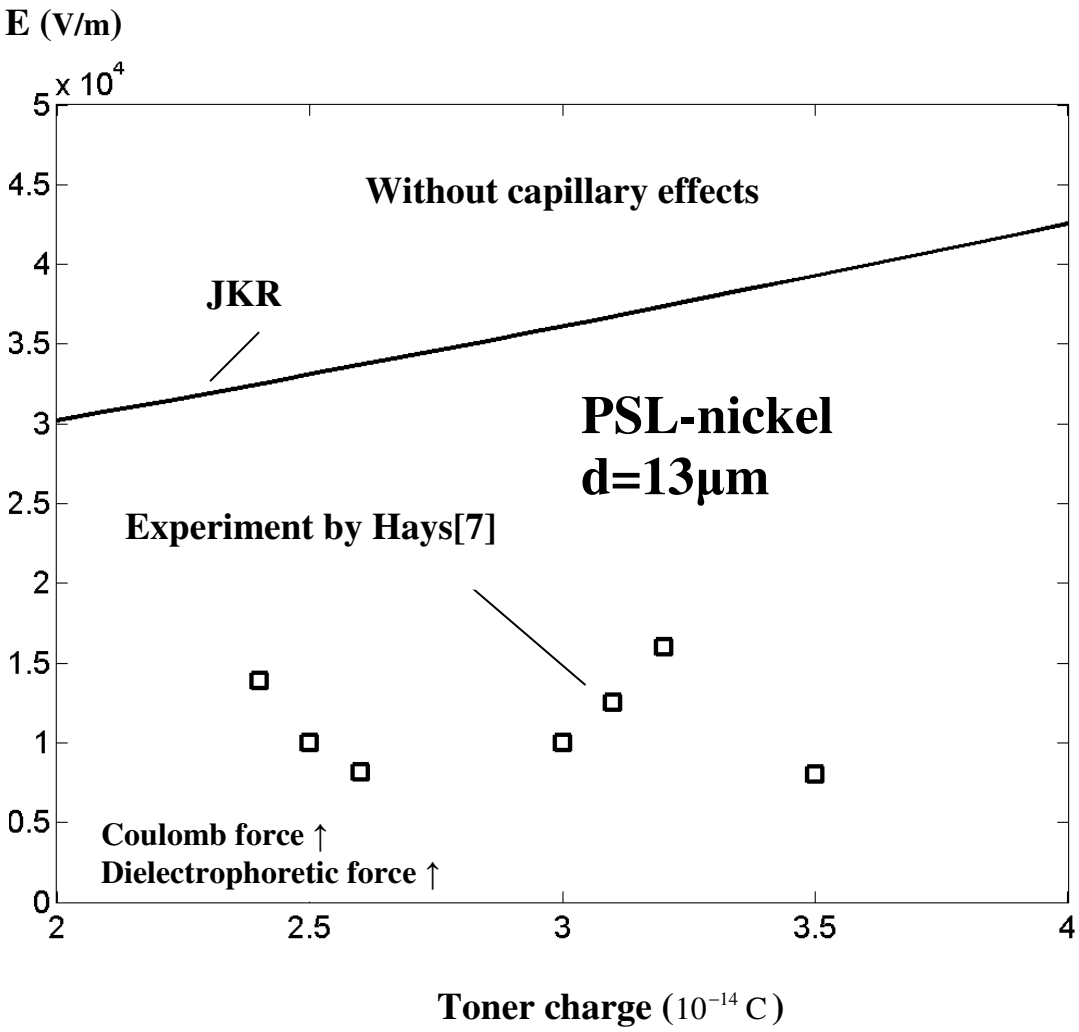

Figure 6-24. Comparison of the electric detachment fields for particles with the experimental data of Hays [7] for toner (PSL) particles on a nickel carrier bead without flow and capillary effects. Coulomb force and dielectrophoretic force are directed away from the substrate.

6.9 CONCLUSIONS

Particle resuspension including the effects of capillary and electrostatic forces based on the maximum adhesion resistance in turbulent flows is studied. The effective thermodynamic work of adhesion including the effects of electrostatic and capillary forces was used in the analysis. The JKR, DMT and Maugis-Pollock models are extended to include the effect of electrostatic and capillary forces. The critical shear velocities for removal of particles of different sizes are evaluated. The model predictions are compared with the available experimental data. Based on the presented results the following conclusions are drawn:

- The capillary forces significantly increases the critical shear velocity for particle detachment; while the electrostatic forces only have major effects on the increases of the critical shear velocity for large particle detachment.
- The critical shear velocity predicted by the JKR adhesion model is somewhat higher than that predicted by the DMT and the Maugis-Pollock model.
- In general, the Maugis-Pollock model leads to the lowest critical shear velocity. While for the rolling detachment of polystyrene particles from a polystyrene substrate in the presence of capillary effects, the predictions from the Maugis-Pollock model for u* are the lowest for large particles, but slightly higher than those from the DMT model for small particles.
- For particles in an electric field of 5000 kV/m or 10000kV/m with Boltzmann charge or saturation charge distribution, the critical shear velocity decreases with the increase of the particle diameter; While for particles with fixed 20μC/g charge distribution, the critical shear velocity decreases with the increase of the particle diameter for small particles, but increases with the increase of the particle diameter for large particles.
- when Coulomb force and dielectrophoretic force are directed towards the substrate, the relative effects of the electrostatic forces decrease in the presence of capillary effects.
- When Coulomb force and dielectrophoretic force are directed towards the substrate, shear velocities for large particles with fixed 20μC/g charges are higher

than that with Boltzmann and saturation charges; While shear velocities for smaller particles with fixed 20μC/g charges are higher than that with Boltzmann charge but lower than that with saturation charge; For very small particles, shear velocities for particles with Boltzmann, saturation and fixed 20μC/g charges are almost same.

- In the presence of capillary force, when Coulomb force and dielectrophoretic force are directed away from the substrate, the relative effects of the electrostatic forces increase. These relative effects are material dependent. Under a strong electric field, Coulomb force and dielectrophoretic force significantly decrease the critical shear velocity for large particle rolling removal.

6.10 Acknowledgements

The financial support of the Environmental Protection Agency (EPA) and the NYSTAR Center of Excellence at Syracuse University is gratefully acknowledged.

6.11 Nomenclature

A	Hamaker constant
a	contact radius, m
a_e	contact radius with capillary force, m
$a\|_M$	contact radius reached at the maximum adhesion resistance moment, m
a_o	contact radius at zero applied load, m
a^*	nondimensional contact radius
$a^*\|_M$	nondimensional contact radius at the maximum adhesion resistance moment
C_c	Cunningham factor
d	particle diameter, m
d_c	particle diameter in cgs units, cm
d^+	nondimensional particle diameter
E	electric field strength in mks units, V/m
E_c	electric field strength in cgs units, V/cm
E_i	Young modulus of material i, N/m^2
e_c	electronic unit charge in cgs units, stC.
e	electronic unit charge in mks units, C.

F_c capillary force, N

F_L lift force, N

F_{po} pull-off force, N

F_{Po}^{DMT} pull-off force evaluated by DMT model, N

F_{po}^{JKR} pull-off force evaluated by JKR model, N

F_t drag force, N

H hardness of material, Pa

K composite Young's modulus, N/m^2

k Boltzmann constant in cgs units, ergs/K.

Kn Knudsen number

M_{Max} maximum adhesion resistance moment due to the applied normal load, N·m

M_t hydrodynamic moment, N·m

M_{Max}^{DMT} maximum resistance moment evaluated by DMT model, N·m

M^{*DMT} nondimensional resistance moment evaluated by DMT model, N·m

M_{Max}^{*DMT} nondimensional maximum resistance moment evaluated by DMT model, N·m

M_{Max}^{JKR} maximum resistance moment evaluated by JKR model, N·m

M^{*JKR} nondimensional resistance moment evaluated by JKR model, N·m

M_{Max}^{*JKR} nondimensional maximum resistance moment evaluated by JKR model, N·m

M^{MP} resistance moment evaluated by Maugis-Pollock model, N·m

M_{Max}^{MP} maximum resistance moment evaluated by Maugis-Pollock model, N·m

n number of units of charge

P applied normal load, N

P^* nondimensional applied normal load

$P\big|_M$ applied normal load at the maximum adhesion resistance moment, N

$P^*\big|_M$ nondimensional applied normal load at the maximum adhesion resistance moment

$(P\cdot a)_{Max}$ maximum adhesion resistance moment, N·m

t	time, s.
T	Temperature, K.
u_c^*	minimum shear velocity needed for detaching a particle from the substrate, m/s
u_M^+	nondimensional maximum gas velocity at the mass center of the particle
u_M	maximum gas velocity at the mass center of the particle
u^*	shear velocity, m/s
W_A	thermodynamic work of adhesion, J/m^2
W_A^e	effective thermodynamic work of adhesion, J/m^2
W_A^{eJKR}	effective thermodynamic work of adhesion for JKR model, J/m^2
W_A^{eDMT}	effective thermodynamic work of adhesion for DMT model, J/m^2
W_A^{eMP}	effective thermodynamic work of adhesion for Maugis-Pollock model, J/m^2
Y	yield stress of the material, Pa
y^+	nondimensional distance from the wall
y	distance from the wall, m
z_o	minimum separation distance, m

Greek letters

α	half particle-liquid contact angle, rad
α_o	overlap between the particle and surface, m
ε	dielectric constant of the particle, dimensionaless.
ε_0	permittivity, amp •s /V•m
θ	wetting angle, rad
λ	mean free path of air, m
ν	kinematic viscosity of air, m^2/s
ν_i	Poisson's ratio of material i
ρ	density of air, kg/m^3
ρ_p	density of particle and substrate material, kg/m^3
σ	surface tension of water, N/m

6.12 REFERENCES

1. D. K. Donald. J. Appl. Phys. **40**. 3013 (1969).
2. D. K. Donald. in: Recent Advances in Adhesion. L. H. Lee (Ed.). p.129. Gordon and Breach. New York (1973).
3. D. K. Donald and P. K. Watson. Photogr. Sci. Eng. **14**. 36 (1970).
4. M. H. Lee and J. Ayala. J. lmaging, Technol. **11**. 279 (1985).
5. D. K. Donald and P. K. Watson. IEEE Trans. Electron Dev. **ED-19**. 458 (1972).
6. N. S Goel and P. R. Spencer. in: Adhesion Science and Technology. L. H. Lee (Ed.). Part B. p. 763. Plenum Press. New York (1975).
7. D. A. Hays. Photogr: Sci. Eng. **22**. 232-235 (1978).
8. D. A. Hays. Electrostatics Inst. Phys. Conf. Ser. No. **66**. p. 237. The Institute of Physics. I.ondon (1983).
9. M. H. Lee and A. B. Jaffe. in: Particles on Surfaces **I**: Detection, Adhesion, and Removal. K. L. Mittal (Ed.). pp. 169-177. Plenum Press. New York (1988)
10. H. A. Mizes. J. Adhesion Sci. Technol. **8**. 937-953 (1994).
11. M. Soltani and G. Ahmadi, J. Adhesion Sci. Technol. Vol. **13**, No. 3. pp325-355 (1999)
12. J. Q. Feng and D. A. Hays, IEEE Transactions on Industry Applications, Vol. 34, Issue 1, pp. 84 – 91 (1998)
13. N. Masashi and T. Manabu, Japan Hardcopy, Vol. 2000, pp.137-140 (2000)
14. D. A. Hays and J. C. Sheflin, J. Electrostatics, Vol. 63, Issues 6-10, pp. 687-692, (2005).
15. W. C. Hinds, Aerosol Technology: *Properties, Behavior, and Measurement of Airborne Particles*, John Wiley and Sons, New York (1982).
16. M. Soltani and G. Ahmadi, J. Adhesion Sci. Technol., **8**, 763-785 (1994).
17. M. Soltani and G. Ahmadi, J. Adhesion, **51**, 105-123 (1995).
18. M. Soltani and G. Ahmadi, Physics Fluid A, **7**, 647-657 (1995).
19. M. Soltani and G. Ahmadi, J. Adhesion Sci. Technol. **13**, 325-355 (1999).
20. A.H. Ibrahim, P.F. Dunn, and R.M. Brach, J. Aerosol Sci. **34**, 765-782 (2003).
21. F. Podczeck, J. M. Newton, and M. B. James, J. Colloid Interface Sci. **187**, 484–491

(1997).

22. A.A. Busnaina and T. Elsawy, In: *Particle Adhesion: Applications and Advances,* D.J. Quesnel, D.S. Rimai and L.H. Sharpe (Eds.), Taylor and Francis, New York, pp. 391-409, (2001).
23. J. Tang and A.A. Busnaina, In: *Particle Adhesion: Applications and Advances,* D.J. Quesnel, D.S. Rimai and L.H. Sharpe (Eds.), Taylor and Francis, New York, pp. 411-419, (2001).
24. D. Zimon, *Adhesion of Dust and Powder*, Consultants Bureau, New York (1982).
25. M. Taheri and G.M. Bragg, Aerosol Sci. Technol., **15**, 15-20 (1992).
26. A. H. Ibrahim , P. F. Dunn, and R. M. Brach, J. Aerosol Sci., **35**, 805-821 (2004).
27. M. Gotzinger and W. Peukert, Powder Technol., **130**, 102-109 (2003).
28. M. Gotzinger and W. Peukert, Powder Technol., **135-136**, 82-91 (2003).
29. G. Ahmadi, S. Guo and X. Zhang, Particulate Sci. Technol., **25**: 1-18, (2007).
30. W. L. Heumann, Industrial Air Pollution Control Systems, McGraw-Hill Professional, New York (1997)

The content of this chapter is submitted to J. Adhesion Sci. Technol.

CHAPTER 7. PARTICLE RESUSPENSION AND TRANSPORT DUE TO HUMAN WALKING IN INDOOR ENVIRONMENT

7.1 INTRODUCTION

Particle resuspension from the flooring due to human walking is believed to be a source of particulate matter (PM) concentration in the indoor environment. PM resuspension from the floor generates the so-called "personal cloud" and could significantly affect the personal exposure of the occupants to the particles. Robinson et al. (1991) reported that people spend around 87% of their time indoors. EPA's Particle Total Exposure Assessment Methodology (PTEAM) report pointed out that about 14% of the $PM_{2.5}$ and 26% of the PM_{10} are from unidentified sources. By applying receptor modeling to the data collected for the PTEAM study, Yakovleva et al. (1999) found that 30% of personal PM_{10} exposure is due to resuspended particles. Munir et al. (1995) and Rullo et al. (2002) reported that daycare centers could be the sources of children's exposure to mites, cockroaches, and dog and cat allergens. Long et al. (2001) reported that indoor activities could result in the increase of PM concentration up to several orders of magnitude higher than the background levels. Thatcher et al. (1995), Long et al. (2000) and Ferro et al. (2004) showed that the indoor activities, including walking, floor vacuum cleaning and sitting on upholstered furniture, leads to elevated PM concentrations. Roberts et al. (2004) hypothesized that deep dust remaining in a carpet is a major source of floor particle emission.

Particle adhesion and removal were reviewed by Krupp (1967), Visser (1972), Tabor (1977), Bowling (1985) and Berkeley (1980). Johnson, Kendall and Roberts (1971) developed the JKR adhesion model to include the effects of the surface energy and surface deformation on particle adhesion and detachment. Derjaguin, Muller and Toporov (1975) developed a particle adhesion theory, which now is referred to as the DMT model.

Particle resuspension has been studied by a number of researchers. More recent models on particle resuspension were reported by Soltani and Ahmadi (1994,1995,1995) and Ibrahim et al. (2003). Podczeck et al. (1997) discussed the influence of relative

humidity on adhesion. Recently, Ahmadi, Guo and Zhang (2007) studied particle adhesion and detachment in turbulent flows including the effects of capillary forces using the JKR adhesion theory and the rolling and sliding detachment models. Ziskind et al. (1997) described a model for rolling detachment of a sphere from a surface. Accordingly, the detachment occurs when the sum of hydrodynamic moments exceeds the maximum adhesion resistance moment evaluated for the JKR and the DMT models. Zhang and Ahmadi (2007) extended this approach to include the effect of capillary force and plastic surface deformation. Madler and Koch (1997, 1999) studied particle resuspension caused by an impacting disk. They used a one-dimensional, compressible, adiabatic flow model for evaluating the radial flow velocity. Their model, however, underestimated the experimental data for high-energy conditions. Recently, Khalifa and Elhadidi (2007) studied particle resuspension due to a uniformly falling disk. They also computed particle trajectories inside the gap between the falling object and the floor and found that particles, levitated from floor locations close to the object center, are eventually driven downward by the descending disk, and are less likely to be resuspended. They suggested that only particles near the outer radius of the disk are likely to be resuspended in the environment.

Gait cycles and the associated foot movement were studied by a number of researchers in the past. Cham and Redfern (2002) reported that after the heel contacts the floor, the foot rotates rapidly to reach the flat position at an angular velocity of 223.8 degrees per second. Henty et al. (1999) found that after the heel contacts the floor, the angular velocity decreases, and the maximum foot angular velocity for the stepping down process is around one half to two thirds of that for the stepping up process. Pachi and Ji (2005) studied the stepping frequency and the speed of people walking. Accordingly, typical people walk with an average frequency of 2.0Hz and a velocity of 1.4 meters per second, with a step-length of 0.75 meter for men and 0.67 meter for women.

In this work, resuspension, deposition and the spreading of particles from floors due to human walking are studied. A model for particle resuspension, deposition and transport is developed. The foot stepping process, down and up, is treated as the motions

of two equivalent circular disks moving toward or away from the floor. The airflow generated from this squeezing film is assumed to be laminar, and the corresponding gas velocity was evaluated. The effects of grooves on the shoe bottom are accounted for in the analysis. The JKR adhesion theory and the hydrodynamic drag and lift forces are included in the rolling detachment model that was used in the analysis. The areas under the shoe for which the particles of different sizes are detached in one gait cycle are evaluated. Particle re-deposition, turbulent dispersion and Brownian diffusion effects are included in the model. PM concentrations in a room due to resuspension of particles of different sizes from the floor for a number of gait cycles are evaluated. Particle resuspension was also investigated experimentally while people walk in a full size chamber in a controlled lab. The particle concentrations for certain size range are measured. The model predictions for the concentration in the room and resuspension rate are compared with the experimental data and good agreements are found.

7.2 FOOT STEP DOWN AND UP MODEL

In this section, a simple model for the foot stepping down and up motion is described and the corresponding near floor airflow velocity is estimated. Figure 7-1 shows the schematic of a foot (shoe) movement near a surface. The toe and the heel part of the foot (shoe) are modeled as two circular disks with radius R connected with a bridge. There are grooves at the toe and the heel of the shoe. The distance between the bottom of the bridge and the floor is much larger than the depth of these grooves, so the gas velocity generated by the bridge is much smaller than those generated by the toe and the heel of the shoe, and therefore its effect on particle resuspension is neglected.

Figure 7-2 shows the schematic of a circular disk with radius R moving toward a stationary plate with velocity V_f. Assuming axisymmetric flows with $V_r = V_r(r,z)$, $V_z = V_z(z)$, $p = p(r)$, the continuity equation is given as

$$\frac{1}{r}\frac{\partial}{\partial r}(rV_r) + \frac{dV_z}{dz} = 0. \qquad (7\text{-}1)$$

The momentum equation in the r direction under the lubrication approximation is given as

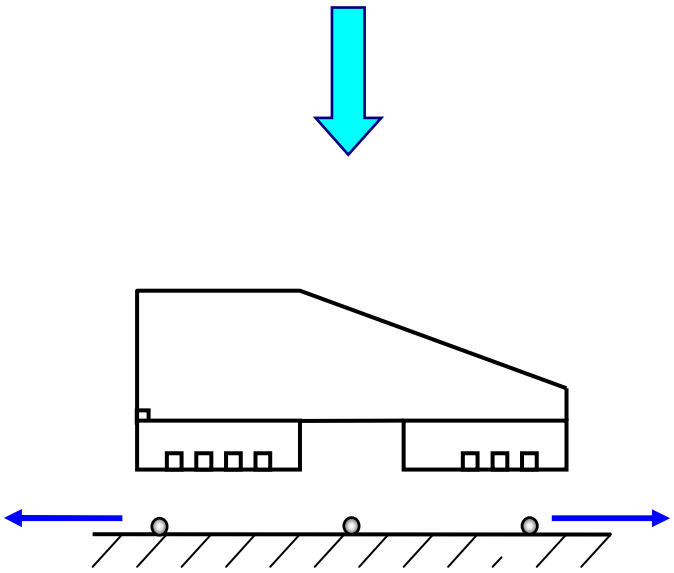

(a) Step down

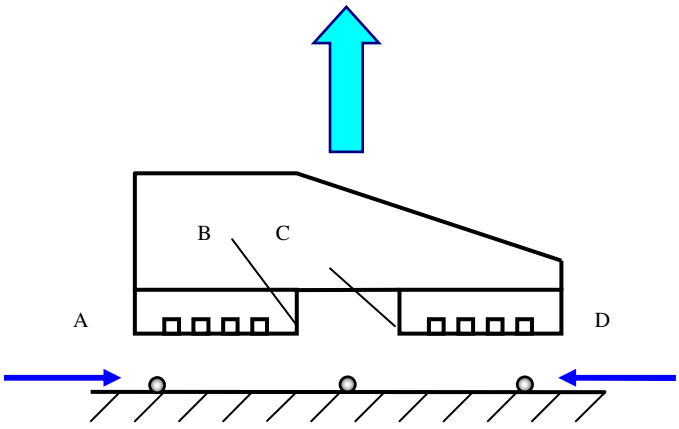

(b) Step up

Figure 7-1. Foot step down and up model

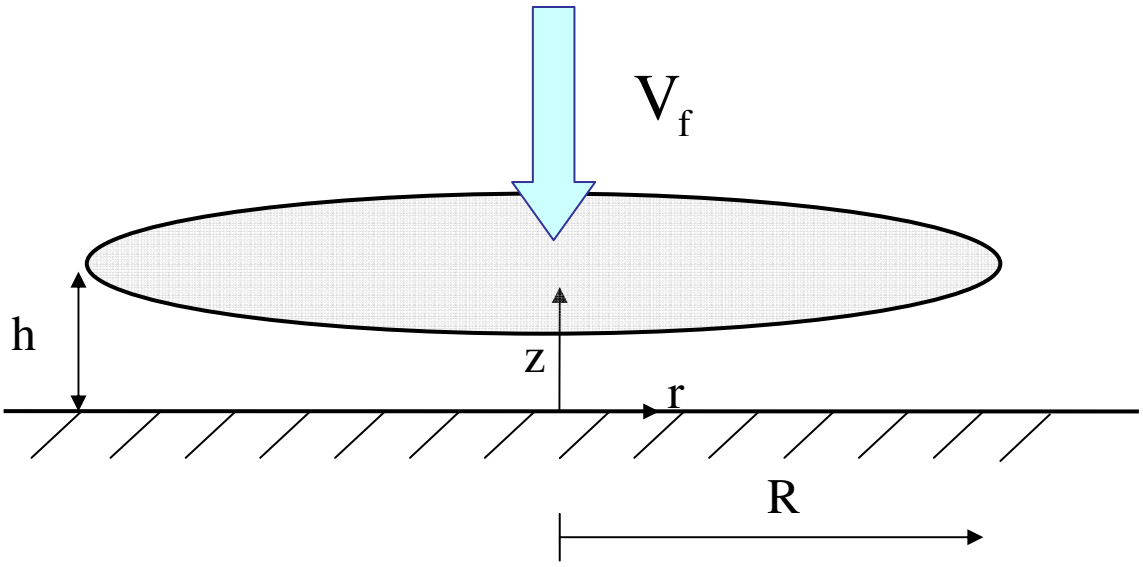

Figure 7-2. Schematic of a circular disk moving toward a stationary infinite plate with velocity V_f.

$$-\frac{dp}{dr}+\mu\left[\frac{\partial}{\partial r}\left(\frac{1}{r}\frac{\partial}{\partial r}(rV_r)\right)+\frac{\partial^2 V_r}{\partial z^2}\right]=0, \tag{7-2}$$

where μ is the dynamic viscosity of the air. Equations (7-1) and (7-2) can be solved with non-slip boundary conditions using a method similar to the one described by Leal (1992). The approach is briefly outlined here.

Differentiate equation (7-1) with respect to r, it follows that:

$$\frac{\partial}{\partial r}\left(\frac{1}{r}\frac{\partial}{\partial r}(rV_r)\right)=0. \tag{7-3}$$

Using equation (7-3) simplifies equation (7-2), that after integration with respect to z, it follows that:

$$V_r=\frac{dp}{dr}\frac{\left(z^2-zh\right)}{2\mu}, \tag{7-4}$$

Integrating equation (7-1) over $\int_0^h\int_0^r 2\pi r dr dz$ and rearranging, it follows that:

$$2\pi r\int_0^h V_r dz+\pi r^2 V_f=0. \tag{7-5}$$

Using equation (7-4), equation (7-5) reduces to:

$$\frac{dp}{dr} = \frac{6\mu r V_f}{h^3}. \tag{7-6}$$

From equations (7-4) and (7-6), it follows that:

$$V_r = \frac{3rV_f\left(zh - z^2\right)}{h^3}, \tag{7-7}$$

where h is the distance between the disk and the plate. For z=0.5h, V_r reaches the maximum value V_{rmax} given by:

$$V_{rmax} = \frac{1}{4}\frac{3rV_f}{h}. \tag{7-8}$$

Cham and Redfern (2002) reported that after the heel contacts the floor, the foot rotates down on the floor rapidly to reach the flat position with an angular velocity of about 224 degrees per second. This rotation happens in about 0.1 second, which is about 15% of the period of heel contact to toe taking off in the gait cycle. Henty et al. (1999) reported that after heel contact, the angular velocity decreases, so it is reasonable to use half of the initial value as an average angular velocity. Assuming that the length of the shoe is 30 cm, the radii of the toe and the heel part of the shoe are both 5 cm, and the average distance from the toe to the back tip of the heel is 25 cm, then the average step down velocity of the toe is about

$$V_f = 0.5 \text{ m/s}, \tag{7-9}$$

and the average step down velocity of the heel is

$$V_f = 0.1 \text{ m/s}. \tag{7-10}$$

These are estimated based on the rotation of the shoe about the heel contact.

When the foot reaches the flat position, it is assumed that there is a gap h of about 1 mm, due to the grooves at the bottom of the shoe. Therefore, the maximum airflow velocity $V_{r\max}$ for the toe and heel are, respectively, about 18.3 m/s and 3.7 m/s. That is, for the stepping down state, the maximum radial velocity of 18.3 m/s occurs at the tips of the toe, and the corresponding Reynolds number R_e is 1220; therefore, the flow is in the laminar regime.

Equations (7-7) and (7-8) are also valid for the stepping up process. As mentioned above, Cham and Redfern (2002) reported that after the heel contacts the floor, the foot rotates down on the floor with an angular velocity of about 224 degrees per second, while Henty et al. (1999) reported that after heel contact, the angular velocity decreases. Here we assume the average angular velocity is 112 degrees per second, 224 degrees per second being the maximum angular velocity during the stepping down process. Henty et al. (1999) also reported that the maximum foot angular velocity at the stepping down process is around one-half to two thirds of that at the stepping up process. In this study, we assume this value is one half, so the foot maximum angular velocity at the stepping up process is double of that at the stepping down process and equals 448 degrees per second.

At the initial stepping up process, the heel is rotating around point C in Figure 7-1b, which is the contact point of the bridge and the toe. The distance between A and C is about 20 cm, and the average rotation radius for the heel is the distance from the center of the heel to point C, which is 15 cm. As for the toe, after the rise of the heel, it begins to rotate around point D in Figure 7-1b, which is the tip of the toes. The average rotation radius for the toe is the distance from the center of the toe to point C, which is 5cm. In addition, based on the measurement by Henty et al. (1999), the initial stepping up angular velocity for the toe is about 1/6 of the maximum stepping up angular velocity, and for the heel, the initial stepping up angular velocity is about 1/36 of the maximum value. Therefore, the initial stepping up angular velocity for the toe and heel are, respectively, about 75 degrees per second and 12 degrees per second with rotation radii of 5 cm and 15 cm. Therefore, the initial step up velocity of the toe is

$$V_f = 0.065 \text{ m/s}, \tag{7-11}$$

and the initial step up velocity of the heel is

$$V_f = 0.033 \text{ m/s}. \tag{7-12}$$

Obviously, the maximum radial velocity at stepping up is much smaller than that at stepping down.

Equations (7-7) and (7-8) are valid for the squeezed airflow between the shoe and the

floor in the range of $r \le R$. Airflow outside the toe and heel of the shoes cannot be estimated by these equations. The external airflows around the toe and the heel regions are modeled as a radial wall jet.

A radial wall jet occurs when one side of the radial jet is constrained by the presence of a wall. Glauert (1956) reported a similarity solution for laminar radial wall jet. Accordingly, the airflow velocity outside the heel and the toe of the foot is given as:

$$V_r = \frac{3RV_f\left(zh - z^2\right)}{h^3}\left(\frac{r}{R}\right)^{-2.75} . \tag{7-13}$$

Here it is assumed that the virtual origin is at the center of the toe or the heel of the foot at r=0. Here z is the vertical coordinate.

7.3 ADHESION MODELS

In this section, a brief summary of the adhesion models used in this study are presented.

7.3.1 JKR Model

The Johnson-Kendall-Robert (1971) (JKR) particle adhesion theory accounts for the effects of surface energy and elastic deformation of a sphere in contact with an elastic half-space. Accordingly, a finite contact area forms and the radius of the contact circle, a, is given as:

$$a^3 = \frac{d}{2K}\left[P + \frac{3}{2}W_A\pi d + \sqrt{3\pi W_A dP + \left(\frac{3\pi W_A d}{2}\right)^2}\right], \tag{7-14}$$

where

$$K = \frac{4}{3}\left[\frac{1-\nu_1^2}{E_1} + \frac{1-\nu_2^2}{E_2}\right]^{-1}, \tag{7-15}$$

is the composite Young's modulus. Here, d is the particle diameter, P is the applied external load, and ν_i and E_i are, respectively, the Poisson ratio, and the Young modulus of material i (i=1 or 2). In Equation (7-14), W_A is the thermodynamic work of adhesion.

According to the JKR model, the pull-off force F_{po} is given by:

$$F_{po}^{JKR} = \frac{3}{4}\pi W_A d . \tag{7-16}$$

At the moment of separation, the contact radius is given by:

$$a = \left(\frac{3\pi W_A d^2}{8K} \right)^{\frac{1}{3}} . \tag{7-17}$$

7.4 DETACHMENT MODELS

Particles can be detached by rolling, sliding or lifting mechanisms. Wang (1990) and Soltani and Ahmadi (1994, 1995) pointed out that the removal of spherical particles is more easily achieved by the rolling motion, rather than sliding or lifting. In this work, therefore, only the rolling detachment of spherical particle is analyzed.

7.4.1 Rolling Detachment Model

Figure 7-3 shows a spherical particle which is attached to a plane surface. Here a is the contact radius, F_g is gravity force, F_{po} is pull-off force. According to Tsai et al. (1991) and Soltani and Ahmadi (1994,1995a), a particle will be detached when the external force moment about point "O", the rear point at the perimeter of the contact circle, overcomes the resisting moment due to the adhesion force F_{po}. That is,

$$M_t + F_t(\frac{d}{2} - \alpha_r) + F_L a \geq F_{po} a , \tag{7-18}$$

where F_t is the total external force acting on the particle (e.g., the fluid drag force), α_r is the relative approach between the particle and surface (at equilibrium condition), M_t is the external moment of the surface stresses about the center of the particle, and F_L is the lift force acting on the particle. In most cases, α_r is negligibly small and can be neglected.

7.4.2 Sliding Detachment Model

The condition for sliding detachment of a particle is given as:

$$F_t \geq k_f (F_{po} - F_L) , \tag{7-19}$$

where k_f is the coefficient of static friction for particle-surface interface.

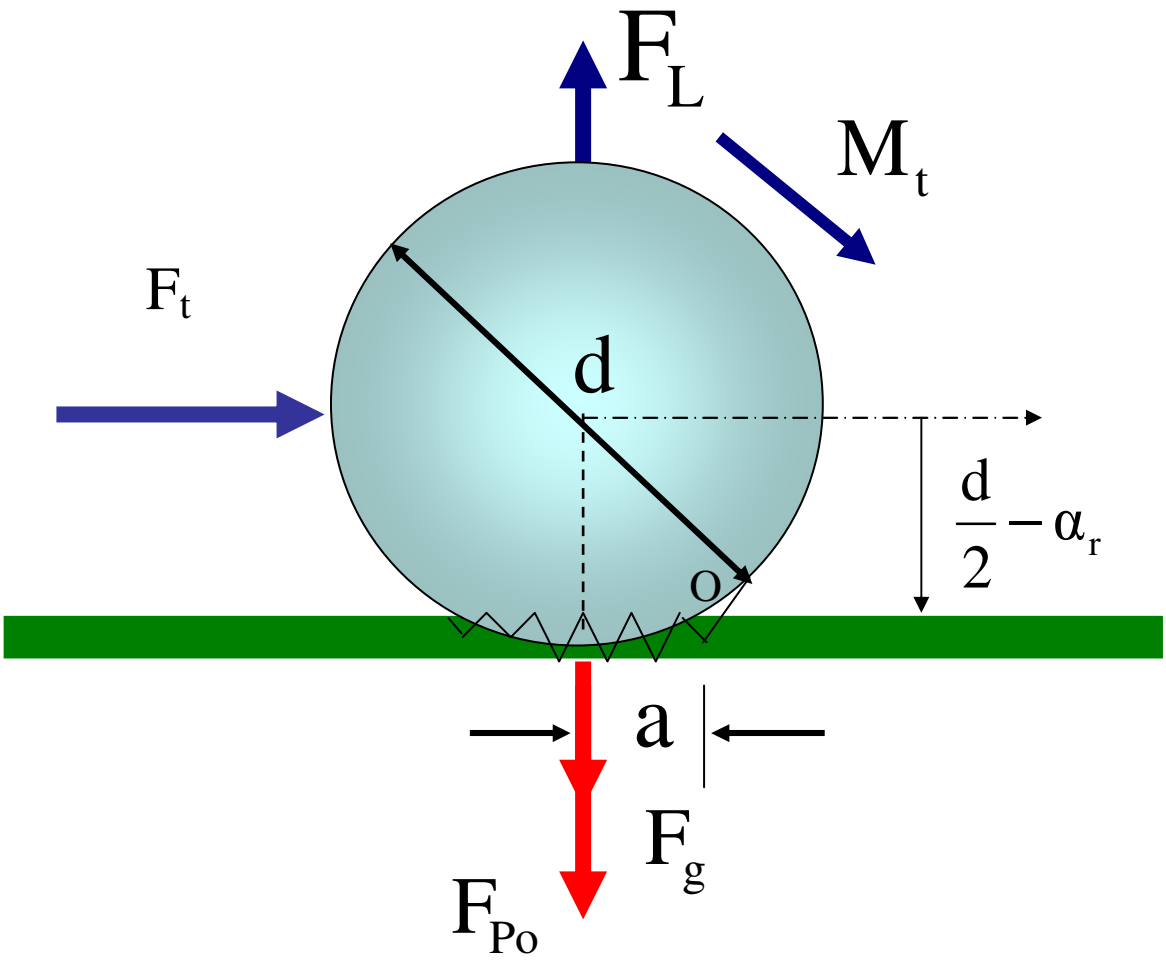

Figure 7-3. Geometric features of a spherical particle attached to a flat floor surface.

7.5 SURFACE ROUGHNESS MODEL

Real surfaces are rough at certain scales and even a small roughness significantly affects the force of adhesion. Fuller and Tabor (1975) studied the influence of surface roughness on the adhesion between rubber and a hard substrate. The analysis of Johnson et al. (1971) of the contact of elastic spheres is applied to the contact of individual asperities. They postulated that all asperities have the same radius with their heights following a Gaussian distribution. Soltani and Ahmadi (1995a) and Soltani et al. (1995) developed an analytical expression for the total pull-off force for detachment of slightly rough particles from rough or smooth surfaces. Accordingly,

$$F_{po} = \pi a^2 N f_{po} \exp[-0.6/(\Delta_c)^2], \tag{7-20}$$

where N is the number of asperities per unit area, and a is the contact radius given by:

$$a = \frac{\pi N f_{po} d \exp[-0.6/(\Delta_c)^2]}{2K}. \tag{7-21}$$

Here f_{po} is the pull-off force for individual asperity contact, which is given by:

$$f_{po} = 1.5\pi W_A \beta, \tag{7-22}$$

where β is the radius of an asperity, which is assumed to be given as:

$$\beta = 0.02d. \tag{7-23}$$

As noted before, these equations are for the cases when the surface roughness is much smaller than the particle size. In Equation (7-21) Δ_c is a nondimensional roughness parameter defined as:

$$\Delta_c = \delta_c/\sigma, \tag{7-24}$$

where δ_c is the maximum extension of the tip of an asperity above its undeformed height before the adhesion contact breaks, and σ is the standard deviation of the surface roughness height. For natural surfaces, σ, β and N are related (Greenwood and Williamson, 1966). That is:

$$\beta\sigma N = 0.1. \tag{7-25}$$

According to the JKR adhesion theory, δ_c is given by:

$$\delta_c = \left(\frac{f_{po}^2}{3K^2\beta}\right)^{1/3}. \tag{7-26}$$

Note that in the presence of compressive loads, relatively soft particles and/or substrates may undergo plastic deformation. In this case the JKR theory is no longer applicable, and the Maugis-Pollock (1984) theory must be extended to rough surfaces and be used.

Combining equations (7-20), (7-21), (7-22) and (7-25), it follows that:

$$a = \frac{0.15\pi^2 W_A d \exp[-0.6/(\Delta_c)^2]}{2K\sigma}, \tag{7-27}$$

and $$F_{po} = \left(\frac{0.15\pi^2 W_A \exp[-0.6/(\Delta_c)^2]}{\sigma} \right)^3 \left(\frac{d}{2K} \right)^2 . \quad (7\text{-}28)$$

Using equation (7-22), (7-23), (7-24) and (7-25), one finds:

$$\sigma = \left(\frac{0.015\pi^2 W_A^2 d}{K^2 (\Delta_c)^3} \right)^{1/3} . \quad (7\text{-}29)$$

For Δ_c, a Gaussian distribution can not get results that agree with all the experimental data, so here Δ_c is assumed in the range of 0.675 to 1.325 and has a dual-Gaussian distribution:

$$\text{For } 0.925 \le \Delta_c \le 1.075, \mu_1 = 1.0, \sigma_1 = 0.012 ; \quad (7\text{-}30)$$

$$\text{For other } \Delta_c, \ \mu_2 = 1.0, \sigma_2 = 15 . \quad (7\text{-}31)$$

Here μ_1 and μ_2 are the expect values of the Δ_c; σ_1 and σ_2 are standard deviations of Δ_c.

7.6 HYDRODYNAMICS FORCES AND TORQUES

In this section, the forces and torques acting on a particle in contact with a surface are briefly outlined. For a particle attached to the floor, the drag force acting in the radial direction is given as:

$$F_t = \frac{3\pi f \mu d}{C_c} V_r , \quad (7\text{-}32)$$

where f =1.7009 is the correction factor for the wall effect given by O'Neill (1968). Here V_r is the radial fluid velocity at the location of the mass center of the particle. The Cunningham factor is given as (Fuchs, 1964; Friedlander, 1977):

$$C_c = 1 + Kn\,[1.257 + 0.4\exp(-1.1/Kn)] . \quad (7\text{-}33)$$

Here the Knudson number is defined as:

$$Kn = \frac{2\lambda}{d} , \quad (7\text{-}34)$$

where λ is the air mean free path (typically about 0.07μm under normal conditions)

In the presence of small surface roughness, the distance of the particle center to the zero velocity point is given as (Soltani and Ahmadi, 1995a):

$$z = \frac{d}{2} + 2.76\sigma . \tag{7-35}$$

Note that the distance of relative approach and elastic deformation of asperities are ignored.

Drag force can be obtained by using equations (7-7), (7-13) and (7-32). That is:
Inside the contact area:

$$F_t = \frac{9\pi f \mu d r V_f (zh - z^2)}{C_c h^3}, \qquad r \le R . \tag{7-36}$$

Outside the contact area:

$$F_t = \frac{9\pi f \mu d r V_f (zh - z^2)}{C_c h^3}\left(\frac{r}{R}\right)^{-2.75}, \qquad r \ge R . \tag{7-37}$$

Note that the distance of the center of the sphere from the zero velocity level, z, is given by equation (7-35).

The corresponding hydrodynamic moment is:

$$M_t = 2\pi\mu g_w V_r d^2 , \tag{7-38}$$

where V_r is the fluid velocity at the location of the mass center of the particle, with $g_w = 0.943993$ accounting for the wall effect. Using (7-7) and (7-13), the expressions for the hydrodynamic moment are given as:
Inside the contact area:

$$M_t = \frac{6\pi\mu g_w d^2 r V_f (zh - z^2)}{h^3}, \qquad r \le R . \tag{7-39}$$

Outside the contact area:

$$M_t = \frac{6\pi\mu g_w d^2 r V_f (zh - z^2)}{h^3}\left(\frac{r}{R}\right)^{-2.75}, \quad r \geq R. \tag{7-40}$$

The lift force acting on the particle as suggested by Mei (1992) is given as:

$$\frac{F_L}{F_{LSaff}} = \left(1 - 0.3314\alpha_0^{1/2}\right)\exp\left[-\frac{R_{es}}{10}\right] + 0.3314\alpha_0^{1/2}, \quad \text{for} \quad R_{es} \leq 40, \tag{7-41}$$

where

$$R_{es} = \frac{|V_r|d}{\nu} \quad \text{and} \quad \alpha_0 = \frac{|\dot{\gamma}|d}{2|V_r|} = \frac{1}{2}R_{es}\varepsilon^2. \tag{7-42}$$

Here

$$\varepsilon = \frac{R_{eG}^{1/2}}{R_{es}}, \quad R_{eG} = \frac{\dot{\gamma}d^2}{\nu}, \quad \dot{\gamma} = \frac{dV_r}{dz}. \tag{7-43}$$

In equation (7-41), F_{LSaff} is the Saffman lift force,

$$F_{LSaff} = 1.61 d^2 V_r (\rho\mu)^{1/2} \frac{dV_r/dz}{|dV_r/dz|^{1/2}}. \tag{7-44}$$

For particles located on the tips of the toe or the heel of a shoe with r=5cm, h=1mm, for stepping down of the toe with V_f =0.49m/s, the airflow velocity at the mass center of particles with diameters of 1μm, 10μm, and 100μm, are, respectively, 0.044m/s, 0.44m/s and 4.16m/s. The corresponding R_{es} are, respectively, 0.0012, 0.24 and 23.2. Therefore, since R_{es} is smaller than 40, equation (7-41) for the lift force can be used.

7.7 PARTICLE DETACHMENT

Soltani and Ahmadi (1994) evaluated the minimum critical shear velocity for removing different size particles in the presence of the adhesion (van der Waals) force. Recently, Ahmadi et al. (2007) studied particle adhesion and detachment in turbulent flows and included the effect of capillary forces using the JKR adhesion theory. In this section, the rolling detachment of particles due to the flow generated by foot motion in

the gait cycle is analyzed and the corresponding critical radii under the toe and heel that particles of different sizes that are removed are evaluated.

During the stepping down or up of the foot in the gait cycle, a squeezing film flow is generated near the contact areas. As a result, a drag force F_t, a lift force F_L and a hydrodynamic moment M_t are exerted on the particles that are attached to the floor. Equation (7-19) implies that when the net external torque overcomes the resisting moment due to the adhesion force F_{po}, the particle is detached.

Equations (7-7) and (7-13) show that the squeezing flow velocity varies with the

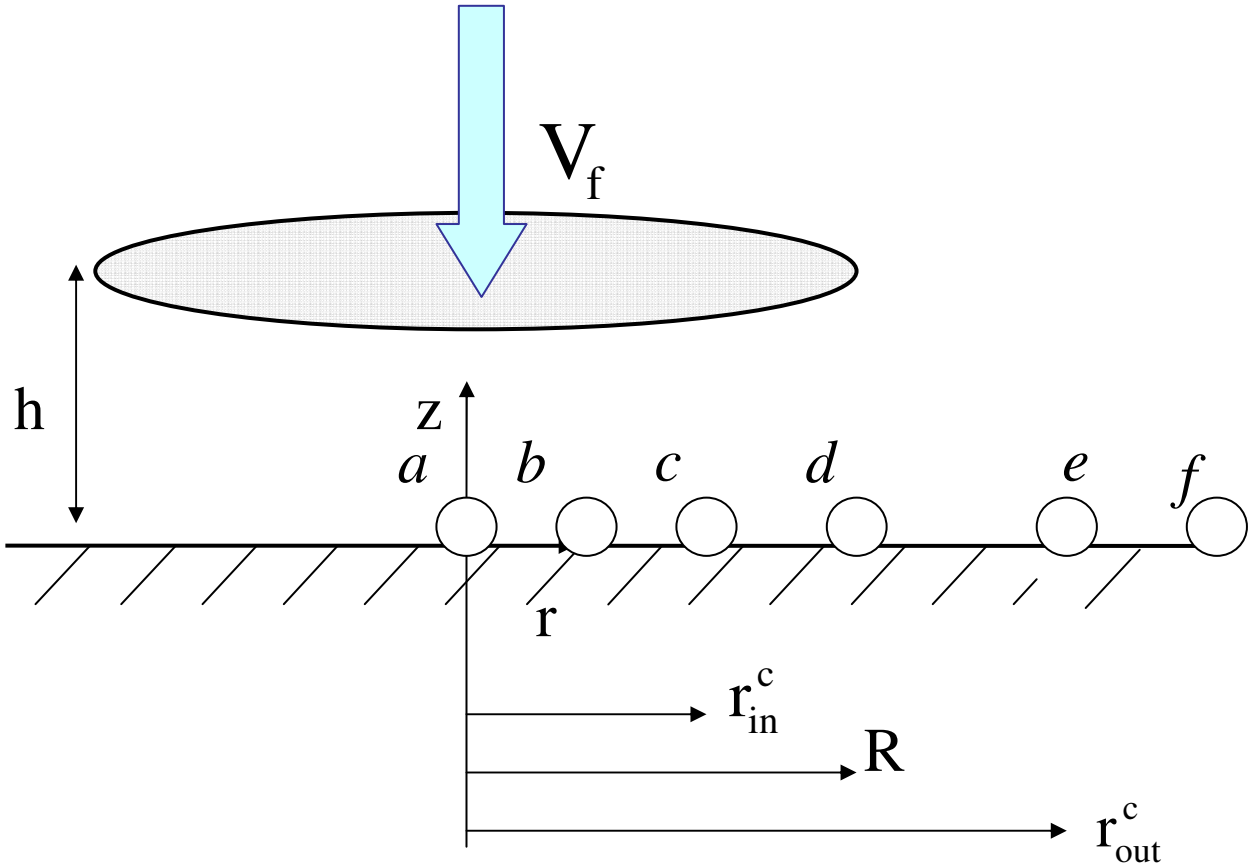

Figure 7-4. Schematic of critical radial distance r_{in}^{c} and r_{out}^{c} for particle detachment.

radial distance from the center of the disk, as well as the distance from the floor. In addition, the velocity magnitude increases as the gap size h decreases and the foot up and down velocity increases. The velocity at the center of the particle increases with particle size as z increases. Thus, larger particles are more easily detached.

Figure 7-4 shows the schematics of typical particles on a smooth floor when the toe or the heel of a shoe, modeled as a circular disk, is approaching. Assume that particle 'a' is at the centerline and particle'd' at the borderline as shown in the figure. Particles 'b' and 'c' are located within the projection area of the heel and toe, particles 'e' and 'f' are outside. The air speeds experienced by these particles vary with the distance from the centerline. Equations (7-7) and (7-13) shows that the air speed increases with distance r within the projection area then decreases with r in the outside region; thus, particles within a certain range of distances are detached.

For particle rolling detachment including the lift force, substituting equations (7-28), (7-36), (7-37), (7-39), (7-40) and (7-41) into equation (7-18), and after some algebra, the critical radii for particle detachment, r_{in}^{c} and r_{out}^{c}, are evaluated. These are:

Inside R:

$$r_{in}^{c} = \frac{(F_{po} - F_L)ah^2}{3\pi\mu d V_f \left(\frac{d}{2} + 2.76\sigma\right)\left(2g_w d + \frac{3fz}{C_c}\right)}, \qquad (7\text{-}45)$$

Outside R

$$r_{out}^{c} = R\left(\frac{(F_{po} - F_L)ah^2}{3\pi\mu d R V_f \left(\frac{d}{2} + 2.76\sigma\right)\left(2g_w d + \frac{3fz}{C_c}\right)}\right)^{-1/2.75}. \qquad (7\text{-}46)$$

That is, for a given particle diameter, particles within the critical radii, r_{in}^{c} and r_{out}^{c}, will be detached. This region is shaded in Figure 7-5.

Similarly, the critical radii for sliding detachment may be obtained. These are,

Inside R

$$r_{in}^{c} = \frac{k\left(F_{po} - F_{L}\right)C_{c}h^{2}}{-9\pi f\mu d V_{f}\left(\frac{d}{2} + 2.76\sigma\right)}, \tag{7-47}$$

Outside R

$$r_{out}^{c} = R\left(\frac{k\left(F_{po} - F_{L}\right)C_{c}h^{2}}{9\pi f\mu d R V_{f}\left(\frac{d}{2} + 2.76\sigma\right)}\right)^{-1/2.75}. \tag{7-48}$$

$$r_{in}^{c} < r < r_{out}^{c}$$

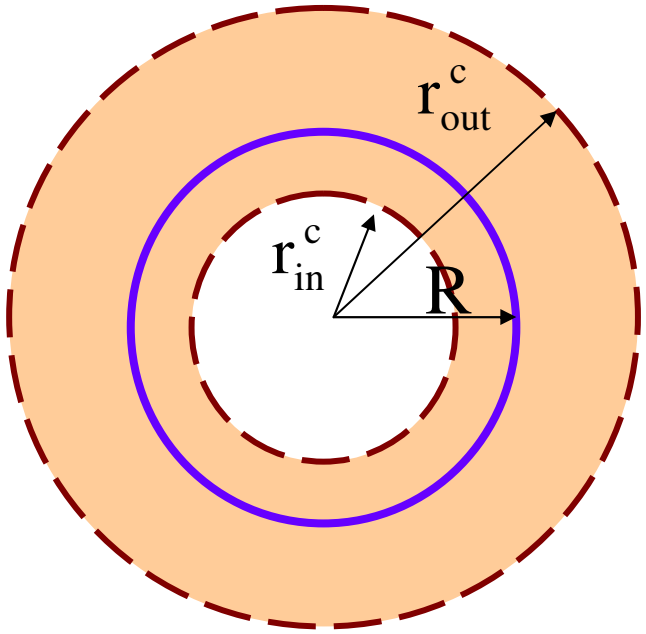

Figure 7-5. Schematic of particle detachment region.

7.8 PARTICLE RESUSPENSION MODEL

After being detached, a particle can roll or slide on the floor, or it could get resuspended into the air. The adhesion force for a detached particle vanishes since the van der Waals force is very short ranged. There, however, could be electrostatic forces

which have longer ranges. The role of electrostatic forces is currently under investigation and the results will be reported in the near future.

The present model assumes that a particle can be resuspended only if the lift force is larger than the gravity force. That is,

$$F_L > F_g . \tag{7-49}$$

The lift force given by equation (7-44) varies with radial position r. Thus, similar to the critical radii for particle detachment, critical radii r_{in}^{s} and r_{out}^{s} for particle resuspension (after detachment) are evaluated by comparing the lift force with the gravity force. Accordingly,

$$r_{in}^{s} = \pi\rho_p g h^3 \left(14.49\, V_f \left(3 r V_f \rho\mu\right)^{0.5}\right)^{-1}, \tag{7-50}$$

$$r_{out}^{s} = R\left(\pi\rho_p g h^3\right)^{-1/2.75}\left(14.49 R V_f (3 R V_f \rho\mu)^{0.5}\left(\frac{r}{R}\right)^{-1.375}\right)^{1/2.75}. \tag{7-51}$$

That is, the detached particles with $r_{in}^{s} \le r \le r_{out}^{s}$ will be resuspended. However, for stepping down process, not all resuspended particles located inside the region of the disk can be released to the environment, many of them will be caught by the falling disk. Assume only resuspended particles located near to the tip, out side R-h region of the disk can be released to the environment. In summary, only particles that are located at a radius larger than the maximum of (r_{in}^{c}, R-h and r_{in}^{s}), and smaller than the minimum of (r_{out}^{c} and r_{out}^{s}) will be detached and resuspended in the environment.

7.9 PARTICLE DEPOSITION MODEL

Resuspended particles could be re-deposited because of Brownian motion, turbulent eddy impaction and gravitational sedimentation. The particle deposition velocity u_D may be estimated as (Wood, 1982):

$$u_D = u^*(0.057 S_c^{-2/3} + 0.00045 \tau^{+2}) + \tau g, \tag{7-52}$$

where S_c is the Schmidt number given by:

$$S_c = \frac{\nu}{D}. \tag{7-53}$$

Here D is the diffusion coefficient given by:

$$D = \frac{kTC_c}{3\pi\mu d}, \tag{7-54}$$

where T is temperature, k is Boltzmann constant and C_c is the Cunningham correction factor. In Equation (7-52), τ and τ^+ are dimensional and nondimensional particle relaxation time, defined by:

$$\tau = \frac{\rho_p d^2 C_c}{18\mu}, \qquad \tau^+ = \frac{u^{*2}\tau}{\nu}. \tag{7-55}$$

Here, u^* is shear velocity, μ is air dynamic viscosity, and ν is air kinematic viscosity.

The deposited mass of a cloud of particles of a given size at the nth time step M_{dn} is calculated by:

$$M_{dn} = u_D C_{m(n-1)} S_n \Delta t, \tag{7-56}$$

where S_n is the average projection area of the particle cloud, Δt is the step time period, $C_{m(n-1)}$ is the particle mass concentration in the cloud at the beginning of the step and is given as:

$$C_{m(n-1)} = \frac{M_{s(n-1)}}{V_{c(n-1)}}, \tag{7-57}$$

where $M_{s(n-1)}$ is the mass of the suspended particles at step period n-1, and $V_{c(n-1)}$ is the corresponding volume of the particle cloud. The transport model for the particle cloud is discussed in the subsequent section.

7.10 PARTICLE CLOUD TRANSPORT MODEL

For every step, a small cloud of resuspended particles is formed. Here we assume that the cloud has a cylindrical shape. These particle clouds are transported and dispersed by the airflow generated by the motion of the foot and the air circulation in the room.

Therefore, the size of the cylindrical clouds grows with time as shown schematically in Figure 7-6. When a person walks back and forth in a room or in a test chamber, an increasing number of growing particle clouds is generated. The volume of the particle clouds increases with time and the corresponding particle concentration decreases. The particle mass concentration at a point at a given time is calculated by summing up the particle mass concentration of all the clouds that reach that point.

Due to the ventilation system, the room background velocity is typically about 0.2m/s, and the corresponding turbulent fluctuation velocity is about 0.01m/s. Therefore, in the absence of human walking, the particle cloud will disperse with a speed of 0.01m/s. However, wake flow generated by the back and forth walking of a person generates large scale eddies and turbulence fluctuations that are much larger than the background.

In the experimental study of Qian and Ferro (2007), human subjects walked back and forth along a 16 feet floor at a speed of about 1.4m/s. The air turbulent velocity fluctuation was u'=0.35m/s (estimated as 25% of the main flow velocity). Assuming that the steps are 0.6m apart, the walking frequency is 2.3 Hz, and every step takes about 0.43

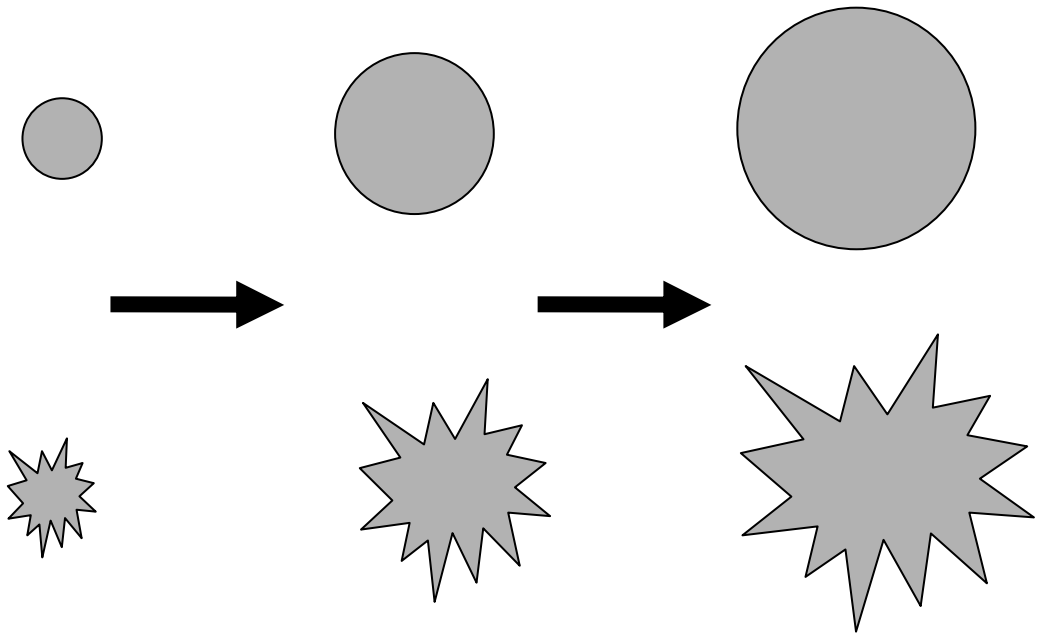

Figure 7-6. Schematic of particle cloud dispersion.

s; thus, the step period Δt is 0.43 s. Therefore, during every step, due to human walking and background air velocity, the particle cloud disperses, respectively, by about 0.15m and 0.02 m. Therefore, the radius of the particle cloud expands on average by about $\ell = 0.17\text{m}$ during one-step period.

The height of the particle cloud also expands. It is assumed that the rate of expansion is the same as the horizontal direction except for the first step when the particle cloud is generated. Near the floor, the vertical velocity is quite low, but during the stepping up process, the particle cloud could expand rapidly. The average shoe bottom height from the floor, B_h, for the stepping up process, is about 0.01m. At the end of the stepping down process, the effective gap between the shoe and the floor is very small of the order of a millimeter. The initial particle cloud height is expected to be of the order of the gap size h but being influenced by the shoe bottom height, B_h. Here the weighted average for the mean cloud height ℓ_{z0} is assumed. That is:

$$\ell_{z0} = 0.9h + 0.1B_h . \tag{7-58}$$

For the subsequent steps, the upward spreading is assumed to be the same as in the horizontal direction. That is, $\ell = 0.17\text{m}$ expansion for every step.

In summary, when a particle cloud is first generated, the height and radius of the particle cloud are, respectively, ℓ_{z0} and $\ell = 0.17\text{m}$. Then, the cloud grows at a rate of $\ell = 0.17\text{m}$ per step period in both vertical and radial directions. Thus, the volume of the particle cloud after the nth step periods is given as:

$$V_{cn} = \pi(n\ell)^2\left(\ell_{z0} + (n-1)\ell\right). \tag{7-59}$$

Here n varies from 1 to n_{max} which is the number of steps that a cloud needs to fill the entire chamber volume. n_{max} is evaluated from Equation (7-59) when $V_{cn} = V_{chamber}$.

Suspended particle mass concentration for a particle cloud after nth step periods, C_{mn} is then given by

$$C_{mn} = \frac{V_{c(n-1)} C_{m(n-1)} - u_D C_{m(n-1)} S_n \Delta t}{V_{cn}}, \tag{7-60}$$

where the numerator is the suspended particle mass at nth step period, $V_{c(n-1)}$ is the cloud volume and $C_{m(n-1)}$ is the particle mass concentration at the (n-1)th step period, and S_n is the average projection area of the particle cloud on the floor at the nth time period.

Iterative application of equations (7-59) and (7-60) leads to particle concentration for the clouds that are generated by particle resuspension due the gait cycle at subsequent times.

7.11 PARTICLE RESUSPENSION RATE MODEL

Particle resuspension rate at a time step is calculated by

$$r_i = \frac{R_i}{L}, \tag{7-61}$$

where r_i is the particle resuspension rate at the time step i, with a unit of $1/\text{hr}$, R_i is the resuspended particle flux at the time step i, in $\text{g}/(\text{m}^2 \cdot \text{hr})$, and L is the floor particles surface concentration g/m^2. Here R_i is evaluated as (Qian and Ferro, 2007)

$$R_i = 3600 \frac{V_{chamber}}{S_{chamber}} \{ \frac{C_n - C_{n-1}}{\Delta t} + (a_e + k_d) C_n \}. \tag{7-62}$$

Here C_n and C_{n-1} are local particle mass concentrations at the end of the nth and (n-1)th step period respectively, which are the sums of the corresponding cloud particle mass concentration. $S_{chamber}$ is the chamber floor area (m^2), a_e is the air exchange rate of the chamber (s^{-1}), and k_d is the particle deposition rate (s^{-1}).

$$r_i = 3600 \frac{V_{chamber}}{S_{chamber} L} \{ \frac{C_n - C_{n-1}}{\Delta t} + (a_e + k_d) C_n \}. \tag{7-63}$$

The floor surface concentration L is given by:

$$L = \frac{m_d}{S_{floor}}, \tag{7-64}$$

where m_d is the mass of the seeded particle of diameter d. and S_{floor} is the seeded area of

the floor.

7.12. EXPERIMENTS

Experimental measurements of the personal cloud generated by particle resuspension due to human activities were carried out in a full size chamber in the BEESL lab at Syracuse University. The details of the experimental study were reported by Qian and Ferro (2007). Here a brief summary is provided. Two different ventilation schemes, namely, mixing and displacement systems for the room were studied. Test floors were 4.88 m long and 1.22 m wide. Different types of flooring, namely, wood floor covered with vinyl tile, wood floor covered by a new carpet and wood floor covered by an old carpet were investigated. The relative humidity was monitored during the

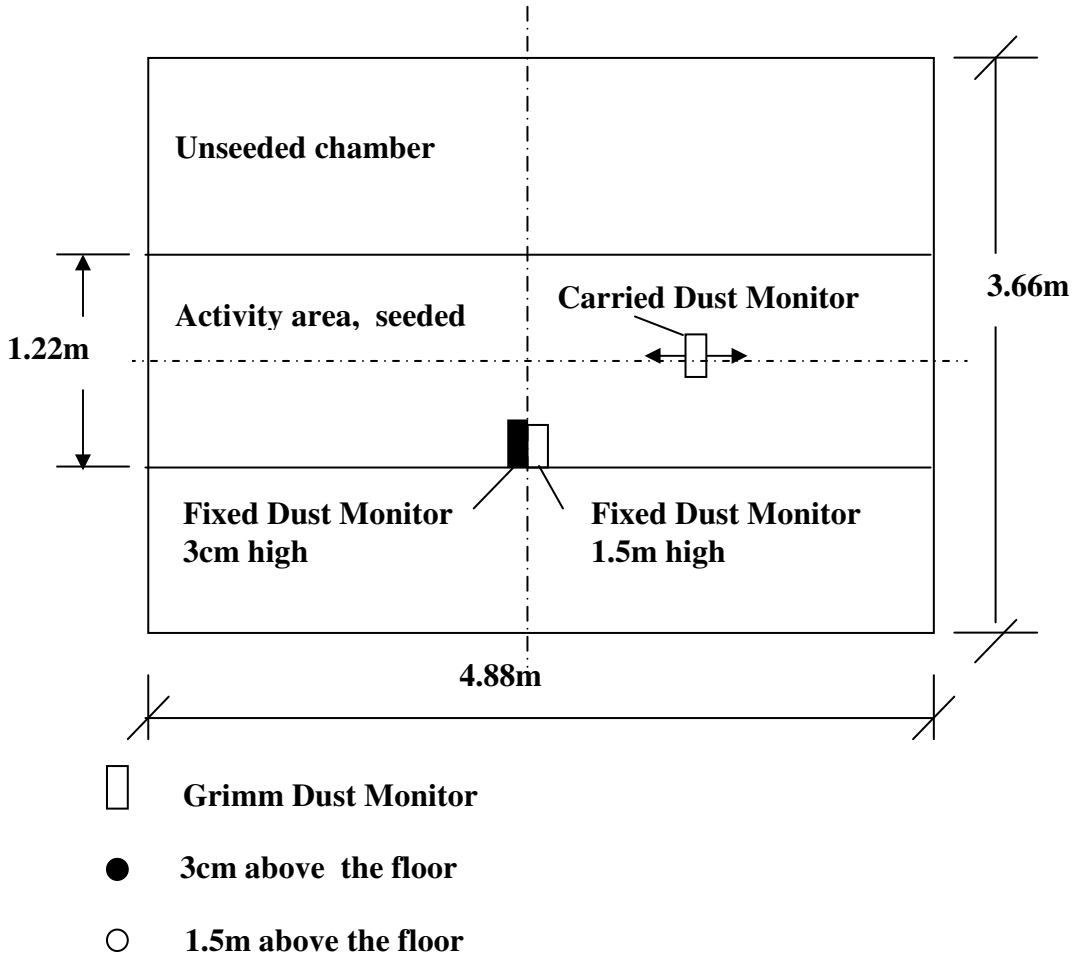

Figure 7-7. Schematic of the locations of particle sampling equipment.

experimentation and typically it was in the range of 30% - 50%, with temperature of 23° C, and an air exchange rate of 0.4 air changes per hour controlled by chamber environment settings.

Figure 7-7 shows the schematic of the experimental chamber and the locations of the instruments used in the study for particle sampling. These instruments include 3 Grimm Technologies (Douglasville, GA) Model 1.106 Portable Dust Monitor, providing a semi-continuous particle number size distribution in the range of 0.3 to 20 μm. Sampling was performed at 1.5 m above the floor, and at 3 cm above the floor. The third Grimm monitor was carried by the human subject with the intake in the breathing zone.

Table 7-1. Participant activity schedule in each experiment

Time (minutes)	Activity
-30~0	empty chamber
0~5	Walk
5~10	Sit
10~15	sit, tapping feet
15~20	sit still
20~25	sit, rocking & tapping feet
25~30	Walk
30~90	empty chamber

Fifty-two participants attended the experiments, and each experiment was recorded for one participant activities. The activity schedule for each participant is shown in Table 7-1. The detailed information about the experiment was reported by Qian and Ferro (2007). Floors with and without seeded particles were involved in the study. Arizona Road Test Dust (ISO 12103-1, A1 Ultra fine Test Dust from Powder Technology, Inc.

South Burnsville, Minnesota) was used to seed the floors in experiments. For the seeded floor, 120 grams of dust was uniformly distributed over the entire floor. Table 7-2 lists the chemical composition of these particles. It is seen that these particles are mostly made of SiO_2 and Al_2O_3; therefore, only these compounds were considered in the simulation. Table 7-3 shows the cumulative volume fraction of these particles, which implies that all the particles are smaller than 20 microns. The floor material is vinyl tile and carpet, but only particle resuspension from vinyl tile floor was analyzed in this study. Table 7-4 shows the properties of these materials.

Table 7-2. Chemical composition of Arizona dust particles used in the experiments

Composition	SiO_2	Al_2O_3	Fe_2O_3	Na_2O_3
Weight percent (%)	68-76	10 -15	2-5	2-4
Composition	CaO	MgO	TiO_2	K_2O
Weight percent (%)	2-5	1-2	0.5-1.0	2-5

Table 7-3. Cumulative volume fraction of particles used in experiments

Size (micrometer)	1	2	3	4	5	7	10	20
Volume fraction (%)	1-3	9-13	21-27	36-44	56-64	83-88	97-100	100

Table 7-4. Material properties for different cases

Material	E (10^{10} N/m^2)	W_A (10^{-3} J/m^2)	ρ_p (10^3 kg/m^3)	ν_i
Silicon dioxide- Silicon dioxide	7.17	10.776	2.203	0.16
Aluminum oxide- Aluminum oxide	37	27.783	3.96	0.2
Vinyl tile -Vinyl tile	420	10.56	1.38	0.41
Silicon dioxide -Vinyl tile	_	10.66	_	_
Aluminum oxide -Vinyl tile	_	15.302	_	_

7.13 RESULTS AND DISCUSSION

As noted before, the particles of a given size in the range of $r_{in}^{c} \le r \le r_{out}^{c}$ are detached. Figure 7-8 shows the variation of the critical radii with a particle diameter as predicted by the JKR model for resuspension of SiO_2 and Al_2O_3 particles from a vinyl tile substrate for the stepping down process. Here the shoe groove depth was assumed to be 1 mm and a roughness ratio of $\Delta_c = 1.0$ was used.

It is seen that the value of the critical radius for SiO_2 and Al_2O_3 particles are very similar. In the range of r<R, the value for SiO_2 is slightly larger than that for Al_2O_3. For the surrounding areas, the critical radius for SiO_2 is slightly smaller than that for Al_2O_3. These imply that it is a little easier to detach the Al_2O_3 particles when compared with the SiO_2 particles. Another interesting result is that the critical radius decreases with the particle diameter in the range of r<R, while it increases with the particle diameter in the range of r>R, which implies that larger particles can be more easily detached compared to smaller particles. It is also found that the toe region can detach particles as small as 3μm, while the heel can only detach particles as small as 10μm, due to the low heel stepping down velocity.

Similarly, for r<R, the critical radius for SiO_2 and Al_2O_3 particles in the heel stepping down process are larger than that in the toe stepping down, while for r>R, these values at the heel stepping down are smaller than that at the toe stepping down; therefore, particles can be detached more easily during the toe stepping down process than in the heel stepping down process. The reason is that the toe stepping down velocity is larger than the heel stepping down velocity, and generates larger air squeezing film velocity.

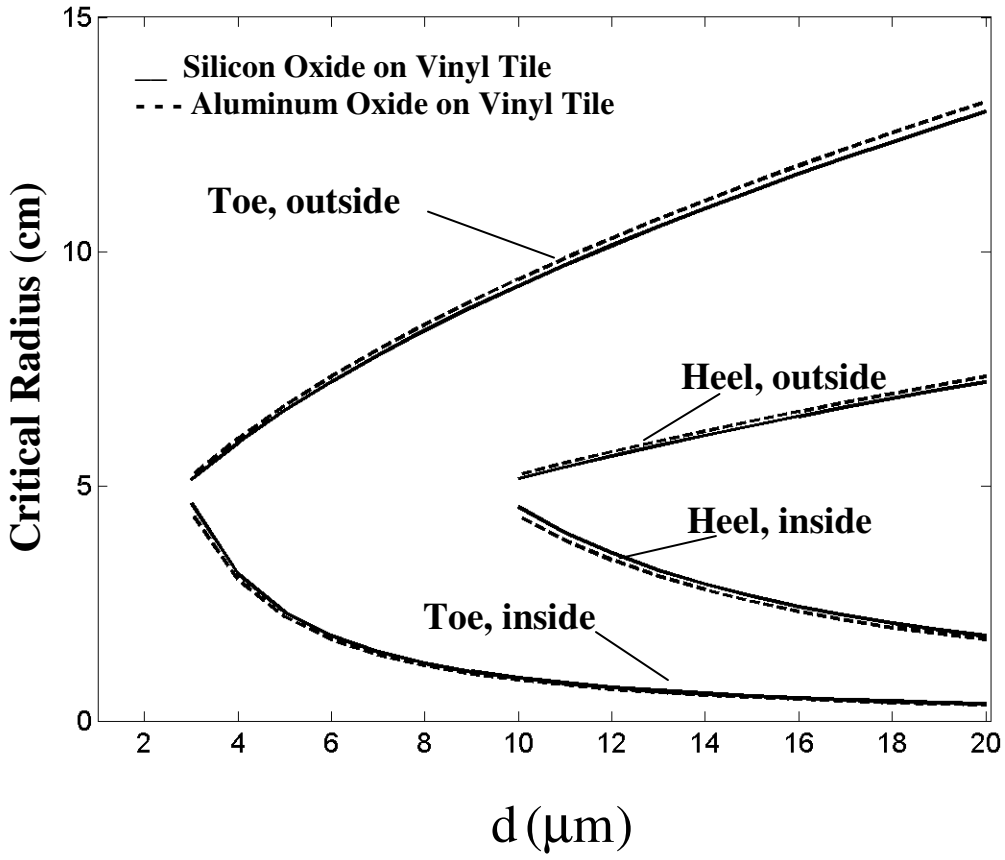

Figure 7-8. Critical radii for rolling detachment of particles with surface roughness during the stepping down process. (h=1.0mm, $\Delta_c = 1.0$)

Figure 7-8 also shows that the detachment region, $r_{in}^c \le r \le r_{out}^c$, for the toe stepping down process is larger than the region for the heel stepping down process. Therefore, larger amount of particles are detached by the toe stepping down in the gait cycle compared to the heel stepping down.

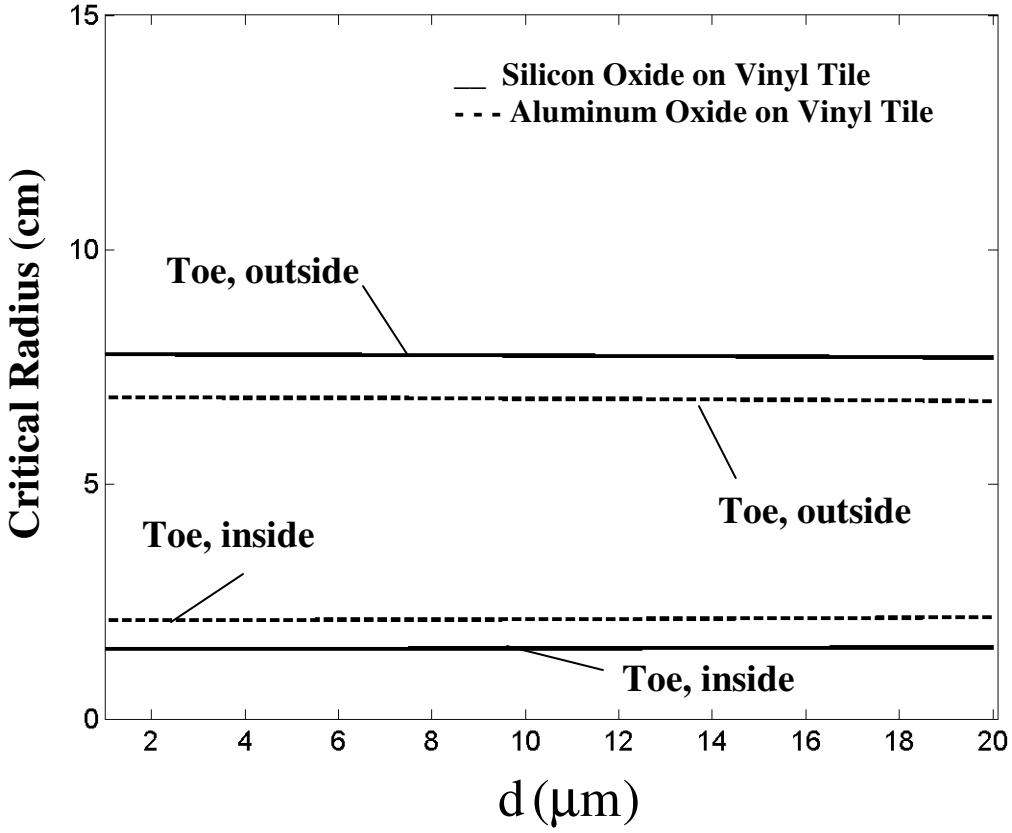

Figure 7-9. Critical radius for particle resuspension during the stepping down process. (h=1mm, $\Delta_c = 1.0$)

Figure 7-9 shows the critical radius for particle resuspension after being detached for the stepping down process. It is seen that the critical radii are roughly constant for different particle sizes. Close examination of the results shows that in the region r>R, the critical radius for particle resuspension decreases slightly with the particle diameter, while in the region r<R, the critical radius for particle resuspension increases slightly with the particle diameter. These trends are opposite to those observed in Figure 7-8 for particle detachment. This implies that though larger particles can be more easily detached compared with smaller particles, their chance for resuspension is slightly smaller than the smaller particles. The reason is that the gravitational force plays a minor role for particle detachment, but has a major role in preventing resuspension of large particles.

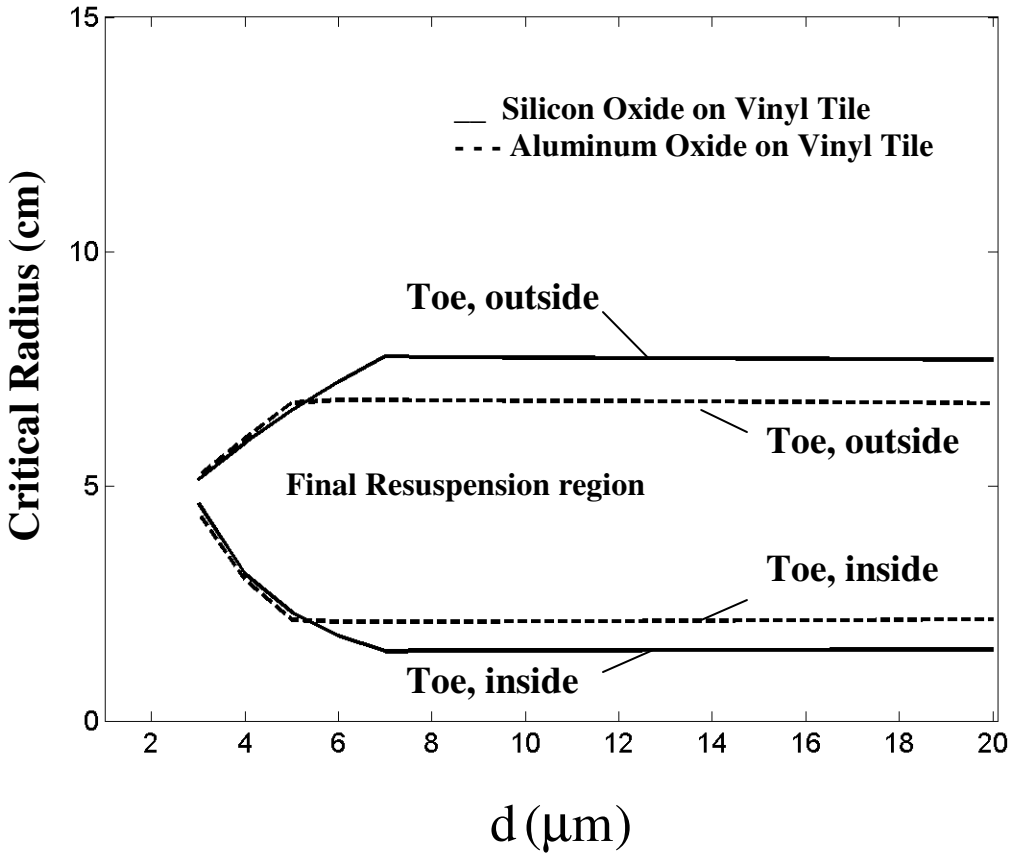

Figure 7-10. Final particle resuspension region during the stepping down process. (h=1mm, $\Delta_c = 1.0$)

Figure 7-9 also shows marked differences of the critical resuspension radii for SiO_2 and Al_2O_3 particles. The Al_2O_3 particles are much heavier than the SiO_2 particles, and therefore are more difficult to be resuspended.

Figures 7-8 and 7-9 imply that only particles in the region larger than the maximum of r_{in}^{c} and r_{in}^{s}, and smaller than the minimum of r_{out}^{c} and r_{out}^{s}, can get detached and resuspended during the gait cycle, as shown in Figure 7-10. Figure 7-10 shows the particle resuspension regions for stepping down process. It is seen that the resuspension region for the SiO_2 particles is larger than that for the Al_2O_3 particles. As noted before, this is because the Al_2O_3 particles have higher densities and slightly larger adhesion

forces.

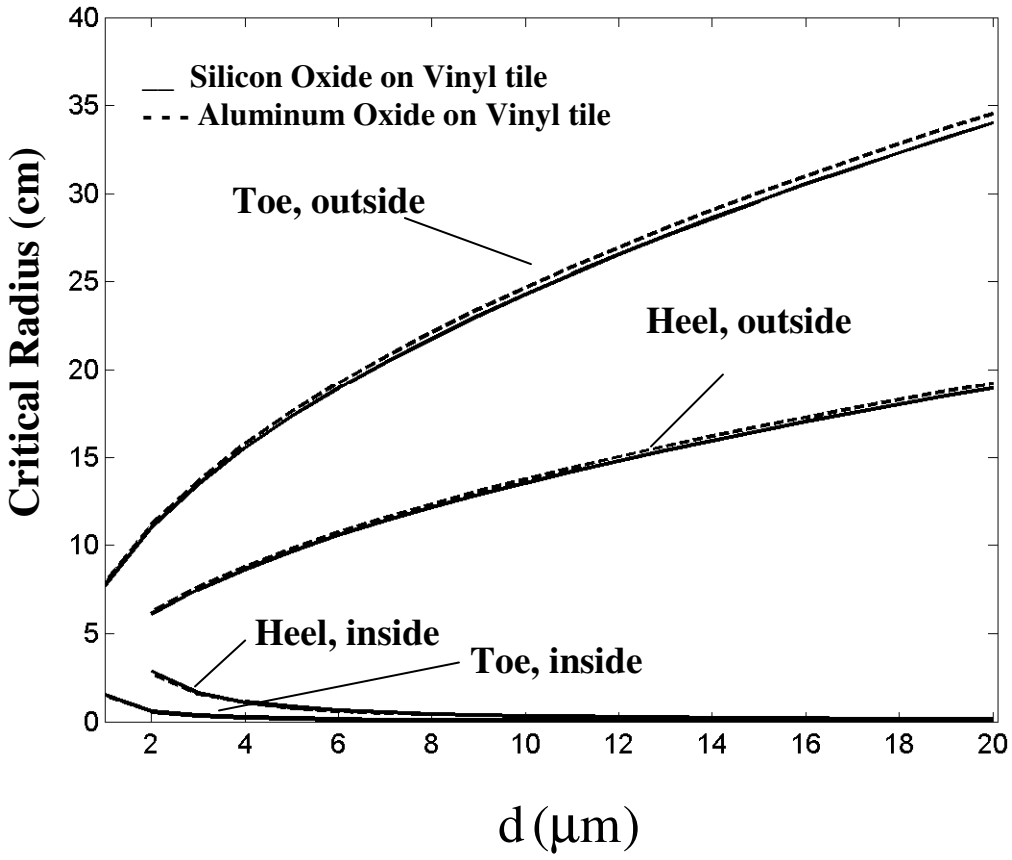

Figure 7-11. Critical radii for rolling detachment of particles with surface roughness during the stepping down process. (h=1.0mm, $\Delta_c = 0.773$)

To study the effect of the gap size and roughness values, a series of simulations was performed where these parameters were changed. For a fixed shoe-floor gap size of h=1.0mm the roughness value was reduced to $\Delta_c = 0.773$. Figure 7-11 shows the simulation results for the variation of the critical radii with particle diameter for the stepping down process. The trend of variation in this figure is similar to those of Figure 7-8. The critical detachment radii for SiO_2 and Al_2O_3 particles are quite similar with the Al_2O_3 particles being slightly easier to detach. It is again seen that the larger particles are more easily detached when compared with the smaller particles.

Compared to Figure 7-8, Figure 7-11 shows lower detachment radii in the region of r<R, and higher values in the region of r>R, which means that the amount of the particles are detached increases as Δ_c decreases. Equation (7-24) shows that a decrease in Δ_c implies an increase in the roughness standard deviation, σ. Therefore, particles with larger surface roughness are more easy to detach. Figure 7-11 also shows that the heel motion could detach particles of the order of 2 μm, while the toe motion detaches particles as small as 1 μm. Figure 7-8 indicates that the heel motion can detach particles as small as 10 μm, while the toe detaches particles as small as 3μm. These observations imply that with increasing particle roughness, smaller particles are detached.

Figure 7-12 shows the results for the simulation for the variation of the critical radii with particle diameter for the stepping down process for a fixed roughness value of $\Delta_c = 0.773$. Here the gap size was increased to h =1.8mm. General trend of variations are similar to those shown in Figures 7-8 and 7-11. Comparing Figures 7-12 and 7-11 shows that higher gap size leads to higher values of critical detachment radii under the shoe (r<R), and lower values outside the shoe (r>R). That is, fewer particles are detached as the gap size increases, due to the decrease in the squeezing film airflow velocity. Figure 7-12 also shows that the heel motion now leads to the detachment of particles larger than 4 μm, while in Figure 7-11, the heel could detach particles as small as 2 μm. Thus, as the gap size increases, the number of smaller particles that are detached decreases. Here, the gap size h is an effective parameter, not a physical value. It includes the effects of the grooves on the shoe bottom and the eddy outside the shoe.

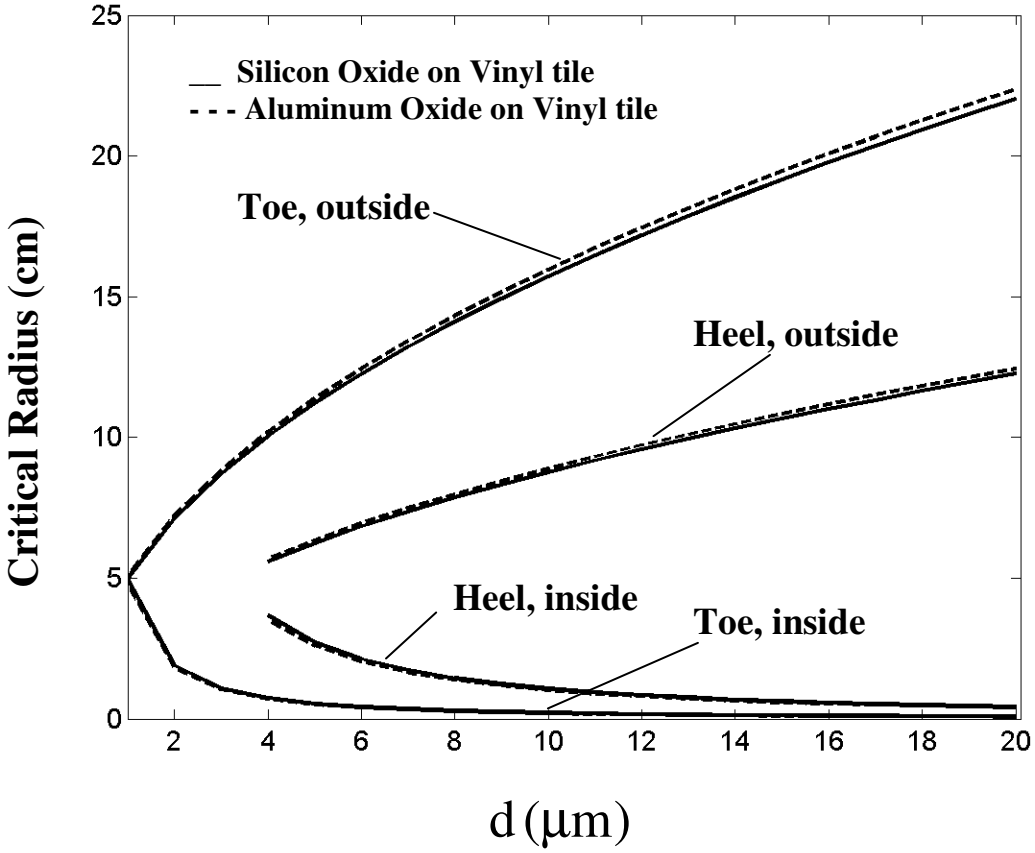

Figure 7-12. Critical radii for rolling detachment of particles with surface roughness during the stepping down process. (h=1.8mm, $\Delta_c = 0.773$)

Figures 7-13 to 7-16 show the measured variation of the particle mass concentration with time in five minutes walking for resuspension of particles of 3-4μm, 4-5μm, 5-7.5μm and 7.5-10μm respectively from a hard floor for different human subjects in the chamber study. The concentration data was obtained with the use of a Grimm Technologies (Douglasville, GA) Model 1.106 Portable Dust Monitor. The data reported here was from the monitor that was located at the floor level with the air intake being at 3 cm above the floor, as shown in Figure 7-7. The sampled data in a time step of 6 seconds are selected and the particle number concentrations are changed to particle mass concentrations. The increasing trend of particle concentration with time can be seen from these figures. Computer simulations for resuspension of 3.5μm, 4.5μm, 6.3μm and 8.8μm particles were performed for the experimental condition of the chamber for the

mixing ventilation system and the simulation results are plotted in Figures 7-13 to 7-16 respectively for comparison. A dual-Gaussian distribution of Δ_c as shown in equations 7-30 and 7-31 is used in the simulation. A gap size of h=1.8 mm for shoe-floor contact, and a density of 2360 kg/m^3 for the Arizona dust was assumed in the simulation. It can be seen from Figures 7-13 to 7-16 that the predicted increasing trend of the concentration is comparable with the experimental data. It also can be seen that the mass concentrations for large particles are larger than that for small particles. One reason is that large particles have large mass, but the most import reason is that more large particles get resuspended. The periodic variation pattern observed in the simulation data is due to arrival of different dust cloud from the source to the monitor.

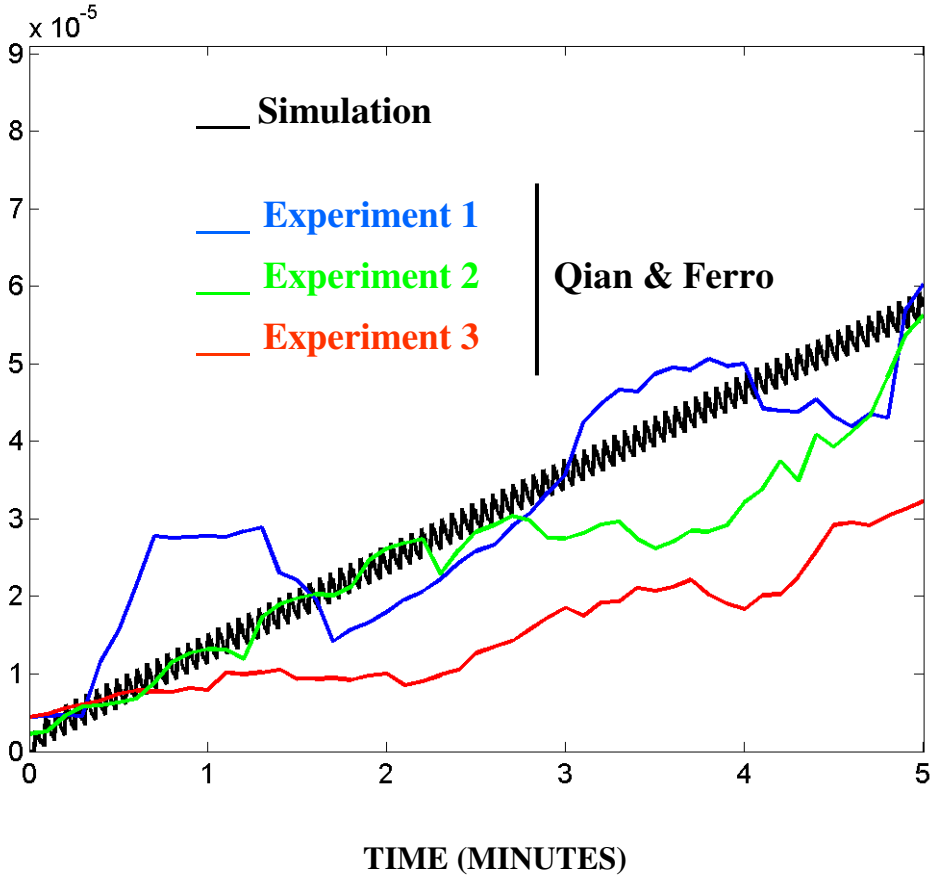

Figure 7-13. Variation of the particle mass concentration with the time for resuspension of particles from a hard floor with roughness, (h=1.8mm, Δ_c = dual-Gaussian

distribution, particle size=3-4μm)

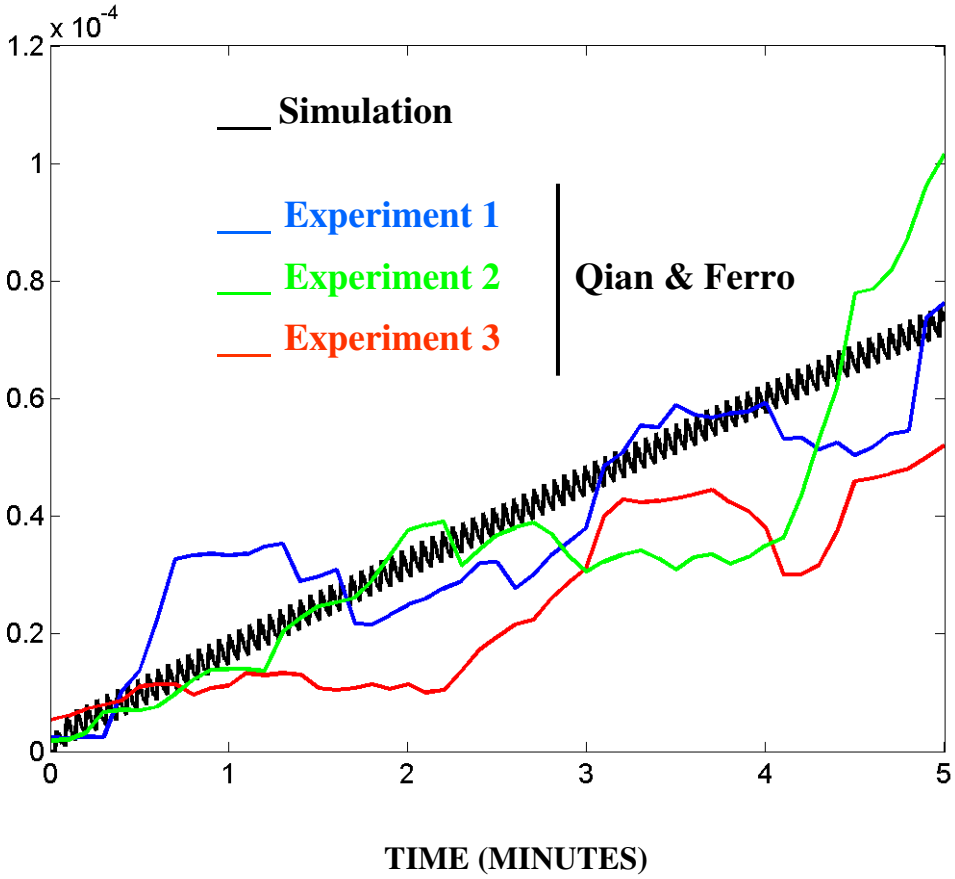

Figure 7-14. Variation of the particle mass concentration with the time for resuspension of particles from a hard floor with roughness, (h=1.8mm, Δ_c = dual-Gaussian distribution, particle size=4-5μm)

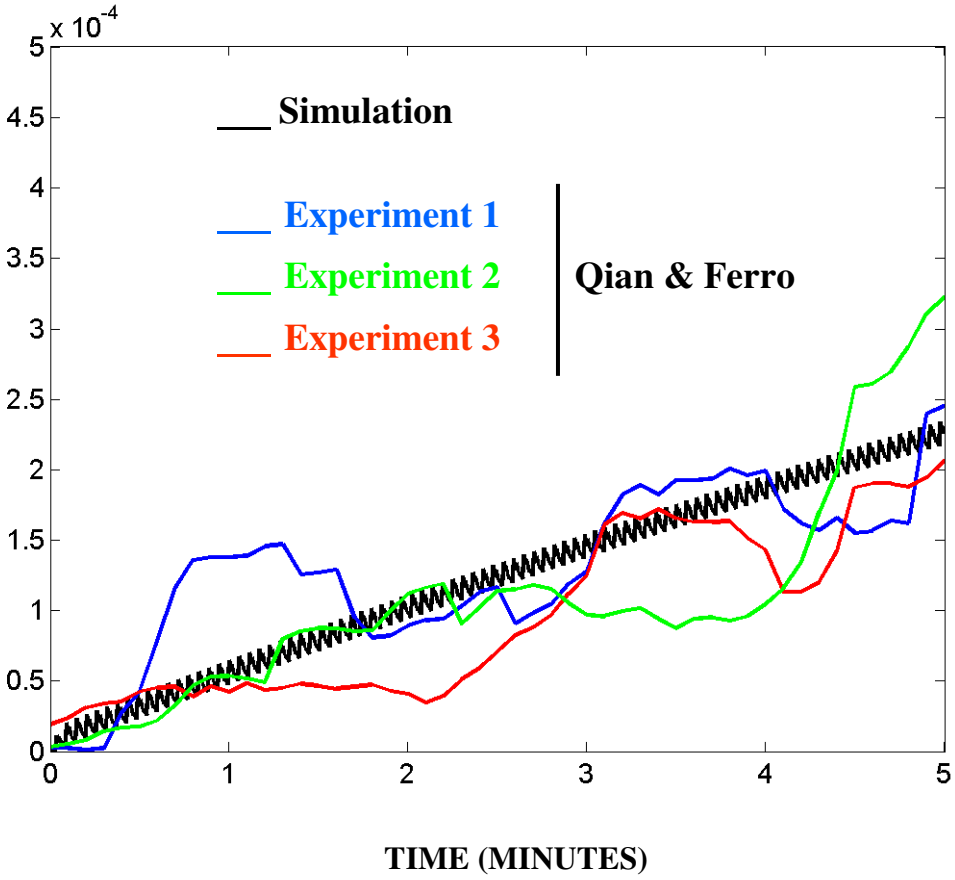

Figure 7-15. Variation of the particle mass concentration with the time for resuspension of particles from a hard floor with roughness, (h=1.8mm, Δ_c = dual-Gaussian distribution, particle size=5-7.5μm)

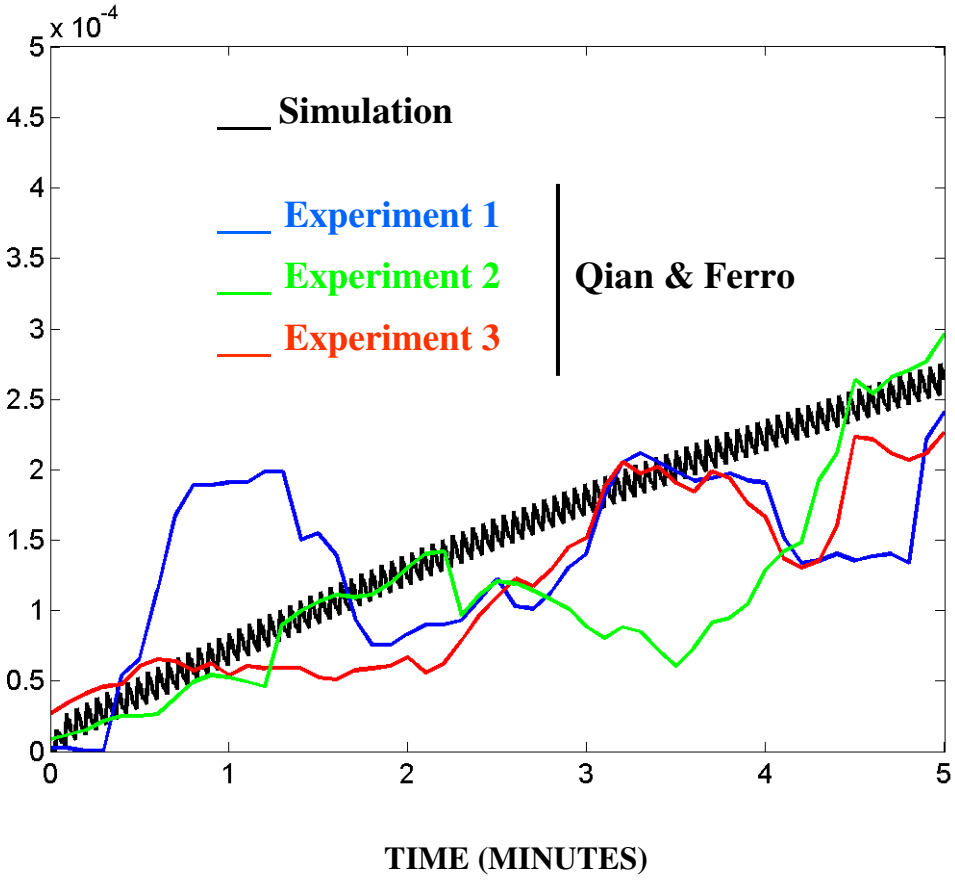

Figure 7-16. Variation of the particle mass concentration with the time for resuspension of particles from a hard floor with roughness, (h=1.8mm, Δ_c = dual-Gaussian distribution, particle size=7.5-10μm)

Figure 7-17 shows the simulated variation of the particle mass concentration with time for shoe-floor gap sizes of 1.7 mm, and1.8mm. Here all other parameters are kept the same. This figure shows that the particle mass concentration for the gap size of h=1.7mm is much higher than that for the gap size of 1.8mm. Thus smaller shoe-floor gap size increases the resuspended particle mass concentration in the room. This is because of higher squeezing film airflow velocity generated by smaller gap size. Figure 7-17 also shows that the amplitude of the periodic pattern for shoe-floor gap size of 1.7mm is larger than that for h=1.8m while their frequencies are roughly the same. This is due to the higher resuspension rate generated by the smaller gap size.

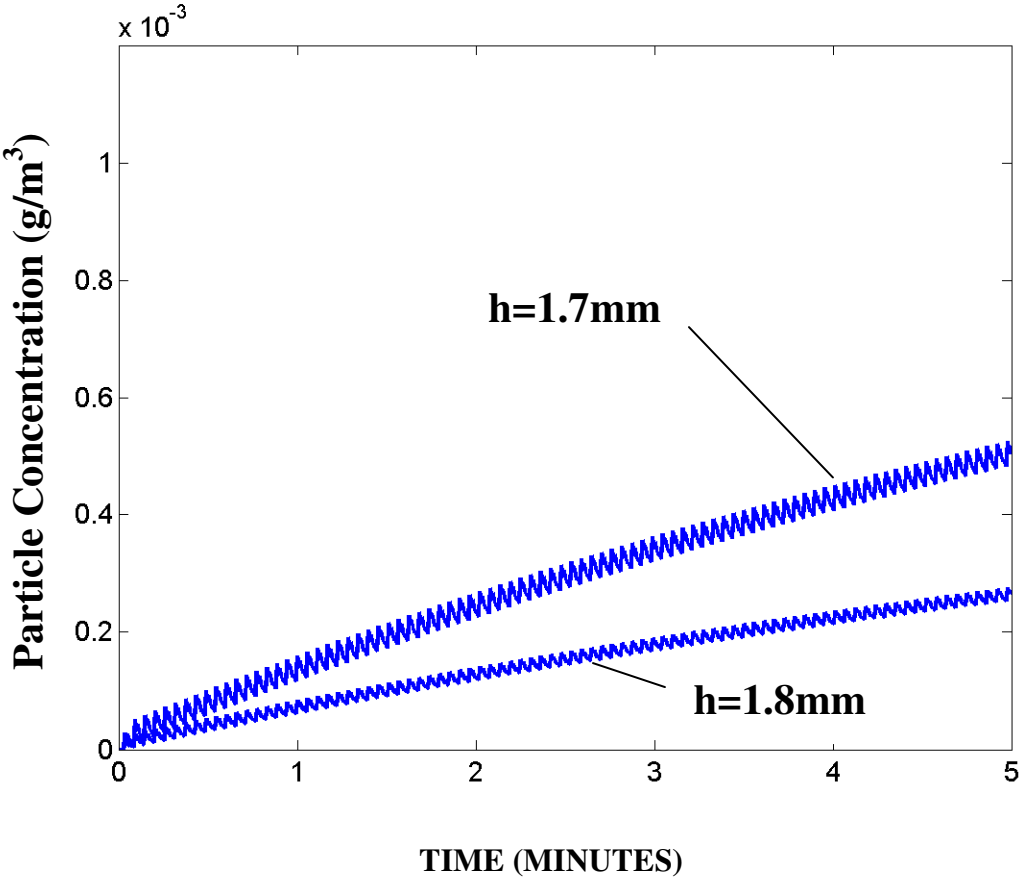

Figure 7-17. Variation of the particle mass concentration with the time at different gap size for resuspension of particles from a hard floor with roughness. (R=5cm, $V_f = 0.5\,m$, Δ_c = dual-Gaussian distribution, particle size=7.5-10μm)

Figure 7-18 shows the variation of the particle mass concentration with time for increased stepping down velocity and shoe size. The reference case for foot stepping sown velocity of 0.5 m/s and shoe radius of 5 cm is shown in this figure for reference. When the foot stepping down velocity increases to 0.515 m/s, the particle mass concentration increases. Similarly, when the shoe size increases to 5.2 cm, Figure 7-18 shows a sharp increase in the resuspended particle mass concentration. Both the increased stepping down velocity and the increased foot size are associated with increased squeezing airflow velocity at the shoe-floor interface that leads to a much higher rate of particle resuspension.

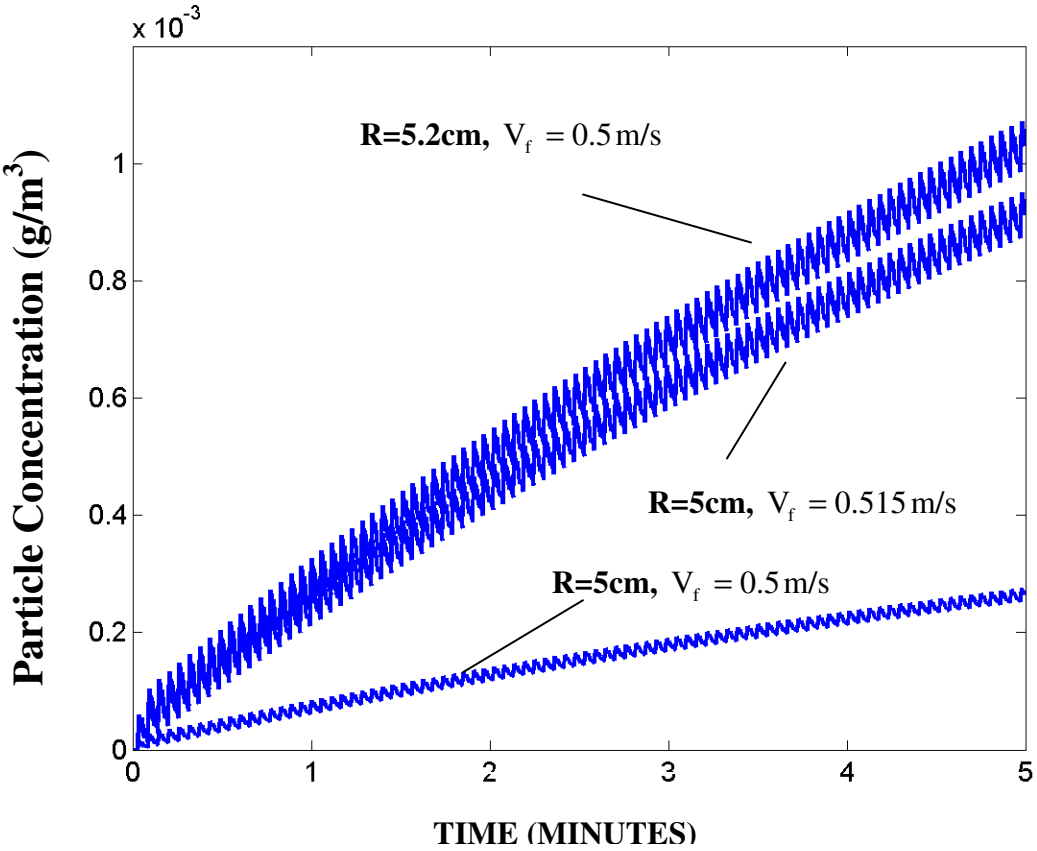

Figure 7-18. Variation of the particle mass concentration with the time at different foot size and step down velocity for resuspension of particles from a hard floor with roughness. (h=1.8mm, Δ_c = dual-Gaussian distribution, particle size=7.5-10μm)

Figures 7-19 to 7-21 show the variation of the particle resuspension rate with time for resuspension of 1-2μm, 2-5 μm and 5-10μm particles respectively from a hard floor. A dual-Gaussian distribution of Δ_c as shown in equations 7-30 and 7-31 is used in the simulation. A gap size of h=1.8 mm for shoe-floor contact, and foot stepping down velocity of $V_f = 0.5\,\text{m/s}$ for the Arizona dust were assumed in the simulation. The shoe radius of R=5cm was also considered. The experimental data of Qian and Ferro (2007) is plotted in these figures for comparison. Figures 7-19 to 7-21 show that the predicted particle resuspension rate is roughly constant and is comparable with the experimental data. It also can be seen that the resuspension rates for large particles are larger than that for small particles, which means that more large particles get resuspended.

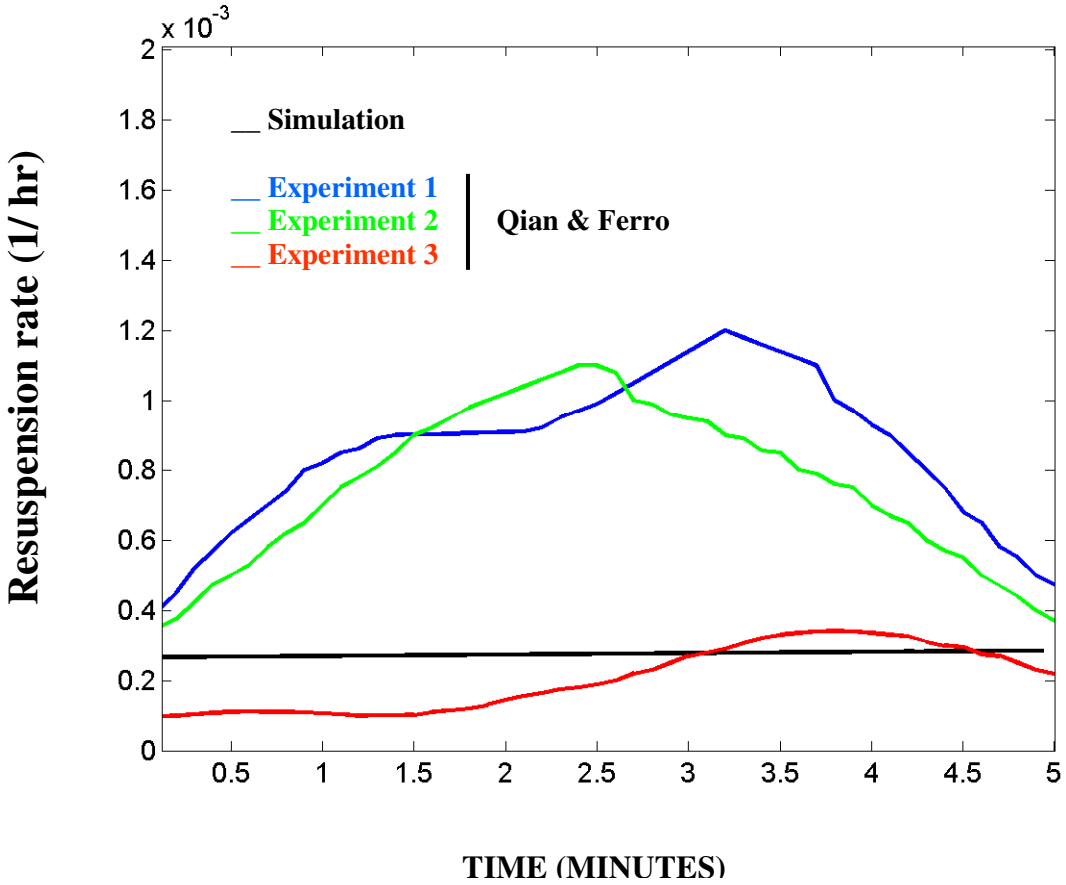

Figure 7-19. Variation of particle resuspension rate with time for resuspension of particles from a hard floor. (h=1.8mm, Δ_c = dual-Gaussian distribution, R=5cm, $V_f = 0.5\,\text{m/s}$, particle size = 1-2μm)

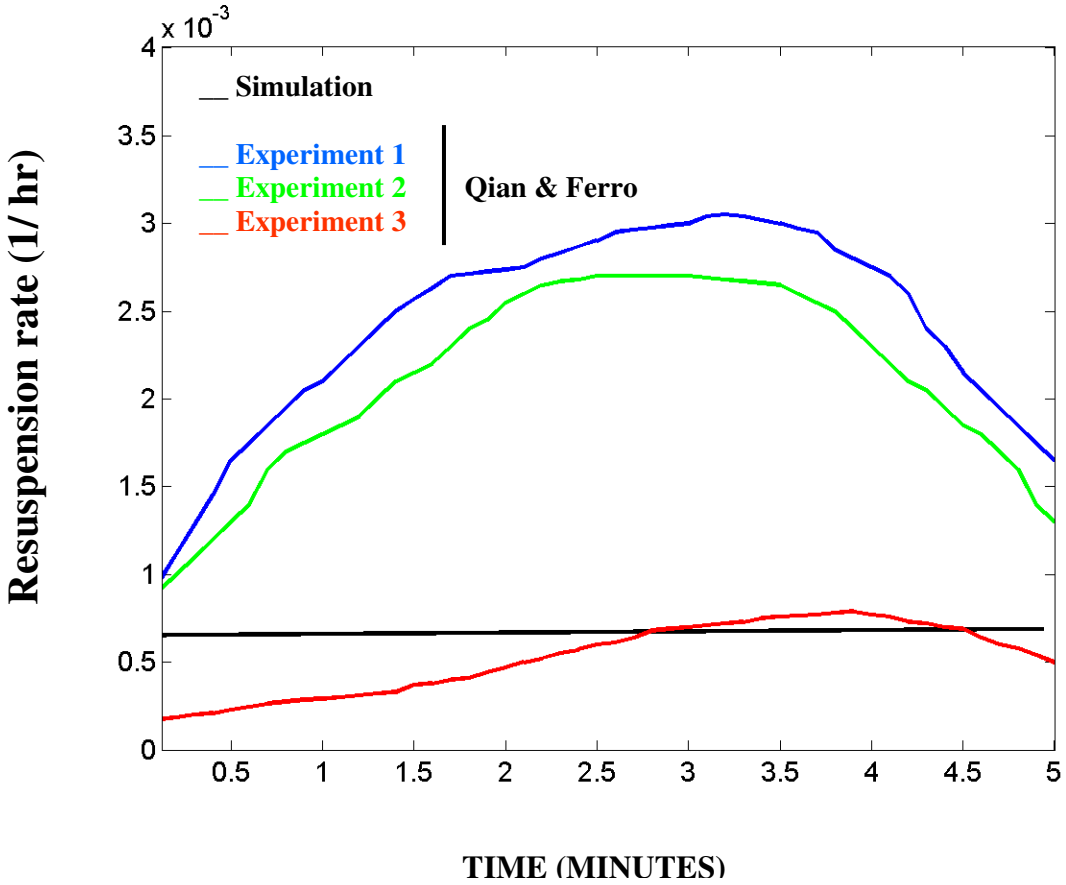

Figure 7-20. Variation of particle resuspension rate with time for resuspension of particles from a hard floor. (h=1.8mm, Δ_c = dual-Gaussian distribution, R=5cm, $V_f = 0.5\,\text{m/s}$, particle size = 2-5μm)

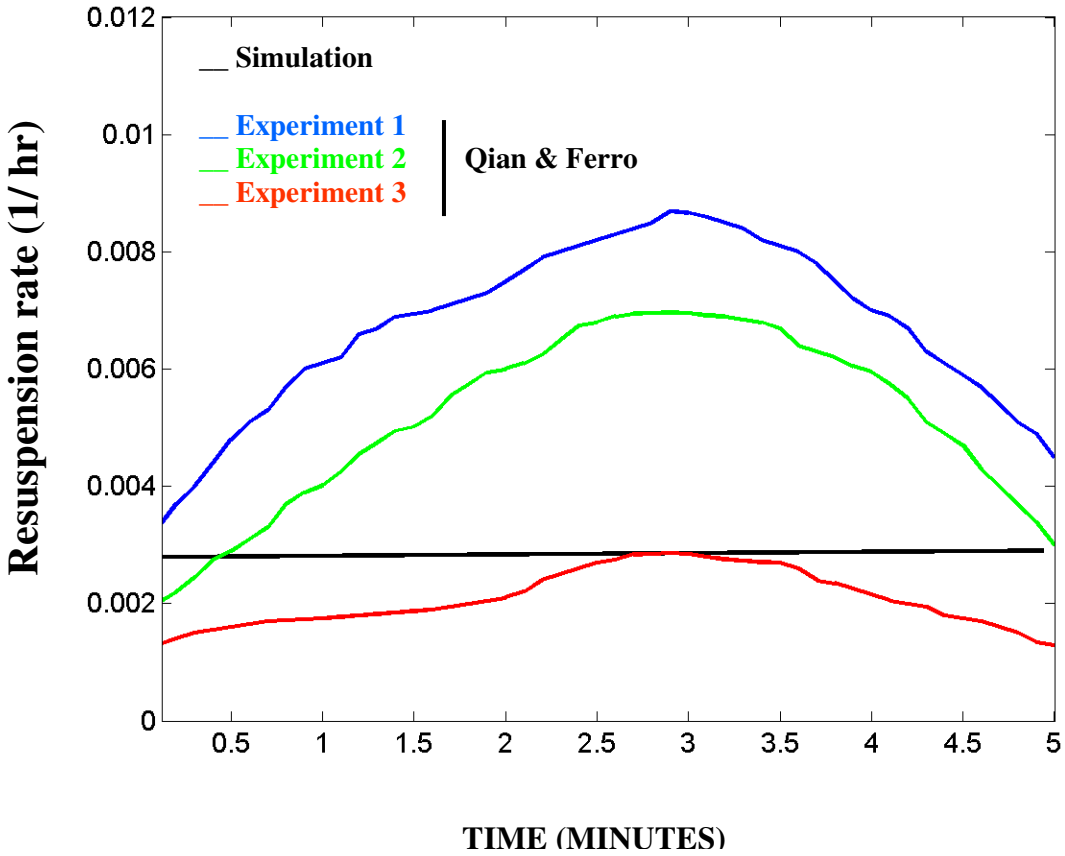

Figure 7-21. Variation of particle resuspension rate with time for resuspension of particles from a hard floor. (h=1.8mm, Δ_c = dual-Gaussian distribution, R=5cm, $V_f = 0.5\,\text{m/s}$, particle size = 5-10μm)

7.14 EMPIRICAL EQUATIONS FOR RESUSPENSION RATE

Based on the predicted resuspension rates, empirical equations for estimating the resuspension rate for practical application can be given as:

$$r = -9.496\times10^{-3} + 0.849\,R - 12.783\,h - 1.866\times10^{-2}\,V_f + 1.214\times10^{13}\,d^3 \qquad (7\text{-}65)$$

Figure 7-22 shows the comparison of the result obtained from equation (7-65) with the simulation result for variation of average particle resuspension rate with particle diameter. It can be seen that particle resuspension rate increases with particle diameter, and equation (7-65) can be used to approximately evaluate the average particle resuspension rate.

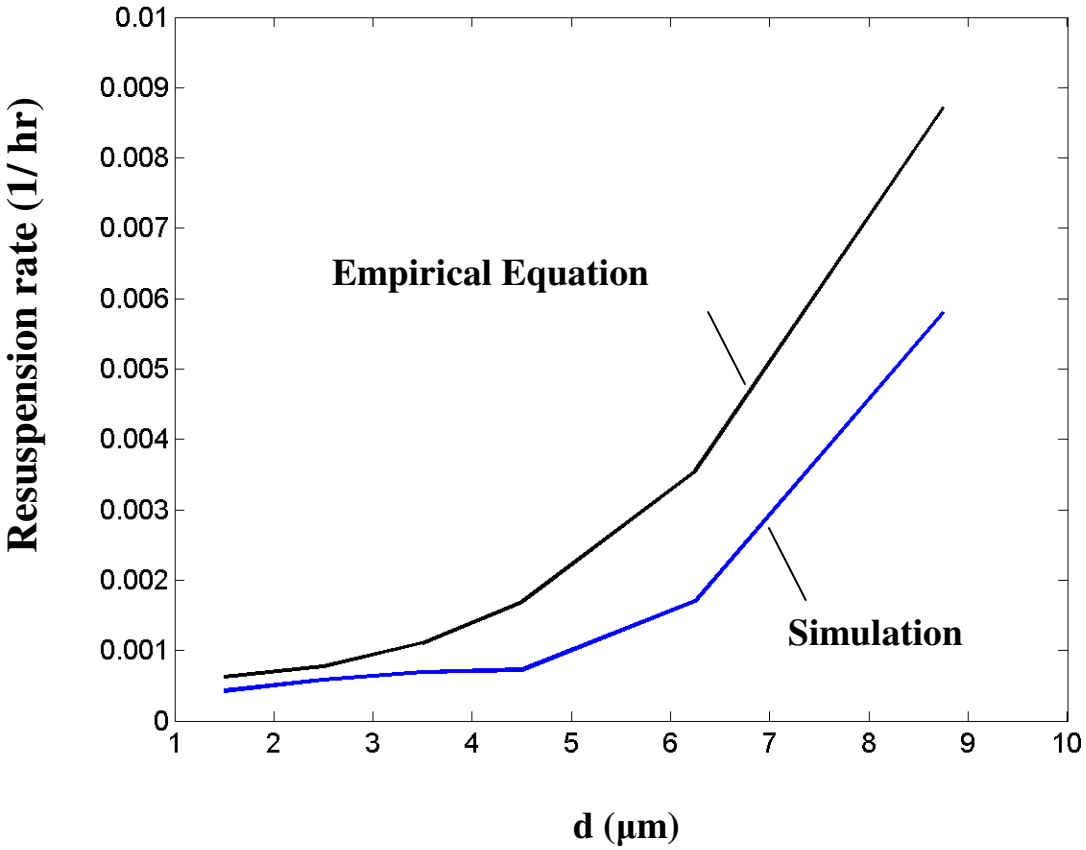

Figure 7-22. Variation of particle resuspension rate with particle diameter for resuspension of particles from a hard floor. (h=1.8mm, Δ_c = dual-Gaussian distribution, R=5cm, $V_f = 0.5\,\text{m/s}$)

7.15 CONCLUSIONS

A detailed model for particle detachment due to human walking in indoor environments is developed. The model accounts for the particle adhesion to the floor, and the airflow generated by stepping down and up of the foot during the gait cycle. The rate of particle resuspension and dispersion due to indoor human walking in an experimental chamber is simulated and the results are compared with the data. On the basis of the presented results, the following conclusions are drawn:

1. Shoe bottom groove depth, floor and particle roughness, foot size, background flow velocity as well as human activity velocity can affect the particle resuspension rate in the indoor environment. Shallower grooves, high roughness,

larger shoe, and high stepping velocity result in higher resuspended particle concentrations.

2. Larger particles are more easily detached, but also are more easily deposited. Smaller particles are more difficult to get detached, but are more easily resuspended. The overall effect is that more large particles get resuspended and larger particles have higher resuspension rate.
3. The simulation results are in agreement with the experimental data.

The present model can be easily used for resuspension of other materials. For example, it is found that cat hires are easier to get resuspended that dog's hires. If the mechanical properties of these hairs are known, then a simulation can be performed based on the present model.

7.16 ACKNOWLEDGEMENTS

The financial support of the Environmental Protection Agency (EPA) and the NYSTAR Center of Excellence at Syracuse University is gratefully acknowledged.

7.17 NOMENCLATURE

a	contact radius (m)
a_e	air exchange rate of the chamber (s^{-1})
B_h	average shoe bottom height for the stepping up process
C_c	Cunningham factor (dimensionless)
C_D	drag coefficient (dimensionless)
$C_{m(n-1)}$	particle mass concentration in the cloud at the end of the (n-1)th step period (kgm^{-3})
C_{mn}	particle mass concentration in the cloud at the end of the n step period (kgm^{-3})
C_n	local particle mass concentrations at the end of the nth step period (kgm^{-3})
C_{n-1}	local particle mass concentrations at the end of (n-1)th step period (kgm^{-3})
D	diffusion coefficient (m^2s^{-1})

d	particle diameter (m)
E	Young modulus of material i (Nm^{-2})
f_d	coefficient used in drag coefficient calculation (dimensionless)
F_g	gravity force (N)
F_L	lift force (N)
F_{Lsaff}	Saffman lift force (N)
F_{po}	pull-off force (N)
f_{po}	maximum force sustained by adhesion before separation of individual asperities (N)
F_{po}^{JKR}	pull-off force evaluated by JKR model (N)
g	acceleration due to gravity force (ms^{-2})
g_w	wall effect coefficient (dimensionless)
H_0	position of the equilibrium separation (m)
H	Groove depth (m)
h	gap size (m)
K	composite Young's modulus (Nm^{-2})
k_f	coefficient of static friction for particle-surface interface (dimensionless)
k	Boltzmann constant, J/K.
k_d	particle deposition rate ($s^{-1)}$
Kn	Knudson number (dimensionless)
m	particle mass (kg)
m_d	particle mass for given size d on the floor (kg)
M_{dn}	mass of deposited particles in the nth step period (kg)
$M_{s(n-1)}$	mass of suspended particles in the cloud in the n-1 step period (kg)
M_t	hydrodynamic moment (N·m)
N	number of asperities per unit area (m^{-2})
n_{max}	the number of steps that a cloud need to take all the chamber volume (dimensionless)

p	pressure (Nm^{-2})
P	applied normal load on particle (N)
R	radius of heel or toe of the shoe (m)
r	resuspension rate (1/hr)
r_{in}^{c}	critical radius for particle detachment in the range of r<R (m)
r_{in}^{s}	critical radius where lift force equals gravity force in the range of r<R (m)
r_{out}^{c}	critical radius for particle detachment in the range of r>R (m)
r_{out}^{s}	critical radius where lift force equals gravity force in the range of r>R (m)
Re	air flow Reynolds number (dimensionless)
R_{eG}	nondimensional number (dimensionless)
Re_s	particle Reynolds number (dimensionless)
S_c	Schmidt number (dimensionless)
$S_{chamber}$	cross-section area of the chamber (m^2)
S_{floor}	cross-section area of the floor (m^2)
S_n	average cross-section area of the particle cloud in the nth step period (m^2)
S_{z0}	cloud expansion distance in vertical direction for the first step period (m)
U_d	particle deposition velocity (ms^{-1})
U^*	shear velocity (ms^{-1})
$V_{chamber}$	the volume of the chamber (m^3)
V_{cn}	the volume of the particle cloud in the end of the nth step period (m^3)
$V_{c(n-1)}$	the volume of the particle cloud in the end of the n-1 step period (m^3)
V_f	foot stepping down or up velocity (ms^{-1})
V_r	air flow in r direction (ms^{-1})
V_{rmax}	the maximum value of V_r (ms^{-1})
V_z	air flow in z direction (ms^{-1})
W_A	thermodynamic work of adhesion (J/m^2)

Greek letters

α_r relative approach between the particle and surface (m)

α_0 nondimensional number (dimensionless)

β radius of an asperity (m)

$\dot{\gamma}$ shear rate (s^{-1})

Δ_c nondimensional number (dimensionless)

Δt time period for a step (s)

δ_c maximum extension of the tip of an asperity (m)

ε nondimensional number (dimensionless)

λ air mean free path of air (m)

μ air dynamic viscosity (pas)

μ_1 expect value of the first Gaussian distribution of Δ_c

μ_2 expect value of the second Gaussian distribution of Δ_c

σ_1 standard deviation of the first Gaussian distribution of Δ_c.

σ_2 standard deviation of the second Gaussian distribution of Δ_c.

ν air kinematic viscosity (m^2s^{-1})

ν_i the Poisson ratio of material i (dimensionless)

ρ_p density of material (kgm^{-3})

ρ air density (kgm^{-3})

σ standard deviation of the height distribution (m)

τ dimensional particle relaxation time (s)

τ^+ nondimensional particle relaxation time (dimensionless)

7.18 REFERENCES

Ahmadi, G. Guo, S. & Zhang, X. Particle Adhesion and Detachment in Turbulent Flows Including Capillary Forces. Particulate Science and Technology, Vol. 25, 1-18 (2007).

Berkeley, R.C.W. Microbial Adhesion to Surfaces. England: Chichester. 93-113 (1980).

Bowling, R.A. An analysis of Particle Adhesion on Semiconductor Surfaces. J. Electrochem. Soc., Vol. 132, 2208-2219 (1985).

Cham, R. & Redfern, M.S. Changes in gait when anticipating slippery floors. Gait and Posture, Vol. 15, 159-171 (2002).

Derjaguin, B.V., Muller, V.M. & Toporov, Yu. P. Effect of Contact Deformation on the Adhesion of Particles. J. Colloid Interface Sci., Vol. 53 314-326 (1975).

Ferro, A.R., Kopperud, R.J., & Hildemann, L. M. Source strengths for indoor human activities that resuspend particles. Environmental Science and technology. Vol. 38 (6), 1759-1764 (2004)

Friedlander, S.K. Smoke, Dust and Haze, John Wiley, New York (1977).

Fuchs, N.A. The Mechanics of Aerosols, MacMillan, New York (1964).

Fuller, K.N.G. & Tabor, D. Proc. R. Soc. London, Ser. A. 345, 327-340 (1975).

Glauert, M.B. The wall jet, J. Fluid Mech., Vol. 1, 625-643 (1956).

Greenwood, J.A. & Williamson, J.B.P. The contact of nominally flat surfaces. Proc. Roy. Soc., A. Vol. 295, 300-319 (1966).

Henty, J.R., Wood, D.E. & Ewins, D.J. student presentation, 4th Annual Conference of the International Functional Electrical Stimulation Society, August 23-27, Sendai, Japan. (1999).

Ibrahim, A.H., Dunn, P.F. & Brach, R.M. Microparticle Detachment from Surfaces Exposed to Turbulent Air Flow: Controlled Experiments and Modeling. J. Aerosol Science, Vol. 34, 765-782 (2003).

Johnson, K.L., Kendall, K. & Roberts, A. D. Surface Energy and Contact of Elastic Solids. Proc. Royal. Soc., Lond. A Vol. 324, 301-313. (1971).

Khalifa, H. Ezzat & Elhadidi, Basman. Particle Levitation Due to a Uniformly Descending Flat Object. Aerosol Science and Technology, Vol. 41:1, 33-42 (2007).

Krupp, H. Particle Adhesion: Theory and Experiment. Adv. Colloid Interface Sci., Vol.

1, 111-140 (1967).

Leal, L. G. Laminar Flow and Convective Transport Processes, Butterworth-Heinemann, Stoneham, MA, (1992).

Long, C.M., Suh, H.H. & Kouitrakis, P. Characterization of indoor particle sources using continuous mass and size monitors. Journal of the Air & Waste Management Association, Vol. 50 (7),1236-1250 (2000).

Long, C.M., Suh, H.H., Catalano, P. J. & Kouitrakis, P. Using time- and size-resolved particulate data to quantify indoor penetration and deposition behavior. Environmental Science and technology, Vol. 35, 2089-2099 (2001).

Maedler, L., & Koch, W. Particle Resuspension from Surfaces by Impacting Objects. J. Aerosol Sci. 28:S85-S86 (1997).

Maedler, L., & Koch, W. Particle Resuspension Burst from Dust Layers Induced by Impacting Objects. J. Aerosol Sci. 30:S731-S732 (1999).

Mei, R. An Approximate Expression For the shear Lift Force on a spherical Particle at Finite Reynolds number, Int. J. Multiphase Flow, Vol. 18, 145-147 (1992).

Munir, A.K.E., Einarsson, R. & Dreborg, S.K.G. Mite (Der-P-I, Der-F-I), Cat (Fel-D-I) and Dog (Can-F-I) Allergens in Dust from Swedish Day-Care-Centers. Clinical and Experimental Allergy, Vol. 25, 119-126 (1995).

Maugis, D. & Pollock, H.M. Surface Forces, Deformation and Adherence at Metal Microcontacts. Acta Metall. 32, 1323-1334 (1984).

O'Neill, M.E. A sphere in contact with a plane wall in slow linear shear flow. Chem. Eng. Sci. 23, 1293-1298 (1968).

Pachi, A. & Ji, T. Frequency and velocity of people walking. The structural engineer, Vol. 83:3, pp.36-39 (2005).

Podczeck, F., Newton, J.M. &. James, M.B. Influence of Relative Humidity of Storage Air on the Adhision and Autoadhesion of Micronized particles to Particulated and Compacted Powder Surfaces. J. Colloid Interface Science, Vol. 187, 484–491 (1997).

Qian, J. & Ferro, A.R. Resuspension of Dust Particles in a Chamber and Associated Environmental Factors, Aerosol Science and Technology, accepted (2008).

Roberts, J.W., Glass, G. & Mickelson, L. A pilot study of the measurement and control of deep dust, surface dust, and lead in 10 old carpets using the 3-spot test while

vacuuming. Archives of Environmental Contamination and Toxicology, Vol. 48, 16-23 (2004).

Robinson, P., Thomas, J. & Behar, J.V. Time spent in activities, locations, and microenvironments: a California-national comparison. EPA Report 9EPA/600/4 -91/006, Las Vegas, NV: U.S. EPA. (1991).

Rullo, V.E.V., Rizzo, M.C., Arruda, L.K., Sole, D. & Naspitz, C.K. Daycare centers and schools as sources of exposure to mites, cockroach, and endotoxin in the city of San Polo, Brazil. Journal of Allergy and Clinical Immunology, Vol. 110 (4), 582-588 (2002).

Soltani, M. & Ahmadi, G. On Particle Adhesion and Removal Mechanics in Turbulent Flows. J. Adhesion Sci. Tech., Vol. 8, 763-785 (1994).

Soltani, M. & Ahmadi, G. Particle Detachment from Rough Surfaces in Turbulent flows. J. Adhesion, Vol. 51, 105-123. (1995a).

Soltani, M. & Ahmadi, G. Direct Numerical Simulation of Particle Entrainment in Turbulent Channel Flow. Physics Fluid, A. Vol. 7, 647-657 (1995b).

Soltani, M., Ahmadi, G., Bayer, R.G. and Gaynes, M.A., Particle Detachment Mechanisms from Rough Surfaces Under Base Acceleration, J. Adhesion Science Technology Vol. 9, 453-473 (1995).

Tabor, D. Surface Forces and Surface Interaction . J. Colloid Interface Sci., Vol. 58, 2-13 (1977).

Thatcher, T.L. & Layton, D.W. Deposition, resuspension, and penetration of particles within a residence. Atmospheric Environment, Vol. 29(13), 1487-1497 (1995).

Tsai, C.J., Pui, D.Y.H. & Liu, B.Y.H. Particle Detachment from Disk Surfaces of Computer Disk Drives. Aerosol Sci. Tech., Vol. 22, 737-764 (1991).

Visser, J. On Hamaker Constants: A Comparison Between Hamaker Constants and Lifshitz-van der Waals Constants. Adv. Colloid Interface Sci., Vol. 3, 331-363 (1972).

Wang, H.C. Effect of Inceptive Motion on Particle Detachment from Surfaces. Aerosol Sci. Tech., Vol. 13, 386-396 (1990).

Yakovleva E, Hopke PK, and Wallace L. Receptor modeling assessment of Particle Total Exposure Assessment Methodology Data. Environ. Sci. Technol., Vol. 33, 3645-3652 (1999).

Ziskind, G., Fichman, M. & Gutfinger, C. Adhesion Moment Model for Estimating Particle Detachment from a Surface, J. Aerosol Sci., Vol. 28 (4), 623-634 (1997).

Zhang, X. & Ahmadi, G. Effects of Capillary and Deformation on Particle Removal in Turbulent Flows, Journal of Adhesion Science and Technology, Vol. 21, 1589-1611 (2007).

The content of this chapter is partly published in J. Adhesion Sci. Technol., (2008)

CHAPTER 8. CONCLUSIONS AND FUTURE WORKS

8.1 CONCLUSIONS

8.1.1 General

This thesis is concerned with numerical studies of gas-liquid-solid flows in bubble columns, particle removal in turbulent flows and particle resuspension and transport due to indoor human walking. A series of new models and approaches are developed. The results are compared with the experimental data and good agreements are observed.

8.1.2 Gas-liquid-solid flows in three–phase slurry reactors

An Eulerian-Lagrangian computational model for simulations of gas-liquid-solid flows in three–phase slurry reactors is presented. The two-way interactions between bubble-liquid and particle-liquid are included in the analysis. Particle-particle interactions and bubble-bubble interactions are accounted for by the hard sphere model approaches, and the bubble coalescence is also included in the model. The transient characteristics of three-phase flows are studied and the effects of bubble size, gravity and G-jitter acceleration on variation of flow patterns are discussed. On the basis of the presented results, the following conclusions are drawn:

For the three-phase flows in the bubble column with gravity, it is found that the transient characteristics of the three-phase flow in the bubble column are dominated by time-dependent staggered vortices. The bubble plumes move along S-shape paths and exhibit an oscillatory behavior. Highest particle concentrations occur in the regions with high liquid velocities. Some bubbles can be captured by the staggered vortices. Bubble upward velocities are much larger than both particle and liquid velocities, but bubble downward velocities are, however, smaller than both particle and liquid velocities. The location of the maximum upward velocities of bubbles, particles and liquid can be different, because of the relaxation effects at the driving of bubbles to the liquid, and the liquid transportation to particle. The bubble volume fraction increases with the evolution of the flow. The highest bubble volume fraction is located at the bottom of the column. The Sauter mean diameter of the bubbles are proportional to the time the bubbles stay.

Due to bubble-bubble coalescence, bubble diameter not only increases along the column height, but also increases with development of the flow. Bubble size and the gravity have major effect on the characteristics of the three-phase flow. Larger bubbles significantly increase the development of the flow characteristics and result in higher bubble, particle and liquid velocities and higher bubble plume oscillation frequency. For the three-phase flows under high gravity, the phase velocities are larger than that of the flow under low gravity, therefore, the flow develops fast. However, due to less bubble-bubble collision and coalescence, bubbles in the high gravity flow are smaller. Besides, there are less separate bubbles in the flow due to high inertia of the bubble plume, and bubble volume fraction is smaller in the flow because of the high bubble velocities.

For the three-phase flows with zero gravity, bubbles accumulate at the bottom of the column and move very slowly, and liquid level is much higher than that of the flow with normal gravity. The flow in zero-gravity has low phase velocities and phase mixing. The velocities of bubbles, liquid and particles are in the same order. Due to more bubble-bubble collision and coalescence, bubbles can become very large. The effect of G-jitter acceleration on the gas-liquid-particle three flows is small.

8.1.3 Particle removal in turbulent flows

Particle resuspension including the effect of electrostatic and capillary forces using different adhesion theories and a new rolling detachment model in turbulent flows is studied. An effective thermodynamic work of adhesion model is developed. The effect of electrostatic force and capillary force for hydrophilic materials is included in the study with the use of an effective thermodynamic work of adhesion. Expressions for the maximum moment due to the applied normal load and the critical shear velocity for particle rolling removal are given and the results are compared with the available experimental data. It is found that the model predictions are in good agreement with the experimental data. The results show that the capillary effect significantly increases the critical shear velocity, while the electrostatic forces only have major effects on the increases of the critical shear velocity for large particle detachment. For elastic deformation at the interface, the critical shear velocity predicted by the JKR adhesion model is somewhat higher than that predicted by the DMT model. The Maugis-Pollock

model that accounts for the plastic surface deformation leads to the lowest critical shear velocity for the materials studied in the present work. For the particles of the same material with different diameters, the capillary effect increases the critical shear velocity by about the same order. The relative importance of the capillary force varies depending on the particle and substrate materials. When Coulomb force and dielectrophoretic force are directed towards the substrate, the relative effects of the electrostatic forces decrease in the presence of capillary effects. However, when Coulomb force and dielectrophoretic force are directed away from the substrate, the relative effects of the electrostatic forces increase. These relative effects are material dependent. Under a strong electric field, Coulomb force and dielectrophoretic force significantly decrease the critical shear velocity for large particle rolling removal. For particles in an electric field of 5000 kV/m or 10000kV/m with Boltzmann charge or saturation charge distribution, the critical shear velocity decreases with the increase of the particle diameter; While for particles with fixed 20μC/g charge distribution, the critical shear velocity decreases with the increase of the particle diameter for small particles, but increases with the increase of the particle diameter for large particles. When Coulomb force and dielectrophoretic force are directed towards the substrate, shear velocities for large particles with fixed 20μC/g charges are higher than that with Boltzmann and saturation charges; While shear velocities for smaller particles with fixed 20μC/g charges are higher than that with Boltzmann charge but lower than that with saturation charge; For very small particles, shear velocities for particles with Boltzmann, saturation and fixed 20μC/g charges are almost same.

8.1.4 Particle resuspension and transport due to indoor human walking

A detailed model for particle detachment due to human walking is developed. The model accounts for the particle adhesion to the floor, and the evaluation of the velocity of the airflow generated by stepping down and up motions of the foot during the gait cycle. The effect of surface roughness is included in the analysis and the roughness parameter is assumed to have a dual-Gaussian distribution. The recapture effect of the falling disk to the resuspended or detached particles is also included. The rate of particle resuspension and dispersion is simulated and the results are compared with the experimental data. It is found that the simulation results are in agreement with the experimental data. The results

show that the shoe bottom groove depth, floor and particle roughness, foot size, background flow velocity as well as human activity velocity can affect the particle resuspension rate. Shallower grooves, high roughness, larger shoe, and high stepping velocity result in higher resuspended particle concentrations. Larger particles are more easily detached, but also are more easily deposited. Smaller particles are more difficult to get detached, but are more easily resuspended.

8.2 FUTURE WORK

This section summarized the future works for different sections.

8.2.1 Gas-liquid-solid flows in three–phase slurry reactors

In general, flows in bubble columns are related with turbulence and chemical reaction. We plan to add turbulence model and chemical reaction to the current code, so that the new code can be used to perform a series of computational studies on gas-liquid-solid three-phase turbulent bubbly flows with chemical reaction.

8.2.2 Charged particle removal in turbulent flows

Hays (1978, 1983) studied the detachment of charged tone particles under an electric field and suggested that the large adhesion force is due to the electrostatic imagine force of nonuniformly charged tone particles where the charges were concentrated on particle asperities. For charged particles under an electric field, we plan to study charge on bumpy particles, charge on rough particles and charge on particles in a substrate with large roughness (must larger than particle size), because all the particles are rough particles, more or less. There is no real smooth particle in the world.

8.2.3 Particle resuspension and transport due to indoor human walking

The study reported in chapter 7 is focused on particle resuspension from hard floors. To study the effects of carpets on particle resuspension, we planned to perform the following studies:

- Develop a model for evaluating airflow generated by human walking on a typical carpeted floor.
- Develop a model for evaluating particle detachment from carpet fibers due to the

airflow.

- Evaluate the critical radii for detachment of particles from carpets due to human walking..
- Evaluate the particle resuspension rate from carpets due to walking.

8.3 Reference

Hays, D. A., Photogr: Sci. Eng. 22. 232-235 (1978).

Hays, D. A., Electrostatics Inst. Phys. Conf. Ser. No. 66. p. 237. The Institute of Physics. London (1983).

PUBLICATIONS

REFEREED JOURNAL ARTICLES:

1. **Xinyu Zhang** and Goodarz ahmadi, Effects of Electrostatic and Capillary Forces and Surface Deformation on Particle Detachment in Turbulent Flows, Journal of Adhesion Science and Technology (submitted).

2. **X. Zhang** , J. Qian, A. Ferro and G. Ahmadi, Particle Detachment, Resuspension and Transport Due to Human Walking in Indoor Environments, Journal of Adhesion Science and Technology, Vol. 22, Issue: 5-6, pp. 591-621. 2008.

3. **Xinyu Zhang** and Goodarz ahmadi, Rolling Particle Removal in Turbulent Flows-Effects of Capillary and Deformation, Journal of Adhesion Science and Technology, Vol. 21, No. 16, pp. 1589-1611, 2007.

4. Goodarz Ahmadi, shiguanjg Guo and **Xinyu Zhang**, Particle Adhesion and Detachment in Turbulent Flows Including Capillary Forces, Particulate Science and Technology 25: no.1, pp.59-76, 2007.

5. **Xinyu Zhang** and Goodarz ahmadi, Eulerian-Lagrangian Simulations of Liquid-Gas -Solid Flows in Three-Phase Slurry Reactors, Chemical Engineering Science 60 (2005) 5089 -5104.

REFEREED CONFERENCE PUBLICATIONS:

1 . **X. Zhang** , G. Ahmadi, J. Qian and A. Ferro, A New Model on Evaluation of the Electrostatic Effect on Particle Detachment Due to Human Walking, 28th Annual Conference of American Association for Aerosol Research, 2009 , October 26-30, Hyatt Regency Minneapolis, Minneapolis, Minnesota, USA.

2. **Xinyu Zhang** and Goodarz Ahmadi, Micro Particles Detachment in Turbulent Flows with Electrostatic and Capillary Effects and Surface Deformation, Proceedings Of FEDSM2009, 2009 ASME Fluids Engineering Summer Meeting, August 2-5, 2009, Vail Cascade Resort and Spa in Vail, Colorado.

3. **X. Zhang,** J. Qian, G. Ahmadi and A. Ferro, Resuspension of Indoor Particles From Floor Due to Human Walking, 27th Annual Conference of American Association for Aerosol Research, 2008, October 20-24, Orlando, Florida,, USA.

4 .**X. Zhang** , G. Ahmadi, Effects of Electrostatic and Capillary Forces and Surface Deformation on Particle Detachment in Turbulent Flows, 27th Annual Conference of American Association for Aerosol Research, 2008 , October 20-24, Orlando, Florida,, USA.

5. **X. Zhang** , J. Qian, A. Ferro and G. Ahmadi, A Model for Resuspension of Particles Due to Human Walking including Electrostatic Effects , 26th Annual Conference of American Association for Aerosol Research, 2007 , September 24-28, Reno, Nevada, USA.

6. **X. Zhang** and G. Ahmadi, Adhesion and Removal Mechanism for Particles in Turbulent flows with Electrostatic Effects, 26th Annual Conference of American Association for Aerosol Research, 2007 , September 24-28, Reno, Nevada, USA.

7. **Xinyu Zhang** and Goodarz Ahmadi, Simulations of Three-phase Liquid-Bubble-Solid Flows under Variable Gravitation Conditions, Proceedings of International Conference on Multiphase Flow, 9.-13.July, 2007. Leipzig,Germany.

8. **Xinyu Zhang** and Goodarz Ahmadi, Particle Resuspension and Transport Due to Human Walking in Indoor Environment, Proceedings of International Conference on Multiphase Flow, 9.-13. July, 2007. Leipzig,Germany.

9. **X. Zhang** and G. Ahmadi, Adhesion and Removal Mechanism for Particle in Turbulent flows with Capillary Effect, International Aerosol Conference 2006, September 10-15, Radisson Riverfront Hotel, St. Paul, Minnesota, USA.

10**. X. Zhang** , J. Qian, A. Ferro and G. Ahmadi, A Model for Particle Resuspension Due to Human Walking, International Aerosol Conference 2006, September 10-15, Radisson Riverfront Hotel, St. Paul, Minnesota, USA.

11. **X. Zhang** and G. Ahmadi, Liquid-Gas-Solid Three-Phase flows in Microgravity, 24nd Annual

AAAR Conference, October 17-21, 2005. Hilton Austin, Austin, TEXAS.

12. Goodarz Ahmadi and **Xinyu Zhang**, Three-Phase Liquid-Gas-Solid Flows in a Bubble Column, Proceedings Of FEDSM2005, 2005 ASME Fluids Engineering Division Summer Meeting and Exhibition, June 19-23, 2005, Houston, TX, USA.

13. **Xinyu Zhang** and Goodarz Ahmadi, A Study of Three-Phase Liquid-Gas-Solid Flows in Microgravity, Proceedings of 79th ACS Colloid and Surface Science Symposium, June 12-15, 2005, Potsdam, NY, USA.

14. **X. Zhang** and G. Ahmadi,Turbulent Three-Phase Flows in a Bubble Column, 23rd Annual AAAR Conference, October 4-8, 2004. Atlanta, Georgia, USA.

15. **X. Zhang** and G. Ahmadi, Three-phase Turbulent Flows in a Bubble Column, 22nd Annual AAAR Conference, October 22-24, 2003. Hilton Anaheim Hotel, Anaheim, California, USA.

16. Goodarz Ahmadi and **Xinyu Zhang**, Gas-Liquid-Particle Three-Phase Flows in Bubble Columns, Proceedings Of ASME-FED/JSME Summer 2003 Meeting 8th International Symposium on Gas-Liquid Flows, July 6-10, 2003, Sheration Waikiki Hotel, Honolulu, Hawaii.

17. **X. Zhang** and G. Ahmadi, Turbulent Three-phase Flows in Bubble Columns, 2003 AAARPM Conference, March 31-April 4, 2003, Pittsburgh, PA, USA.

18. **X. Zhang** and G. Ahmadi, Turbulent Gas-liquid-particle Three-phase Flows in Bubble Columns, 21st Annual AAAR Conference, October 6-12, 2002. Adams Mark Hotel, Charlotte, North Carolina, USA.

19. **X. Zhang** and G. Ahmadi, Gas-particle Two-phase Turbulent Flow in a Horizontal Channel, 20th Annual AAAR Conference, October 15-19, 2001. Doubletree Hotel Portland Lloyd Center, Portland, Oregon, USA.

NON-REFEREED CONFERENCE AND TECHNICAL MEETING POSTERS:

1. G**.** Ahmadi, **X. Zhang,** S. Guo**,** Irregular Charged Particle Adhesion and Removal, Symposium on Chemical-Mechanical Planarization, Crown Plaza Resort Hotel & Golf Club, Lake Placid, NY, August 9-12, 2009.

2. **X. Zhang,** J. Qian, G. Ahmadi and A. Ferro, Study of the Electrostatic Effect on Particle Detachment Due to Human Walking, The 2009 CAMP (the Center for Advanced Material Processing) Technical Meeting, Canandaigua, NY, May 13-15,2009.

3. **X. Zhang,** J. Qian, G. Ahmadi and A. Ferro, Application of the Capacitor Theory on Evaluation of the Electrostatic Effect on Particle Detachment Due to Human Walking, The Poster Session of the Center for the Environment, March 11, 2009, Cheel, Potsdam, NY, USA.

4. **X. Zhang** , G. Ahmadi, Particle Detachment in Turbulent Flows with Electrostatic and Capillary Forces and Surface Deformation, 2008 Syracuse Symposium on Environmental and Energy Systems, Oncenter Conference Center, Syracuse, NY, October 29- 30, 2008.

5. **X. Zhang,** J. Qian, G. Ahmadi and A. Ferro, Effect of Human Walking on Particle Resuspension, 2008 Syracuse Symposium on Environmental and Energy Systems, Oncenter Conference Center, Syracuse, NY, October 29- 30, 2008.

6. **X. Zhang,** J. Qian, G. Ahmadi and A. Ferro, Resuspension of Indoor Rough Particles Due to Human Walking, The CAMP (the Center for Advanced Material Processing)' Fall Meeting, Poster Session, October 16, 2008, Cheel, Potsdam, NY, USA.

7. **X. Zhang** and G. Ahmadi, Electrostatic and Capillary Effects on Particle Detachment in Turbulent Flows, The CAMP (the Center for Advanced Material Processing)' Fall Meeting, Poster Session, October 16, 2008, Cheel, Potsdam, NY, USA.

8. **X. Zhang** and G. Ahmadi, Particle Detachment with Electrostatic and Capillary Forces in Turbulent Flows, The 2008 CAMP (the Center for Advanced Material Processing) Technical

Meeting, Canandaigua, NY, May 14-16,2008.

9. **X. Zhang** and G. Ahmadi, A Study of Indoor Particle Resuspension via Human Activity Clarkson's Biomedical Engineering, Science, and Technology (BEST) Spring 2008 Conference, Clarkson University, Potsdam, NY, USA. April 23, 2008.

10. **X. Zhang** and G. Ahmadi, J. Qian and A. Ferro, Particle Resuspension from Floor via Human Activity, The Center for Environment get together/open house /poster session, February 07, 2008, Barben Room, Cheel, Clarkson University.

11. **X. Zhang,** J. Qian, G. Ahmadi and A. Ferro, Particle Resuspension from Floor Due to Human Walking, 2007 Syracuse Symposium on Environmental and Energy Systems, Oncenter Conference Center, Syracuse, NY, October 22- 23, 2007.

12. **X. Zhang** and G.Ahmadi, Adhesion and Removal Mechanism for Particles in Turbulent flows with Electrostatic and Capillary Effects, 2007 Syracuse Symposium on Environmental and Energy Systems, Oncenter Conference Center, Syracuse, NY, October 22- 23, 2007.

13. **X. Zhang** and G. Ahmadi, Particle Adhesion and Removal Mechanism in Turbulent flows with Electrostatic Forces, CAMP (the Center for Advanced Material Processing)'s Fall Meeting, Poster Session, October 16, 2007, Cheel, Potsdam, NY, USA.

14. **X. Zhang** and G. Ahmadi, Particle Rolling Detachment in Turbulent Flows with Capillary and Deformation, The 2007 SAC Project Review, July 31, 2007, Link Hall, Syracuse University, NY, USA.

15. **X. Zhang** and G. Ahmadi, A Practical Model for Indoor Particle Resuspension Due to Human Walking , The 2007 SAC Project Review, July 31, 2007, Link Hall, Syracuse University, NY, USA.

16. **X. Zhang** and G. Ahmadi, Indoor Particle Resuspension Due to Human Walking , The 2007 CAMP (the Center for Advanced Material Processing) Technical Meeting, Canandaigua, NY, May 16-18,2007.

17. **X. Zhang** and G. Ahmadi, A Model for Particle Adhesion and Removal in Turbulent Flows with Capillary Effect, The 2007 CAMP Technical Meeting, Canandaigua, NY, May 16-18,2007.

18. **X. Zhang** , J. Qian, A. Ferro and G. Ahmadi, Indoor Particle Detachment and Resuspension Due to Human Activity, The Center for Environment get together/open house /poster session, February 2, 2007, Barben Room, Cheel, Clarkson University.

19. **X. Zhang** , J. Qian, A. Ferro and G. Ahmadi, Particle Resuspension Due to Human Walking – A Practical Model, The 6th Annual Syracuse COE Symposium, October 30-31, 2006,Marx Hotel and Conference center, Syracuse.

20. **X. Zhang**, J. Qian, A. Ferro and G. Ahmadi, Resuspension of particles from floor due to human activities, CAMP (the Center for Advanced Material Processing)'s Fall Meeting poster session, October 19, 2006, Cheel, Potsdam, NY, USA.

21. **X. Zhang** and G. Ahmadi, Particle adhesion and Removal Mechanism in Turbulent Flows with Capillary Effect, The 2006 CAMP (the Center for Advanced Material Processing) Technical Meeting, Canandaigua, NY, May 17-19,2006.

22. **X. Zhang** and G. Ahmadi, Particle adhesion and Removal in Turbulent Flows with Capillary Forces, 2005 Syracuse Syposium on Environmental and Energy Systems, October 24-25, 2005. Sheraton Syracuse University Hotel & Conference Center, Syracuse, New York.

23. **X. Zhang** and G. Ahmadi, Industrial Applications of Three-Phase Slurry Reactors, CAMP (the Center for Advanced Material Processing) 2005 Fall Meeting, Cheel Campus Center, Potsdam, NY, USA.

24. **X. Zhang** and G. Ahmadi, Liquid-Gas-Solid Three-Phase Slurry Reactor in Microgravity, The 2005 CAMP (the Center for Advanced Material Processing) Technical Meeting, Canandaigua, NY, May 11-13, 2005.

25. **X. Zhang** and G. Ahmadi, Numerical Simulations of Turbulent Three-phase Bubbly flows in a Bubble Column, The 2004 CAMP (the Center for Advanced Material Processing)

Technical Meeting, Canandaigua, NY, May 12-14, 2004.

26. **X. Zhang** and G. Ahmadi, Numerical Simulations of Three-phase Bubbly Flows in a Bubble Column, CAMP (the Center for Advanced Material Processing)'s poster session, October 16, 2003, Cheel, Potsdam, NY, USA.

27. G. Ahmadi and **X. Zhang,** Three Phase Flows in a Bubble Column, Department of Energy. Morgontown, July, 2003.

28. **X. Zhang** and G. Ahmadi, Gas-liquid-particle Three-phase Flows in a Bubble Column, Annual Technical Meeting of the Center for Advanced Material Processing (CAMP),May 14-16, 2003, Gideon-Putnam hotel, Saratoga Spring,NY,USA.

29 .**X. Zhang** and G. Ahmadi, Three-phase Slurry Gas-liquid-particle Flows in a Bubble Column, Annual Technical Meeting of the Center for Advanced Material Processing (CAMP),May 13-15, 2002,Gideon Putnam hotel,Saratoga Spring,NY,USA.

30. **X. Zhang** and G. Ahmadi, Eulerian-Lagrangian Simulations of Liquid-gas-solid Flows in Three-phase Slurry Reactors, CAMP (the Center for Advanced Material Processing)'s poster session, October 18, 2001, Cheel, Potsdam, NY, USA.

31. **X. Zhang** and G. Ahmadi, Gas-liquid-particle Three-phase Turbulent Flow in a Bubble Column, Annual Technical Meeting of the Center for Advanced Material Processing (CAMP), May 15, 2001, Gideon- Putnam hotel,Saratoga Spring,NY,USA.